CO_2 interaction with aquifer and seal on geological timescales: the Miller oilfield, UK North Sea

Jiemin Lu

Ph.D.

University of Edinburgh

2008

Declaration

This dissertation is entirely my own work except where indicated otherwise.

Jiemin Lu

ABSTRACT

CO_2 interaction with aquifer and seal on geological timescales

Ph.D., University of Edinburgh, 2008

Jiemin Lu

Carbon Capture and Storage (CCS) has been identified as a feasible technology to reduce CO_2 emissions whilst permitting the continued use of fossil fuels. Injected CO_2 must remain efficiently isolated from the atmosphere on a timescale of the order of10^4 years and greater. Natural CO_2-rich sites can be investigated to understand the behaviour of CO_2 in geological formations on such a timescale. This thesis examines the reservoir and seal on one such oilfield. Several hydrocarbon fields in the South Viking Graben of the North Sea naturally contain CO_2, which is thought to have charged from depth along the western boundary fault of the graben. The Miller oil field which contains ~ 28 mol% CO_2, of isotopic composition $\delta^{13}C$ = -8.2‰. The Upper Jurassic Brae Formation reservoir sandstones and the Kimmeridge Clay Formation (KCF) seal have been exposed to the CO_2 accumulation since its emplacement.

Rock samples from the reservoir sandstone and bottom of the seal mudrock were examined using multiple techniques, including XRD, SEM, fluid inclusion and carbonate stable isotope analyses. The sandstones show no features directly attributable to abundant CO_2 charge. SEM analyses reveal significant heterogeneities in diagenesis within the KCF. The silt/sand lithologies of the KCF have undergone a diagenetic history similar to that of the Brae Formation sandstones. In contrast, the KCF shales display a distinctly different diagenesis of dominant dissolution of quartz and feldspar with little evidence of mineral precipitation. In both the Brae Formation and the KCF, pore-filling kaolinite, illite and carbonates are relatively late diagenetic events which can be associated with CO_2-induced feldspar dissolution.

Mudrock X-ray diffraction mineralogical data reveal abrupt vertical mineralogical variations across the reservoir crest in the Miller Field, while such variations are absent in a low-CO_2 control well in the same geological settings. This suggests that reactions induced by abundant CO_2 dissolved feldspar and produced kaolinite, carbonates and quartz in the seal, while oil emplacement inhibited the reactions in the oil leg. However, petrographic evidence and comparison between different sections argue against CO_2 reactions as the sole cause for such large mineralogical variations, especially for quartz. The vertical mineralogical variations to a certain extend represent original sedimentary heterogeneity.

Linear variations of carbonate $\delta^{13}C$ with depth were discovered in both shale and silt/sand lithologies of the KCF in a 12m zone immediately above the reservoir. These features are absent in the low-CO_2 control well. These trends are interpreted as dissolution of original carbonates by CO_2 slowly ascending from the reservoir. New carbonates precipitated from a carbon source with upwards decreasing $\delta^{13}C$ due to mixing between three carbon sources with different C isotopes at systematically varying ratios. The isotopes in the reservoir and the bottom of the seal suggests initial CO_2 charge at about 70-80 Ma. CO_2 infiltration rate is estimated at about $9.8\times10^{-7}g\cdot cm^{-2}\cdot y^{-1}$. Geochemical modelling was applied to reconstruct the reservoir fluid evolution by calibrating it to mineralogy, fluid chemistry, diagenesis and fluid inclusion data. The modelling suggests that CO_2 migrated into the reservoir together with a saline basinal fluid derived from the underlying evaporites at ~ 70 Ma. The CO_2 and basinal water charge imposed an important influence on the mineral reactions and fluid chemistry. This study suggests that the KCF has formed an excellent CO_2 seal, with no substantial breach since its charge at 70-80 Ma.

ACKNOWLEDGEMENTS

I would like to start by thanking Dorothy Hodgkin Postgraduate Awards Scheme for funding my Ph.D. study at Edinburgh. Many thanks go to my supervisors Stuart Haszeldine and Mark Wilkinson for offering me the opportunity to work on such an interesting project and for their support from the very beginning. I would like to thank BGS Edinburgh for allowing me to sample the drill cores and its staff for their warm receptions and great assistance. Many thanks to Tony Fallick for his advice and guidance on the isotope study and the SUERC staff for their analysing my samples. I'm indebted to Malcolm Rider and Gordon Macleod whose teaching and guidance are essential for the project. I would like to thank the academic and technical staff of the university for their assistance, Nicola Meller and Ingo Loa at CSEC; Nicola Cayzer, Ann Mennim, Michael Hall, Nicholas Odling and John Craven at Geology Department. I would like to extend my thanks to Kejian Wu at Heriot-Watt University for his help and hospitality on numerous occasions.

Many thanks to my good friends, without whom life would be dull during the last three years: Tim, Hector, Raquel, Edmund, Daniel, Niina and many others. Thanks are also given to the fellows at Grant Institute.

CONTENTS

CHAPTER I

INTRODUCTION

1.1. Introduction

The risks associated with climate change have been the subject of severe debate in recent years. Today, many experts believe that these risks are real and directly related to the emission of greenhouse gases, especially anthropogenic CO_2. The atmospheric CO_2 concentration has been increasing due to ever-increasing practice of burning fossil fuels since the start of industrialization. Recent decades have witnessed a more rapid rise in CO_2 emissions. As of January 2007, the earth's atmospheric CO_2 concentration was about 383 ppm measured at Mauna Loa Observatory (Figure 1.1) (Tans, 2007). This is 99 ppm (38%) above the 1832 ice core levels of 284.3 ppm (Etheridge et al., 1998). Increased amounts of CO_2 in the atmosphere is thought to be responsible for the global warming trend already observed since the latter half of the 20th century, and could have even more severe consequences unless measures are taken. It becomes urgent to undertake decisive actions.

A potential technology to curb CO_2 emissions is Carbon Capture and Storage (CCS). The basic concept is to capture man-made CO_2 at major emission sites, to concentrate and transport it to suitable geological storage sites, and then, inject and store it in underground geological formations. Compared to other options aimed at reducing anthropogenic CO_2 emissions, the CCS presents an important advantage that it enables continued use of fossil carbon sources during the transition period in a much cleaner way.

For capacity reasons, CO_2 has to be compressed at a high pressure and injected deeper than 800 meter below the surface in order to achieve the density close to water at the supercritical

status. After injection a part of the injected CO_2 is slowly dissolved by the formation water or permanently trapped in micropores. The remaining part rises towards the sealing cap rock as CO_2 is lighter than the formation water and slightly buoyant. Water containing CO_2 being heavier than water without, tends to sink to the bottom. Eventually, over a very long time, all the CO_2 present should dissolve in the formation water. Over an even longer time period, some of the dissolved CO_2 will react with the formation minerals and precipitate solids, which constitutes long lasting storage mode. All these physical phenomena contribute to reduce the risks of CO_2 leakage over time.

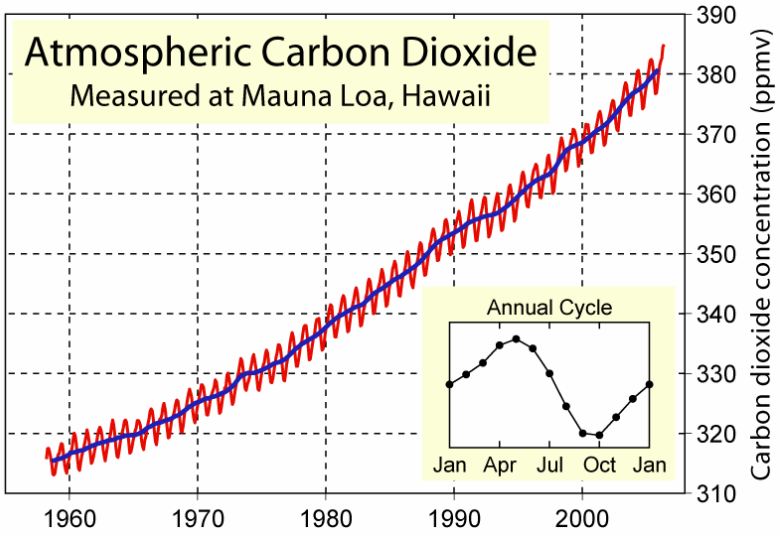

Figure 1.1 Atmospheric CO_2 concentrations measured at Mauna Loa Observatory (Tans, 2007). The red curve shows the average monthly concentrations, and blue curve is a moving 12 month average. This annual cycle is shown in the inset figure by taking the average concentration for each month across all measured years.

Injected CO_2 would have to remain efficiently isolated from the atmosphere until natural buffering processes have sufficient time to reduce its concentration to the pre-industrial level. This is the minimum timescale required for effective storage. Kheshgi et al. (1996) model the timescale to be 10^3 years if CO_2 emissions are halved by 2015 or, more probably, 10^4 years if CO_2 emissions continue at the present increasing rate. A climate model which relates climate change to escaping CO_2 from possible storage sites also suggests that the minimum average CO_2 residence time should be at least 10^4 years if the impact of leaking CO_2 on the climate should be avoided for coming generations (Lindeberg, 2002). As the performance of geological storage is difficult to quantify precisely, it would be safer to allow a factor of 10 error. Consequently, timescales for CO_2 retention could be considered on the 10^5 year timescale as a minimum.

However there is geological uncertainty concerning the possibility of long-term leakage through a rock seal or engineered boreholes. To ensure a robust disposal it is necessary to understand and predict the pathways, volumes, and, critically, the timescales, of the reactions between brine, mineral and CO_2 in sandstone reservoir and mudrock seal. Many laboratory studies have been conducted to understand CO_2-related reactions. But laboratory experiments are usually run in a very short time and under high temperatures. When these results are used in geochemical modelling, the predicted reaction rates and mineral types do not fit well to the natural examples. Natural CO_2-rich sites provide ideal analogues for CO_2 geological storage, because high content of CO_2 have been emplaced on geologic timescales and under normal burial temperatures. By obtaining and analyzing the field data from these sites, the long-term fate of the CO_2 retained in the geological formations can be accessed. This will improve our understanding of the long-term behaviour of injected CO_2 and its effects on the storage sites.

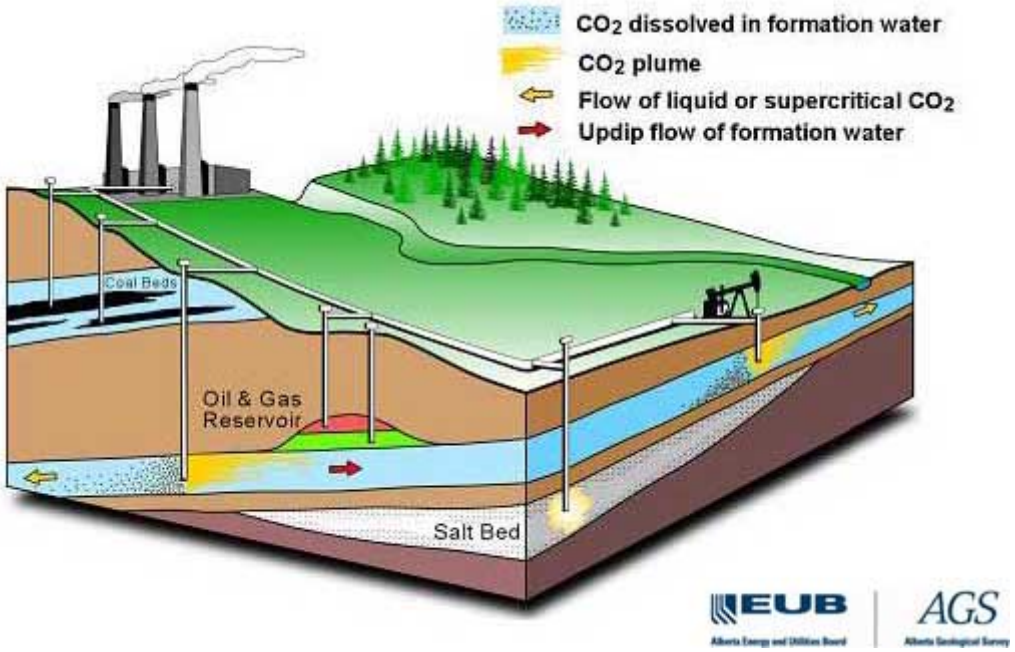

Figure 1.2 Illustration of various options for CO_2 geological storage, showing injection into oil and gas reservoir, saline aquifer, coal bed and salt bed (Alberta Energy and Utilities Board; Alberta Geological Survey).

1.2. Options of storage

There are a number of proposed methods by which CO_2 can be stored (Figure 1.2). The main options for geological storage include injection of CO_2 in depleted oil and gas fields, deep saline aquifers, unmineable coal beds, and mineral trapping. Storage in the deep ocean is also proposed.

1.2.1. Depleted oil & gas fields

Oil and gas fields have proven their capability to hold oil and gas over geological time periods and, therefore, can act as long-term storage sites for CO2 as well. The use of depleted oil and gas fields has a number of advantages. In particular, these fields are known to have served as oil or gas traps for millions of years, their geology is well studied and there is substantial storage capacity available. Thousands of oil and gas fields are approaching the end of their economic lives. They commonly have lowered formation pressures, which makes them particularly suitable for injecting CO_2. The worldwide storage potential, around 920 Gt CO_2 would cover about half of aggregate emissions by 2050 (Rojey and Torp, 2005).

Furthermore, CO_2 injection has already been applied for about three decades to enhance oil recovery (EOR), in particular in the United States. When CO_2 is injected into an oilfield it dissolves with the crude oil, causing the crude to swell and thereby reduce its viscosity. This also helps to maintain or increase the pressure in the reservoir. The combination of these processes allows more of the crude oil to flow to the production wells. Up to half of the injected CO_2 will be stored in the immobile oil remaining in the reservoir at the end of production. The rest is collected from the production well and re-circulated. Globally, 130 Gt of CO_2 could be stored as a result of CO_2-EOR operations (IEA GGRDP, 1999a). CO_2-EOR is commercially proven. It is used extensively in the USA, where 74 projects are now operating, injecting some 33 Mt of CO_2 annually (IEA GGRDP, 1999a).

Similarly, in a depleted gas field the injection of CO_2 would occupy some of the void space that had previously been occupied by the natural gas. Some depleted gas fields are reused as buffer stores for natural gas production. The techniques of gas re-injection can be adapted to store CO_2 in these fields. Globally, 900 Gt of CO_2 could be stored in depleted natural gas fields, substantially more than in depleted oil fields.

A potential drawback of storage in old hydrocarbon fields includes the possibility of leakage through abandoned wells. There is also the possibility that reduction of formation pressures during the production stage, followed by re-pressuring during CO_2 injection, may damage reservoir caprock integrity (Chadwick et al, 2004).

1.2.2. Deep saline aquifers

Due to the depth of these formations and their high salt content, deep saline aquifers cannot be used as sources of drinking or irrigation water. On a global scale, saline aquifers represent

the greatest potential in terms of storage capacity, up to 10 000 Gt CO_2 and can provide storage volumes for 20 to 500 % of projected total emitted CO_2 to 2050 (Davison et al., 2001; Rojey and Torp, 2005). Within the UK, it is estimated that the Bunter sandstone saline aquifer could store about 350 years of UK derived emissions (Chadwick et al., 2000). But large uncertainties remain around present assessments.

These aquifers can be open or closed. The configuration of closed aquifers is similar to that of oil and gas reservoirs, which ensures effective confinement both vertically and laterally. A number of this type of aquifer has been used as buffer stores for natural gas, giving confidence that CO_2 could be stored safely for thousands of years in carefully selected reservoirs. Open aquifers lie along a horizontal or slightly inclined plane. The absence of lateral confinement enables CO_2 to migrate. Nevertheless, due to the slow flow rate and large size of the reservoir, confinement can be ensured if the overburden is of sufficiently good quality. In this case, the main trapping mechanism is the dissolution of gas in water. The main drawback of this option is the lack of knowledge about the reservoir. As such formations do not contain resources of interest, they have virtually never been studied. A major characterization effort is therefore required, in order to qualify this type of aquifer for geological storage, especially onshore.

At the world's first industrial CO_2 geological storage programme, the Sleipner condensate field in the North sea, the oil company Statoil has re-injected CO_2 from the 3.3 km deep gas reservoir into 1 km deep Utsira Formation. Injection started in October 1996; nearly 1 million tonnes of CO_2 per year have been injected without any significant operational problems observed. A series seismic survey have clearly shown that injected CO_2 moves, due to buoyancy effects, from the injection point and accumulates under the overlying shale package (Arts et al., 2001).

1.2.3. Unminable coal beds

CO_2 can be injected into suitable coal seams where it will be adsorbed onto the coal, locking it up permanently provided the coal is never mined. This trapping mechanism also enables the recovery of methane as CO_2 preferentially displaces methane that exists in the coal and brings a potentially attractive economic benefit. Coal can adsorb about twice as much CO_2 by volume as methane, so even if the recovered methane is burned and the resulting CO_2 is re-injected, the coal bed can still provide net storage of CO_2 (Reeves, 2003). A substantial amount of coal bed methane is already produced in the USA and elsewhere. A CO_2-

enhanced coal bed methane project in San Juan, New Mexico, USA suggests that injection CO_2 could increase methane production from extensive coal beds by 75% (Reeves et al., 2001). The absorption and replacement tests on Akabira Coal suggest that the absorption volume of CO_2 could amount to three times as much as those of methane. Also, it is found that the higher ratio of CO_2 sequestration to coal and lower methane replacement ration can be obtained if lower concentration of CO_2 is injected (Ohga et al., 2003). This means that CO_2 of low concentration can be efficiently stored with small amount of releasing methane.

The key problem is the very low permeability of this type of formation compared to the rock holding hydrocarbon reservoirs and the kind of aquifers suitable for CO_2 storage. Therefore a large number of injecting wells may be required in order to inject large quantities of CO_2. Because of this, this method is considered to be limited in application to the UK, but maybe significant in China and USA. The global storage potential is limited to around 40 Gt CO_2 (Rojey and Torp, 2005). But, in many instances the coal reserves are close to industrial centres with CO_2 emitting power plants, they would provide convenient storage sites.

1.2.4. Mineral trapping in the Subsurface

Another process leading to long-term storage is mineral trapping by reaction of the injected CO_2 with formation water and reservoir rock. The volume potential of mineral trapping and the reaction timescale depend on fluid chemistry and rock mineralogy (Czernichowski-Lauriol et al., 1996). Injecting CO_2 tends to increase acidity of the formation water because dissolved CO_2 partially dissociates into protons, bicarbonate and subordinate carbonate anions. Precursor minerals capable being dissolved and providing divalent cations (e.g. Ca^{2+}, Mg^{2+} and Fe^{2+}) could act as pH-buffer, and react with subordinate carbonate anions to form neo-carbonate minerals. A variety of minerals which can be considered as reaction precursors include Ca-feldspar, volcanogenic silicates, detrital mica such as biotite, Fe-, Ca-, and Mg-bearing clay minerals (such as chlorite, glauconite and other smectite minerals) and some zeolite minerals (Brosse et al., 2002; Baines and Worden, 2004). A generic reaction could be written according to Baines and Worden (2004):

$$M^{(II)}Al_xSi_yO_z + CO_{2\,(aq)} + H_2O \rightarrow \text{Al-silicate mineral} + M^{(II)}CO_3 \qquad (1.1)$$

The resulting Al-silicate mineral is most likely to be kaolinite. Mineral trapping is also predicted to occur in the form of dawsonite [$NaAlCO_3(OH)_2$] as catalyzed by high Na concentration, CO_2 aqueous saturation, and acid-induced kinetic dissolution of K-feldspar

(Johnson et al., 2001). The reaction can be expressed as:

$$KAlSi_3O_8 + Na^+ + CO_{2\,(aq)} + H_2O \rightarrow NaAlCO_3(OH)_2 + 3\,SiO_{2(aq)} + K^+ \quad (1.2)$$

Mineral trapping may offer three distinct advantages: storage capacity is maximized, mobility is minimized, and aquifer/shale permeability is reduced (Johnson et al., 2001). But the capacity and reaction rate can be limited. Baines and Worden (2004) suggest that the timescales of the chemical trapping reactions are greater than tens to hundreds of thousands of years. The dissolution rate of the reactive minerals probably controls the sequestration rate.

1.2.5. Ocean storage of CO_2

Since first suggested 25 years ago by Marchetti (1977), the ocean has become an interesting option because it is the largest potential disposal medium. Subsequent investigations (Cole et al., 1993) emphasized the need to dispose of the gas at great depths and to use sinking currents to avoid rapid outgassing to the atmosphere. Some studies (e.g. Haugen, 1992) have indicated that even shallow injection could be considered, because dissolution of CO_2 would increase water density and, thus, transport the dissolved gas to greater depths. Various disposal methods have been proposed including: 1) CO_2 dispersal in a very dilute form at depths of 1000-2000m; 2) Discharge at 3000m to form a lake of liquid CO_2 on the seabed; 3) Formation of a sinking plume to carry most of the CO_2 into deeper water; and 4) Release of solid CO_2 at depth. Of these options, the first is thought to be the most promising in the short-term (IEA GGR&DP, 1999b). There are, however, extremely significant problems such as ocean water acidification and legal objections to dumping.

1.3. Potential leakage

Due to its buoyancy effect, leakage of injected CO_2 may take place. Leaking CO_2 would lead to numerous problems. When CO_2 comes into contact with groundwater the water becomes more acid. CO_2 is not toxic, but in large accumulations it may be suffocating, especially in low situated areas where the CO_2 gathers like a pond. Also, as a result of pressure changes in the subsurface related to injection local seismicity may occur. Leakage is the key concern of any storage project.

The depth of injection and the nature of the rock and soil imply that transport via traditional Darcy flow will occur over long time periods. A geological storage project requires that CO_2

be separated from the atmosphere on a timescale of 10^5 years as a minimum. A relatively low volume leakage of a large reservoir may well be deemed acceptable in a large sequestration project. Hepple and Benson (2003) modelled leakage rates, with respect to the allowable emissions for stabilization of atmospheric CO_2 at 350-750 ppm. For stabilization at currently accepted concentration of 550 ppm, a leakage rate of less than 0.01 %/y is requested.

The critical leakage pathways include natural faults and fracture systems. Large-scale open-fault and fracture systems can provide strong connectivity and reduce CO_2-storage efficiency. Increasing formation pressures due to CO_2 injection can potentially open fractures and cause slip on faults that exist in a reservoir (Holloway and Savage, 1993; Sminchak et al., 2002). This would create or enhance fracture permeability. The maximum sustainable formation pressure should be estimated in order to avoid activating existing faults or inducing new fractures at any potential CO_2 storage sites (e.g. Jürgen and Hillis, 2003). A number of sites of the natural CO_2 basin system of the Colorado Plateau occur with CO_2 discharge to the surface at modern cool saline water springs (Shipton et al., 2004). In such locations, faults appear to cut naturally occurring CO_2 reservoirs, and allow CO_2 gas to escape by flowing along the faults. Active springs and travertine deposits along the faults suggest that leakage over human timescales may be significant.

Another key concern is the sealing capacity of sealing mudrock. Leakage could occur as slow migration either laterally or vertically through seal. Mudrock formations, containing organic matter, generally serve as cap rock. Supercritical CO_2 underground has the capability to extract organic matter, thereby change the pore structure and could increase permeability drastically. Hence, dissolution of a small amount of organic matter in the cap rock may induce leakage and reduce the storage amount of CO_2 (Okamoto et al., 2003). On the other hand, sealing mudrock usually contains relatively large volumes of Mg/Fe-bearing clay minerals. Dissolution of Mg/Fe-bearing clay minerals (e.g. Mg-chlorite) as a result of reaction with CO_2 leads to precipitation of Fe/Mg carbonates (e.g. magnesite). Hence, the rate ratio of mineral dissolution/precipitation to advection/diffusion is much larger in mudrock than in the underlying sandstone aquifer. This is geochemically simulated to be highly conducive to precipitate Fe/Mg-carbonate, reduces porosity and permeability, and thus, enhances cap rock integrity (Johnson and Nitao, 2002).

There is a theoretical possibility that CO_2-brine may create dissolution pathways vertically

through seals, in exactly the same way that ‘wormholes’ can be dissolved in carbonate rocks. Pre-existing micro-fractures in a mudrock may permit CO_2-brine migration, which enables bitumen, carbonate and feldspar dissolution, or clay transformation. If permeability is enhanced along the micro-fractures, then increased CO_2-brine flow will produce even greater permeability. This potentially leads to propagation of focused permeable pathways through an otherwise poor-permeable seal.

Well boreholes, which always penetrate the geological seal, may act as leakage pathway. Care has to be taken to avoid sites and formations in which abandoned wells offer leak paths, and active wells will need to be well maintained.

1.4. Monitoring

Successful geological storage of CO_2 requires careful monitoring both during active injection and for verification of long-term safety. Monitoring can be applied from the surface, but also near the injected formations in the wells. In the latter case these are in general point measurements and do not provide a lateral 2D or 3D image of CO_2 concentrations, unless a large number of wells are available. The CO_2 sensors at the surface measure directly CO_2 concentrations in the atmosphere or in soil, while geophysical monitoring at the surface or in wells acquires data that can be interpreted to CO_2 accumulations.

In general, the currently applied monitoring techniques were developed for the oil and gas industry. The monitoring technology falls in the following groups: engineering, geophysical, geochemical and geodetic techniques (Winthaegen, 2005). These techniques have a different location of application and focus at different systems. The engineering techniques are focused at the reservoir and the wells. Seismic measurements are focused at the reservoir and the overburden. Geochemical techniques can be applied in the wells and in the surface system.

In reservoir system, for instance, sensor can be placed to obtain continuous or repeated measurements of downhole pressure and temperature from the injected reservoir upwards. Chemical tracers can be injected in one well and migrate to another well where they can be measured. Reservoir gas and water analysis are repeatedly applied and used to monitor changes in isotope signatures and chemical components as a result of possible reactions of the CO_2 with the host rock or the sealing cap rock. In particular, seismic reflection has been proved a powerful tool to monitor the movement of the injected CO_2 in the formation and

possible leaks to above laying strata. The saline Aquifer CO_2 Storage (SACS) project, which is monitoring the injection of CO_2 into the Utsira Formation in the North Sea, has shown that the bulk of the injected CO_2 is currently being trapped beneath the intra-reservoir shales (Figure 1.3) (Arts et al., 2001; Chadwick et al., 2003). The project suggests that it is possible to map CO_2 distribution and to image pathways using time-lapse seismic data. However, seismic monitoring has its own limitations. First, its vertical resolution for CO_2 accumulations is of the order of many meters. The leakage through local faults may not be able to be detected. Second, the monitoring is not predictive. Which means that migration and leakage need to have occurred before a monitoring project can detect leakage. The possible leakage still could occur in the future. Third, as only very short timescales are available, monitoring data are not sufficient to predict the long-term fate of injected CO_2.

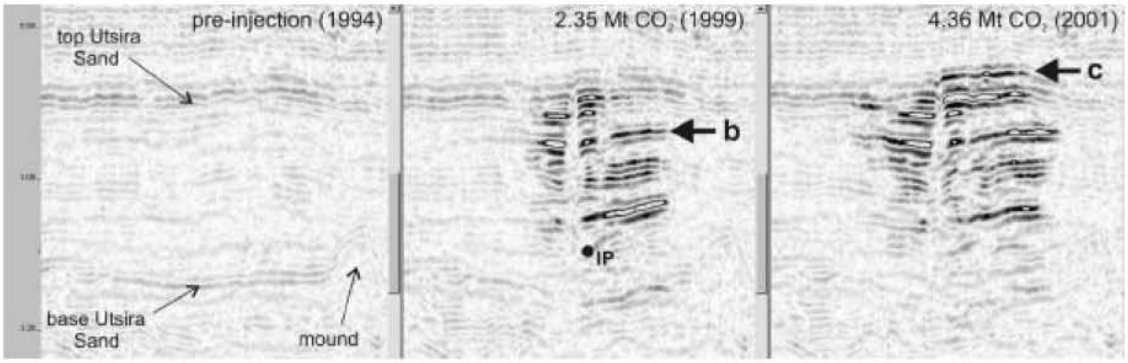

Figure 1.3 Time-lapse seismic images showing changes in reflectivity due to injected CO_2 (Chadwick et al., 2003).

1.5. Natural analogues

For the required timescale of 10^5 years storage, there is a necessity that the timescales of the migration and reactions of CO_2 in the subsurface should be fully understood. It is particularly crucial to understand the behaviour of seal rocks in the presence of CO_2 in the long-term. Analogues, which are systems where CO_2-brines are in contact with rock material, similar to the reservoirs and seals prepared for engineered storage, provide powerful method to address these concerns. By analyzing analogue systems, we can improve our understanding of CO_2 behaviour in geological formations. Several short-term analogues can be utilised, ranging from laboratory experiments to engineered storage. But the autoclave experiments and engineered injection projects only have operation timescale of months to tens of years. Apparently, the required timescale for geological storage can only be matched by natural CO_2-rich sites as natural analogues.

Many laboratory studies have been made, but, as we know, laboratory experiments are usually run in very short time, under high temperature. High temperatures greatly increase reaction rates to several orders of magnitude faster than rates in nature. When experimental results are used in geochemical modelling software, the predicted reaction rates of mineral reaction and CO_2 sequestration do not fit well with the observations of real CO_2 sites, so that prediction of rapid mineral dissolution and precipitation will be unreliable. Consequently, rates derived from laboratory experiments are only a general guide to rates in natural systems, not an exact guide.

One very important way to address some of the key technical issues is through practical research, development and demonstration projects. Storage projects such as Sleipner provide commercial scale examples that can help provide the knowledge to allow further storage projects to develop. Sequential surveys by seismic reflection show that 1m thick mudrocks within the Utsira Formation could not retain CO_2, only delayed its buoyant rise. Neither has the 5m mudrock top seal formed a robust seal (Zweigel et al., 2001; Chadwick et al., 2003). There is no seismic reflection evidence that the vertical plume of CO_2 has penetrated the thick top seal mudrocks which overlie the top most '30-metre sand wedge' sandstone of the Utsira Formation (Figure 1.3). However, none of these projects have been operating for longer than 15 years and will only be able to demonstrate long-term storage through predictive modelling. At present, several key issues need to be addressed – will there be significant geochemical interactions in the CO_2 saturated reservoir rocks and the overlying mudrock? Will leakage occur at all through the mudrock top seal? If so, at what rate?

Since the early 1980s, in the USA and several other countries, CO_2 has been injected on a large scale into depleted oil fields for enhanced oil recovery (EOR). The safety record of this activity has been excellent (Stevens et al., 2000). However, geochemical evidences from Enhanced Oil Recovery (about 30 year duration) are again too short in timescale comparing with the required storage timescale of 10^5 yr.

Geochemical modelling is convenient approach to predict storage performance. However, it is apparent that existing geochemical modelling is not capable of accurate mineral predictions in natural sandstones at cool temperatures on the required timescales. Predictions of disposal site performance are not yet adequate, because of a combination of reasons, two of which are: lack of understanding of natural CO_2 sealing, and lack of understanding of CO_2 reaction paths and rates with reservoirs and seals. To help to bridge the gap between current

laboratory experiments and enhanced oil recovery practices (months-tens years), to safe storage (10^5 yr), an empirical approach is taken to examine sites where large volumes of CO_2 have naturally accumulated and have been stored in geologic formations over a long time period (10^4-10^6 years). These naturally occurring CO_2 deposits provide unique analogues for evaluating the long-term safety and efficacy of storing anthropogenic CO_2 in geologic formations. CO_2 has been trapped for geologic time scales in reservoirs with effective cap rocks, such as thick salt or shale deposits. More convincingly than any model or laboratory experiment, natural analogues can demonstrate the long-term chemical and physical interactions of CO_2 with reservoir and sealing rocks. There is a need to examine these sites in a quantitative way, to establish natural reaction rates and products, so that geochemical software can be calibrated to the natural world.

Several studies of natural CO_2 reservoirs have been made to investigate CO_2-mineral reactions. Pearce et al. (1996) suggested that the influx of CO_2 into the Bravo Dome of New Mexico resulted in the dissolution of anhydrite, dolomite, and plagioclase, and in the formation of kaolinite and zeolites. The study on the Springerville-St. Johns CO_2 field observes that the CO_2-reactions resulted in the dissolution of carbonate cements and detrital feldspars and the formation of dawsonite and kaolinite. However, CO_2 storage in the field occurs primarily as dissolved carbonate species and as gas accumulations. Only a small percentage of the CO_2 was sequestered in solids (Moore et al., 2005). CO_2 in the Ladbroke Grove Field in the western Otway Basin, southeastern South Australia, is also believed to be stored mainly in the gaseous and aqueous phases with minor proportion of ferroan carbonate precipitation (Watson et al., 2003). However, these studies mainly focus on the reservoir sandstones without adequately addressing concerns about integrity of mudrock seal. There is a need to fully investigate conventional sealing mudrocks in terms of their ability to retain CO_2. In this study, we used the Miller Field, a CO_2-rich oil field sealed by an organic-rich mudrock formation, as a natural analogue in order to demonstrate CO_2 evolution and long-term behaviour both in the reservoir sandstone and the sealing mudrock.

1.6. The objectives of this thesis

There is a need to improve understanding of the processes and develop confidence in the long-term storage performance. One way to demonstrate CO_2 behaviour in the target formations at geologically significant timescales is to study the examples of naturally occurring CO_2 accumulations. These natural CO_2-rich sites can be seen as direct analogues for the storage of man-made CO_2 over periods of time that can not be match for through any

laboratory experiment and demonstration project. Therefore, they provide specific examples to investigate the long-term behaviour of CO_2 underground and the CO_2-related reactions.

For this Ph.D. project, the Miller Field in the North Sea, which contains 28 mol% CO_2 in its Upper Jurassic sandstone reservoir, was chosen as a study area. A huge amount of CO_2 is believed to have emplaced for many millions years. Both reservoir sandstones and sealing mudrocks have been exposed to high concentration of CO_2 for that period of time, which makes the field an ideal site to investigate long-term interactions between CO_2, porewater and rock-forming minerals.

Nine exploration wells and 25 producing wells have been drilled across the field. Most of them cored the reservoir sandstones and 5 of them cored up to 55 m sealing mudrock. The drilling cores are publicly available at BGS corestore in Edinburgh. Logs of these wells are also accessible at Schlumberger CDA Datastore. In addition, formation water chemistry is published. Previous studies have conducted extensive petrographic, diagenetic, geochemical and microthermometric research on the Brae Formation in the region (e.g. McLaughlin et al., 1994, 1996; Larter et al., 1995; Macaulay et al., 1997, 1998; Marchand, 2001; Marchand et al., 2001, 2002). With these available samples and data, a comprehensive investigation on both reservoir and seal is feasible.

The project aims to improve understanding of the long-term behaviour of CO_2 in storage sites and give a better estimation on the effects of stored CO_2 on the reservoir and cap rock. Evidence that the mudrock seal have efficiently retained CO_2 for millions years will be provided and will increase our confidence for engineered storage. The thesis also aims to provide a valuable petrographic and geochemical dataset for both the Brae Formation sandstone and the Kimmeridge Clay Formation seal of the Miller Field.

The objectives of this study are to extensively examine the core samples in order to identify any change of mineralogy and mudrock texture associated with CO_2-related reactions vertically above a reservoir top-seal; to describe quantitatively the mineral products and volumes varying with distance from CO_2 zone and the varying effect of CO_2 on sandstone and mudrock; to constrain the reaction pathways and rates in the reservoir and mudrock seal; to construct pore fluid evolution and CO_2 charge model; to make geochemical modelling, using Geochemists Workbench and other software; to adjust modelling conditions and kinetic rates in order to calibrate a model to observations of natural CO_2 sites and to provide

confidence in the predictions of numerical simulations. In addition, an attempt will be made to compare the rock samples from the high- CO_2 Miller Field with a low-CO_2 site in order to identify and highlight the CO_2 effects. The comparative study will allow improved estimation of the effects of the CO_2-induced reactions.

1.7. Thesis Format

After this first chapter, the thesis contains 7 more chapters which discuss various approaches and techniques applied in this study.

Chapter 2 This chapter gives a general introduction of the geological setting of the field and sedimentology of the Brae Formation (the reservoir sandstone) and the Kimmeridge Clay Formation (the seal). The stratigraphic and spatial relationship between the two formations is discussed. A description of lithofacies of the reservoir sandstones and sealing mudrock is provided to give an insight into the sampling strategy used in this project. The hydrocarbon migration is also discussed because it is relevant to CO_2 migration. CO_2 occurrence and distribution in the Brae-Miller area is also reported.

Chapter 3 In this chapter, diagenesis within the Kimmeridge Clay Formation (KCF) and the Brae Formation is discussed based on Scanning Electron Micrographs and XRD mineralogical data. We give emphasis on the heterogeneous nature of the KCF and the different diagenesis between the KCF and the Brae Formation sandstone. The object is to investigate any influence of CO_2 accumulation on diagenesis of both the seal KCF and reservoir sandstone. The mass balance of the diagenetic reactions between the two formations is also discussed.

Chapter 4 In this chapter, the results of quantitative X-Ray diffraction mineralogical analysis of the KCF samples are reported and interpreted. The aim of the study is to investigate the spatial mineralogical variations in relation to the CO_2 source in the underlying reservoir. This study will discuss the reactants and products of the CO_2-induced reactions and reaction rates in the mudrock seal. Comparison between the samples from CO_2-rich wells and those from the low-CO_2 control well will help to reveal the CO_2 reactions and their effects on the mudrocks.

Chapter 5 A isotopic dataset of whole rock carbonates of the KCF are reported in this chapter. This dataset is used to illustrate the pore fluid evolution in the KCF which is

compared with that of the reservoir sandstone. The same analysis is applied on the low-CO_2 control well. The difference between their carbonate isotopes are explained as isotopic affects of CO_2 accumulation on the newly precipitated carbonates. Isotopic evidence of CO_2 influence immediately above the reservoir is reported and interpreted.

Chapter 6 This chapter reports laser Raman spectroscopic and microthermometric analyses on fluid inclusions in quartz cements of the Brae Formation sandstones. The aim of this study is to identify CO_2-rich fluid inclusions using laser Raman microprobe, and, then, to measure homogenization temperature of these fluid inclusions. This approach can constrain the timing of the CO_2 emplacement. The origin of the trapped CO_2 is discussed.

Chapter 7 In this chapter, a fluid evolution model of the Miller reservoir is constructed using geochemical modelling software Geochemist's Workbench based on the data discussed in the previous chapters. The model outputs are constrained by calibrating to the site-specific observations in order to produce outputs that closely match the field data. By varying CO_2 input parameters, the diagenetic consequences of CO_2 charge can be revealed.

Chapter 8 This chapter provides a summary of the results presented in the previous chapters. An overview of the history of CO_2 and its affects on the reservoir system is given. Implications for engineered storage are also discussed.

CHAPTER II

GEOLOGY AND SEDIMENTOLOGY OF THE MILLER FIELD

2.1. Introduction

A complex of oil and gas condensate reservoirs in the Upper Jurassic Brae Formation sandstones were discovered in the western margin of the fault-bounded South Viking Graben in the early 1970s (Figure 2.1). The North Brae, South Brae and Central Brae Fields are located along the graben margin in UK block 16/7a. The East Brae Field sits further north in block 16/3a and 16/3b. The Miller Field is situated more basinward in the adjacent blocks 16/7b and 16/8b (Figure 2.2).

The Miller Field was discovered in March 1983 by well 16/7b-20. It came into production in 1992 with estimated reserves of 240 Mbbl (Garland, 1993). Production peaked in 1995 at 150,000 barrels of oil and 220 million cubic feet of gas per day. The field in 2007 produces some 10,000 barrels of oil and 15 million cubic feet of gas a day. During 2005 to 2007, the field was planned by BP to be the world's first site to store CO_2 from an onshore hydrogen generation plant. The project would have been expected to capture and store around 1.3 million tonnes of carbon dioxide each year for the 350MW Peterhead Power Station. The injection of carbon dioxide into the reservoir could potentially produce up to 40 million additional barrels of oil and extend the life of the field by 15 to 20 years. However, BP abandoned the plan due to financial reasons and received permission to shut down operations from the Miller Field in September 2007.

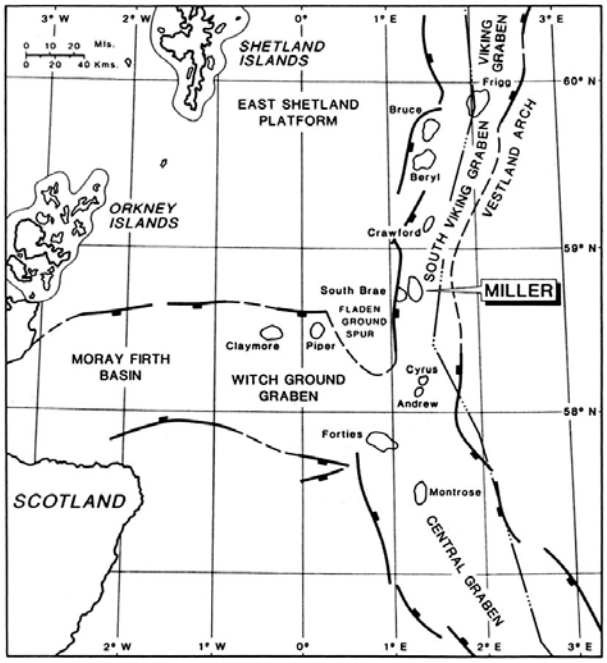

Figure 2.1 The Miller Field regional setting (Rooksby, 1991).

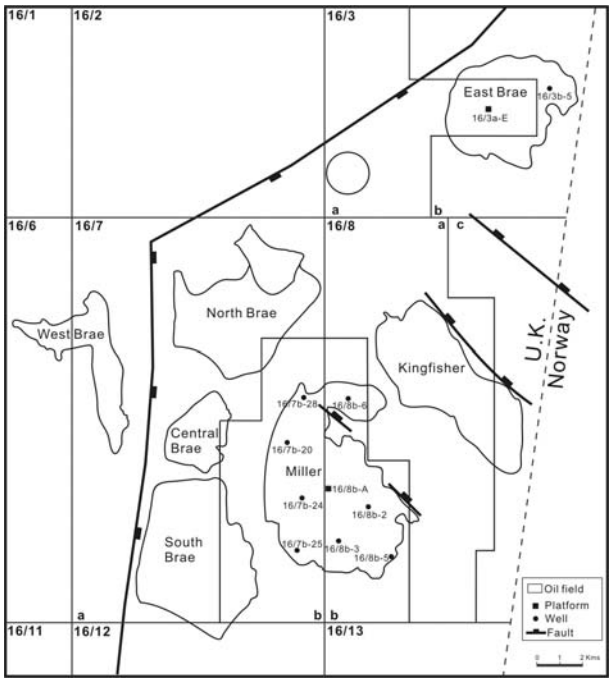

Figure 2.2 Location map of the Brae Formation reservoirs in the Brae-Miller area. The South, Central and North Brae fields are located along the western margin of the South Viking Graben fault. East Brae is not sealed by the Viking Graben fault. The Miller and Kingfisher fields are situated further basinward in the same depositional systems as South Brae. Wells sampled are also shown. The black squares indicate platforms from which production wells are drilled (After the map from Schlumberger CDA datastore).

The Miller reservoir comprises Upper Jurassic submarine fan sandstones of the Brae Formation, lying at a depth of 3970 – 4090 m TVD, covering an area of 45 km^2 with a vertical relief of 120 m. It is a combined structural and stratigraphic trap (Garland, 1993). The sediments, which were mainly sourced from the Devonian sandstones of the Fladen Ground Spur to the west, form the distal part of an extensive syn-rift submarine fan. Rifting of the South Viking Graben was initiated in the Late Jurassic. Faulting generally becomes

younger towards the western margin of the graben. The regional setting of the Miller Field is illustrated in Figure 2.3, which shows the thick Jurassic wedge juxtaposed against the fault-bounded basement of the Fladen Ground Spur (Rooksby, 1991). The Kimmeridge Clay Formation, which laterally interfingers with, directly overlies and underlies the reservoir sandstones, provides the source and seals for the hydrocarbons (MacKenzie et al., 1987; Rooksby, 1991).

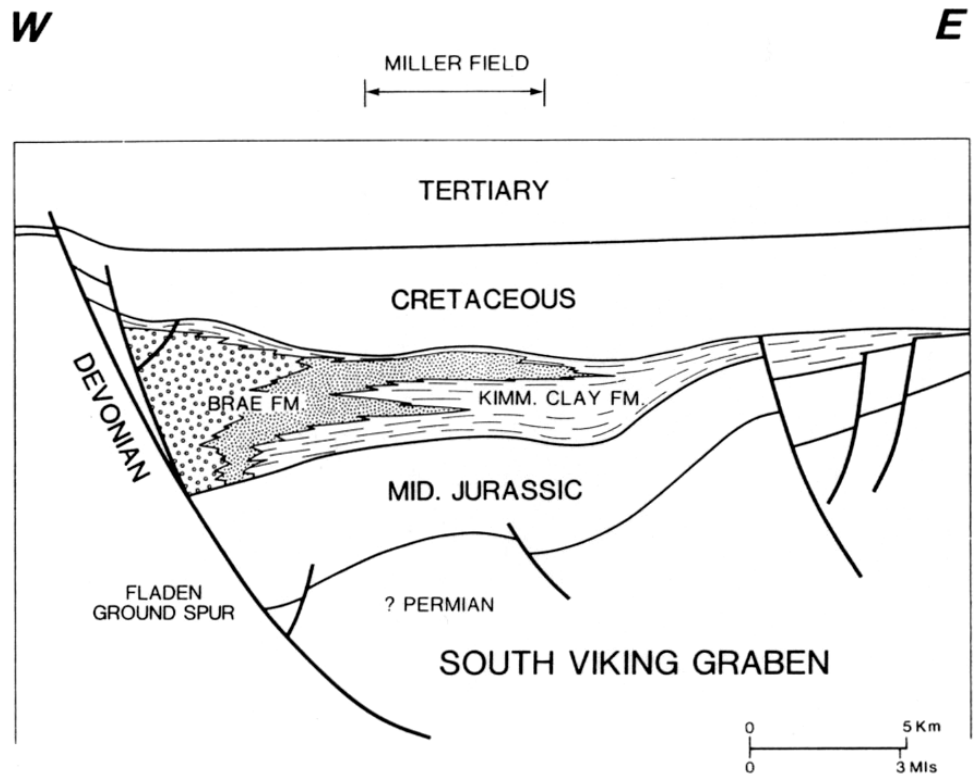

Figure 2.3 Schematic cross section of the South Viking Graben, showing approximate position of the Miller Field (Rooksby, 1991).

Several oil and gas fields in the Brae-Miller area are known to contain naturally high contents of CO_2, such as South Brae (35 mol%), Central Brae (30 mol%), Miller (28 mol%), Kingfisher (14 mol%), T-Block (up to 19 mol%) and Sleipner West (9 mol%) (Ranaweera, 1987; Fletcher, 2003a, b; Gambardo and Donagemma, 2003; Spence and Kreutz, 2003; Baines and Worden, 2004). Figure 2.4 shows an eastwards decrease of CO_2 content in the reservoirs. The timing and pathway of CO_2 migration and emplacement are not well constrained. The source of the CO_2 is also poorly understood.

This chapter gives a brief overview of the regional geology of the Brae Formation and Kimmeridge Clay Formation in the Brae area. An introduction to the depositional history of

both formations is also given. Hydrocarbon and CO_2 emplacement in the Miller reservoir will also be discussed.

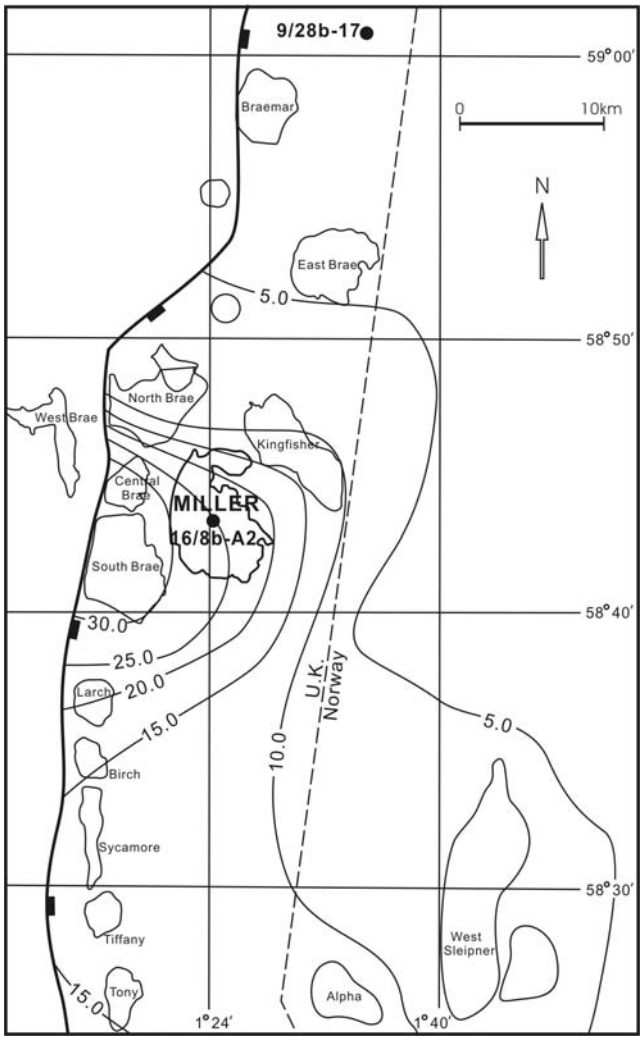

Figure 2.4 Distribution of CO_2 in the Brae-Miller area showing CO_2 contents of Upper Jurassic sandstone reservoirs (contours in mol %) decreasing away from the Brae fields. The two wells from which carbonate isotope samples were taken are also shown (see Chapter 5) (Modified after James, 1990; Baines and Worden, 2004).

2.2. Regional setting

The South Viking Graben is the northern arm of the North Sea triple rift system centred on the Forties Volcanic province. The half-graben is fault-bounded to the west against the basement of the Fladen Ground Spur (Figure 2.3). The graben floor rises gently eastward to the Vestland arch. The eastern margin is defined by smaller northwest-southeast trending faults (Figure 2.2) (Harris and Fowler, 1987). South-north regional palaeo-slope in the South Viking Graben was induced by uplift at the triple junction in early Middle Jurassic. The Mid-Late Jurassic crustal extension across the graben (3-5%) led to the growth, propagation and linkage of planar normal faults through the rift interval (Underhill, 1998; Young et al., 2001). Consequent subsidence in the graben occurred asymmetrically so that the thickest Middle-

Late Jurassic sequence is close to the western margin (Figure 2.3). In the Late Jurassic, the extension rate reached a maximum. Uplift of the footwalls of the extensional faults led to pronounced erosion. Distribution of Late Jurassic submarine fan systems were concentrated at the western graben margin and controlled by very rapid syn-depositional subsidence. The fans become thinner and finer-grained away from the western margin faults (Figure 2.5) (Harris and Fowler, 1987). Extensional movement continued intermittently on the western boundary fault until the Tertiary, when there was a brief phase of inversion before activity ceased (McClue and Brown, 1990).

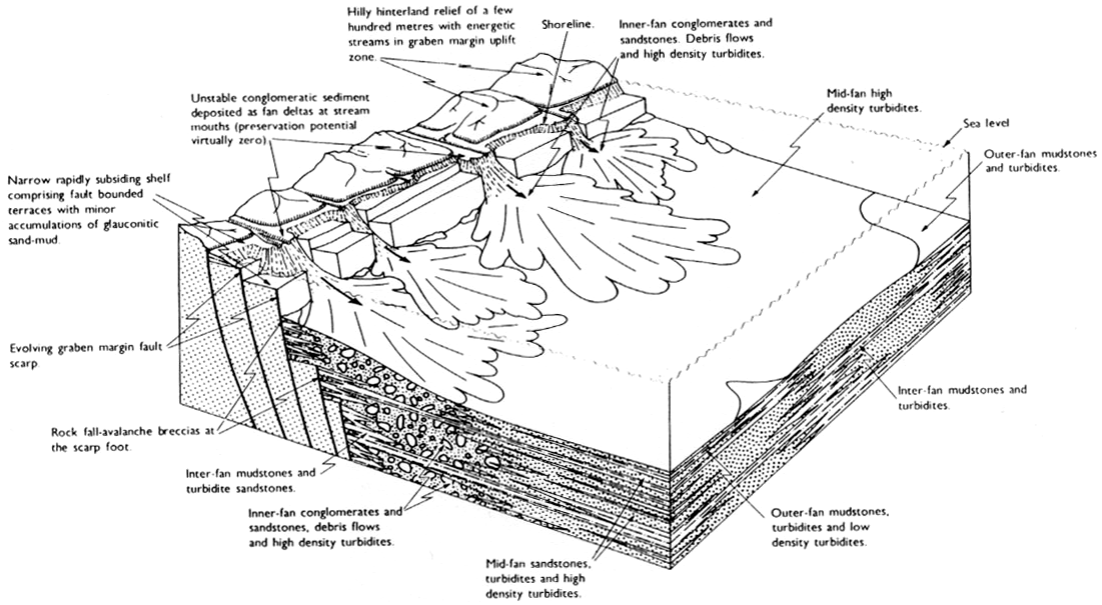

Figure 2.5 Depositional model illustrating facies relationships in the Brae Formation submarine-fan system (Harris and Fowler, 1987).

Over three kilometers of thickness of Late Jurassic and Cretaceous sediments are estimated to be present at the graben margin, about half of which form the Brae Formation. The Brae Formation comprises a fining-upwards sequence, up to 600 m thick, composed of composite fining-upwards sequences about 40 m thick. On a large scale (50 km), there are distinct compositional differences across the graben. Near the western margin, the Brae Formation sandstones consist of thick units of mud- and sand-supported conglomerates and coarse-grained sandstones at the North, Central, South and East Brae Fields. Further eastwards in the Miller and Kingfisher Fields, these sandstones prograde into medium- to fine-grained mid- and distal-fan deposits (Marchand, 2001). Pebbles and boulders in the sandstones on

the west side were derived from the marginal uplift zone of the Fladen Ground Spur, and consist of vein quartz, quartzite and Old Red Sandstones and siltstones. On the eastern side of the graben, pebbles in sands comprise granitic fragments and quartzites which are probably derived from the Utsira High (Harris and Fowler, 1987).

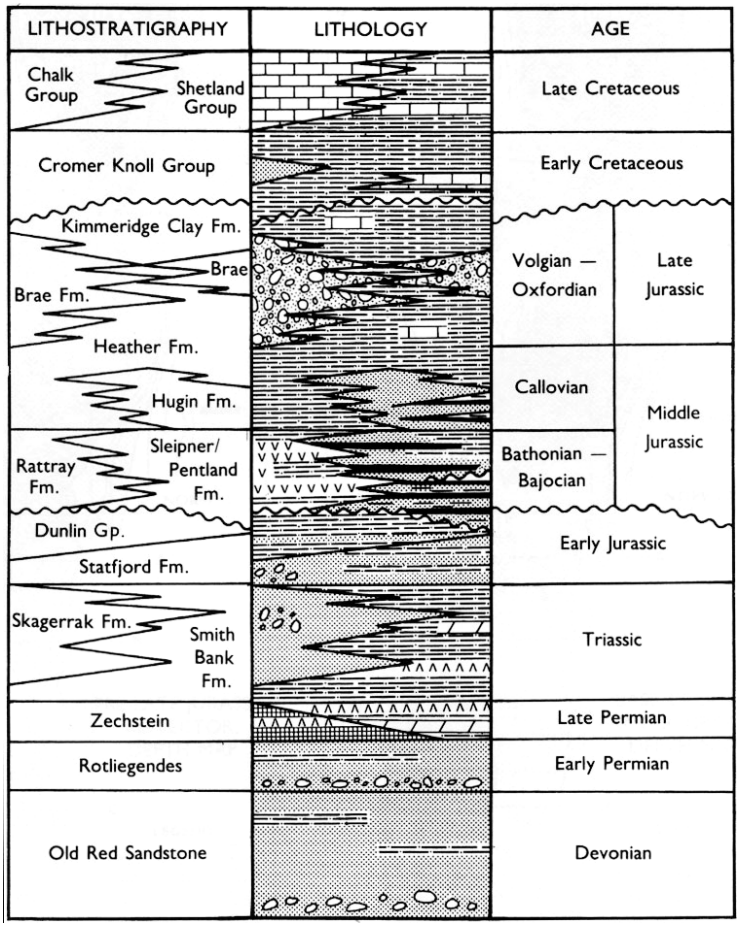

Figure 2.6 Schematic stratigraphic section of the Palaeozoic and Mesozoic rocks in the South Viking Graben. The Brae Formation is Upper Jurassic in age and was deposited from Oxfordian to Volgian times (Harris and Fowler, 1987).

2.3. Stratigraphy

The stratigraphic column in Figure 2.6 summarizes the regional stratigraphy of the South Viking Graben. The Brae Formation is Upper Jurassic in age and was deposited during Oxfordian-Volgian times (Harris and Fowler, 1987). On a regional scale the formation is both overlain by and underlain by, and interdigitates with, the Kimmeridge Clay Formation. The Brae Formation in the Miller Field mainly consist of fine- to medium-grained, moderately- to well-sorted sandstones, characterized by a low gamma response. The formation is divided into Unit 1, 2 and 3 at Miller (Figure 2.7). Unit 3 is the oldest and

represented by thin sandstones interbedded with mudstones. Unit 2 is subdivided into layers A-D. It includes all the reservoir sandstones (Garland et al., 1999). Over most of the Miller Field, Unit 1 is predominantly shaly, although interbedded with turbidite sands in the northern part of the field (Turner et al., 1987).

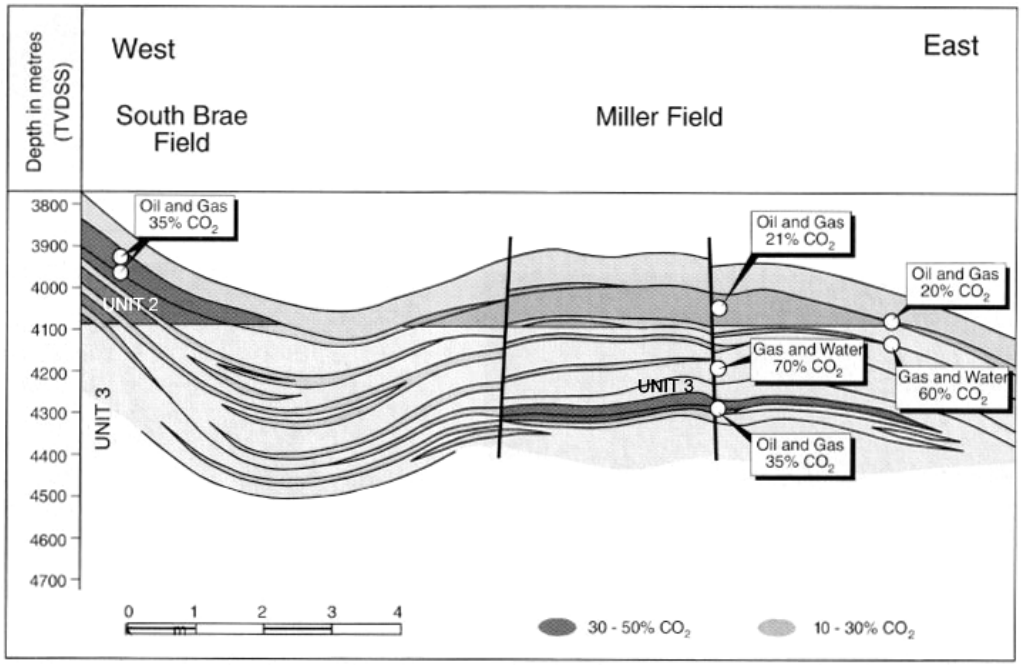

Figure 2.7 Structural cross section of South Brae and Miller Field combined with CO_2 content in oil and water zone (Baines and Worden, 2004).

2.4. Depositional model

The sediments of the Brae Formation were interpreted as a series of overlapping submarine fans (Stow et al., 1982; Turner et al., 1987). Deposition models and stratigraphic relationships between South Brae, Central Brae, North Brae, East Brae and Miller reservoirs have been discussed in several studies (Harris and Fowler, 1987; Tuner and Connell, 1991; Garland, 1993). Figure 2.5 illustrates the general depositional model. A series of normal faults developed during the Mid-Late Jurassic crustal extension and rifting episode. Uplift of the footwalls of these extensional faults led to significant erosion of the Fladen Ground Spur in the west which served as a source area for the submarine fan sediments. Consequent subsidence in the graben occurred asymmetrically so that the thickest Late Jurassic submarine fan deposits were concentrated at the western graben margin and controlled by very rapid syn-deposition subsidence. The boundary fault downthrowing to the east was intermittently active through the Late Jurassic. The edge of the marine basin at the foot of the fault scarp received the coarse-grained sediments of the proximal submarine fans to form the

North, Central and South Brae reservoirs. A sandy fan was deposited further basinward east of the fault slope apron and constituted the Miller reservoir.

Figure 2.8 Photograph of drill core of interval 5056-5059 m (driller's depth), well 16/8b-A2, the Miller Field. The top of the Brae Formation (reservoir section) is marked. The Kimmeridge Clay Formation overlying the Brae Formation sandstone mainly consists of shale-sand/silt alternations, so called 'tiger stripe' facies.

2.5. The Brae Formation lithology

The Miller reservoir is composed of three main lithologies which are described in Garland (1993). Clean fine- to medium-grained, well-sorted quartzose sandstone is the dominant lithology. The sandstone is subarkosic to sublithic in composition, and commonly massive or displaying parallel lamination. Individual beds are commonly amalgamated up to 30 m in thickness. The average porosity ranges from 13 to 17 % with permeability from 100 to 300 mD. The medium-grained sandstones in the upper part of the reservoir display much higher reservoir quality with porosity of 18-22 % and permeability up to 1500 mD. This sandstone is interpreted to have been transported by, and deposited from, sand-rich, high-density, low-efficiency turbidity currents.

The second lithology, thinly bedded alternations of sandstone and mudstone, are usually interbedded with the clean sandstones. They are readily identified in wireline logs by high gamma response. The lithofacies includes sandstone beds up to 20 cm thick. These intervals are generally parallel laminated, forming 'tiger-stripes'. Porosity in the thin sandstones is in the range 8-10 %, with permeability of 1-10 mD. The interbedded intervals are considered to be the deposit of low-density turbidity currents.

The third lithology is isolated mudstones of the order of 20-50 cm thickness, locally interbedded within the main part of the reservoir. The mudstones represent normal background sedimentation at the margins of the fan system, or during periods of non-deposition within the fan. The mudstone lithofacies display an increasing volumetric importance below the pay zone and around the periphery of the field.

2.6. The Kimmeridge Clay Formation

The Kimmeridge Clay Formation acts as both source rock and seal for the hydrocarbon accumulations in the South Viking Graben. It usually overlies and underlies, and interfingers with, Brae Formation reservoir sandstones (Figure 2.3 and 2.6). The Kimmeridge Clay Formation was deposited in a deep water anoxic environment during regional rifting and subsidence in the latest Jurassic (Ziegler, 1982). Widespread development of dysaerobic to anoxic conditions lead to the deposition of organic-rich mudrocks which form prolific hydrocarbon source rocks (Cornford, 1998). The deposition was syntectonic, occurring during rapid subsidence along the graben axis (Field, 1985) and below wave base in the oxygen-deficient environment, with high organic productivity and high sedimentation rates. The consequent subsidence resulting from fault movement controlled the sea floor depressions in which the highly organic facies have accumulated (Cornford, 1998). Sedimentation rates were high with resultant rapid burial in the central areas of the graben where thickness of the whole shale sequence reaches 500-1000 m (Scotchman, 1993). The anoxic water with stratified water oxygenation and high sedimentation rates preserved the organic matter.

The KCF mainly consists of organic-rich 'black' shales interbedded with thin sand/silt beds in the most of the graben areas of the North Sea (Ziegler, 1982). The drilling cores of the Miller wells show typical 'tiger stripes' in the KCF seal, which are lithologic alternations between black shales and grey silt/sand beds (Figure 2.8). The laminated black facies were

deposited in a turbidite flowing from the north, down into the graben. The kerogen of the Kimmeridge Clay Formation is one of the world standards for a marine Type II kerogen, which is a mixture of bacterially degraded algal debris of marine planktonic origin and degraded humic matter of terrigenous origin (Cornford, 1998).

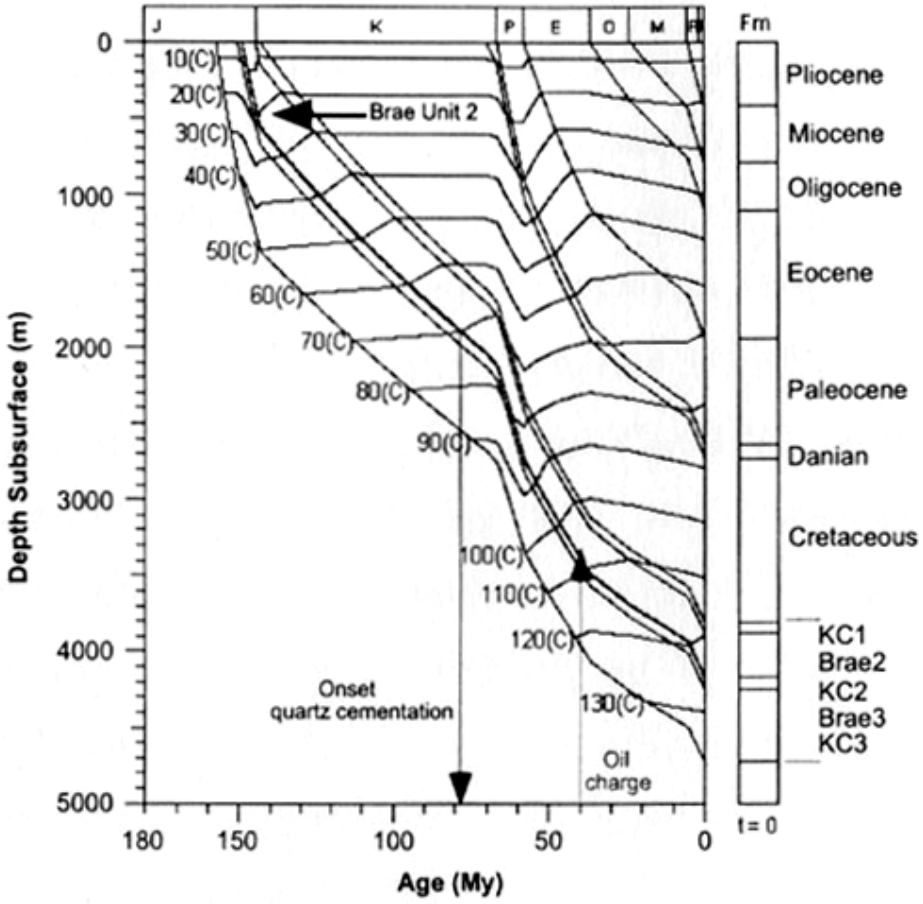

Figure 2.9 Burial history with isotherms for well 16/8b-3 in the Miller Field (Marchand, 2001).

2.7. Source rock maturity and hydrocarbon migration

The maturity of the Upper Jurassic source rock in the North Sea is largely controlled by burial heating during Neogene to recent. During the early Cretaceous, the KCF mudrocks underwent several phases of burial and minor uplift, followed by the rapid regional burial initiated in the late Cretaceous. Burial continued through the early Tertiary, before the rapid Late Tertiary to Recent subsidence, resulting in present-day depths of 3-4 km (Burley et al., 1989). Peak hydrocarbon generation took place in the Eocene around 40 Ma in the Central Graben according to the basin modelling studies by Barnard and Bastow (1991). Glasmann et al. (1989) investigated the timing of oil migration using K/Ar dating of neo-formed illites

and suggested that the hydrocarbon charge initiated in the latest Palaeocene-early Eocene (about 58 Ma) and ended by the early Oligocene (about 38 Ma) in the Huldra Field, the Viking Graben. In the Miller Field, maturity calculations indicate that the Kimmeridge Clay source rocks started generating oil at around 40 Ma, when the source rocks were buried to 3100-3400 m (Figure 2.9) (Marchand, 2001). The oil is believed to be generated on the flanks of the structure in the immediately surrounding source rocks and, thus, the migration path is very short (e.g. Turner and Allen, 1991; Marchand et al., 2002).

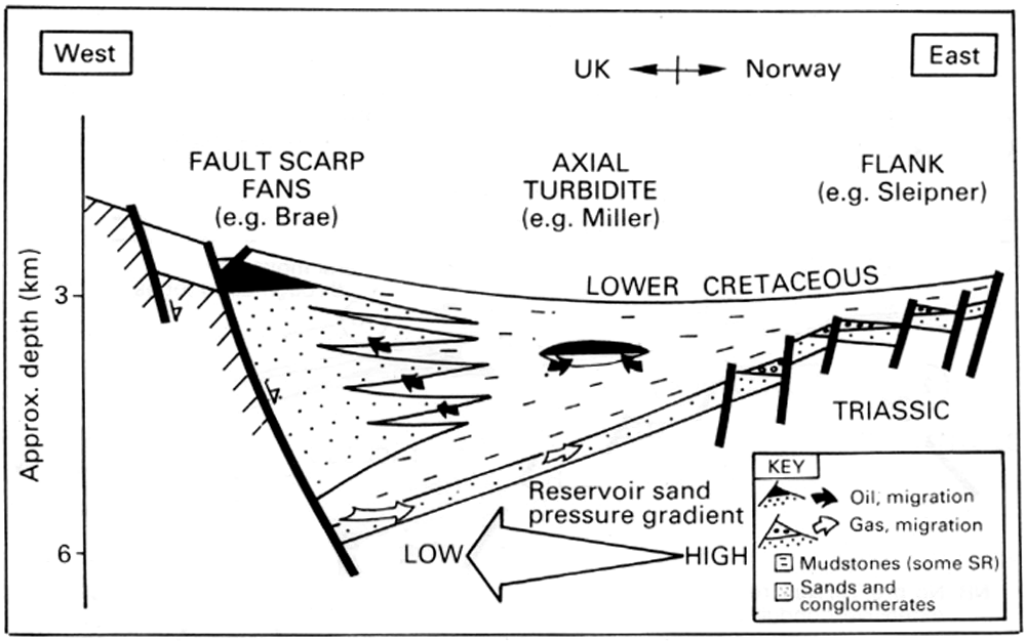

Figure 2.10 Oil and gas migration routes in the South Viking Graben, North Sea (Cornford, 1998).

The oil and gas migration routes in the southern South Viking Graben are illustrated in an east-west cross-section (Figure 2.10). The asymmetry of the graben favours high-efficiency oil migration to the west into Brae and T-Block fields, while the late-mature wet gas tends to migrate to the east to the Sleipner Field, and mid-graben generation of hydrocarbons are trapped by distal fans or turbidites of the Miller Field (Cornford, 1998). Gas clouds and gas chimneys are widely identified in the South Viking Graben. It is believed that the deep gas migrated laterally up-dip, before vertical migration became more efficient than lateral migration in shallower depths. Vertical gas migration is interpreted to be the result of the local failure of the seal integrity, partially resulting from overpressure (Buhrig, 1989). CO_2 is not specially examined or mentioned in these studies.

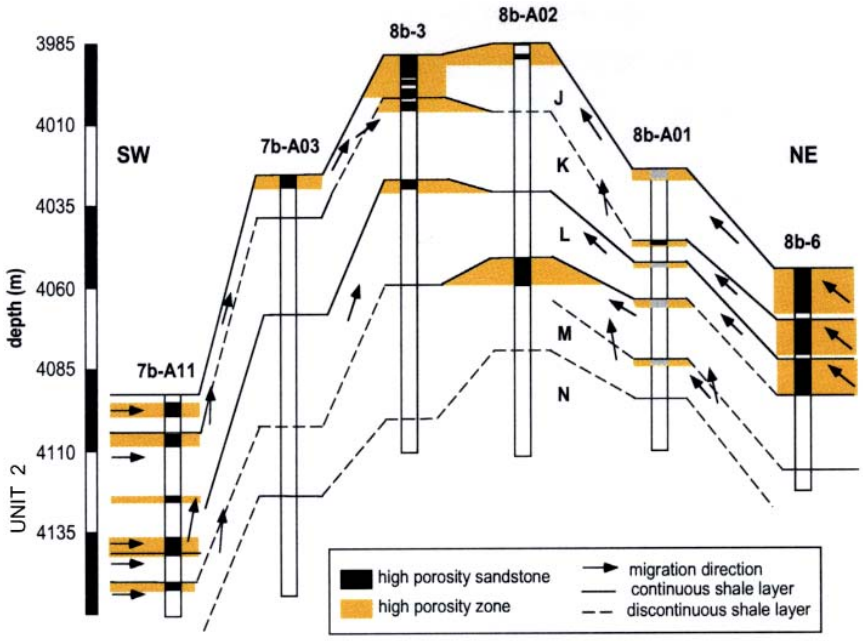

Figure 2.11 Model of hydrocarbon migration and accumulation in the reservoir of the Miller Field (Smalley et al., 1993).

In the model of hydrocarbon migration and accumulation in Miller, oil enters the reservoir via the flanks of the anticline structure and migrates along shale barriers (Figure 2.11) (Smalley et al., 1993). The first oil accumulated in small closures beneath intra-formational shales. Some oil ponded at the top of the reservoir. With progressive filling, oil migrates upwards and accumulates at the Miller Field crest and the shales became engulfed by downward movement of the OWC. At the present day, there are just two OWCs in the south part of the field. All the previous smaller intra-reservoir shale seals have now been totally engulfed by the main OWCs. A number of laterally extensive mudrocks were suggested to be barriers to vertical permeability (BP et al., 1988). Though the Miller Field seems to be compartmentalized on a small scale, geochemical data of produced oil on a large scale has generally failed to identify compositional differences between the different positions of the field charge. No quantifiable vertical or areal trends in fluid PVT properties were recognized by the BP report (BP et al., 1988). Data from gas chromatograms (GC), mass chromatograms, biomarker parameters and GC-IRMS of produced oils from the Miller Field also indicate that the petroleums are very homogeneous throughout the reservoir (Petch et al., 1994; Larter et al., 1995). These various lines of evidence suggest that the petroluems in the field were generated from a single source. Hence, the petroleums from different structural parts now show a homogeneous composition, though they have undergone

different filling histories and are trapped in different positions as a result of the presence of intra-reservoir shales.

2.8. CO_2 accumulation in the reservoirs

The CO_2 content in natural gases increases with depth and temperature in normal sedimentary basins. Linear correlations between temperature and the log of the partial pressure of CO_2 (the product of the mol% CO_2 × the reservoir pressure) exist in clastic hydrocarbon reservoirs in the Gulf Coast and Norwegian continental shelf (Smith and Ehrenberg, 1989). It is suggested that the correlation is the result of inorganic chemical equilibria between silicates, clay, and carbonate minerals (Smith and Ehrenberg, 1989; Hutcheon and Abercrombie, 1990). The reactions between these minerals maintain CO_2 concentrations at levels of less than 5 mol% in the lower temperature reservoirs (<170 ºC).

The reservoirs in the Brae-Miller area contain abnormally higher CO_2 contents than normal clastic reservoirs (Figure 2.4 and 2.7). This could result from major addition of CO_2 from deep or high-temperature sources, such as thermal destruction of marine carbonates and exsolution from magmas (Thrasher and Fleet, 1995). Present-day CO_2 in the Miller reservoir has an average $\delta^{13}C$ value of -8.2 ‰ V-PDB, similar to those from other CO_2-rich fields in the region (James, 1990). CO_2 in the neighbouring Sleipner West Field also has a similar average $\delta^{13}C$ value of -7.9 ‰, with a range from -6.5 to -10.4 ‰ (B. Tocher, Statoil, 2007, personal communication). The variability of carbon isotopic compositions in this region (-3.0 to -10.4 ‰) suggests against sole mantle origin which gives CO_2 $\delta^{13}C$ values of -4 to -7 ‰ and appears to be the result of mixing in varying proportions between different types of sources (Clayton et al., 1990; James, 1990; Thrasher and Fleet, 1995). The relative heavy values in the region indicate an inorganic origin resulting from either metamorphic reactions at depth or from magmagenesis (Thrasher and Fleet, 1995). Thermal destruction of deeper Zechstein marine dolomites which are juxtaposed against the Jurassic reservoir sandstones is suggested to be the source for this CO_2 (Baines and Worden, 2004). The lower isotope values, as James (1990) suggests, are typical of that derived from thermal maturation of organic matter.

The CO_2 content in the different oilfield reservoirs within this stratigraphic interval shows a decrease away from the Central Brae and South Brae fields, which are bounded to the west by the boundary fault of the South Viking Graben (Figure 2.4). This suggests that CO_2 may have migrated from depth along point conduits associated with the boundary fault below the

Brae fields. CO_2 first filled the Central Brae and South Brae fields, then, migrated laterally to reach the surrounding fields. The timing of emplacement of such large amount of CO_2 in this area is not well understood.

CO_2 is present within all compartments of the Miller Field. CO_2 contents in the different units are significantly differentiated. The black oil phase contains 15-25 mol% CO_2, whereas up to 60-70 mol% CO_2 was found from separator gas during water testing (Figure 2.7) (Baines and Worden, 2004). This implies that the Miller Field is compartmentalized to CO_2. The laterally extensive mudrocks interbedded in the reservoir sandstones probably act as barriers to vertical permeability, controlling or affecting CO_2 migration path and accumulation (BP et al., 1988).

2.9. Summary

- The Miller Field is located on the western margin of the South Viking Graben in block 16/7b and 16/8b. The South Viking Graben is a half graben fault-bounded to the west against the basement of the Fladen Ground Spur. Late Jurassic rifting and subsidence in the graben led to deposition of submarine fan systems which constitute the reservoirs in the Brae-Miller area.

- The Miller reservoir sequence comprises Upper Jurassic submarine fan sandstones of the Brae Formation which were sourced from the Devonian sandstones at the Fladen Ground Spur to the west. The fan deposits form the distal part of an extensive syn-rift submarine fan in the late Jurassic rifting of the South Viking Graben. The Brae Formation generally comprises a fining-upwards sequence. It also shows distinct compositional differences across the graben. Near the western margin, the Brae Formation sandstones consist of thick units of mud- and sand-supported conglomerates and coarse-grained sandstones at the North, Central, South and East Brae Fields. Further eastwards in the Miller and Kingfisher fields, these sandstones prograde into medium- to fine-grained mid- and distal-fan deposits.

- The Miller reservoir sandstones are composed of three main lithofacies. Clean fine- to medium-grained, well-sorted quartzose sandstone is the dominant lithology. The sandstone is subarkosic to sublithic in composition and is interpreted to have been transported by, and deposited from, sand-rich, high-density, low-efficiency turbidity

currents. The second lithofacies, thinly bedded alternations of sandstone and mudstone, are usually interbedded with the clean sandstones. This facies is considered to be the deposits of low-density turbidity currents. The third lithofacies is isolated mudstones locally interbedded within the main part of the reservoir. The mudstones represent normal background sedimentation at margins of the fan system, or during periods of non-deposition within the fan.

- The Kimmeridge Clay Formation, which laterally interfingers with the Brae Formation sandstones and also directly overlies and underlies the main reservoir, is the source and seal at the Miller Field. The KCF mainly consists of organic-rich 'black' shales interbedded with thin sand/silt beds. It was deposited in a deep water anoxic environment during regional rifting and subsidence in the latest Jurassic. The consequent subsidence resulting from fault movement, controlled the sea floor depressions in which the highly organic facies have accumulated. Sedimentation rates were high in the central areas of the graben where thickness of the whole shale sequence reaches 500-1000 m.

- In the Miller Field, the Kimmeridge Clay source rocks started generating oil at around 40 Ma, when the source rocks were buried to 3100-3400 m. The oil is believed to be generated on the flanks of the structure in the surrounding source rocks and, thus, the migration path is very short. The first oil accumulated in small closures in shales followed by progressive upwards filling and accumulation in the crest. The shales became engulfed by downward movement of the OWC.

- The oil and gas fields in the Brae-Miller area contain various contents of CO_2, from over 30 mol% in the Central and South Brae Fields to less than 10 mol% in the Sleipner West Field. The eastwards decrease in concentration suggests that the CO_2 may have migrated from depth along the western boundary fault before laterally infilling the surrounding fields. CO_2 is present within all compartments of the Miller reservoir with significantly different contents in the different units, indicating that the Field is compartmentalized. The laterally extensive shale layers interbedded with the reservoir sandstones probably acted as barriers to vertical permeability. The CO_2 is thought to be a mixture of organically-derived CO_2 from normal maturation of organic matter, with a component of inorganic CO_2 generated from thermal

degradation of Zechstein marine carbonates. The timing of emplacement of such large amount of CO_2 in this area is not well understood.

CHAPTER III

X-RAY DIFFRACTION MINERALOGY

3.1. Introduction

Interactions between CO_2, brine and rock forming minerals are very likely to occur when CO_2 charge disrupts and established equilibrium of the original geochemical system of rock and porewater. CO_2 can react directly or indirectly with minerals in the geologic formation, leading to the dissolution of aluminosilicate minerals and carbonates and precipitation of clay minerals and carbonates. (Gunter 1996; Gunter et al., 1997; Brosse et al., 2002; Baines and Worden, 2004). These reactions would alter the mineralogical compositions. Therefore, it is possible to identify the CO_2-reactions if the alterations in mineralogy can be quantified. At Miller Field, the bottom of the sealing Kimmeridge Clay Formation (KCF) has been in contact with the CO_2 accumulation in the Brae Formation reservoir since the emplacement. The variations of mineralogy with depth through the reservoir top, if there are any, are the most plausible position to seek evidence of a record of the CO_2-induced reactions.

Due to fine particle size, quantitative analysis of mudrock mineralogy is difficult using the conventional optical microscope methods used for coarser-grained rock types. X-ray diffraction has the proven ability to be a quantitative method of mineral analysis for shale. This has been demonstrated by previous studies (e.g. Hillier, 2000; 2003; Bish and Post, 1993; Ruan and Ward, 2002), though XRD has also traditionally been thought to have limitations for this type of task (see section 2 below). This study uses XRD analyses of mudrock samples, and includes a validation analysis, which demonstrates that desirable accuracy can be achieved in quantitative XRD analysis by using Rietveld method.

In this chapter, I report and interpret the results of quantitative X-Ray diffraction mineralogical analysis of the KCF samples. The aim of the study is to investigate the spatial variations in mineralogy in relation to the CO_2 source in the underlying reservoir. I expect that, if CO_2 accumulation resulted in dissolution and precipitation of certain minerals, there should be vertical increase or decrease of these minerals away from the reservoir. The types of the reactions can be determined by comparing the CO_2-altered and unaffected intervals. Another purpose of this study is to investigate if there is any CO_2-related mineralogical variation between oil zone and water zone in the reservoir section. It is expected that oil zone samples should bear weaker effects of CO_2 reactions than water zone samples because oil could have hindered digenesis (e.g. Marchand, 2001). By comparing mineralogy in different zones, light can be shed on spatial distribution of the reactions.

Although general statements about the accuracy to be expected from XRD methods are often quoted in the literature, there are, in fact, relatively few studies which demonstrate the degree of accuracy (Hillier, 2000, 2003). In order to estimate the accuracy of the XRD method applied in this study, a test experiment on a set of synthetic samples was conducted. The test samples comprise a variety of clay and non-clay minerals with known weight percent. By comparing the results of XRD analysis with the known answer, it enables validation of the method accuracy and precision.

3.2. Methodology

X-ray diffraction (XRD) has long been regarded as one of principal tools for identifying minerals, especially clay minerals (Moore and Reynolds, 1997). Also it is frequently used for quantitative analysis of geological materials containing clay minerals (e.g. Hillier, 2000; 2003). However XRD has traditionally been thought to have limitations in quantitative analysis in multi-component samples. Potential limitations include effects caused by variations in mineral crystallinity, preferred orientation in the sample mount, grain size of the different particles and differential absorption of X-rays by the various minerals in the mixture (Ruan and Ward, 2002).

Several methods have been proposed to provide quantitative mineralogical analyses of rocks based on X-ray diffractometry (e.g. Hardy and Tucher, 1988; Bish and Post, 1989). There are essentially two common approaches to quantitative analysis. The first of these include addition of a known proportion of mineral spike to the powdered sample and evaluation of the ratio of particular peak intensities of the minerals present to those generated by the added

spike component. The second approach, which is applied in this study, is the analysis of the full profile of an XRD pattern to refine the crystal structure of a mineral or other crystalline phase (Rietveld, 1969). Rietveld methodology allows a calculated XRD profile of each mineral to be generated from its refined crystal structure, and the sum of all calculated patterns to be fitted to the observed XRD profile of mineral mixture by least-squares analysis to find the optimum phase scales. The phase scales are then used to determine the individual mineral percentages in the sample (Bish and Post, 1993).

3.3. Issues of sample preparation

Quantitative analysis of whole rock samples generally requires that the sample is prepared as a random powder. The random powder insures that the incident X-rays have an equal chance of diffracting off any given crystal lattice face of the minerals in the sample. There are many features that should be considered when preparing random powder samples (Snyder and Bish, 1989; Bish, 1994). However, when quantitative analysis is the aim there are two very important factors that must be controlled. The first concerns the size of the powder particles and the second is preferred orientation of certain minerals. If either or both size and preferred orientation are not controlled, the reproducibility of the diffraction data will not be good enough for quantitative analysis (Hillier, 2003).

Particle size needs to be reduced to the order of 10μm or less for a number of reasons (Bish, 1994). If particle size is coarser than 10μm, there will simply be an insufficient number of particles in the right orientation to obtain reproducible intensity measurements, especially for phases of low concentrations. To gain sufficiently small grains, wet grinding using a McCrone MicroNising mill is applied. This mill, which has a set of agate elements as grinders, is very effective at reducing particle size without altering the diffraction characteristic of the sample. Grinding experiments conducted by Hillier (2003) show that a grinding time of 12 minutes for 2g of pure quartz sample effectively reduces most particles to <10μm in size .

There are a number of methods of preparing a random oriented powder mount. Making a random powder is difficult because most minerals have anisotropic shapes. These minerals tend to adopt a preferred orientation with the slightest amount of pressure. Thus, diffraction from some planes is over presented while it is diminished for others. This leads to variation in peak intensities that are not related to concentration. Spray drying is a method capable of producing truly random powder samples (Hillier, 2000). But conventional top-loading

method is applied in this study to produce randomly oriented powder mount because its procedures are relatively easy to perform. However, one must bear in mind that even the most careful packing of a powder sample into a standard holder results in some degree of preferred orientation. In fact, the problems posed by preferred orientation have been one of the biggest obstacles to the development of reliable methods of quantitative analysis of random powders. Although some orientation is inevitable, the method applied in this study demonstrated sufficient control on preferred orientation as a testing experiment on 9 synthetic samples yielded good accuracy and reproducibility.

In this study, the rock chips were first ground in a steel TEMA mill for 35 s. The weighed powder mixtures (~2 g) were transferred to McCrone MicroNising mill for further grinding. Fifteen millilitre of water was added to the mill for each sample. Each sample was ground for 12 minutes. The resulting slurries were freeze-dried before being loaded into cavity holders for X-ray examination. The grain size of these powder samples is likely to be bigger and less homogeneous. Note that the samples of well 16/7b-20 were only gound by the TEMA mill, not treated by a McCrone mill and by the following freeze-drying.

Powder samples were top loaded into 2.5 cm diameter circular cavity holders. A flat metal slide with rough surface was used to press powders into the sample holder firmly enough so that it will not fall out, but not so firmly that severe preferred orientation would be induced on the surface. This provides a somewhat roughened surface on the powder for exposure to the X-ray beam, reducing but not eliminating preferred orientation effects. This procedure is vital for the final analysis results, especially, when platy minerals are involved, such as muscovite, illite, or kaolinite, all of which strongly tend to be preferentially oriented are involved. It is helpful to load a right amount of powder into the sample holder to ensure that powder just fills up the holder by pressing lightly.

3.4. Analytical methods

3.4.1. Identification

X-ray diffraction analysis was conducted on a Bruker AXS D8 diffractometer at Edinburgh University. Diffraction patters were recorded by step scanning from 2-75°2θ, with a step size of 0.013605°and counting for 0.7 s per step. With these conditions, it takes 72 min to run one sample. Bruker AXS Diffrac AT Eva 9.0 software by SOCABIM (2003) is used to identify the mineral phases.

There are usually numerous structure files for each mineral because of the variations of crystallinity. The particular structures which best fit the observed XRD profile can be identified by comparing the peak position and peak height in Eva program. The structure files for each mineral phase which are used to produce synthetic XRD profiles can be found and downloaded from Chemical Database Service (http://cds.dl.ac.uk) as CIF files. Then, the CIF files were converted to STR files which are required by Topas program.

Illite is characterized by a series of peaks at about 10, 5 and 3.3 Å, that at 5 Å being about a third the intensity of the other two. The term of illite is usually used both for a specific mineral and in a more general sense to refer to the more heterogeneous micaceous component of sedimentary rocks (Hillier, 2003). XRD patterns of mica minerals resemble closely the patterns of illite. In this study, therefore, muscovite is used as the proxy mineral for both mica minerals and illite. Mica and illite are not separated and are both represented as 'Illite' in the results. Far less mica than illite can be seen in examination of the same samples by scanning electron microscopy. Therefore, illite should be the dominant phase among them.

In mudrocks, illite and smectite often form mixed-layer illite/smectite which most commonly occurs mixed with discrete illite. The identification of smectite and mixed-layer illite/smectite is a subject in itself (Środoń, 1984; Moore and Reynolds, 1997; Hillier, 2003). The identification of these phases requires various pre-preparation treatments including glycolating and heating. In this study, these mineral phases are included in a single phase as 'illite'.

Kaolinite is primarily identified by two peaks, one at 7.15 Å and the other at 3.58 Å. It can be problematic to distinguish kaolinite from chlorites. Often the precise position of the kaolinite 002 peak is diagnostic and may be easily resolved from the 004 peak of Fe-rich chlorites. Furthermore, it is rare to observe Mg-rich chlorite in the same sample as kaolinite (Hillier, 2003).

Albite was used as proxy for sodium plagioclase minerals. However, rather than referring to a particular mineral with a specific chemical composition, plagioclase is a solid solution series ranging from albite to anorthite. Sodium and calcium atoms can substitute for each other in the mineral's crystal lattice structure. Therefore, the structure files of albite only approximate the actual occurrence of sodium plagioclase.

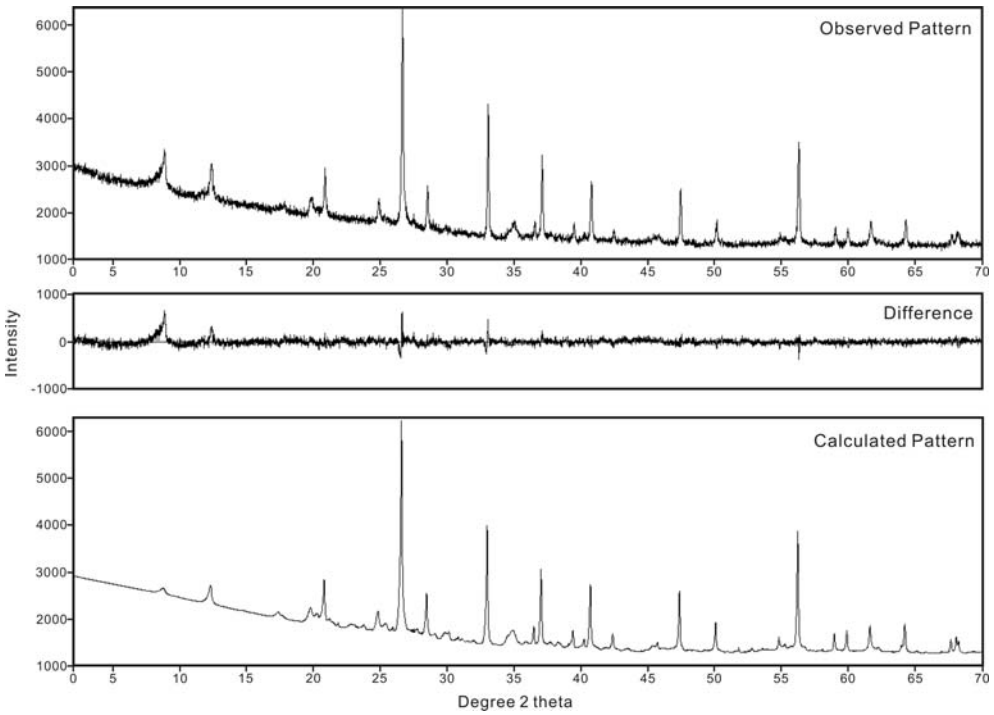

Figure 3.1 Output from Topas Rietveld processing, showing observed XRD pattern (top), calculated pattern based on refined mineral structures (bottom) and difference between them (middle). Sample from 4291.7 TVD m, well 16/8b-5, the Miller Field.

3.4.2. Quantification

Quantitative analysis was conducted using Topas 2.1, personal computer software based on Rietveld method by BRUKER AXS GmbH (2003). The Rietveld method is known as a full-pattern fitting method, as a software generated pattern is synthesized from calculating for each mineral in the sample and fits with the observed diffraction pattern. The difference between the synthetic pattern and the observed pattern is minimized by an interactive refinement/optimization procedure (Bish, 1994). The Rietveld parameters for each mineral phase can be adjusted within the program, to replicate more closely the mineral's contribution to the measured pattern and allow for variation due to layer disordering, preferred orientation, and other factors. In effect, the Rietveld method uses calculated standards which are amended to match the actual mineral phases present during the refinement process. Overall intensities of the individual mineral phase, together with unit-cell dimensions, line widths and preferred orientation for the minerals and the zero setting of the diffractometer, are progressively refined by the operator to fit the full profile of the sample's XRD pattern. Weight percentages of the minerals are calculated along with overall goodness of the fit (global chi^2) between the observed and computed profiles (Figure 3.1). The results of the Rietveld analyses represent the final output from each task when the best

possible fit had been achieved between the observed and computed XRD patterns (minimum global chi^2 is achieved).

3.5. Samples

Mudrock samples were taken from nine wells in the Brae and Miller area. Six of them are located in the Miller Field (well 16/7b-20, 16/7b-24, 16/8b-3, 16/8b-5, 16/8b-A1 and 16/8b-A2), two in the East Brae Field (well 16/3a-E1 and 16/3b-5) and one in block 9 (well 9/28b-17), ~ 30 km northeast to the Miller Field (for well location, see Figure 2.2 and 2.4. Well 16/8b-A1, 16/8b-A2 and 16/3a-E1 are shown as black squares as production platforms in Figure 2.2). The last well is from a low-CO_2 area and serves as a control well to compare with the Miller wells which have been exposed to high concentration of CO_2.

All the samples were taken from the shale lithology in the sealing KCF and the Brae Formation. Samples were not taken from sandstones. The samples are variously spaced with depth due to the random occurrence of shale beds in the formations. The intervals with highest sampling frequency are those immediately above and below the reservoir top because emphasis is placed on investigating mineralogical variations vertically upwards into the seal at the reservoir crest.

In order to put constraints on the accuracy and reproducibility on the XRD method, a test experiment was conducted on a set of synthetic powder samples with known composition. Nine synthetic samples were made by mixing a number of weighed minerals which are commonly present in shale. The pure mineral samples were crushed into fine powder in a TEMA mill for 35 s. The mineral powders were weighed and mixed to produce the mixing samples in a total weight of ~2 g. In order to assure validation across a range of abundances, the samples were prepared so that each mineral constituted various known percent of the mixtures. Then, the powder mixtures were transferred to McCrone MicroNising mill for further grinding and thorough mixing. All the resultant synthetic samples were analyzed following the same procedures and methods for the field samples.

3.6. Results

3.6.1. Synthetic samples

The results of XRD analysis for the first eight of the nine synthetic samples are compared with the actual mineral compositions in Table 3.1. Absolute error (difference between percentage found and actual percentage) and relative error (absolute error divided by actual

percentage) are also shown. The actual percentages and the measurements of the minerals are cross-plotted in Figure 3.2 which shows a very good correlation along 1:1 line.

The last synthetic sample was used to test the reproducibility of the XRD method. The experiment procedures starting from loading into the sample holder were repeated ten times for the same sample. The results for the ten runs are displayed in Table 3.2. Average and standard deviation are presented.

Table 3.1 Comparison between actual percentage of each mineral (wt.% known) and detected percentage by the XRD method (wt.% found) for the eight synthetic samples. Absolute and relative errors (%) are also given for each mineral phase.

Mineral		Quartz	Albite	Kaolinite	Muscovite	Calcite	Pyrite	Total
No. 1	% known	49.18	9.8	21.36	8.35	11.31		100
	% found	50.36	9.8	21.36	7.53	10.95		100
	abs. error	1.18	0	0	-0.82	-0.36		
	% rel. error	2.40	0	0	-9.82	-3.18		
No. 2	% known	45.28	7.48	24.70	15.08	7.46		100
	% found	47.04	7.32	24.93	13.64	7.07		100
	abs. error	1.76	0.16	0.23	-1.44	-0.39		
	% rel. error	3.89	2.14	0.93	-9.55	-5.23		
No. 3	% known	39.96	4.98	31.11	12.99	10.96		100
	% found	41.24	4.77	31.82	11.88	10.28		99.99
	abs. error	1.28	-0.21	0.71	-1.11	-0.68		
	% rel. error	3.20	-4.22	2.28	-8.55	-6.20		
No. 4	% known	35.05	15.13	12.44	15.19	22.19		100
	% found	38.18	13.62	13.21	14.14	20.85		100
	abs. error	3.13	-1.51	0.77	-1.05	1.34		
	% rel. error	8.93	-9.98	6.19	-6.91	-6.04		
No. 5	% known	30.78	24.74	17.24	7.47	9.96	9.8	99.99
	% found	32.94	22.13	18.01	9.73	9.22	7.97	100
	abs. error	2.16	-2.61	0.77	2.26	-0.74	-1.83	
	% rel. error	7.02	-10.55	4.47	30.25	-7.43	-18.67	
No. 6	% known	24.44	24.56	20.22	5.40	5.08	20.29	99.99
	% found	26.00	21.39	24.06	7.61	4.34	16.59	99.99
	abs. error	1.56	-3.17	3.84	2.21	-0.74	-3.70	
	% rel. error	6.38	-12.91	18.99	40.93	-14.57	-18.24	
No. 7	% known	25.12	5.29	31.13	21.28	11.63	5.55	100
	% found	27.06	5.84	31.42	20.87	10.34	4.48	100.01
	abs. error	1.94	0.55	0.29	-0.41	-1.29	-1.07	
	% rel. error	7.72	10.4	0.93	-1.93	-11.09	-19.28	
No. 8	% known	12.56	30.04	5.00	29.91	17.44	5.04	99.99
	% found	13.40	31.22	3.68	27.79	18.96	4.95	100
	abs. error	0.84	1.18	-1.32	-2.12	1.52	-0.09	
	% rel. error	6.69	3.93	-26.40	-7.09	8.72	-1.79	

Table 3.2 The results of ten runs on a synthetic sample following the same loading and analysis methods. Standard devidation and standard error of mean are also shown for the ten runs. The consistency of the results of different runs demonstrates the desirable reproducibility of the methods.

Mineral	Quartz	Albite	Kaolinite	Calcite	Pyrite	Illite	Total
% known*	46.19	8.68	12.96	9.72	9.95	12.48	99.98
1st	48.48	9.71	16.87	10.3	8.62	6.01	99.99
2nd	47.78	10.62	15.99	10.07	8.68	6.87	100.01
3rd	49.23	10.09	15.58	10.28	8.64	6.18	100
4th	48.99	10.5	15.18	10.41	8.48	6.45	100.01
5th	47.98	10.34	16.17	10.04	8.54	6.94	100.01
6th	49.58	10.13	15.13	10.7	8.58	5.88	100
7th	48.43	10.41	15.86	10.04	8.55	6.71	100
8th	49.93	9.56	14.81	10.24	8.89	6.58	100.01
9th	48.12	10.91	15.96	9.96	8.56	6.49	100
10th	48.04	10.27	16.25	10.08	8.70	6.66	100
average	48.66	10.25	15.78	10.21	8.62	6.48	100
st. dev.	0.74	0.41	0.62	0.22	0.12	0.35	
st. error	0.23	0.13	0.20	0.07	0.04	0.11	

*Note that the illite sample used to make this synthetic sample is not pure and contains only ~63 % of illite and certain amount of quartz, kaolinite and feldspar. Therefore, the 'known percentages' of the minerals are not the actual percentages. This is the reason for the large 'absolute errors' for illite and kaolinite.

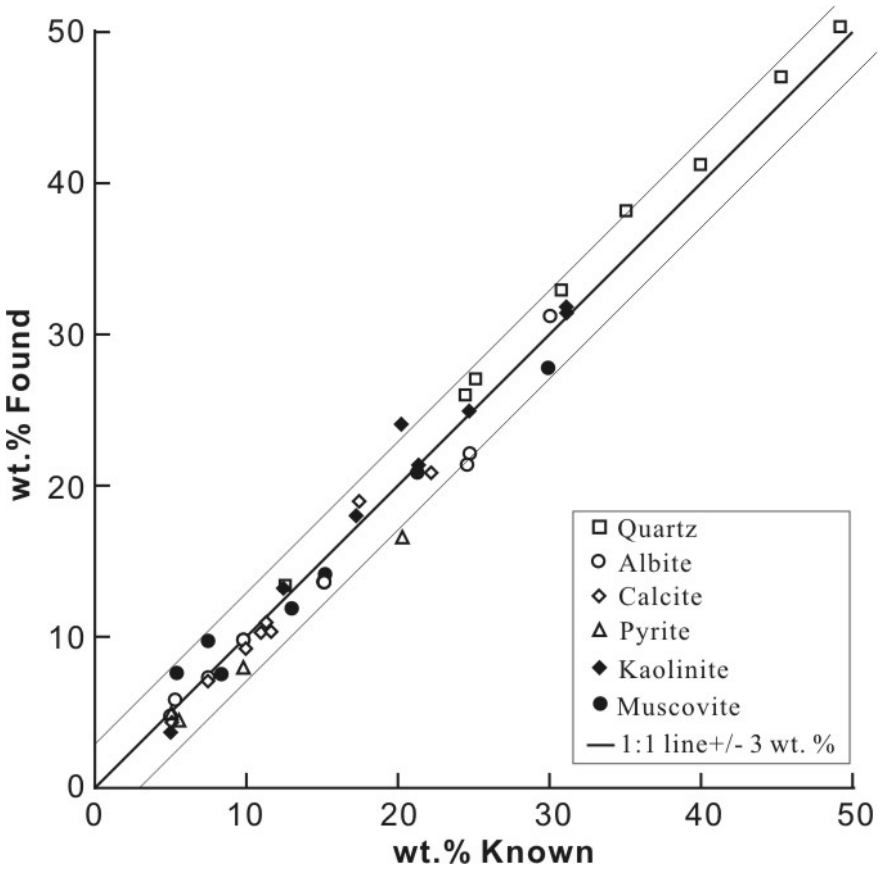

Figure 3.2 Comparison of weight percent known versus weight percent found by the XRD analyses for the eight synthetic samples.

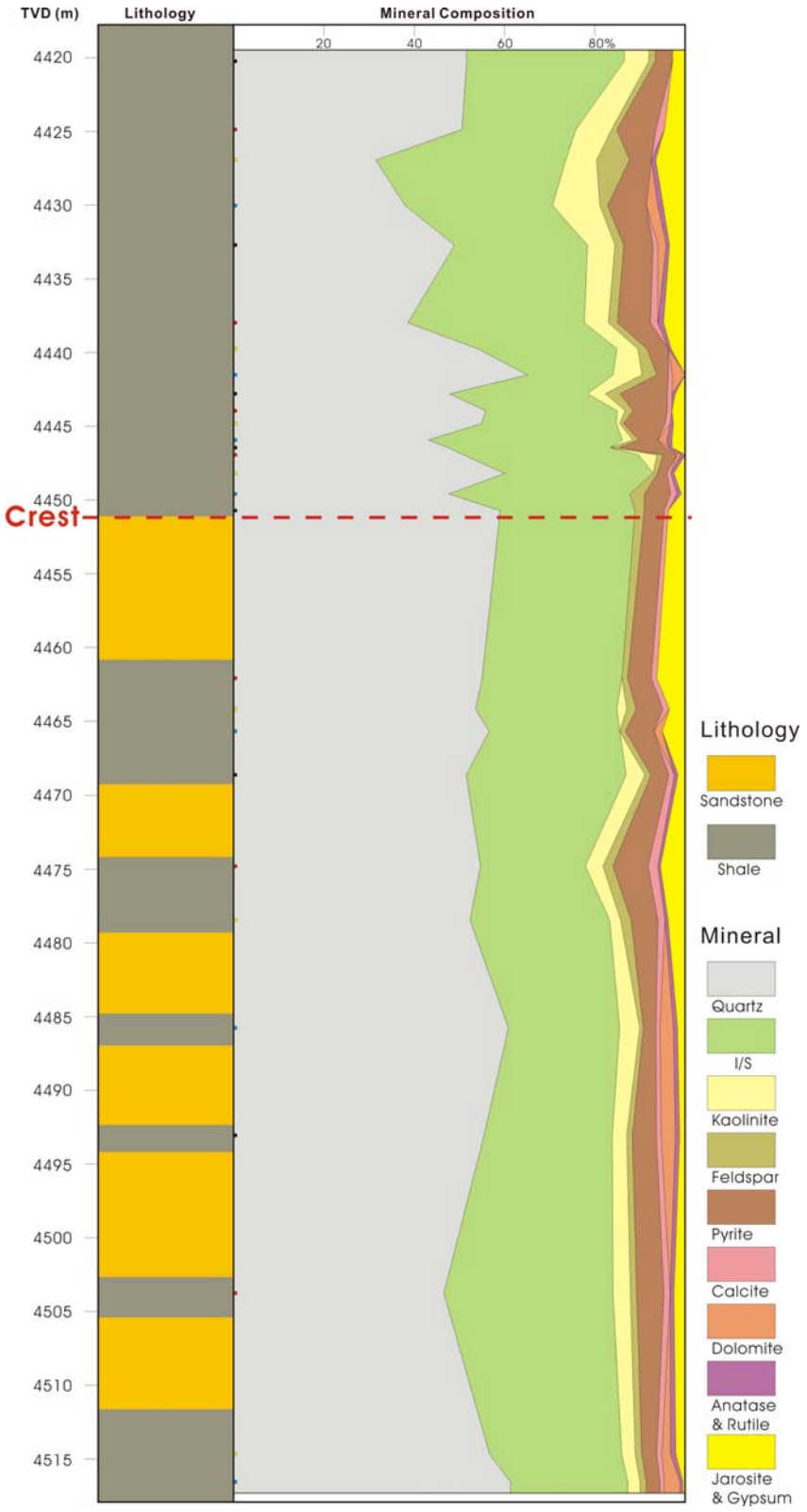

Figure 3.3 Mineral compositions of shale samples plotted against a lithologic column, well 9/28b-17, the control well. Little dots on the column indicate sample positions. Reservoir crest is marked. Note that the profile is not continuous with depth.

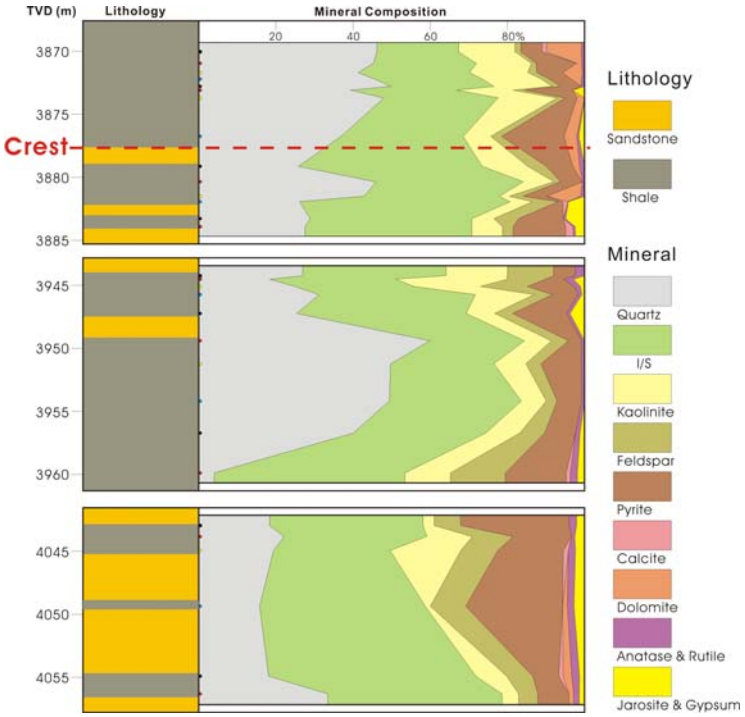

Figure 3.4 Mineral compositions of shale samples, well 16/3a-E1, the East Brae Field. Note that the profile is not continuous with depth.

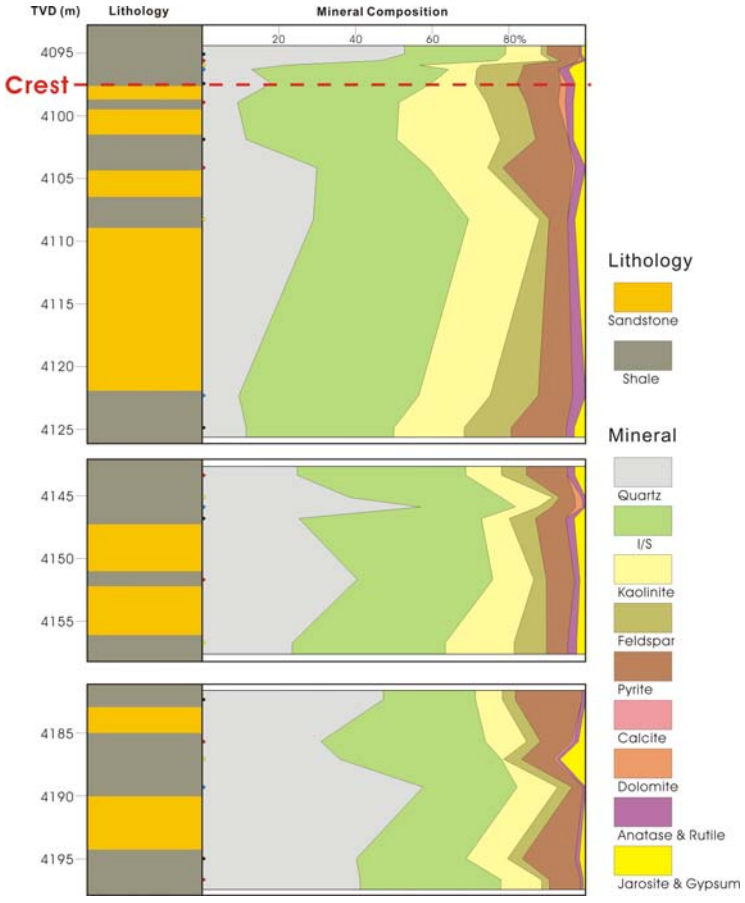

Figure 3.5 Mineral compositions of shale samples, well 16/3b-5, the East Brae Field. Note that the profile is not continuous with depth.

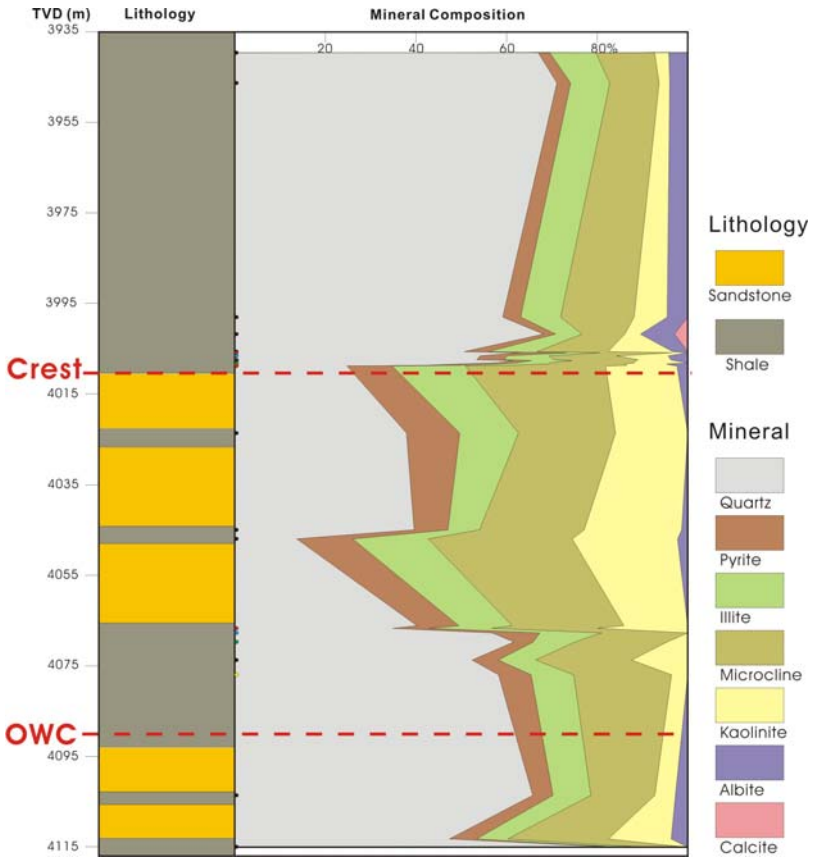

Figure 3.6 Mineral compositions of shale samples, well 16/7b-20, the Miller Field. Reservoir crest and Oil-Water Contact (OWC) are marked. Note that the profile is not continuous with depth.

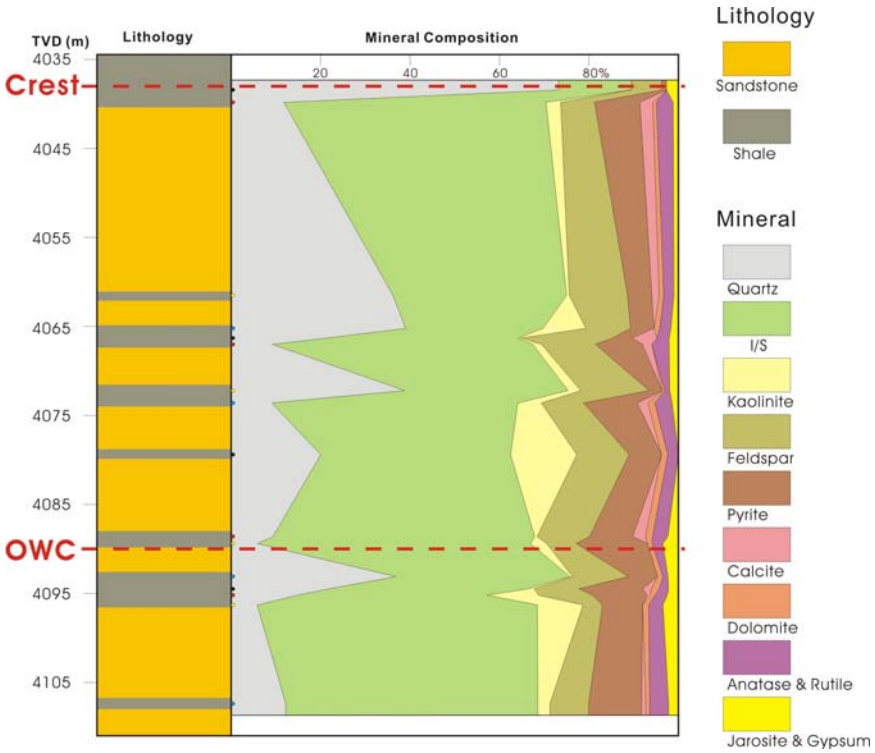

Figure 3.7 Mineral compositions of shale samples, well 16/7b-24, the Miller Field. Note that the profile is not continuous with depth.

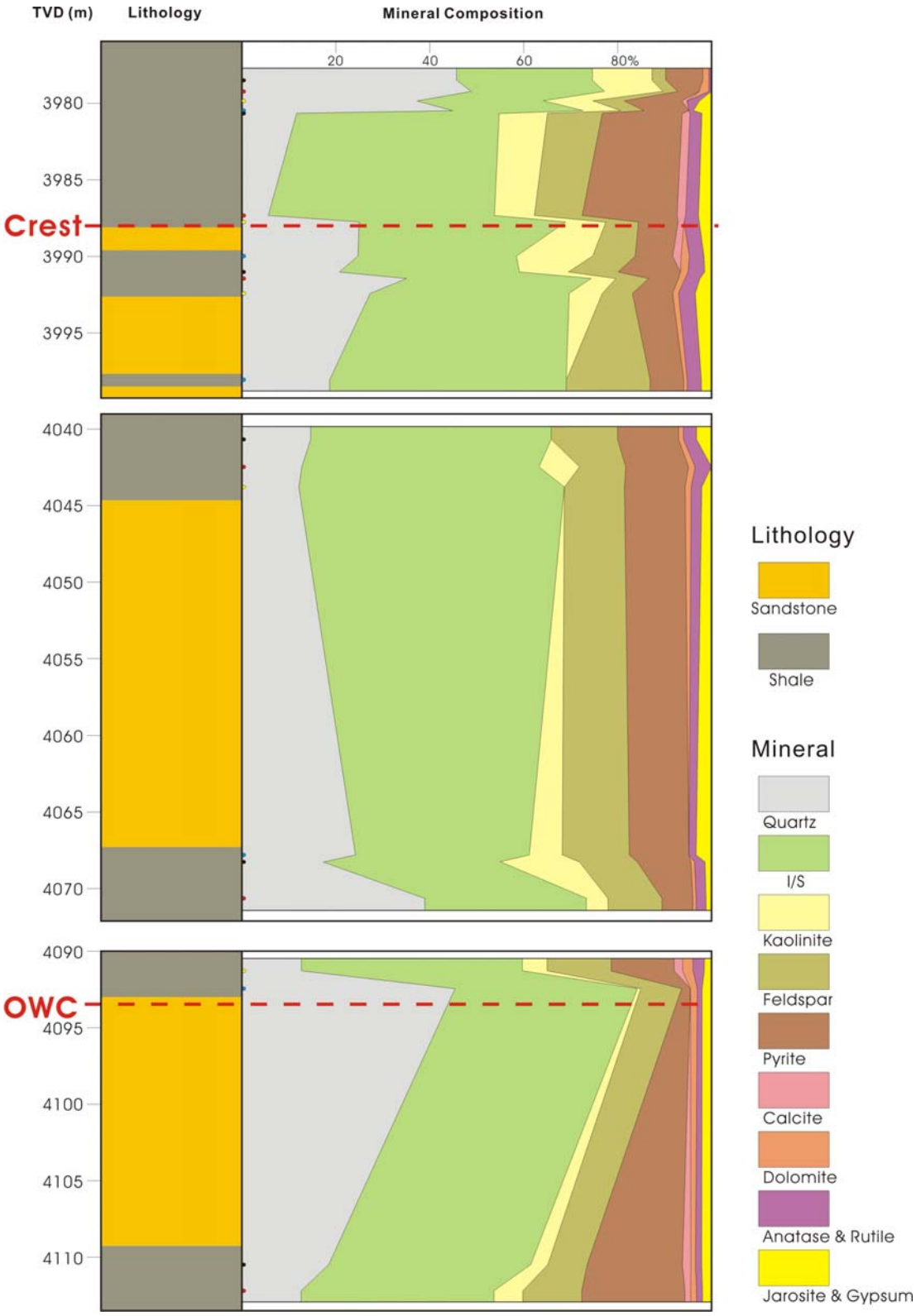

Figure 3.8 Mineral compositions of shale samples, well 16/8b-3, the Miller Field. Note that the profile is not continuous with depth.

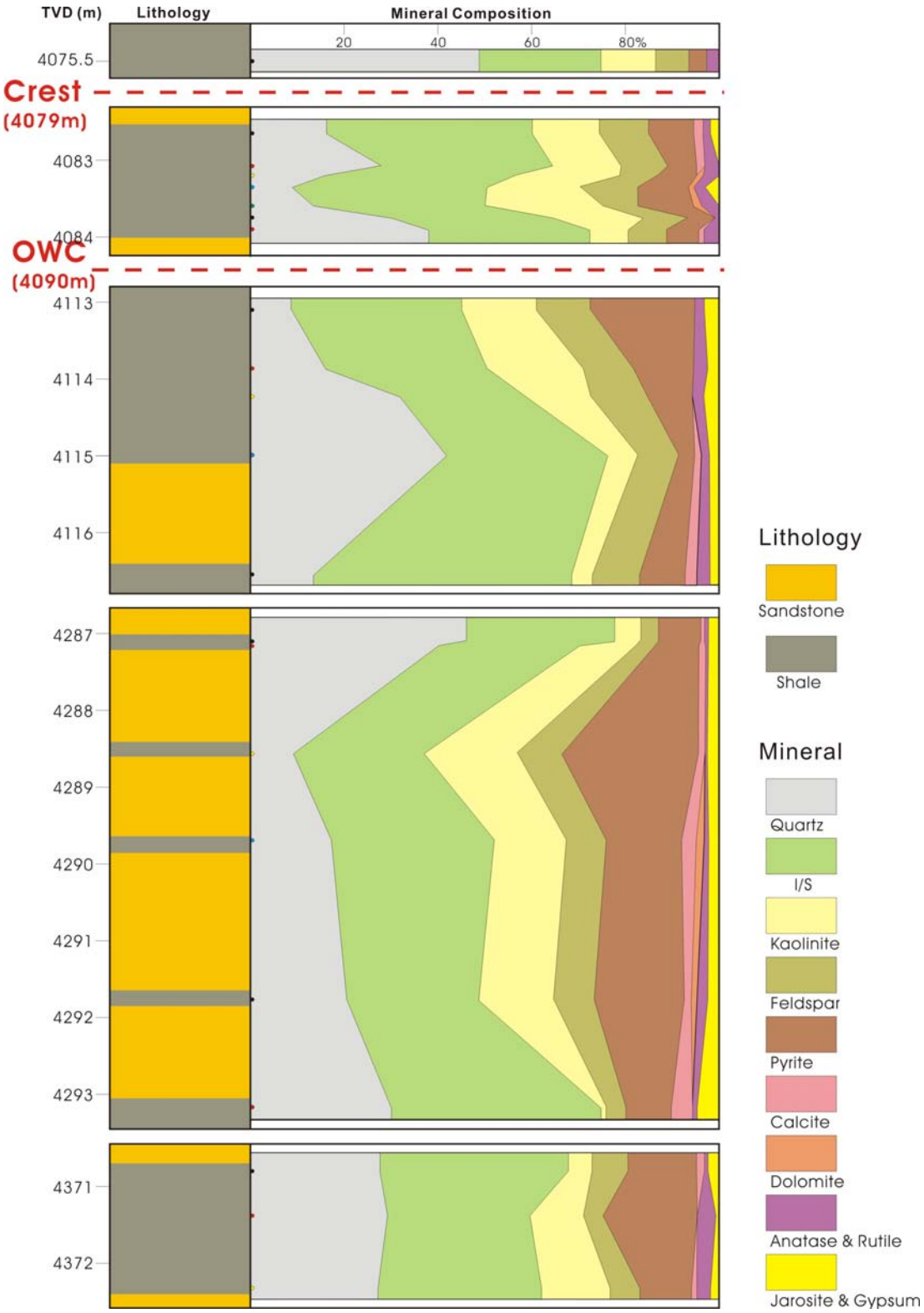

Figure 3.9 Mineral compositions of shale samples, well 16/8b-5, the Miller Field. Note that the profile is not continuous with depth.

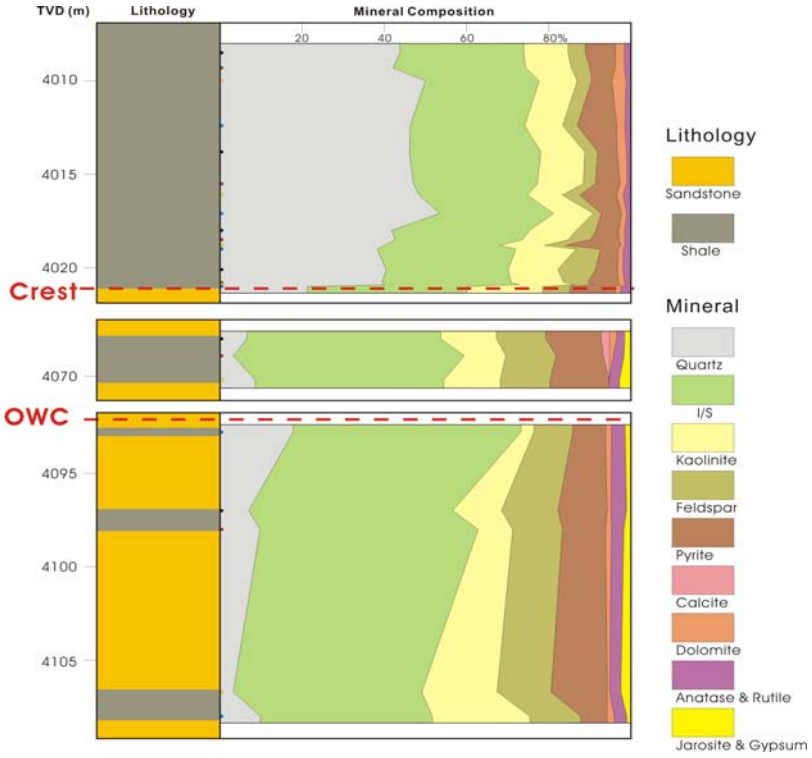

Figure 3.10 Mineral compositions of shale samples, well 16/8b-A1, the Miller Field. Note that the profile is not continuous with depth.

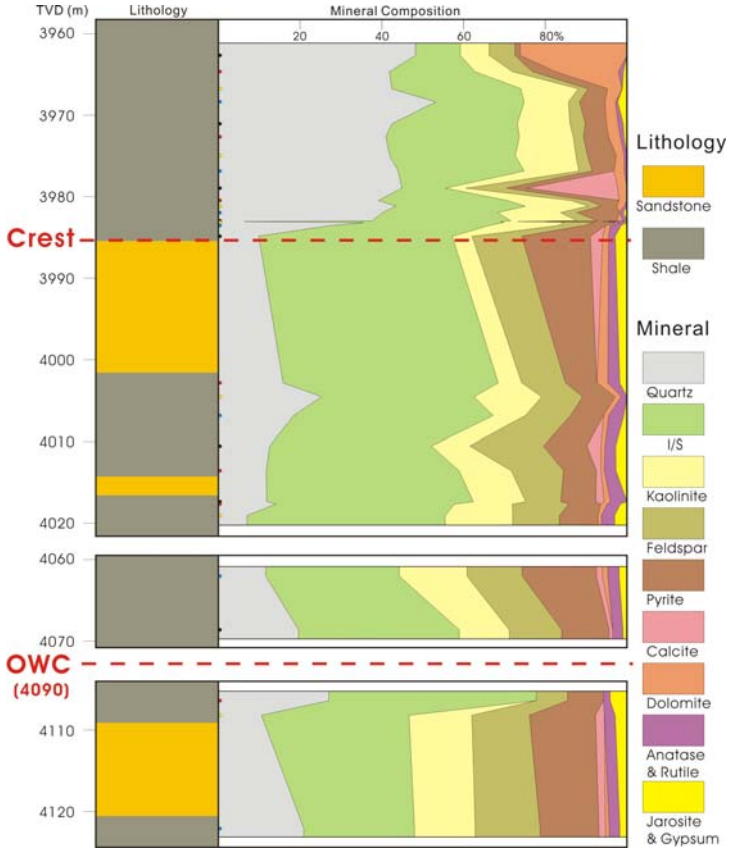

Figure 3.11 Mineral compositions of shale samples, well 16/8b-A2, the Miller Field. Note that the profile is not continuous with depth.

3.6.2. Field samples

The results of the samples from the nine wells are presented in Tables 3.3 to 3.11. The mineralogical data are also projected against the stratigraphic columns in Figures 3.3 to 3.11. Note that, in these figures, K-feldspar and albite are combined into 'Feldspar' phase. Ankerite is put into the dolomite category. Anatase and rutile, jarosite and gypsum are represented by a single colour key. The figures illustrate the overall shale mineralogy with depth.

Interpretation of the diffraction patterns shows that the shale almost entirely consists of five minerals: quartz, illite, kaolinite, K-feldspar and pyrite. Quartz is the most abundant clastic component, ranging from under 5 % to over 70 %. K-feldspar varies up to 30 %, but is mostly under 10 %. It is the most abundant feldspar mineral present. There is small amount of sodium plagioclase (albite) in most of the samples.

Illite is the dominant clay mineral, making up between a little under 10 % and over 60 % of components. Kaolinite is the only other clay mineral identified. It makes up as much as 30 % of the shale components. Pyrite is also among the most abundant minerals, with content up to ~ 30 %, but under 15 % in most samples.

Calcite and dolomite are the main carbonate minerals. Ankerite was also found in three wells. The total concentrations of carbonates vary between zero and ~ 25 %, but most of samples contain less than 5 % carbonates.

Trace amounts of gypsum, anatase, rutile and jarosite are identified in many samples. But none of these trace mineral phases were identified in the samples from well 16/7b-20. This is mainly because these samples were not ground by a McCrone mill and the grain size was not reduced to the ideal level. This also implies poorer quality of this set of data.

Large vertical variation across top reservoir

Except for well 9/28b-17, the low-CO_2 well, and well 16/7b-24 which has no samples from the KCF, all other wells show abrupt variations in mineralogical composition of the shales across the boundary between the KCF and the Brae Formation (Figures 3.3 to 3.11).

Quartz content in these shale samples shows the most obvious vertical variation. Almost all the wells from the Miller Field show an abrupt upwards increase of quartz content from the

reservoir shale section to the seal shale (Figures 3.3 to 3.11). Quartz concentration increases from an average16 % in the Brae Formation shale to 38 % in KCF shale in well 16/8b-A2 (Figure 3.11 and Table 3.11), and from less than average of 8 % to 42 % in well 16/8b-A1 (Figure 3. 10; Table 3.10). Well 16/7b-20 also shows a rapid increase upwards across the reservoir top (Figure 3.6; Table 3.6). In well 9/28b-17, however, quartz concentration does not exhibit significant variations with depth. It averages about 50 wt% in both reservoir shale and cap rock shale sections.

In well 16/7b-20, 16/8b-3, 16/8b-5, 16/8b-A1 and 16/8b-A2 of the Miller Field, the Brae Formation shales generally contain more illite than the KCF shales (Table 3.6, 3.8-3.11; Figure 3.6, 3.8-3.11). Well 16/3a-E1 in the East Brae Field also shows a much lower illite content of 28 wt% in the KCF comparing with 41 % in the Brae Formation shales (Table 3.4; Figure 3.4). However, illite concentration in well 9/28b-17, the control well, is roughly constant vertically as shown in Figure 3.3. No obvious variation with depth can be seen. The average illite content is similar between the cap rock shale (33 %) and reservoir shale (32 %).

Kaolinite has higher concentrations in the KCF shales in one Miller wells (well 16/8b-3) and one East Brae well (well 16/3a-E1) (Table 3.8 and 3.4) while two wells (16/7b-20 and 16/8b-5) display obviously higher contents in the oil leg (Table 3.6 and 3.9).

Five out of six Miller wells (16/7b-20, 16/8b-3, 16/8b-5, 16/8b-A1 and16/8b-A2) show a K-feldspar upwards decrease across the reservoir top (Tables 3.6, 3.8 to 3.11; Figures 3.6, 3.8 to 3.11). The most significant decrease occurs in well 16/8b-A1 and 16/8b-A2. About 4 % of K-feldspar is found in the KCF while about 12 % in the Brae reservoir section. One of the East Brae wells (16/3a-E1) also shows a significant lower K-feldspar content in the KCF with an average of 1.9 % comparing with average 6.3 % in the Brae Formation shales (Table 3.4; Figure 3.4). The shales in well 9/28b-17 contain low content of K-feldspar in both formations (1.4 % in the KCF and 1.7 % in the Brae Formation) and no obvious variation exists in the vertical section (Table 3.3; Figure 3.3).

The mudrocks generally contain few carbonates so that it is less reliable to determine the content variations between two formations. The small difference displayed in the data tables may be within or close the uncertainty of the XRD method. However, Figure 3.4, 3.6, 3.10 and 3.11 still show that shale samples from the overlying KCF generally contain high carbonate contents than those of the Brae Formation. For example, up to 26 wt% carbonates

were found in several KCF samples in well 16/8b-A1 while all the shale samples in the Brae Formation contain less than 4 % carbonate.

The variations between oil leg and water leg in the reservoir section were examined in several wells where samples from both sections are available. Apart from well 16/7b-20, no wells display large mineralogical variations across Oil-Water Contact (OWC) (Table 3.5 to 3.11; Figure 3.12).

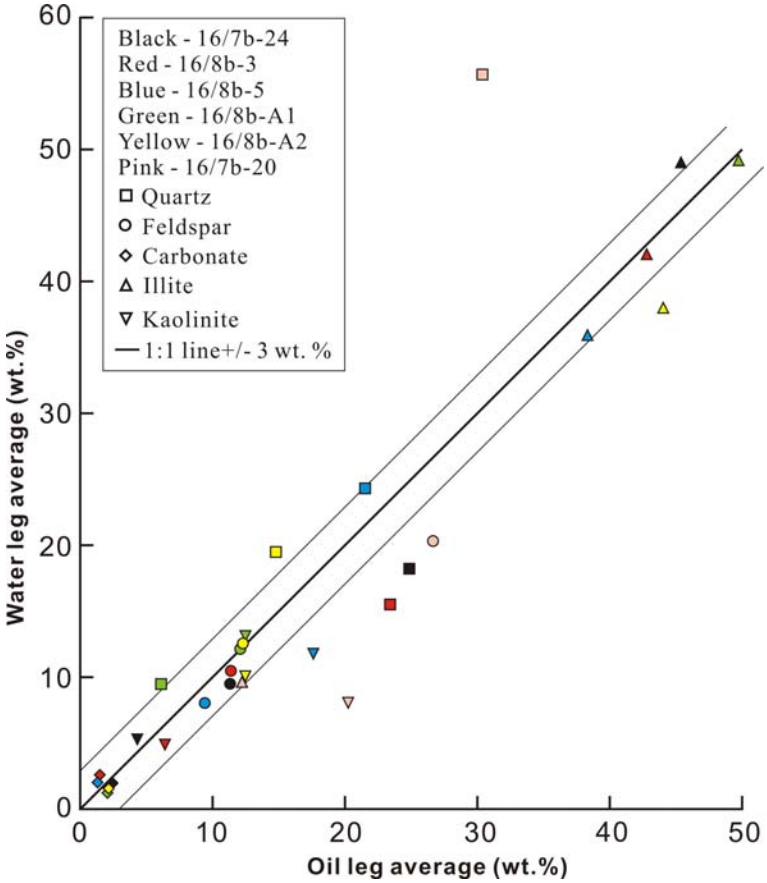

Figure 3.12 Comparison between mineral abundances in shale of the oil leg and water leg. Five minerals associated with CO_2 reactions are included. No large differences between the oil and water leg exist in the Miller wells except well 16/7b-20. The differences for each mineral are not consistent in different wells, indicating no significant difference in diagenetic reactions between the oil leg and water leg.

3.7. Discussion

3.7.1. Accuracy and reproducibility of the XRD method

A comparison of the weight percent known and the weight percent found for the eight synthetic samples is presented in Table 3.1. In all cases, absolute errors are typically several

weight percent or less. Relative errors are mostly under 10 %. Muscovite (proxy mineral for illite), kaolinite and pyrite generally have relatively larger relative errors, indicating the undesirable effects of preferred orientation associated with these minerals.

Figure 3.2 summarises results for 44 data points of the six component minerals in terms of actual percent versus percent found in the XRD analysis. The spread of data along the 1:1 line indicates the sort of accuracy that can be achieved by the method applied in this study. According to Calvert et al. (1989), results within 3 wt% absolute or 10 % relative of the true concentration are considered highly accurate results. Based on research of a selection of previous quantitative studies, Hillier (2000) confirmed that XRD results within 3 wt% absolute represent 'highly accurate' results. In this study, most data fall within ± 3 wt% of the true value. In fact, only three out of forty four (~ 7 %) results fall out of the suggested uncertainty envelope. Indeed, >80 % data are within 2 % absolute error of the known concentration. The results are very encouraging since they demonstrate that the quantitative analysis based on Rietveld method works.

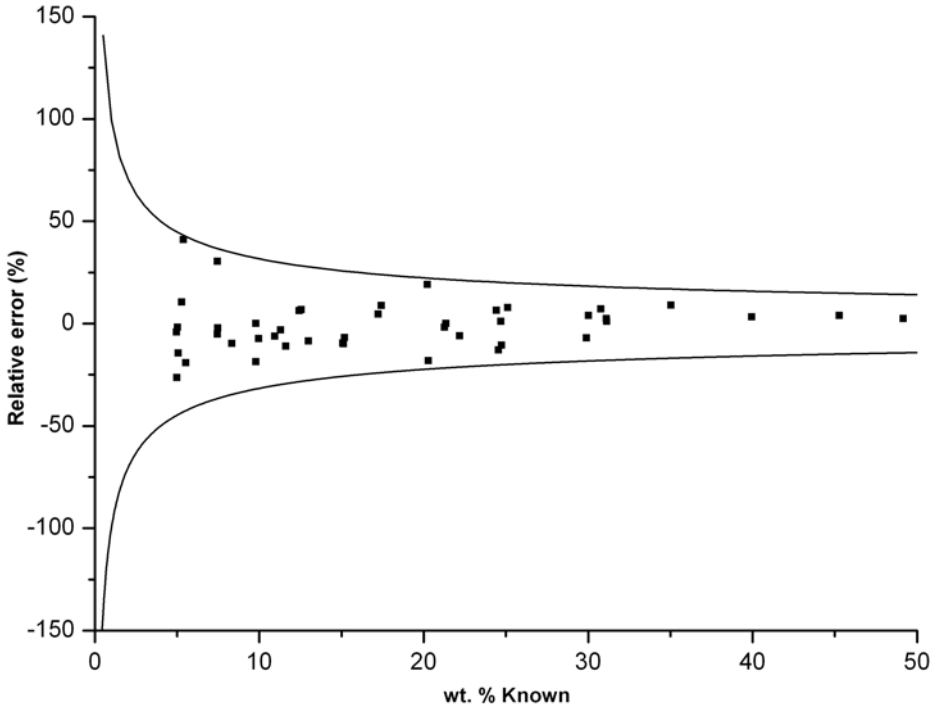

Figure 3.13 Relative error versus actual concentration for the same 44 measurements illustrated in Figure 3.2.

Hughes and Hurley (1987) discussed equations in the form of $y = cx^b$ (where c and b are constants) that relate accuracy with concentration for a variety of chemical analysis methods.

Hillier (2003) demonstrated that the equations of this form can also be applied to describing the relationship between uncertainty and concentration for quantitative XRD methods. It was suggested that, to qualify as a quantitative method, uncertainty should be less than $\pm X^{-0.5}$ at 95 % confidence, where X is concentration in weight percent. The same 44 data points are plotted in Figure 3.13 as relative error versus concentration. These data can be used to derive general models of the relationship of uncertainty to concentration. The lines in Figure 3.13 illustrate this relationship for relative error in percentage ($\pm 100X^{-0.5}$) at 95 % confidence. Note that any other level of confidence can be obtained simply by scaling the first term in the equation by the required number of standard deviations e.g. $\pm 50X^{-0.5}$ at 67 % confidence. Such an estimate is controlled by the phases which have the largest associated errors. For phases that are easy to analyze accurately, uncertainty will be overestimated (Hillier, 2003).

The results of ten repeated runs on the same synthetic sample show desirable reproducibility of the method applied. Due to impurity of the illite sample which contains only ~63 % of illite and certain amount of quartz, kaolinite and feldspar, the 'known percentages' of the minerals in this synthetic sample are not the actual percentages. That is the reason for the large 'absolute errors' for illite and kaolinite. The standard deviations for each mineral of the ten runs are all less than 1 (Table 3.2). Since each run started from an independent loading of the sample holders, the data demonstrate the reliability of this loading technique in controlling the effects of preferred orientation. The desirable reproducibility is believed to be largely a result of the application of wet grinding using a McCrone milling which ensures an adequate reduction of particle size and the proper loading method which avoids severe preferred orientation. Proper reduction of particle size reduces the possibility of serious errors associated with particle statistics, microabsorption and extinction (Snyder and Bish, 1989; Bish, 1994), while sufficient reduction of particle size helps to eliminate preferred orientation. The combination of wet grinding and top loading is, therefore, an ideal preparation technique for XRD quantitative analysis of mudrocks.

In summary, the results of testing the technique show that reproducible analyses can be obtained on the types of mudrock to be investigated. Thus presence or absence of a mineral can be determined at less than 1 wt %. Errors of analyses are typically less than 3 wt %, and do not appear to vary with mineral abundance. Quantification errors are consequently very significant on individual samples aliquots for minerals at less than 5 % abundance. These errors can be reduced by running multiple aliquots of the same sample. Spray drying method

would future improve the accuracy as it can eliminate preferred orientations of clay minerals (Hillier, 2000, 2003).

3.7.2. Vertical mineralogical variations in the wells

Differences in mudrock mineralogy with depth within a given stratigraphic unit are commonly interpreted as evidence that a diagenetic reaction has taken place. For example, increasing illite with depth is interpreted as illite/smectite diagenesis in the study of argillaceous sediments (Hower et al., 1976). In this study, little evidence of gradual increase or decrease of mineral contents with depth can be seen, while abrupt change in mineralogy across the reservoir top is present in most of the Miller wells. This suggests against diagenetic variations with depth.

Possible mudrock reactions with CO_2

Since CO_2 has accumulated in the reservoir for a geological time span in the Miller Field, it might have caused detectable alterations on the rocks exposed to it. Therefore, the mineralogical data of the KCF seal are valuable for identifying potential CO_2 reactions. If it is assumed that the amounts of the CO_2-reaction products have a linear relationship with the vertical distance from the CO_2 pool in the reservoir; it is possible to reveal which specific type of reactions have occurred by analyzing vertical mineralogical variations.

Theoretically, CO_2 reacts directly or indirectly with minerals in the geologic formation, leading to the dissolution of aluminosilicate minerals or carbonates, and the precipitation of clay minerals and carbonates (Gunter et al., 1996, 1997; Brosse et al., 2002; Baines and Worden, 2004). First, CO_2 will acidify pore water which is able to dissolve carbonates (Pearce et al., 1996),

$$CaCO_3 + CO_{2(aq)} + H_2O \rightarrow Ca^{2+} + 2HCO_3^- \quad (3.1)$$

CO_2 is very likely to cause dissolution of Ca/Mg/Fe-bearing silicate minerals (such as feldspar and micas) and precipitation of clay minerals, carbonates and quartz when the acidity has been reduced by silicate dissolution (Gunter et al., 1997; Hitchon et al., 1999). According to studies on diagenesis in sandstones, the formation of quartz and kaolinite is usually accompanied by the precipitation of carbonate such as calcite (Worden and Morad, 2000). The precipitation of calcite is encouraged by feldspar dissolution which lowers pH. Subsequently, the precipitation of calcite releases protons that can in turn be used in further

dissolution of feldspar. Thus, silicate diagenesis is intimately linked to the carbonate diagenesis through their mutual, yet opposite, sensitivity to pH which can be controlled by CO_2 (Worden and Morad, 2000). Thus, the above reactions can be summarized in a single reaction (Hitchon et al., 1999):

$$\text{Feldspar} + \text{Clays} + CO_{2(aq)} + H_2O \rightarrow \text{Kaolinite} + \text{Ca/Mg/Fe carbonate} + \text{Quartz} \qquad (3.2)$$

Dissolution of plagioclase feldspar and precipitation of kaolinite induced by CO_2-derived acid is also proposed by Kirste et al. (2004):

$$2NaAlSi_3O_8 + 2CO_2 + 3H_2O \rightarrow 2Na^+ + Al_2Si_2O_5(OH)_4 + SiO_{2(aq)} + 2HCO_3^- \qquad (3.3)$$

These reactions all predict dissolution of feldspar minerals, while dissolution or precipitation of carbonates depends on actual water acidity and chemistry.

Well 16/7b-20, 16/8b-3, 16/8b-A1 and 16/8b-A2 in the Miller Field have more than five samples available from the sealing KCF; therefore they can be used to compare sealing mudrock with the shales in reservoir section (Figure 3.6, 3.8, 3.10 and 3.11). These wells show rather abrupt variations in mineral proportions across the reservoir top, including upwards increase of quartz and decrease of feldspar, together with heavy carbonate cementation in some samples of the KCF (e.g. well 16/8b-A2). In addition, well 16/8b-3 and 16/8b-A2 show upwards increasing kaolinite abundance. Other Miller wells also exhibit the similar trends, though there are only a limited number of samples of the seal.

No such vertical mineralogy variations can be seen in the control well 9/28b-17. The mineral contents in this well are roughly constant in the vertical profile (Figure 3.3). It is assumed that the original deposition in the Miller wells is similar to that of the control well as they are located within the same geological settings. Consequently, the observed abrupt vertical changes of mineralogy in the Miller wells are thought to be associated with high CO_2 accumulation in the Miller reservoir.

Additional CO_2 charge into feldspar-bearing sediments is most likely to induce the reactions of dissolving K-feldspar and producing clay minerals and carbonates, as has been summarized by Hitchon et al. (1999) in Equation 3.2. It is found that a large volume of K-feldspar has apparently dissolved in coarse-grained sandstones of the Brae Formation in the

Brae fields (McLaughlin et al., 1994) and that dissolution of K-feldspar is typically accompanied by clay mineral precipitation in the Miller Field. If the reaction had also occurred in the mudrocks due to CO_2 accumulation, we would expect to see lowered feldspar and elevated quartz and kaolinite concentrations in the reservoir shales. However, the XRD data suggest that no such CO_2 reactions have occurred in the Brae Formation shales. Instead, they could have taken place in the overlying KCF seal, with XRD data showing higher quartz and lower feldspar abundances.

Mudrock reactions in oil leg inhibited by oil charge?

This paradox can be explained by the proposal that quartz cementation and other diagenetic reactions can be inhibited by oil presence. Quartz cement volumes within the reservoir sandstones have been found to be significantly higher in the water zone than in the oil zone of the Miller Field. The cause for this, within reservoir sandstone, is interpreted as quartz cementation being retarded by oil emplacement. It is suggested that the rates of quartz precipitation and other diagenetic reactions in oil leg were reduced due to the increased tortuosity of the diffusion path for silica ions in solution (Marchand, 2001; Marchand et al., 2001; 2002). Analogous effects in shales are more likely to be the case for the thin shale layers in the reservoir because the oil charge may have enclosed the thin shales and largely cut off the exchange paths from the surrounding porewater and CO_2 accumulation in the reservoir sandstone.

Meanwhile, CO_2 breached into the overlying KCF possibly induced or enhanced the reactions of dissolving feldspar and producing quartz, kaolinite and carbonates. It is more difficult for oil molecules to infiltrate the sealing mudrock. The CO_2-reactions could have occurred without inhibition from oil. Thus, the observed mineralogical changes across the reservoir top in the Miller wells may have been induced by the CO_2-reactions occurred unevenly in different sections (Figures 3.6, 3.8 to 3.11).

Contrary evidence: was deposition heterogeneous?

For the above discussion, the fundamental assumption of initial compositional homogeneity within the studied interval is made. This assumption may not be true. In fact, attribution of the vertical mineralogical variations to the CO_2-reactions occurred in the sealing KCF incurs some difficulties. First difficulty is concerned about quartz abundance. In well 16/8b-A2 and 16/7b-20, for example, the KCF shales contain over 20 wt% more quartz than the shales in oil leg (table 3.10 and 3.11). It is difficult to consider that more than one fifth of the whole

rock consists of authigenic quartz derived from feldspar dissolution, because it requires dissolution of ~ 46 wt% equivalent K-feldspar or other silicate minerals. Average feldspar content in the oil leg shales is less than 12 % in most of the Miller wells. The difference between the seal and the oil leg shales is less than 8 % which, even assuming all the difference resulted from dissolution in the seal, only contributes less than 4 % quartz precipitation. Apparently, the variation of quartz abundance observed is mainly due to original sedimentary variations.

Previous studies reveal that quartz cement content in the Miller reservoir sandstones ranges from 3.2 to 12.2 % and it increases towards the oil-water contact (OWC) (Marchand, 2001; Marchand et al., 2001). Feldspar dissolution in the reservoir sandstones created up to 15 % secondary porosity (Baines and Worden, 2004). It is generally believed that, in organic-rich mudrocks, organic reactions increase acidity in the ambient porewaters and enhance dissolution of silicate minerals including quartz and feldspar (Carothers and Kharaka, 1978; Drever and Stillings, 1997). Astin and Evans (1990) proposed that mudrocks may typically lose 10-20 % of their solid volume through quartz dissolution and silica exportation to adjacent sandstones. The original detrital quartz should have been corroded and removed before the CO_2 charge. It is impossible to attribute the high present-day abundances in the KCF shales only to diagenetic processes related to the CO_2 reactions. It must be due to the original high abundances.

The second difficulty lies in the kaolinite content variations. The difference of kaolinite and feldspar contents between the seal and oil leg in some wells can not be interpreted the CO_2-reactions. For example, in well 16/8b-A1 and 16/8b-A2 (Tables 3.10 and 3.11), feldspar contents in the seal are about 7 % less than the oil leg, while average kaolinite abundances in shale are similar to or lower than those in the oil leg. This argues against the reaction of feldspar dissolution and kaolinite precipitation in the seal.

Furthermore, the formation water of the reservoir should have been saturated with CO_2 since the CO_2 charge. Absence of oil in the water leg should have allowed CO_2 reactions to take place. If CO_2 reactions were hindered in oil leg, there should be mineralogical variations across the OWC and the mineralogical proportions in water leg should be similar to those in the seal. However, most Miller wells do not show large differences in shale mineralogy between the oil leg and water leg (except well 16/7b-20) (Figure 3.12). And difference for the minerals between the oil and water leg is not consistent from well to well. This also

suggests against significant CO_2 reactions which occurred in the water leg whilst inhibited by oil in the oil leg. However, the present OWC could have been in the place only for a very short period, during which the CO_2 reactions in the water leg have yet to produce noticeable variations across the contact.

The observed mineralogical variations across the formation boundary, especially those of quartz, could represent the original sedimentary heterogeneity. It has long been thought that the Brae Formation was deposited in a submarine fan setting on the eastern downthrow side of the boundary fault of the South Viking Graben (Turner et al., 1987; Turner and Connell, 1991; Garland, 1993). The fan deposits were supplied by feeder channels which supplied deposits from the source area in the west. The occurrence of laterally continuous shale beds within the Brae Formation is believed to represent a rise in sea level which inundated the fault scarp, thereby removing the most proximal sediment source and closing down the feeder channel. Several shale beds within the Brae Formation are interpreted as marine condensed horizons each marking a 'maximum flooding surface' (Garland, 1993). These changes of depositional environment could have changed the depositional sediment mix. On the other hand, the KCF shales were deposited with very slow sedimentary rates during the major period of rifting and subsidence in the most of the graben areas of the North Sea (Ziegler, 1982). Widespread dysaerobic to anoxic conditions led to the deposition of organic-rich mudrocks (Cornford, 1998). This would imply very uniform conditions of mudrock sedimentation in deep water, which were not greatly altered by a few metres change of relative sea level. Thus, potentially, the different depositional mechanisms of two types of shale (low stand and high stand) is a plausible reason for their mineralogical differences.

The lack of definite mineralogical evidence does not necessarily rule out CO_2 reactions. It just means that the CO_2 did not cause all the significant alterations which whole rock XRD analysis can detect. High CO_2 contents have probably enhanced quartz dissolution, feldspar dissolution and kaolinite precipitation in the KCF as is suggested in some wells. But those effects are largely obscured by the original heterogeneities of the rocks. The large variations in quartz content, which are related to original deposition, act as loud background noise for identifying relatively small mineral variations induced by CO_2 reactions.

3.8. Conclusions

- X-ray diffraction analysis enables quantitative estimation of mineralogical compositions of mudrocks. The test experiment on synthetic samples containing clay

minerals was conducted to validate the methods. The results demonstrate desirable accuracy and reproducibility of the quantitative method based on Rietveld method.

- The application of wet grinding using a McCrone MicroNising mill combined with top loading method was demonstrated to be capable of achieving less than 3 wt % absolute errors for all the mineral phases from synthetic samples of a mudrock similar to Miller oilfield shales. However, larger relative errors were found associated with muscovite (proxy mineral for illite), kaolinite and pyrite, indicating a certain degree of preferred orientation induced during sample loading.

- The results of ten repeated runs on the same synthetic sample (of known composition) show desirable reproducibility. Since each run starts from an independent loading of the powder sample, this also validates the reliability of the top loading technique in controlling the effects of preferred orientation.

- The XRD quantitative analysis enables comparison of mineral compositions of the shales from the high CO_2 area (the Miller Field) with those from the low CO_2 area. It is found that the Miller wells show abrupt variations in mineral proportions vertically across the reservoir top, such as sudden increase of quartz, decrease of feldspar and increase of kaolinite above the crest. High contents of carbonate cement were also found in the seal. No similar mineralogical variations can be seen in the low- CO_2 control well 9/28b-17. These unique mineralogy profiles of the Miller wells might suggest that reactions were induced by CO_2 infiltration to dissolve feldspar and produce kaolinite, carbonates and quartz in the lowest part of the sealing KCF while oil emplacement inhibited the reactions in the oil leg of the reservoir.

- However, the differences in shale mineral composition, especially quartz abundance, between the sealing KCF and the Brae Formation are too large to be explained solely by CO_2-reactions. If assume the additional quartz in the KCF is product of the CO_2 reactions, it requires feldspar equivalent 46 wt% of the whole rock to dissolve. It is not possible for the original mudrocks to contain such amount of feldspar. In addition, no significant mineralogical variations between the oil leg and water leg can be seen in most Miller wells, suggesting against CO_2-related reactions. Hence,

the differences in quartz abundance between the KCF and the Brae Formation shale are likely to be associated with original sedimentary variations.

- Little evidence of the CO_2-related reactions can be observed in the shales across the oil leg and water leg, suggesting the CO_2 accumulation has not caused any noticeable alteration on the host rocks since its emplacement. It is suggested that storage of man-made CO_2 would not result in severe damage of the reservoir rocks in the much shorter storage lifespan.

Table 3.3 Mineral percentages determined by X-ray diffraction for shale samples of well 9/28b-17 (weight %).

Sample TVD (m)	Quartz	Illite	Kaolinite	K-feldspar	Albite	Pyrite	Marcasite	Calcite	Dolomite	Anatase	Rutile	Jarosite	Gypsum	Total	Global chi^2
4420.3	51.63	34.84	5.50	1.13	0.26	3.85				0.43	0.03		2.34	100.01	6.34
4424.8	50.55	25.25	7.90	0.05	1.07	7.87	0.81	1.87		0.07		0.78	3.79	100.01	3.60
4426.9	31.50	42.05	6.83	6.58	0.70	4.84				0.29	0.68	1.75	4.77	99.99	5.52
4430.0	37.98	32.65	10.46	1.21	0.52	8.25	0.35		2.52	0.59	0.56	0.89	4.02	100.00	4.62
4432.7	48.91	29.45	6.12	0.49	1.45	5.90	0.59	0.99	1.93	0.38	0.28	0.68	2.85	100.02	5.24
4437.9	38.59	39.06	5.35	1.02	0.97	6.32	0.98	1.64		0.49	0.72	0.95	3.92	100.01	5.03
4439.7	54.07	30.82	4.62	1.47	0.53	4.76				0.41	0.15	0.92	2.24	99.99	5.89
4441.5	65.03	19.02	6.44	0.22	3.05	2.36	0.14	0.91	2.37	0.30	0.16			100.00	8.16
4442.8	47.86	30.52	3.91	2.17	1.10	9.53	0.93	1.07		0.32	0.38	0.95	1.24	99.98	4.86
4443.9	55.85	29.06	1.80	1.35	0.42	7.51		1.07				0.83	2.10	99.99	5.22
4444.8	54.84	29.92	0.68	0.04	0.86	8.70	0.49	1.23		0.36	0.27	0.91	1.70	100.00	4.84
4445.9	43.16	42.90	2.37	1.02	0.28	4.21			1.94	0.41	0.74	1.11	1.85	99.99	6.67
4446.4	47.54	35.48	0.45	1.30	0.60	9.13	1.02	0.76		0.16	0.64	1.06	1.85	99.99	4.94
4446.9	50.84	38.86	4.06	0.98	0.36	2.98			0.98	0.53	0.40			99.99	7.09
4448.2	60.04	32.87		0.74	0.20	2.09		0.89		0.35	0.30	0.85	1.66	99.99	7.43
4449.6	47.67	39.74	0.30	2.77	0.53	5.73		1.39		0.24	0.72		0.90	99.99	6.17
4450.7	59.01	29.87		0.70	1.34	4.45		0.70		0.15	0.05	1.08	2.65	100.00	6.31
Average KCF	**49.71**	**33.08**	**3.93**	**1.37**	**0.84**	**5.79**	**0.31**	**0.74**	**0.57**	**0.32**	**0.36**	**0.75**	**2.23**		
4462.1	55.01	30.96		0.70	0.58	4.81	0.39	1.23		0.24	0.44	1.21	4.42	99.99	4.86
4464.2	53.61	31.27	2.18	1.53	0.58	5.79	0.13	0.94		0.20	0.26	0.93	2.57	99.99	5.53
4465.7	56.58	28.61	0.32	0.72	0.51	5.91	0.37		1.42	0.24	0.22	0.81	4.30	100.01	5.53
4468.6	51.52	35.37	4.19	1.00	0.34	3.79	0.16	1.23		0.52	0.27	0.80	0.80	99.99	6.53
4474.8	54.66	24.34	3.86	0.59	1.63	7.27	0.49	0.87	0.35	0.24	0.29	0.74	4.67	100.00	5.04
4478.4	52.36	30.92	2.46	0.93	1.37	5.52	0.41	1.54		0.36	0.34	1.24	2.54	99.99	5.65
4485.7	60.83	24.66	4.43	0.26	0.55	2.77		0.84	3.06	0.51	0.36		1.75	100.02	7.46
4493.0	55.45	28.39	3.22		1.24	5.03	0.27	1.06	3.16	0.33	0.60		1.24	99.99	6.15
4503.7	46.55	37.47	3.86	1.02	0.38	6.00		1.39		0.43	0.40	0.96	1.55	100.01	5.66
4514.6	56.69	29.24	3.01	1.10	0.34	3.30		1.14	1.93	0.32	0.85	0.93	1.13	99.98	8.30
4516.5	61.32	25.96	2.72	0.54	0.87	2.99		0.95	3.51	0.37	0.21		0.56	100.00	7.86
5063.7	35.00	46.59	1.18	4.24	0.55	7.56			2.32	0.39	1.39		0.78	100.00	6.58
5069.7	8.22	45.16	10.99	9.94	1.24	13.87	2.13	1.49	3.36	0.65	1.13	1.53	0.30	100.01	4.34
Average Brae Fm.	**49.83**	**32.23**	**3.26**	**1.74**	**0.78**	**5.74**	**0.33**	**0.98**	**1.47**	**0.37**	**0.52**	**0.70**	**2.05**		

Table 3.4 Mineral percentages determined by X-ray diffraction for shale samples of well 16/3a-E1 (weight %).

Sample TVD (m)	Quartz	Illite	Kaolinite	K-feldspar	Albite	Pyrite	Marcasite	Calcite	Dolomite	Ankerite	Anatase	Rutile	Jarosite	Gypsum	Total	Global chi^2
3870.4	46.16	21.18	14.60	1.15	0.38	5.55		1.13	9.01		0.72	0.12			100.00	5.55
3871.3	45.24	26.77	14.22	1.13	0.07	10.52			1.30		0.57	0.19			100.01	4.66
3872.0	41.26	28.87	15.14	1.44	0.94	6.58			2.46	2.77	0.49	0.05			100.00	5.35
3872.5	45.67	27.78	15.36	2.01	0.04	5.63			2.67		0.75	0.09			100.00	5.85
3873.1	49.75	26.75	15.04	2.17	0.10	5.35					0.72	0.11			99.99	6.07
3873.4	39.28	27.52	14.64	2.91	0.11	12.40					0.42	0.01	1.15	1.55	99.99	4.14
3874.0	48.00	29.62	15.24	1.85	0.26	3.09			1.50		0.43	0.01			100.00	6.72
3877.1	36.86	31.70	7.10	2.62	0.23	15.35	0.80		3.33		0.28	0.22		1.52	100.01	3.76
Average KCF	**44.03**	**27.52**	**13.92**	**1.91**	**0.27**	**8.06**	**0.10**	**0.14**	**2.53**	**0.35**	**0.55**	**0.10**	**0.14**	**0.38**		
3879.4	25.85	47.61	11.81	4.84	0.01	6.84			1.77		0.51	0.76			100.00	5.67
3880.7	45.95	38.17	7.91	1.73	0.02	5.66					0.27	0.30			100.01	5.72
3881.8	42.85	35.01	2.58	3.60		6.14			4.51	4.30	0.20	0.80			99.99	5.98
3882.2	26.13	54.56	0.01	5.56	0.24	6.61		1.27			0.19	1.18	1.37	2.88	100.00	5.88
3883.6	28.93	41.89	5.67	5.65	0.79	10.67	0.85				0.14	0.48	1.72	3.22	100.01	3.98
3884.2	27.56	43.24	7.90	2.78		13.64		1.92			0.35	0.19	1.19	1.23	100.00	3.74
3944.2	26.97	37.11	15.90	10.22	1.75	5.63					1.81	0.59			99.98	7.05
3944.5	18.45	32.57	28.84	9.82	0.18	4.76					2.46	0.10	0.83	2.00	100.01	6.30
3945.1	24.87	30.92	17.17	11.26	0.94	11.28	1.00				1.06	0.46	1.03		99.99	4.96
3945.7	31.14	40.55	15.24	4.50	0.21	6.58					0.66	0.40	0.72		100.00	5.43
3947.2	25.31	43.99	7.43	3.85	0.76	13.06	0.91				0.50	0.42	1.27	2.50	100.00	4.14
3949.4	59.89	24.53	6.96	3.49	0.95	3.37					0.47	0.34			100.00	7.24
3951.2	49.72	26.74	8.34	3.83	0.08	10.45					0.32	0.52			100.00	5.15
3954.2	49.37	34.27	6.44	2.64	0.16	6.24	0.14				0.36	0.37			99.99	6.11
3956.7	39.98	34.40	8.88	6.11	0.28	7.99					0.48	0.71	1.17		100.00	6.15
3959.9	4.03	49.36	11.86	14.20		14.47	1.31	1.04			1.38	0.49	1.53	0.32	99.99	4.75
4008.9	5.89	69.64	2.03	3.17	0.58	9.47		2.06	2.13		1.75	1.33	1.75	0.20	100.00	6.43
4043.0	18.39	39.50	2.88	6.84		26.09	2.05		0.26		0.76	1.17	1.35	0.72	100.01	3.24
4043.9	22.10	37.00	11.75	10.50		14.62	0.67				0.31	0.49	1.38	1.18	100.00	4.29
4045.0	19.43	30.17	18.29	9.26	0.33	16.26	0.76	1.31			1.43	0.41	0.86	1.50	100.01	3.83
4049.4	15.79	42.89	1.33	9.20		24.66	0.40		1.23		0.22	1.54	1.39	1.36	100.01	3.78
4054.9	18.09	53.76	7.98	6.40	0.37	6.70		1.14	2.26		0.54	1.44	1.31		99.99	6.73
4056.3	33.42	45.21	4.27	4.94		8.08			1.25		0.49	0.99	0.76	0.59	100.00	5.61
Average Brae Fm.	**28.70**	**40.57**	**9.19**	**6.28**	**0.33**	**10.40**	**0.35**	**0.40**	**0.58**	**0.19**	**0.72**	**0.67**	**0.85**	**0.80**		

Table 3.5 Mineral percentages determined by X-ray diffraction for shale samples of well 16/3b-5 (weight %).

Sample TVD (m)	Quartz	Illite	Kaolinite	K-feldspar	Albite	Pyrite	Marcasite	Calcite	Dolomite	Anatase	Rutile	Jarosite	Gypsum	Total	Global chi^2
4095.1	52.77	26.37	9.26	1.57		8.00		0.38		0.33	0.25		1.06	99.99	5.37
4095.6	46.62	30.33	13.98	2.51		4.60			1.12	0.44	0.40			100.00	6.37
4096.0	21.50	35.28	15.86	11.18		10.26	1.62			0.36	0.84	1.81	1.29	100.00	5.97
4096.3	12.93	51.36	7.35	11.12	0.88	8.69	0.43		0.16	1.62	1.04	1.99	2.43	100.00	6.02
4097.4	17.93	41.78	11.45	9.59	1.34	10.06	1.34		1.65	1.28	0.90	1.16	1.50	99.98	5.73
Average KCF	**30.35**	**37.02**	**11.58**	**7.19**	**0.44**	**8.32**	**0.68**	**0.08**	**0.59**	**0.81**	**0.69**	**0.99**	**1.26**		
4098.9	9.21	42.14	22.87	10.01	0.40	8.14			1.90	1.91	0.24	0.92	2.24	99.98	5.38
4101.9	11.46	39.31	27.07	8.06	1.15	8.50			1.27	2.74	0.43			99.99	5.24
4104.1	29.84	29.27	15.40	3.94		16.60	1.60			0.38	0.39	1.03	1.55	100.00	3.54
4108.2	29.01	40.48	18.52	2.51		4.82			1.87	2.18	0.62			100.01	6.33
4122.3	9.56	46.93	18.61	12.54	0.02	8.51	0.45			2.75	0.63			100.00	6.15
4124.9	11.48	38.49	18.39	10.92	1.31	14.37				1.71	0.38	1.07	1.87	99.99	4.35
4143.4	24.78	43.95	9.30	6.56		9.84	0.82			0.60	1.34	1.06	1.74	99.99	5.31
4145.1	38.49	39.45	13.41	1.82		4.04			1.84	0.46	0.49			100.00	6.24
4145.9	56.85	24.86	6.01	3.46		5.44	0.76		1.98	0.29	0.35			100.00	5.89
4146.8	25.24	47.58	7.30	6.87		7.87				1.38	0.77	1.38	1.62	100.01	6.03
4151.7	40.40	35.37	10.76	3.26		7.37				0.46	0.89		1.50	100.01	5.39
4156.7	23.50	39.90	17.96	7.71	0.79	5.51				1.68	0.64	0.70	1.61	100.00	5.76
4182.3	47.22	24.05	7.03	3.39		15.84	1.56			0.44	0.48			100.01	3.88
4185.6	30.99	42.92	10.71	3.63	0.01	7.50	0.72	0.57		0.38	0.67	0.70	1.20	100.00	4.92
4187.0	35.94	42.11	0.56	4.71		8.22	0.26	0.68		0.38	0.45	1.35	5.35	100.01	4.78
4189.3	57.60	24.50	10.63	3.73		2.93				0.45	0.16			100.00	7.28
4195.0	40.22	28.57	10.85	3.01	0.85	12.77	0.65	0.37		0.38	0.71	0.68	0.93	99.99	4.27
4196.6	41.17	36.74	10.60	2.05		7.36	0.60	0.15		0.25	0.50	0.58		100.00	5.06
Average Brae Fm.	**31.28**	**37.03**	**13.11**	**5.45**	**0.25**	**8.65**	**0.41**	**0.10**	**0.49**	**1.05**	**0.56**	**0.53**	**1.09**		

Table 3.6 Mineral percentages determined by X-ray diffraction for shale samples of well 16/7b-20 (weigh %). (McCrone mill grinding was not applied to this set of samples)

Sample TVD (m)	Quartz	Illite	Kaolinite	K-feldspar	Albite	Pyrite	Calcite	Total	Global chi^2
3939.4	66.95	10.13	3.26	13.08	4.09	2.49		100.00	8.79
3946.1	71.07	8.61	2.37	10.80	4.02	3.04		99.91	9.30
3997.9	59.16	8.86	7.28	16.21	4.56	3.93		100.00	8.05
4001.6	68.12	5.82	3.53	9.45	7.46	2.68	2.93	99.99	11.52
4005.5	50.67	10.71	14.27	15.68	3.36	5.31		100.00	6.77
4005.7	62.81	7.35	3.51	15.93		10.40		100.00	6.60
4006.4	54.11	9.14	11.40	14.91	4.32	6.11		99.99	7.41
4007.3	53.39	11.05	7.18	18.63	3.78	5.95		99.98	7.55
4007.5	61.35	8.99	8.59	14.08	2.92	4.08		100.01	9.35
4008.0	57.78	7.57	11.85	18.70		4.09		99.99	9.26
4008.1	54.63	9.12	7.59	17.49	4.41	6.76		100.00	8.52
4008.2	49.74	11.63	9.15	16.88	4.75	7.85		100.00	6.96
4008.5	42.11	11.84	10.06	25.45	3.50	7.05		100.01	7.54
4008.6	24.74	16.20	15.73	30.93	2.43	9.97		100.00	6.68
Average KCF	**55.47**	**9.79**	**8.27**	**17.02**	**3.54**	**5.69**	**0.21**		
4023.5	37.91	12.97	15.97	21.42		11.73		100.00	4.90
4044.7	39.57	6.97	21.51	23.13	1.36	7.46		100.00	6.71
4046.7	13.66	16.71	23.24	31.76	2.26	12.36		99.99	5.53
Average Oil leg	**30.38**	**12.22**	**20.24**	**25.44**	**1.21**	**10.52**			
4065.9	40.18	11.76	14.11	24.67		9.27		99.99	6.73
4066.5	34.86	13.82	19.98	23.37		7.97		100.00	7.35
4067.5	56.79	13.61		19.06		10.54		100.00	6.84
4069.5	61.58	9.21	4.59	20.33		4.31		100.02	9.63
4073.5	52.38	8.20	12.41	21.22		5.80		100.01	8.19
4076.8	58.62	9.59	3.03	21.50		7.25		99.99	8.15
4103.4	65.79	8.36	4.55	14.14	2.73	4.44		100.01	8.60
4113.1	47.39	6.85	13.87	22.27	3.67	5.95		100.00	8.28
4114.8	83.25	5.38		9.97		1.40		100.00	14.53
Average Water leg	**55.65**	**9.64**	**8.06**	**19.61**	**0.71**	**6.33**			

Table 3.7 Mineral percentages determined by X-ray diffraction for shale samples of well 16/7b-24 (weight %).

Sample TVD (m)	Quartz	Illite	Kaolinite	K-feldspar	Albite	Pyrite	Marcasite	Calcite	Dolomite	Anatase	Rutile	Jarosite	Gypsum	Total	Global chi^2
4038.4	73.20	16.26		6.78		1.10			0.33	0.03	0.01	0.66	1.64	100.01	10.04
4039.8	11.76	58.63	3.28	7.56		10.15		2.87	0.83	1.75	2.01	1.14		99.98	5.31
4061.5	36.16	38.85	0.58	13.02		5.45		1.60	1.07	1.02	1.25	0.99		99.99	6.22
4065.2	38.96	30.75	9.58	9.93		5.32			1.27	1.63	0.90		1.66	100.00	6.89
4066.3	21.26	42.84	0.69	20.45		2.64	1.71	5.10	0.50	0.76	1.47	2.22	0.36	100.00	4.73
4067.0	9.16	58.22	1.99	11.02	1.03	9.05	1.45	2.12		1.46	2.40	2.00	0.10	100.00	6.33
4072.2	38.75	36.58	2.84	15.28		2.91			0.56	0.60	0.51	1.98		100.01	6.61
4073.6	9.07	55.00	5.25	8.31	1.12	11.05	1.02	2.31	1.58	1.55	2.31	1.42		99.99	5.39
4079.4	20.01	42.42	14.83	11.68		7.28		0.11	1.26	1.73	0.68			100.00	5.37
4088.6	9.33	58.54	0.50	11.72		9.66		2.87	1.57	0.71	2.76	1.78	0.57	100.01	5.46
4089.4	5.85	61.08	3.59	6.61		15.94			1.00	1.64	0.79	1.90	1.61	100.01	4.50
Average Oil leg	**24.86**	**45.38**	**4.31**	**11.12**	**0.20**	**7.32**	**0.38**	**1.54**	**0.91**	**1.17**	**1.37**	**1.28**	**0.54**		
4093.1	36.79	38.92	0.60	12.45		5.40	1.13		1.24	0.04	1.06	2.36		99.99	6.27
4094.5	21.54	44.72	1.48	9.94		13.14	1.16	1.94	1.75	1.51	0.62	1.71	0.49	100.00	4.26
4095.2	14.77	42.45	11.54	11.13	0.91	12.19		0.69	1.06	1.83	0.90	1.06	1.47	100.00	4.38
4096.3	5.81	62.62	10.19	3.78	0.59	8.97			1.37	2.37	0.84	1.37	2.09	100.00	5.76
4107.4	12.19	56.38	2.66	8.68		11.86		0.93	0.86	2.10	2.14	1.18	1.01	99.99	5.20
Average Water leg	**18.22**	**49.02**	**5.29**	**9.20**	**0.30**	**10.31**	**0.46**	**0.71**	**1.26**	**1.57**	**1.11**	**1.54**	**1.01**		

Table 3.8 Mineral percentages determined by X-ray diffraction for shale samples of well 16/8b-3 (weight %).

Sample TVD (m)	Quartz	Illite	Kaolinite	K-feldspar	Albite	Pyrite	Marcasite	Calcite	Dolomite	Anatase	Rutile	Jarosite	Gypsum	Total	Global chi^2
3978.5	45.70	28.93	12.72	2.87		7.89			1.32	0.33	0.25			100.01	4.96
3979.2	48.83	28.36	12.45	3.12		4.58			2.11	0.32	0.23			100.00	5.80
3979.8	37.28	26.89	10.54	6.56	0.17	12.21		1.15		2.02	0.59	0.84	1.75	100.00	4.29
3980.5	44.84	27.85	8.04	4.83		9.61				0.53	0.43	1.03	2.83	99.99	4.40
3980.7	11.67	43.11	10.29	11.63		17.04		1.68		2.31	0.22	1.63	0.42	100.00	3.66
3987.3	5.61	48.13	8.55	10.18		20.18		1.86		1.95	0.76	1.67	1.11	100.00	3.81
3987.8	24.97	43.99	8.53	6.93		8.44		1.29		2.26	0.98	1.07	1.53	99.99	5.22
3987.9	53.85	28.13	3.49	5.93	1.01	3.63		0.68		0.80	0.81	0.79	0.88	100.00	7.47
Average KCF	**34.09**	**34.42**	**9.33**	**6.51**	**0.15**	**10.45**		**0.83**	**0.43**	**1.32**	**0.53**	**0.88**	**1.07**		
3990.0	24.70	33.74	16.23	8.59	0.49	7.97		1.78	1.79	2.28	0.83	0.94	0.67	100.01	6.75
3991.0	20.75	38.34	10.42	10.56		13.32			1.60	2.34	1.21		1.46	100.00	4.87
3991.4	35.02	39.35	5.24	6.99		6.36			1.38	1.91	1.25	1.06	1.44	100.00	6.35
3992.4	27.29	42.37	7.06	6.41		8.55			1.30	2.60	0.96	1.27	2.19	100.00	5.93
3998.1	18.66	49.95	0.44	17.86		7.18			0.72	0.67	2.34	1.59	0.58	99.99	7.31
4040.7	14.64	50.80	0.40	14.14		11.71	1.26		1.05	0.31	2.49	2.14	1.04	99.98	5.45
4042.5	12.76	50.47	8.66	9.83		12.57	0.81		1.38	2.44	1.08			100.00	4.84
4043.8	12.13	56.16	0.36	12.80		11.32	1.58		1.28	0.25	2.04	2.07		99.99	5.56
4067.8	24.17	37.04	6.99	14.28		11.80	0.89			0.32	1.20	1.83	1.48	100.00	4.40
4068.3	17.31	37.70	16.89	12.25		11.38	0.05		0.77	1.92	0.33	1.39		99.99	
4070.6	38.91	34.42	4.60	11.52		6.54			0.73	0.56	1.51	1.20		99.99	6.70
4091.6	12.67	47.05	5.27	12.12	1.50	11.40	2.01	1.83	2.18	0.45	1.96	1.58		100.02	5.55
4092.8	45.35	38.87	0.69	8.68		1.92			1.45	0.29	0.75	2.01		100.01	5.51
Average Oil leg	**23.41**	**42.79**	**6.40**	**11.23**	**0.15**	**9.39**	**0.51**	**0.28**	**1.20**	**1.26**	**1.38**	**1.42**	**0.68**		
4110.8	18.45	43.04	3.64	7.83	0.56	19.18	1.09	1.82	0.95	0.23	1.12	1.62	0.48	100.01	3.32
4112.5	12.57	41.08	6.14	12.57		20.71	1.27	1.18	1.24	0.01	1.30	1.51	0.42	100.00	3.68
Average Water leg	**15.51**	**42.06**	**4.89**	**10.20**	**0.28**	**19.95**	**1.18**	**1.50**	**1.10**	**0.12**	**1.21**	**1.57**	**0.45**		

Table 3.9 Mineral percentages determined by X-ray diffraction for shale samples of well 16/8b-5 (weight %).

Sample TVD (m)	Quartz	Illite	Kaolinite	K-feldspar	Albite	Pyrite	Marcasite	Calcite	Dolomite	Anatase	Rutile	Jarosite	Gypsum	Total	Global chi^2
4075.5	48.80	26.03	11.85	7.13		3.64				1.38	1.18			100.01	8.69
Average KCF	**48.80**	**26.03**	**11.85**	**7.13**		**3.64**				**1.38**	**1.18**				
4082.6	16.25	43.87	14.34	10.50		8.26	1.37	2.01		0.56	1.01	1.56	0.27	100.00	5.69
4083.0	27.82	36.67	14.60	9.29	0.62	6.21		1.74		2.53	0.52			96.95	7.01
4083.2	15.95	40.77	22.09	6.68	1.29	8.41		0.19	1.25	2.76	0.61			100.00	5.76
4083.3	8.89	41.58	19.84	12.19	0.14	10.83			1.12	2.48		1.42	1.51	100.00	5.53
4083.6	13.43	36.64	25.08	7.53		11.87			1.73	3.13	0.59			100.00	4.69
4083.7	30.28	34.33	19.18	8.57	0.85	5.90				0.89				100.00	6.35
4083.9	38.03	34.37	8.15	7.42	0.83	6.83		1.13		1.92	1.34			96.76	6.49
Average Oil leg	**21.52**	**38.32**	**17.61**	**8.88**	**0.53**	**8.33**	**0.20**	**0.72**	**0.59**	**2.04**	**0.58**	**0.43**	**0.25**		
4113.1	8.66	36.42	15.91	11.51		22.31				1.56	0.47	1.51	1.65	100.00	3.43
4113.9	16.02	34.43	20.56	10.74		12.55			0.26	2.30	0.70	0.91	1.51	99.98	4.82
4114.2	31.87	26.92	13.79	12.10	0.02	8.09	1.48			1.16	1.32	1.51	1.73	99.99	6.22
4115.0	41.86	34.38	6.38	8.44	0.32	3.42		1.41		0.75	0.98	1.32	0.76	100.02	7.12
4116.5	13.47	55.06	4.41	9.84	0.24	8.25	1.47	2.49		0.57	2.32	1.86		99.98	6.12
4143.1	5.32	49.03	14.71	9.43	0.93	12.64	0.75	2.37		2.76	0.25	1.62	0.18	99.99	4.55
4287.1	46.07	31.63	5.57	3.76		9.03		0.80		0.16	0.70	0.86	1.41	99.99	5.15
4287.1	40.15	30.09	12.02	3.69	0.33	9.39		1.40		0.34	0.26	1.15	1.18	100.00	
4288.5	9.21	27.88	19.81	9.31	0.25	29.12		1.38		0.38	0.16	1.63	0.89	100.02	3.06
4289.7	17.27	34.72	15.39	8.32	0.24	15.30	0.72	3.15	1.70	0.33	0.66	1.50	0.70	100.00	3.56
4291.7	20.55	28.17	15.96	8.65	0.01	18.40	0.80	1.51	1.23	1.56	0.74	0.88	1.53	99.99	3.57
4293.1	30.05	44.76	1.06	3.24	0.98	9.54	0.16	4.49		0.08	0.97	1.95	2.73	100.01	4.18
4370.8	27.62	40.22	5.03	7.48	0.20	14.48	0.18	1.35	0.32	0.24	0.47	1.15	1.26	100.00	4.15
4371.4	29.24	30.40	11.43	4.17	0.01	19.40	0.69		2.44	1.01	0.50		0.72	100.01	3.64
4372.3	27.22	34.88	14.62	6.17	0.21	10.51	0.48	1.12	2.95	0.71	1.12			99.99	5.41
Average Water leg	**24.31**	**35.93**	**11.78**	**7.79**	**0.25**	**13.50**	**0.45**	**1.43**	**0.59**	**0.93**	**0.77**	**1.19**	**1.08**		

Table 3.10 Mineral percentages determined by X-ray diffraction for shale samples of well 16/8b-A1 (weight %).

Sample TVD (m)	Quartz	Illite	Kaolinite	K-feldspar	Albite	Pyrite	Marcasite	Calcite	Dolomite	Ankerite	Anatase	Rutile	Jarosite	Gypsum	Total	Global chi^2
4008.5	43.81	30.12	10.78	4.10	0.01	7.35			2.26		1.22	0.35			100.00	5.50
4009.3	42.04	32.32	11.06	4.48	0.11	6.15			2.27		1.33	0.25			100.01	5.61
4010.0	50.01	27.62	9.26	3.47	0.06	4.92			2.09	1.35	1.00	0.22			100.00	
4012.4	46.28	27.84	9.26	3.60		9.55			0.52	1.49	1.23	0.22			99.99	4.93
4013.8	46.09	31.98	10.70	2.81	0.34	4.67			2.29		0.96	0.16			100.00	6.01
4015.5	47.07	30.13	11.15	2.98	0.02	5.95			1.75		0.75	0.21			100.01	5.73
4016.1	48.44	26.35	8.47	4.27	0.02	8.97			1.56		1.33	0.59			100.00	5.31
4017.1	53.40	27.76	9.66	1.89		4.95			1.32		0.87	0.14			99.99	6.22
4018.0	41.73	33.53	11.37	4.11	0.76	5.45			0.46	1.03	1.24	0.32			100.00	6.02
4018.5	42.59	30.91	11.18	5.52	0.01	6.84			1.44		1.29	0.23			100.01	5.68
4018.8	40.08	27.97	10.91	5.09	0.01	13.53			0.89		1.22	0.30			100.00	4.07
4019.0	38.23	33.71	14.61	5.06	0.95	4.35			1.24		1.64	0.22			100.01	6.50
4020.1	40.43	29.66	12.04	7.39	1.83	5.26			0.15	1.25	1.67	0.32			100.00	
4020.8	39.33	31.48	12.84	4.38	1.38	7.49		0.16	0.18	1.25	1.11	0.40			100.00	5.25
4020.9	40.11	32.78	13.43	3.87	0.74	6.52		0.07	1.18		1.05	0.26			100.01	5.37
4020.9	38.58	31.17	14.09	6.52	0.03	6.37			1.51		1.42	0.31			100.00	5.66
4021.0	21.23	38.89	18.35	6.65		11.00			1.34		2.19	0.33			99.98	4.89
Average KCF	**42.32**	**30.84**	**11.72**	**4.48**	**0.37**	**7.02**		**0.01**	**1.32**	**0.37**	**1.27**	**0.28**				
4068.0	6.54	47.18	13.54	11.34	0.61	12.92	0.61	2.07	1.76		1.30	0.60	1.18	0.37	100.02	4.09
4068.9	3.22	56.18	10.10	11.48	0.80	11.31	0.15	1.61	0.72		1.14	1.59	1.22	0.48	100.00	4.99
4070.2	8.58	45.84	13.80	12.04		14.38					1.55	1.01	1.16	1.63	99.99	4.65
Average oil leg	**6.11**	**49.73**	**12.48**	**11.62**	**0.47**	**12.87**	**0.25**	**1.23**	**0.83**		**1.33**	**1.07**	**1.19**	**0.83**		
4092.8	17.76	55.43	3.20	9.45		7.97			1.42		1.56	1.78		1.44	100.01	5.88
4097.0	6.93	49.66	11.91	13.66	0.04	11.97			0.07	0.91	2.49	1.28		1.08	100.00	4.99
4098.0	9.71	53.12	8.36	11.00	1.13	10.48			1.45		1.61	1.40	1.21	0.53	100.00	5.63
4106.7	3.23	45.84	18.36	12.79	0.31	13.72			0.56		1.90	0.79	1.39	1.11	100.00	4.66
4108.0	9.77	41.87	23.75	11.50	0.83	6.42		0.40	1.37		2.88	0.19		1.03	100.01	5.85
Average water leg	**9.48**	**49.18**	**13.12**	**11.68**	**0.46**	**10.11**	**0.00**	**0.08**	**0.97**	**0.18**	**2.09**	**1.09**	**0.52**	**1.04**		

Table 3.11 Mineral percentages determined by X-ray diffraction for shale samples of well 16/8b-A2 (weight %).

Sample TVD (m)	Quartz	Illite	Kaolinite	K-feldspar	Albite	Pyrite	Marcasite	Calcite	Dolomite	Ankerite	Anatase	Rutile	Jarosite	Gypsum	Total	Global chi^2
3962.6	48.23	10.97	7.04	4.40	1.93	1.30			15.37	10.58		0.19			100.01	6.16
3964.6	41.85	20.92	9.19	2.66	2.24	5.62			15.35		0.85	0.46		0.85	99.99	5.40
3966.7	42.49	31.47	14.14	1.87	0.51	4.75		0.33	1.35	1.92	0.46			0.72	100.01	5.44
3968.3	53.20	21.59	10.91	2.26	0.39	5.75	0.44	0.26	0.66	1.73	0.36	0.16		2.29	100.00	5.22
3971.0	42.44	30.70	12.93	2.84	0.91	5.11			0.68	2.20	0.82	0.47		0.90	100.00	
3972.6	40.99	32.67	13.16	1.63	0.86	6.18		0.09	0.47	2.31	0.33	0.59		0.73	100.01	5.69
3974.9	41.93	30.71	14.89	2.02	0.80	7.00		0.08	0.92	0.99	0.39	0.26			99.99	5.17
3976.8	44.03	30.79	13.43	2.72	0.44	5.40			0.76	1.81	0.35	0.26			99.99	5.92
3978.9	44.90	10.66	5.01	5.33	4.61	2.66	2.20	22.38	1.69	0.56					100.00	6.84
3980.4	39.22	31.43	15.62	3.79	0.36	7.62			0.35	1.14	0.22	0.26			100.01	5.23
3981.1	43.43	31.72	15.41	2.28	0.75	3.88			1.80		0.35	0.37			99.99	6.22
3981.9	40.12	28.17	15.38	4.02		10.38					0.49	0.50		0.95	100.01	4.71
3982.9	37.62	33.96	16.05	4.06	1.04	4.76			1.56		0.57	0.38			100.00	6.21
3983.0	6.37	62.60	4.16	5.36	1.72	13.89				1.33	1.19	2.21		1.19	100.02	5.16
3983.1	35.59	34.39	14.72	6.95	0.30	5.19			0.39	0.91	1.47	0.09			100.00	6.07
3983.5	27.39	38.74	16.89	5.55	0.79	5.28			1.26		2.13	0.50		1.46	99.99	6.18
3984.8	9.84	47.37	4.87	11.33	0.81	15.52	1.24	3.07	0.16	1.31	0.25	1.38	2.30	0.53	99.98	3.99
Average KCF	**37.63**	**31.11**	**11.99**	**4.06**	**1.09**	**6.49**	**0.23**	**1.54**	**2.52**	**1.58**	**0.60**	**0.48**	**0.14**	**0.57**		
4002.8	15.88	52.61	5.74	10.70		7.71		1.66	0.63	0.40	0.64	2.24	0.99	0.80	100.00	5.82
4004.5	25.25	37.31	16.57	9.22	0.80	7.93		0.09		1.45	0.52	0.85			99.99	5.69
4006.8	18.34	48.91	7.85	9.77	1.31	8.09		0.17	0.12	0.95	2.21	1.49		0.79	100.00	6.17
4010.5	12.52	39.64	9.34	16.58	1.50	9.43	1.21	3.38		1.01	1.20	1.41	2.23	0.54	99.99	4.06
4013.5	11.74	47.17	12.78	12.51	0.28	7.38	0.59	1.16	0.84		2.08	0.78	1.17	1.52	100.00	5.73
4017.3	11.82	50.54	12.87	7.39	1.17	8.58		2.02	0.19	1.36	2.39	1.57		0.10	100.00	6.13
4017.6	14.02	43.74	14.17	13.16	0.70	7.30	0.45		0.18	1.42	1.93	1.30	1.65		100.02	7.30
4019.0	7.00	48.49	16.52	10.98	0.43	9.46			0.24	0.58	1.98	1.28	1.30	1.75	100.01	5.07
4062.0	11.57	32.68	16.62	12.77	0.72	17.46	0.65	1.44	0.26	1.14	2.08	0.68	1.27	0.66	100.00	3.90
4068.6	19.61	39.32	12.25	12.48	0.34	11.05	0.61	0.80			1.65	0.91	0.96		99.98	4.82
Average Oil leg	**14.78**	**44.04**	**12.47**	**11.56**	**0.73**	**9.44**	**0.35**	**1.07**	**0.25**	**0.83**	**1.67**	**1.25**	**0.96**	**0.62**		
4106.5	27.03	50.81		7.63		8.77					0.28	1.36	1.75	2.35	99.98	
4108.3	10.54	36.11	15.37	13.90	0.21	15.90	0.25	1.97	0.21		2.39	0.26	1.77	1.11	99.99	3.70
4122.2	20.90	27.09	14.85	15.81	0.12	13.62	0.75	1.55	0.96		1.75	0.86	1.25	0.48	99.99	4.61
Average Water leg	**19.49**	**38.00**	**10.07**	**12.45**	**0.11**	**12.76**	**0.33**	**1.17**	**0.39**		**1.47**	**0.83**	**1.59**	**1.31**		

CHAPTER IV

DIAGENESIS OF THE KIMMERIDGE CLAY FORMATION

4.1. Introduction

The Kimmeridge Clay Formation (KCF) is the most important source rock and seal in the central and Northern North Sea. To date, most diagenetic studies of the KCF mudstones have been mainly based on interpretations of bulk mineralogical and geochemical data (e.g. Pearson et al., 1983; Scotchman et al., 2002). Previous studies, employing back-scattered scanning electron microscopy and transmission electron microscopy, have shown the heterogeneous nature of these mudstones and the complexity of the diagenetic reactions that have occurred within them (Glasmann et al., 1989; Shaw and Primmer, 1991; Huggett and Shaw, 1993). This chapter presents the results of Scanning Electron Microscopic (SEM) analyses on the KCF. The purpose of this study is to illustrate the heterogeneity in diagenesis within the KCF and reconstruct diagenetic sequences in the different lithologic domains. The diagenesis of the Brae Formation and the KCF will be compared and synthesized in order to establish an overall process of mass interchange between them. The potential effects of the CO_2 accumulation on the diagenesis in both formations will be discussed.

4.2. Methods

The materials examined are core samples of shale, siltstone and sandstone of the KCF in the wells from the Miller Field. The samples are from the 30 metres interval immediately above

the reservoir. All samples were examined by X-ray diffraction (XRD). The results of the XRD analysis are reported in Chapter 3. The core samples were made into resin blocks from which polished thin sections or polished blocks were made to give flat polished specimens required for SEM. The specimens were coated with amorphous carbon to make them conductive for SEM imaging. Sample surfaces were generally cut perpendicularly to bedding. Sample blocks with rough surfaces coated in gold were prepared for secondary electron mode.

High resolution scanning electron microscopy was used to examine the KCF samples. Secondary electron (SE), back-scattered electron (BSE) and cathodoluminescence (CL) mode were applied. In back-scattered mode, the proportion of back-scattered electrons in the signal is a function of the mean atomic number of the mineral being imaged. Hence, the higher the mean atomic number of the mineral the brighter it appears in the image, which enables identification of particles of different composition (Huggett and Shaw, 1993). The analyses were carried out using a Philips XL30CP with PGT Spirit X-ray analysis system at University of Edinburgh. The energy dispersive X-ray analysis system helps qualitative and quantitative analysis with respect to minerals' chemistry, and consequently, identification of the mineral phases.

4.3. Results

A strong compaction texture was commonly observed in the shales of the KCF. Platy and elongated minerals, such as quartz, feldspar and mica, are aligned along sedimentary bedding (Figure 4.1). The 'flattened' shape and irregular outline of the quartz and feldspar grains indicate that severe pressure solution occurred along the vertical axis. But, no mineral precipitation associated with the dissolution can be observed locally. Originally elongate feldspar grains which still preserve their subeuhedral to euhedral shapes parallel to bedding show a high certain degree of compaction orientation (Figure 4.1).

As XRD data show, BSE analyses also suggest relatively constant mineral composition of the KCF with depth and between the wells (see Chapter 3). Quartz is ubiquitous and is the most abundant mineral. Ubiquitous corrosion features and pressure solution textures are found in organic-rich shales (Figure 4.1). They are the evidence of large scale of quartz dissolution. Though most quartz grains also show leaching features in silty and sandy lithologies with lower organic contents, the dissolution features is less common than in the shales (Figures 4.2 to 4.4).

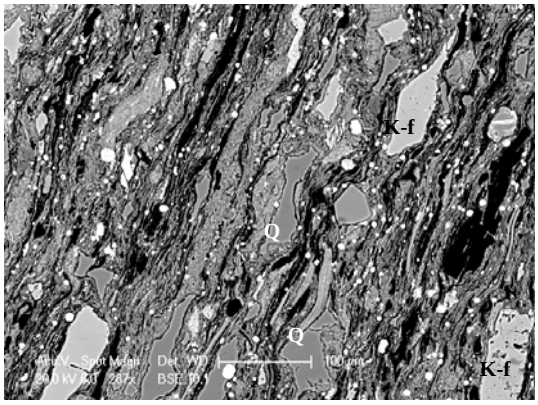

Figure 4.1 Dissolution of quartz (Q) and K-feldspar (K-f) producing elongate grains along bedding. The bright spots are pyrite framboids. Bedding NNE-SSW. BSE image of KCF shale, 4008.6 m TVD, well 16/7b-20.

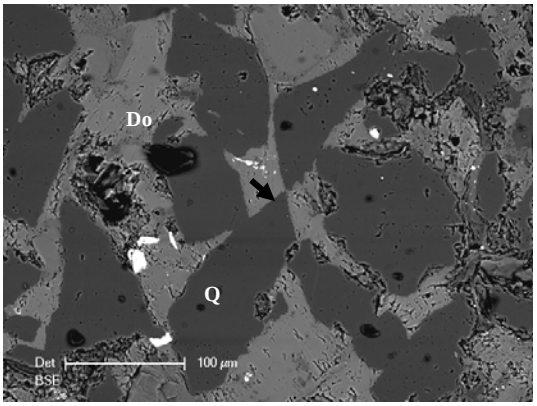

Figure 4.2 Dolomite (Do) cemented coarse-grained sediments. The arrow shows quartz overgrowth. BSE image of KCF sand, 3961.3 m TVD, Well 16/8b-A2.

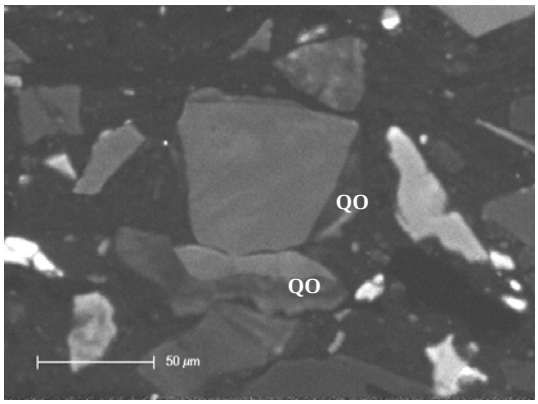

Figure 4.3 SEM-CL image showing polyphase quartz overgrowth (QO). The two phases of overgrowth show different grey scale. KCF silt, 3946.1 m TVD, well 16/7b-20.

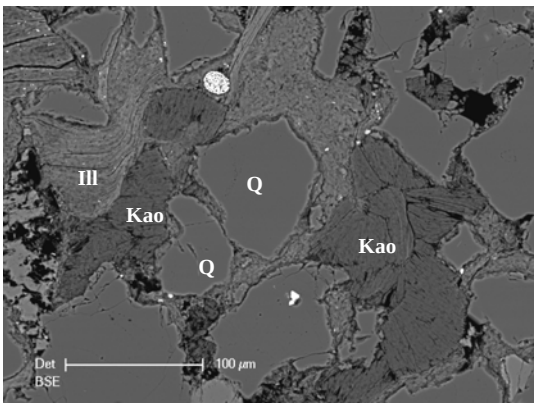

Figure 4.4 Quartz grains show moderate dissolution. Kaolinite (Kao) and illite (Ill) are main pore filling cements. Kaolinite grains on right show sign of compaction. BSE image of KCF sand, 3983.5 m TVD, well 16/8b-A2.

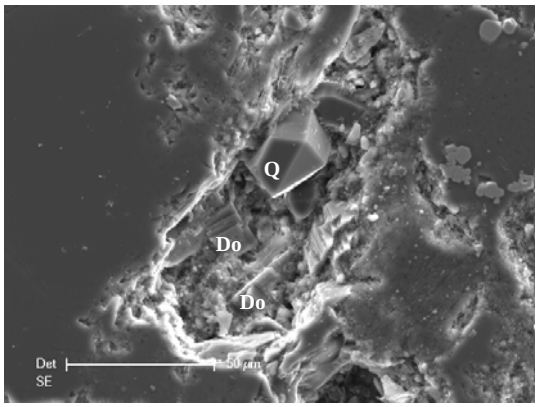

Figure 4.5 Euhedral quartz and dolomite grains growing into a secondary pore. SE image of KCF silt, 3971.7 m TVD, well 16/8b-A2.

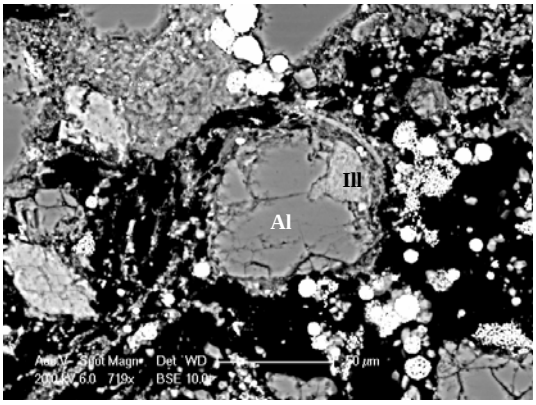

Figure 4.6 Albite (Al) partial dissolution with illite infilling the cavity. BSE image of KCF shale, 4005.7 m TVD, well 16/7b-20.

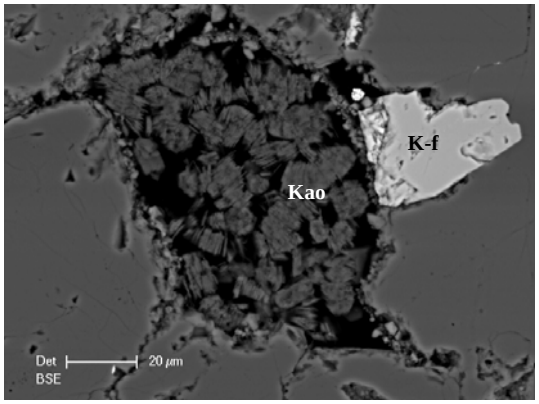

Figure 4.7 Kaolinite booklets (Kao) infilling a secondary pore which may be derived from K-feldspar dissolution. BSE image of KCF silt. 3983.5 m TVD, well 16/8b-A2.

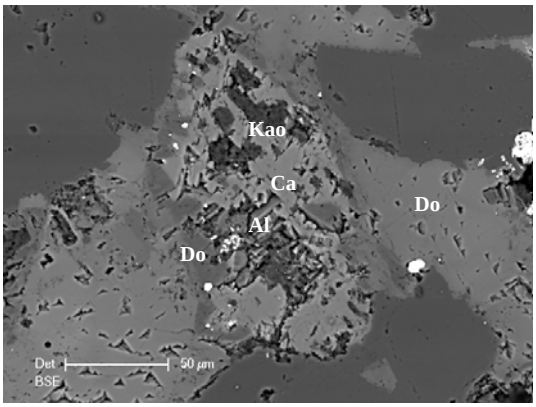

Figure 4.8 Calcite (Ca) and kaolinite filling a secondary pore derived from albite dissolution. BSE image of KCF sand, 3971.7 m, well 16/8b-A2.

Quartz overgrowth mostly occurred in coarser lithologies (Figures 4.2 and 4.3). However, the overall amount of quartz overgrowth is insignificant compared to the extent of dissolution. Quartz overgrowths are present in the samples which had been heavily cemented by carbonates before the sediments were greatly compacted. Euhedral quartz grains were also seen in secondary pores (Figure 4.5).

Illite and kaolinite are the second and third most abundant components in the mudstone samples. Illite generally amounts to about 30 % in the KCF mudstone samples by XRD. It sometimes displays pore-filling texture related to the dissolution of K-feldspar and albite (Figure 4.6). But most illite occurs in the matrix, making it impossible to determine whether

it is detrital, recrystallised or authigenic.

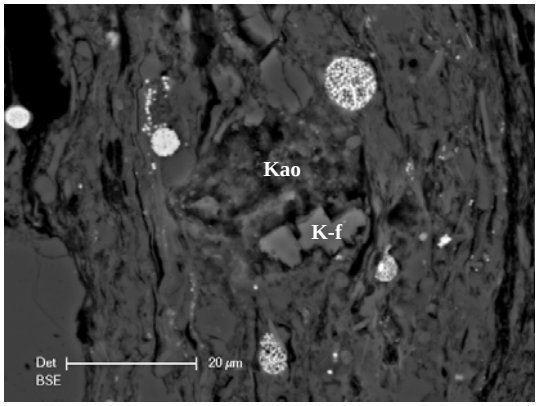

Figure 4.9 Authigenic kaolinite infilling a cavity derived from partial dissolution of a K-feldspar grain. BSE image of KCF shale, 4013.8 m TVD, well 16/8b-A1.

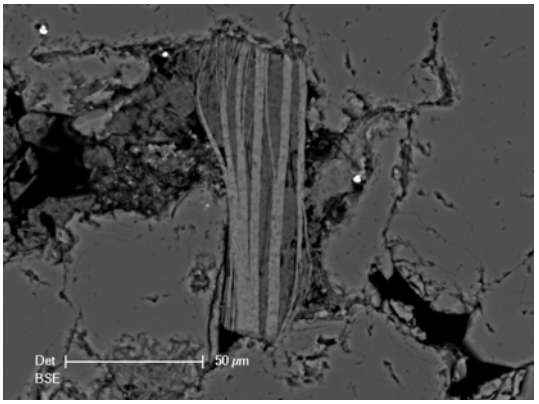

Figure 4.10 Kaolinite (dark grey stripes) partly replacing muscovite (light grey) in the central upright grain. BSE image of KCF sand. 3983.5 m TVD, well 16/8b-A2.

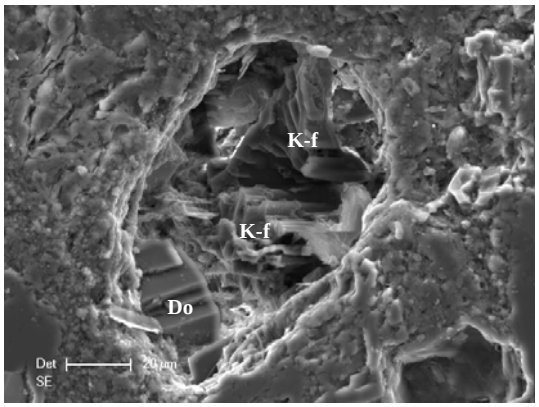

Figure 4.11 K-feldspar dissolution with dolomite cement protruding into the secondary pore. SE image of KCF silt, 3961.6 m TVD, well 16/8b-A2.

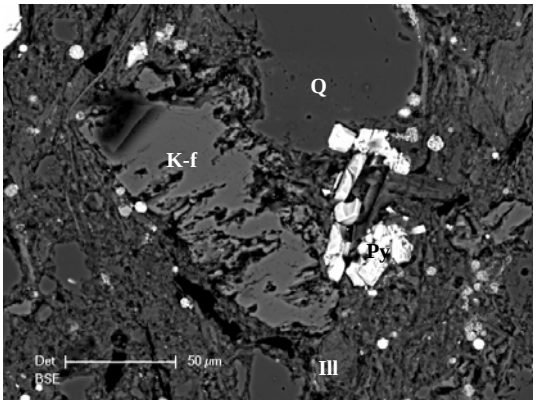

Figure 4.12 K-feldspar partial dissolution. Euhedral pyrite (Py) formed in the cavities derived from quartz and K-feldspar dissolution. BSE image of KCF silt, 4008.5 m TVD, 16/8b-A1.

Kaolinite is ubiquitous and occurs in the matrix, and as pore filling booklets, and less commonly, as a replacement of muscovite and feldspar. It typically ranges from 3 % to 18 %. Authigenic kaolinite is more readily observed than authigenic illite. Authigenic kaolinite is relatively more abundant in coarser-grained samples where it is closely associated with a large number of secondary pores. Kaolinite booklets are commonly related to the secondary pores derived from dissolution of feldspar or quartz (Figure 4.7). Blocky kaolinite may partly occupy pore spaces with other authigenic minerals (Figure 4.8) or completely infill pores

alone (Figure 4.9). Flakes of detrital mica were seen partially or completely altered to kaolinite (Figure 4.10), but it is difficult to tell whether this represents in situ diagenetic alteration of the mica or whether it occurred before the micas were deposited via weathering or diagenesis in a previous sedimentary history. Detrital kaolinite booklets show compaction evidence in the coarser-grained lithologies (Figure 4.4).

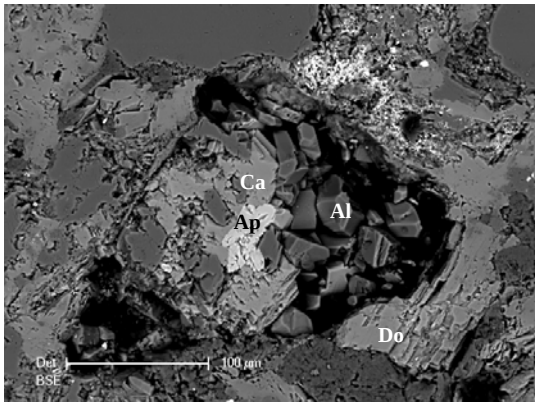

Figure 4.13 Authigenic albite, calcite and apatite (Ap) filling a secondary pore with little remnants of the original mineral present. BSE image of KCF silt, 3971.7 m TVD, well 16/8b-A2.

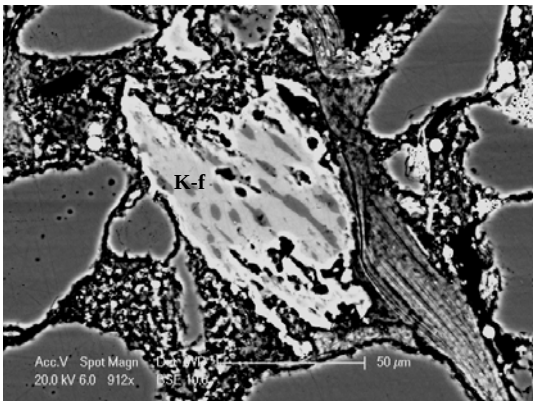

Figure 4.14 K-feldspar (bright grey) and albite (darker worms) exsolution texture. BSE image of KCF silt, 4005.7 m, well 16/7b-20.

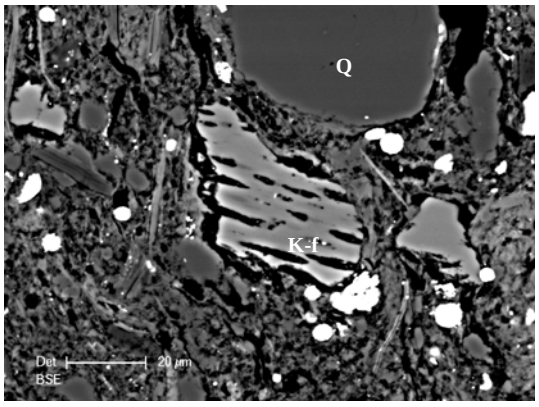

Figure 4.15 Preferred dissolution of albite produces stripe pores in a K-feldspar grain. BSE image of KCF silt, 3981.1 m TVD, well 16/8b-A2.

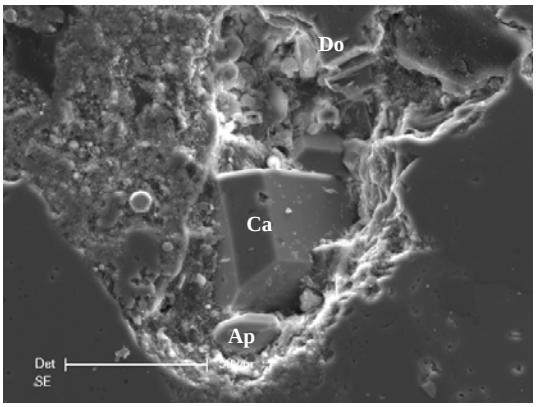

Figure 4.16 Euhedral calcite and apatite growing in the pore. SE image of KCF silt, 3971.7 m TVD, well 16/8b-A2.

Feldspar contents in the KCF shales are highly variable. XRD data show that K-feldspar content ranges from less than 1 % to about 12 % with several samples containing up to 30 %, while less than 1 % of albite was detected. In SEM images, both K-feldspar and albite show dissolution features which are often accompanied by pore-filling clay and carbonate minerals

(Figures 4.6, 4.9 and 4.11). The feldspar dissolution can be easily recognized in silt/sand, where oversized pores derived from dissolution are preserved by a rigid framework of quartz or carbonate cements. Substantial dissolution of feldspar typically leaves an etched skeletal fragment that still displays the original grain shape (Figure 4.12). There are also grain-sized pores with little remaining of the precursor grains, but they are most likely to be feldspar (Figure 4.13). The dissolution-derived secondary pores are generally filled with clay minerals and carbonates. Though evidences of dissolution can be easily observed in the silty and sandy lithologies, more significant dissolution may have occurred in the shales where most quartz and feldspar grains were 'flattened' by pressure solution (Figure 4.1).

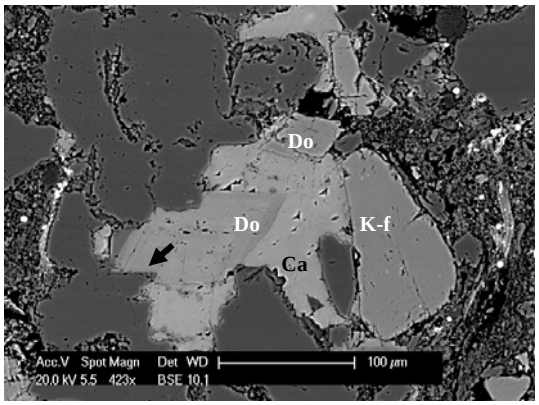

Figure 4.17 Calcite coating dolomite rhombs which coat quartz overgrowths (arrow), suggesting carbonate precipitation is a late event. BSE image of KCF sand, 3997.9 m TVD, well 16/7b-20.

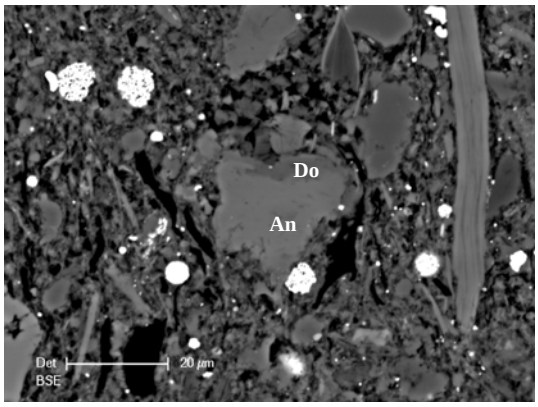

Figure 4.18 An ankerite (An) grain with a darker outer margin (dolomite) (Do). The zonation suggests that dolomite precipitation postdates the ferroan centre. BSE image of KCF shale, 3981.1 m TVD, well 16/8b-A2.

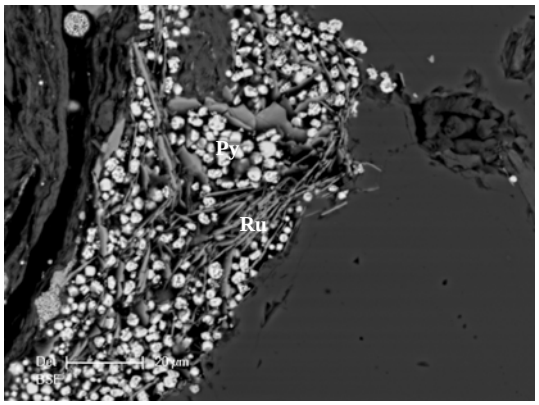

Figure 4.19 Pore-filling authigenic pyrite and rutile (Ru). SEM image of KCF silt, 3986.7 m TVD, well 16/8b-A2.

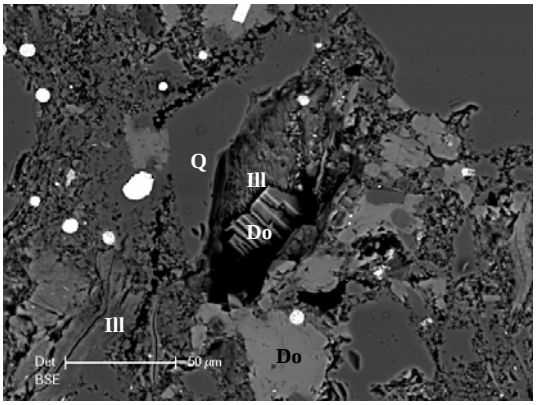

Figure 4.20 A secondary pore occupied by dolomite and illite cements. SEM image of KCF sand, 3961.6 m TVD, well 16/8b-A2.

K-feldspar and albite exsolution texture was observed. Figure 4.14 shows stringers of albite (dark grey) in a K-feldspar grain. Albite exsolution stripes within the K-feldspar grains often show preferred dissolution, leading to cavities in the grain (Figure 4.15). Authigenic albite was found in a coarser-grained sample. Figure 4.13 shows a group of euhedral albite grains (10-30 μm) growing in a secondary pore. The original mineral could not be determined.

Carbonate minerals are present mainly as cements. Calcite appears to be the most abundant carbonate phase in silty and sandy beds, while dolomite and ankerite seem to preferably occur in the shales. In the coarser-grained lithology, the carbonates occur as pervasive cements which greatly reduce the porosity (Figures 4.2 and 4.8). Carbonate cements usually postdate quartz and feldspar dissolution as plenty of evidence shows that they protrude into or completely fill the secondary pores (Figures 4.8, 4.11 and 4.16). Figures 4.2 and 4.17 show dolomite cements coating quartz overgrowth, indicating that carbonate cementation occurred later. In Figure 4.2, the sample is heavily cemented by dolomite and preserves pre-compaction features of grain contact, suggesting cementation prior to the main burial compaction phase. Calcite cements are often seen coating dolomites rhombs, indicating that it is the latest major cementation event (Figure 4.17).

In the shales, calcite, dolomite and ankerite have very low abundances (carbon content < 0.3 %) and small grain sizes (< 15 μm). There is little physical contact between calcite and dolomite to allow elucidation of the diagenetic sequence. However, intergrowth zonation between dolomite and ferroan-dolomite/ankerite can be seen in BSE images, suggesting several phases of growth. In most cases, dolomite consists of syntaxial rims around ferroan centres (Figure 4.18), but ankerite also can be seen as overgrowth rims on dolomite. In Figure 4.18, the centre of the magnesium carbonate grain is ferroan, therefore, bright under SEM; the outer margin is non-ferroan. The dolomite phase postdates ankerite in this case. The carbon and oxygen isotopes of these carbonate phases will be discussed in Chapter 5.

Pyrite is present in all samples (up to 20 %). It mainly occurs as a pre-compaction framboidal cement (Figures 4.1, 4.6 and 4.9), and, less commonly, as a post-compaction euhedral cements filling secondary pores (Figures 4.12 and 4.19). Pyrite framboids are more abundant in the organic-rich shales than in the coarser lithologies.

Authigenic apatite, anatase, zircon and rutile are present as trace minerals (e.g. Figures 4.13 and 4.19). They usually appear as euhedral grains filling secondary pores with other authigenic minerals including carbonate, albite and clay minerals.

4.4. Diagenesis in the KCF

Electron microscopy provides detailed information on the texture of the samples and enables to illuminate the diagenetic history of the KCF (Figure 4.21A). The SEM analyses illustrate that different lithologies within the KCF in the Miller area have undergone distinctly different diagenesis.

A **B**

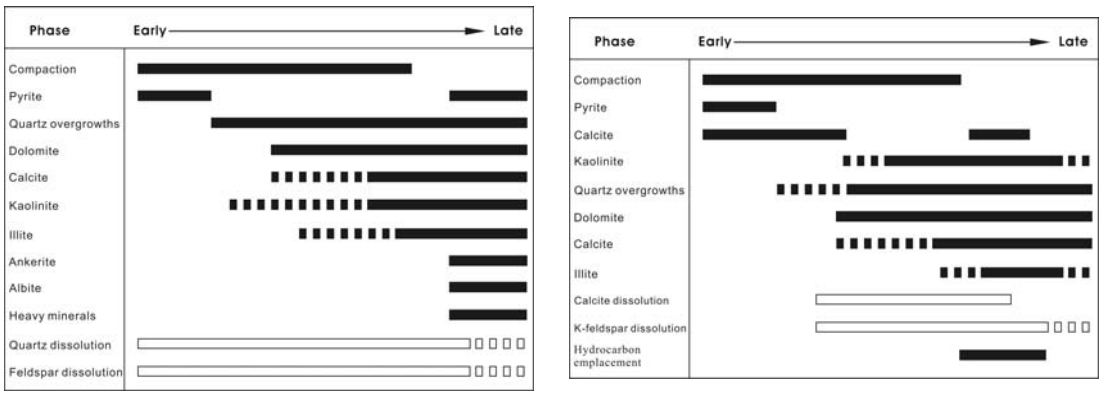

Figure 4.21 Paragenetic sequence for the Kimmeridge Clay Formation (A) and the Brae Formation sandstones (B), illustrating the chronological order of key diagenetic events. The sequence of events is mainly based on SEM petrography. B is modified after Marchand (2001) and Baines and Worden (2004).

In the shales, framboidal pyrite precipitated pervasively prior to significant compaction. The pyrite framboids appear to be closely associated with organic materials, while much less pyrite framboids are present in coarser-grained lithologies where organic content is lower.

Dissolution of quartz and feldspar initiated at the earliest burial stage and probably prevailed during the burial. Both minerals show ubiquitous corrosion features and strong pressure solution textures (Figure 4.1), indicating large volume of dissolution occurred during compaction. However, little evidence of precipitation (except pyrite) exists within the shale beds, suggesting the shales mainly underwent corrosion and did not receive any significant precipitation.

The silty and sandy lithologies underwent more complex diagenetic sequences. Shortly after deposition of the sediments, framboidal pyrite precipitated first, though its abundance is much lower than in the shales. Dissolution of quartz and feldspar also started at early stage and may have lasted till present-day time. The large number of the secondary pores suggests extensive dissolution. Quartz overgrowth started prior to the main compaction phase. Quartz cementation was sometimes observed to be polyphase. At least two phases can be seen under Cathodoluminescence (Figure 4.3). The latest precipitation produced euhedral quartz grains in newly formed secondary pores, indicating overgrowth lasted until the latest burial stage (Figure 4.5).

The next major diagenetic event in the silt/sand is carbonate cementation. Calcite, dolomite and ankerite cements of pervasive and pore-filling nature commonly postdate quartz and feldspar dissolution (Figures 4.8, 4.11 and 4.16). They also postdate early quartz overgrowths (Figures 4.2 and 4.17). Carbonate cementation continued until the latest burial stage (Figures 4.8, 4.13, 4.16 and 4.20). Dolomite appears to be the earlier cement, followed by calcite (Figure 4.17).

Authigenic kaolinite precipitated in relatively same period as carbonate cementation. They are often seen infilling the same secondary pores and coating each other (Figure 4.8). Kaolinite precipitation may have started at the beginning of feldspar dissolution because authigenic kaolinite is found as the sole pore-filling minerals in some secondary pores

(Figure 4.7). It is difficult to determine when illite started to precipitate. Illite sometimes shows mild compacted texture which suggests precipitation occurred before the end of burial compaction (Figure 4.4). However, it is certain that illite precipitation lasted until very recent as it coats quartz overgrowths and carbonate cements and infills secondary pores (Figures 4.6 and 4.20). No clear evidence of kaolinite converting to illite can be found.

Euhedral albite and pyrite formed in secondary pores are among the latest precipitation products (Figures 4.12, 4.13 and 4.19) in silt/sand. Together with them, all the trace minerals such as apatite, anatase, rutile and zircon show euhedral shapes and fresh surfaces, suggesting very late precipitation (e.g. Figures 4.13 and 4.19).

4.5. Diagenesis in the Brae Formation sandstones

Previous studies have focused on diagenesis of the Brae Formation reservoir sandstones (McLaughlin et al., 1994; Marchand, 2001; Marchand et al., 2001; Baines and Worden, 2004). The paragenetic sequence for the Brae Formation at Miller is shown in Figure 4.21B which is based on the studies by Marchand (2001) and Baines and Worden (2004). The pre-petroleum diagenetic history includes the precipitation of an early diagenetic assemblage of framboidal pyrite and large carbonate concretions. This was followed by quartz overgrowth which grew at the same time as the initial migration of petroleum into the reservoir sandstones. Feldspar dissolution occurred either concomitantly with, or shortly after, the onset of quartz precipitation. Significant secondary porosity (up to 15 %) was formed due to the dissolution of feldspar. K-feldspar dissolution sometimes is accompanied by typical products of its dissolution, such as kaolinite. Calcite cement from the margins of concretions suffered significant leaching and dissolution at later stage. But late carbonate cements were also observed.

To summarise, Miller with its high CO_2 content, has undergone extensive feldspar dissolution and the creation of secondary porosity followed by precipitation of minor

volumes of calcite cements and kaolinite. The influx of CO_2 is thought to be responsible for mineral dissolution and late-stage carbonate cements (Baines and Worden, 2004). The major CO_2-reactants within the Brae Formation were identified as K-feldspar, plagioclase, volcanic rock fragments and calcite. Feldspars are the most affected minerals and were substantially dissolved. The main mineral products of CO_2-reactions are quartz, kaolinite and ferroan carbonates. Illite and Kaolinite are the dominant clay phase.

4.6. Discussion

Comparing the diagenesis within various lithologies of the KCF, it is clear that the coarser-grained silty and sandy lithologies have undergone a diagenetic history similar to that of the Brae Formation sandstones, while the shaly lithology of KCF shows a distinctly different diagenesis.

The overall profile of diagenesis of the KCF shales is extensive mineral dissolution with little precipitation. High organic content which generates organic acids and increase acidity in the ambient is an important factor encouraging dissolution (Carothers and Kharaka, 1978). In a closed system these acids may affect dissolution rate of silicate minerals directly through three mechanisms: by affecting the dissolution rate far from equilibrium; by affecting the saturation state; and by affecting the speciation of Al (and possibly other elements) in solution (Drever and Stillings, 1997). Taguchi et al. (1988) also suggested that solubility of quartz and other silicates may be enhanced through complexing with organic compounds which are released during the transformation of organic materials.

Widespread quartz dissolution but little overgrowth occurred in shale, which is the dominant lithology in the KCF with a ratio of about 10:1 over silt/sand in thickness. This indicates that most dissolved silica did not reprecipitate locally. It must have been largely removed from the shales. The silica could have migrated some distance and may have been a source for quartz cementation in the adjacent sandstones. Astin and Evans (1990) have estimated that

shales may typically lose 10-20 % of their solid volume during digenesis, primarily through quartz dissolution and silica export. Whilst diagenesis of the KCF involves a net export of silica and thus possibly provides sources for quartz cementation in the adjacent sandstones, it should be borne in mind that there is also evidence of quartz cementation in the coarser-grained lithologies within the KCF and that not all of the mobilized silica is exported. However, it is difficult to quantify net export of silica.

In the Brae Formation sandstones, quartz cement abundance ranges from several percent to 15 % and is a critical control on reservoir quality (Marchand, 2001; Marchand et al., 2001). Silica released from the KCF shales, which are adjacent to or interbedded with the Brae Formation sandstones, should be an external silica source for the cementation in the sandstones, though K-feldspar and bioclast dissolution and pressure solution of quartz within the sandstone are believed to be local sources (Marchand, 2001).

The KCF shales generally contain a large amount of pyrite framboids which are closely associated with organic material. Precipitation appears to be prior to main compaction phase. Berner (1984) suggests that precipitation of pyrite is mainly controlled by the supply rates of organic matter in normal marine sediments where dissolved sulphate and iron minerals are abundant. The reaction of organic matter by sulphate-reducing bacteria releases HS^-, which reacts with any available Fe^{2+} to precipitate pyrite. Sulphate reduction is among the earliest reactions of organic matter and it occurs at depth less than 10 m (Irwin et al., 1977). Therefore, the observed abundant pyrite framboids probably mainly formed at this depth interval. No carbonates are found associated with the pyrite framboids, indicating that the sulphate reduction conditions in this case were not conducive for carbonate precipitation.

CO_2 has been proposed to be an important drive for feldspar dissolution and quartz cementation by several studies in which quartz is suggested as a product of feldspar dissolution (e.g. Hitchon et al., 1999; Baines and Worden, 2004; Kirste et al., 2004). The

pervasive K-feldspar dissolution within the Brae Formation is suggested as a CO_2-driven reaction (Baines and Worden, 2004). Worden and Morad (2000) suggest that K-Feldspar acts as the most important pH-buffer mineral in the Brae Formation sandstones and its dissolution is coupled with calcite precipitation. This reaction which also includes precipitation of quartz and kaolinite is sensitive to pH. Through controlling pH, CO_2 charge drives the reaction of feldspar dissolution. In this study, K-feldspar is also widely corroded in the KCF shales but it did not lead to widespread quartz precipitation. However, the extensive feldspar dissolution is more likely to have been induced by pressure solution during compaction at the early burial stage. Organic acids generated from the large volume of organic matter may have enhanced the dissolution. Feldspar dissolution in the silty and sandy lithologies displays similar features to that of the Brae Formation. It is apparently later than main compaction phase, therefore, may be related to CO_2 influence in the bottom of the KCF.

There is the problem as to why quartz should have preferentially precipitated in the reservoir sandstones, but not in the KCF. One probable reason is that clay coats on the quartz grains in the KCF is much thicker and, thus, more likely to inhibit the formation of quartz overgrowths (Huggett and Shaw, 1993). As has been suggested above, organic acids generated from organic material may also be an important inhibiting factor for quartz precipitation in the KCF (Drever and Stillings, 1997).

Mass balance of aluminium in the KCF and Brae Formation imposes another problem. In the KCF, though authigenic kaolinite was generally observed in the silty and sandy lithologies, little evidence of kaolinite precipitation exists in the shales where extensive feldspar dissolution occurred. Since shale is the dominant lithology, the overall amount of dissolved aluminium should exceed that of precipitation. Aluminium loss from the Brae Formation sandstones has also long being noticed (McLaughlin et al., 1994). In the sandstones, dissolution of feldspar created up to 15 % secondary porosity, but only less than 3.5 % authigenic clay is present (Marchand, 2001). Apparently, the diagenesis in the sandstones has

also been running an alumina surplus. Therefore, both the KCF and the Brae Formation have been exporting alumina and other associated components derived from widespread feldspar dissolution. The alumina mass balance cannot be achieved within these formations.

4.7. Conclusions

- SEM analyses reveal that various lithologies in the Kimmeridge Clay Formation show different diagenetic sequences. The silty and sandy lithologies of the KCF have undergone a diagenetic history similar to that of the Brae Formation reservoir sandstone, while the KCF shales experienced distinctly different diagenesis.

- The KCF shales suffered serious pressure solution of the detrital quartz and feldspars during compaction. Dissolution and compaction dominated the whole diagenetic history. Little mineral precipitation was observed, indicating the shales have been exporting dissolved materials. The quartz dissolution in the shales provides sources for quartz cementation in both the silty and sandy beds within the KCF and the adjacent Brae Formation sandstones.

- High organic contents in the KCF shales are probably responsible for the prevailing dissolution and little precipitation within the KCF shales. The organic acids generated by organic material increase acidity and encourage dissolution. Large amount of pyrite framboids in the shales are also related to the reactions of organic matter through sulphate-reducing microbial methanogenesis.

- The coarser-grained silty and sandy lithologies in the KCF show a more complex diagenetic history which is similar to that of the Brae Formation sandstones. It started with precipitation of framboidal pyrite and dissolution of quartz and feldspar at early burial stage. Quartz overgrowth started prior to main compaction phase and lasted until the late burial. Carbonate cementation with pervasive and pore-filling

nature is the major diagenetic event which postdates quartz and feldspar dissolution and early quartz overgrowths. It continued until the latest diagenetic history. Kaolinite and illite precipitation which are widely associated with the secondary porosity probably occurred in a same large time span as that of carbonate cementation. Precipitation of euhedral albite and pyrite and heavy minerals such as apatite, anatase, rutile and zircon are among the latest precipitation products.

- The CO_2 accumulation may have influenced feldspar dissolution both in the Brae Formation sandstone and the silt/sand lithologies in the KCF. K-feldspar in the shale lithology of the KCF also suffered severe corrosion. However, this dissolution was largely induced by pressure during compaction and associated with high contents of organic matter.

- Little quartz overgrowth occurred in the KCF. The overall high clay contents in the KCF may be a prohibitive factor for quartz overgrowth through forming thick coats on the quartz grains. Organic acids generated from organic material may be another inhibitor for quartz precipitation in the KCF.

- Both the KCF and the Brae Formation sandstones have undergone extensive feldspar dissolution with very small amount of dissolution products, such as kaolinite, precipitated within. Apparently, both formations have been exporting aluminium and other associated components derived from feldspar dissolution.

CHAPTER V

CARBONATE STABLE ISOTOPES

5.1. Introduction

Stable isotopes of carbonate cements are widely used to investigate fluid evolution of sedimentary basins. The carbon and oxygen isotopic signature of carbonate can be used to study origin of the porewater and carbon source from which the carbonate grew if precipitation temperature can be independently estimated. A large amount of isotopic data on carbonate cements in Jurassic reservoirs in the North Sea has been published. Within this extensive dataset, upper Jurassic reservoir sandstones such as the Brae, Fulmar, Magnus and Piper Formation show a number of diagenetic similarities between them, suggesting a more or less similar basinal fluid evolution (Greenwood et al., 1994; McLaughlin et al., 1994; Macaulay & Haszeldine, 1993; Hendry et al., 2000a). However, most of the diagenetic studies are focused on reservoir sandstones with only a few studies have been conducted on the Kimmeridge Clay Formation (KCF), the main source rock and sealing cap rock in the northern North Sea (e.g. Irwin et al., 1977; Scotchman, 1989; 1991; 1993).

Normal carbon sources for carbonate cementation include dissolved bicarbonate in the original marine-type porewater ($\delta^{13}C$ of ~0‰), dissolution of shell fragments (~0‰) and bicarbonate produced by oxidation of organic matter. The reactions of organic matter are thought to be the major carbon source during early diagenesis. They are depth-related and can be simplified to several processes operating at different burial depths as shown in Figure 5.1: (1) aerobic oxidation; (2) microbially-mediated iron reduction; (3) bacterial sulphate reduction (SR); (4) Methanogenesis (M) and (5) thermally-induced decarboxylation (D) (Irwin et al., 1977; Curtis, 1978). The first three processes take place at very shallow burial

(depth $<10^{-2}$ m). Thermally-induced decarboxylation usually occurs at burial depths greater than 1 km (Scotchman, 1993). The application of the diagenetic reaction zone scheme to the organic-rich mudrocks of the Upper Jurassic Kimmeridge Clay Formation has been demonstrated in several studies (Irwin et al., 1977; Scotchman, 1989; 1991; 1993). In these studies, burial depth and sedimentary rate are suggested to be major controls on the diagenetic reactions in marine organic-rich mudrocks (Irwin et al., 1977; Curtis, 1987) and on the evolution of their pore fluids (Scotchman, 1991; Scotchman et al., 2002). It is believed that these organic matter-based reactions have profound effects on the compositions of pore fluids both in the KCF and the interbedded Brae Formation. Many studies suggest that sandstones in close spatial association with thick organic-rich mudrocks receive fluids rich in carboxylic acids which control or largely influence carbonate cementation in the sandstones (e.g. Macaulay et al., 1998; Hendry et al., 2000a).

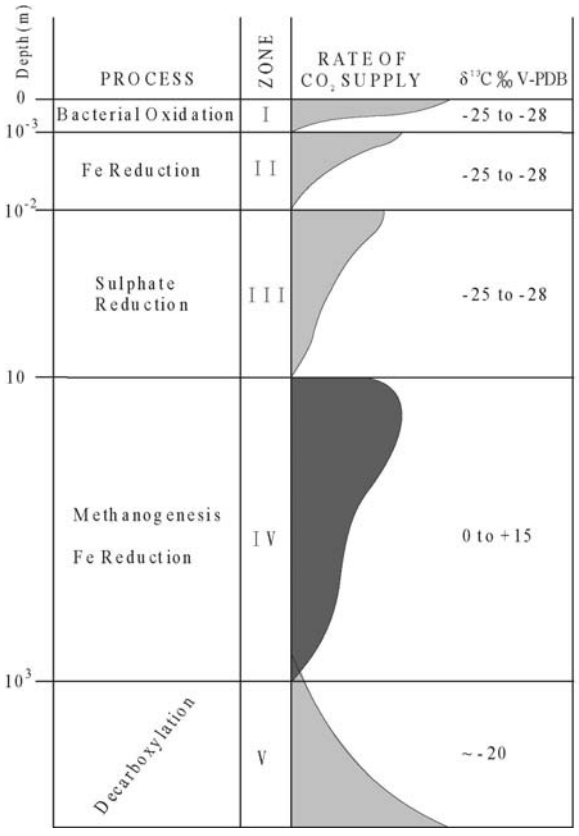

Figure 5.1 Depth-related diagenetic reaction zones based on the degradation of organic matter showing $\delta^{13}C$ composition of carbonate product (After Curtis, 1978 and Scotchman, 1993).

In the Miller Field, the Brae Formation reservoir sandstone is interdigitated with the Kimmeridge Clay Formation (KCF) which acts as both source rock and sealing cap rock (MacKenzie et al., 1987). Both the reservoir rock and the bottom of the KCF seal have been in contact with the CO_2 accumulation since its emplacement. CO_2 charge should have had a major impact on isotopic compositions of the carbon source in the reservoir. The carbonate

cements in the reservoir rock may record the isotopic variations that resulted from the charge. If CO_2 had breached the seal and produced carbonates there, these carbonates would bear information of the CO_2 breaching. By analysing carbonate isotopes, therefore, it is possible to distinguish between the carbonates influenced by the CO_2 charge and those formed during normal depth-related geochemical processes. The former carbonates provide information on timing and effects of the CO_2 emplacement. The control well (9/28b-17) from a low CO_2 area, 30 km northeast to the Miller Field, is chosen as a comparison to the Miller Field (Figure 2.4). This will help to identify the isotopic signatures associated with the CO_2 charge at Miller.

5.2. Occurrence of carbonate cements

5.2.1. Carbonate cements in the Brae Formation sandstone

In the Miller Field, carbonate cementation mainly occurs in the submarine fan facies of Brae Formation sandstones. The vast majority of the carbonate cement is calcite, which is the first major diagenetic product following deposition of the sediments (Marchand, 2001). Calcite-cemented zones in core often show curved edges, suggesting concretionary shape. The concretions examined in previous studies (Larter et al., 1995; Marchand, 2001) and this study range from 2 to 11 m in thickness. Calcite abundances vary from 25-40 % in the concretion centres to 10-20 % at the concretion edges. Calculated minus cement porosity (MCP) values range accordingly from 40-25 % in the centres to 25-20 % at the edges, which indicates that calcite cementation began prior to compaction (Marchand, 2001).

Based on core observations and log interpretations of 29 wells, it is found that concretion abundance varies between the different sections (oil and water legs) and between the wells. Figure 5.2 shows the percentages of concretion in different sections of nine exploration wells determined as % of cemented conventional core. The greater abundance occurs in the northern part of the field. Well 16/7b-28 has the greatest cumulative thickness of concretions, 354 m, equivalent to 11 % of overall sandstone. Well 16/8b-6 has the highest cementation rate, 27.6 % of the examined sandstone. In the oil leg, the exploration wells across the field show significant difference in concretion percentages from north to south. Three wells from the northeast flank contain an average of 27.1 % of concretion, while the wells from south have an average as low as 4.3 %. In the water leg, in contrast, the southern wells show generally high concretion abundances, ranging from 9.8 to 19.4 %, while two of the three northern wells contain lower abundances (8.3 and 8.7 %) with the third one (well 16/8b-6) showing a abnormally high concretion percentage of 28.2 %. Overall, in the three northern

wells, higher concretion abundance occurs in oil leg (27.1 %) than in water leg (15.1 %). In the southern wells, however, oil leg (3.7 %) contains much less concretions than does water leg (15.3 %).

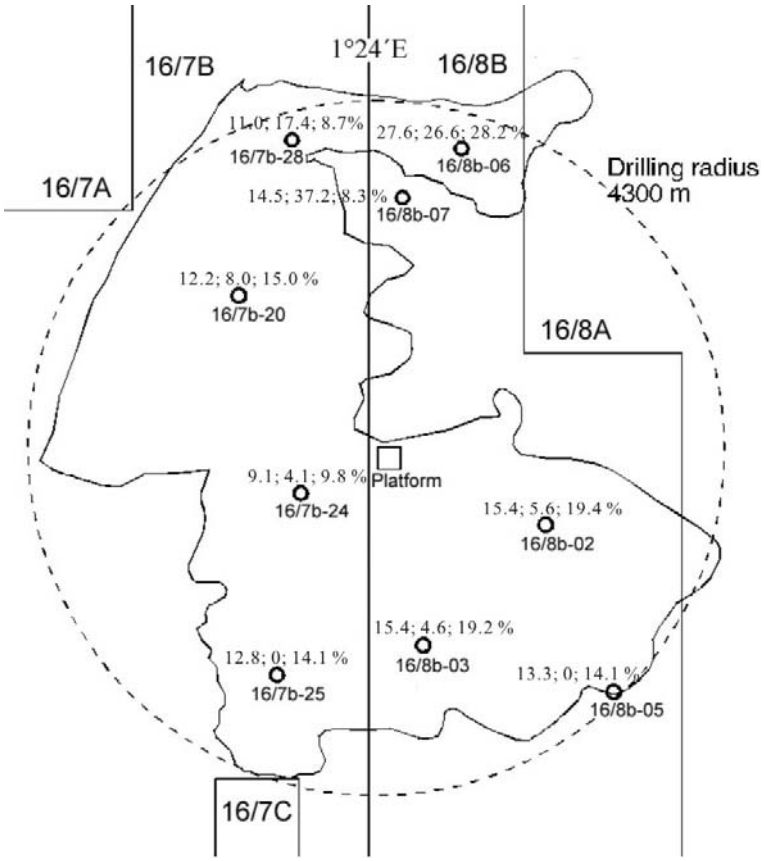

Figure 5.2 Percentage of concretion in the nine exploration wells. Concretions are recognized in gamma ray, sonic, resistivity logs. The three numbers showed for each well are: overall percentage of concretion; percentage in oil leg and percentage in water leg.

5.2.2. Carbonates in the Kimmeridge Clay Formation

Early diagenesis produced widespread carbonate concretions and stone bands in the KCF (Irwin et al., 1977; Scotchman, 1993; Scotchman et al., 2002). In the Miller Field, as has been discussed, several phases of diagenetic carbonate were detected by SEM in the KCF, including calcite, dolomite and ankerite. In coarser-grained silt/sand beds, calcite and dolomite are present. Calcite is the pervasive cement with abundance up to ~30 wt %. Dolomite, which is much less abundant (up to ~15 wt %), usually appears as euhedral rhombs and subhedral pore-filling cement. Both carbonate cements postdate quartz overgrowth as textural relationship suggests. Calcite cements are often seen surrounding dolomites rhombs, indicating that precipitation of calcite is the latest major cementation event (Figure 4.17). In the shales, calcite, dolomite and ankerite were found, but in very small abundance (inorganic carbon content < 0.3 %) (Table 5.3) and with a very small grain

size (<15 μm). There is little physical contact between different carbonate phases to allow elucidation of diagenetic sequences. However, intergrowth zonation between dolomite and ferroan-dolomite/ankerite can be seen in backscattered SEM images which show several phases of precipitation. In most cases, dolomite consists of syntaxial rims around ferroan centres (Figure 4.18), suggesting that non-ferroan dolomite phase postdates the ferroan phase.

5.3. Sampling method

Most samples were taken from the KCF immediately overlying the reservoir section for isotopic analysis. The others were taken from the thin shale beds in the reservoir section, the Brae Formation. Calcite concretions and disseminated carbonate cements in the Brae Formation sandstone were also sampled. The samples were collected separately as two groups according to lithology: shale and silt/sand.

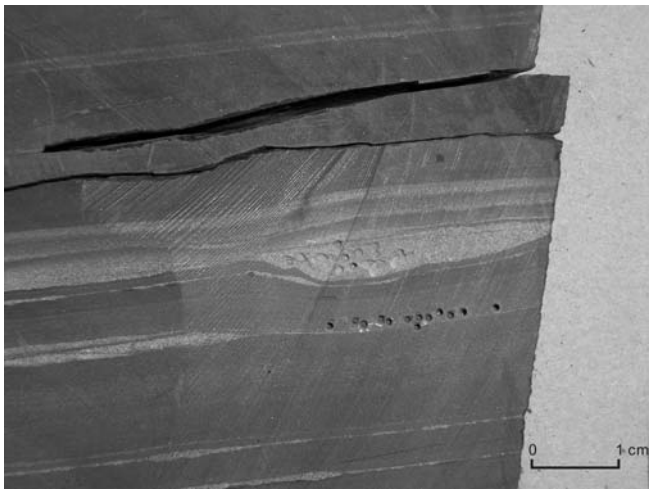

Figure 5.3 Photograph of the KCF core, showing positions of collecting powder samples from different lithologies using micro-drill. Drilling core from 3982.6 m (TVD), well 16/8b-A2, the Miller Field.

Most of the samples were from a rather small interval overlying the reservoir. This study focuses on the bottom of the seal in order to identify any isotopic signals of possible CO_2 infiltration. Rock powder samples were collected from the cores at spacing of ~ 20 cm adjacent to the reservoir top and at progressively wider spacing further up and down. Electric drill with a tungsten carbide drill bit was used to drill off whole-rock powders which were collected on weighing paper before being transferred into 1.5 ml tubes. In order to prevent mixing different lithologies, each drilling was confined to a stripe area of ~2 mm wide within the same sedimentary layer, as Figure 5.3 shows.

131 samples were collected from well 16/8b-A2 of the Miller Field (Figure 2.4). 115 of them were taken from a depth interval of ~23m immediately above the reservoir top. The other 16

samples were from the reservoir section down to ~21m below the crest. Only one shale sample contains too little carbonate to yield sufficient CO_2 for analyses.

110 samples were taken from well 9/28b-17, the control well (Figure 2.4). The samples are from a depth interval of ~40m thick, ~35m into the KCF and ~5m in the Brae Formation. But only 85 samples yielded sufficient amount of CO_2 to provide isotopic measurements because of the very low carbonate abundances (< 3 wt %).

5.4. Analytical methods

Oxygen and carbon isotopic analyses were performed at Scottish Universities Environmental Research Centre (SUERC), East Kilbride, Scotland. Bulk isotopes were measured because different carbonate minerals in the KCF samples could not be physically separated. Carbon and oxygen isotope ratios of carbonate were measured using conventional procedures. CO_2 gas was extracted from rock powder by overnight reaction with 100% phosphoric acid at 70°C. The evolved CO_2 gas was dried and purified before isotopic analysis on an Analytical Precision AP 2003 Mass Spectrometer. Both C and O isotopic values are reported and discussed as δ‰ values relative to V-PDB (Vienna Standard Pee Dee Belemnite). $\delta^{18}O$ values relative to V-SMOW (Vienna Standard Mean Ocean Water) are also presented in Table 5.1 and 5.2 (attached at the end of chapter). Precision and accuracy are better than ±0.2 ‰ at 1σ.

Carbonate mineral abundance in shale was determined by measuring total inorganic carbon using a CM 5012 CO_2 coulometer supplied by UIC Coulometrics Inc. Approximately 80 mg of powder for each sample was acidified with two molar perchloric acid. The evolved CO_2 was extracted from solution using ultra high purity N_2 as an inert carrier gas and transferred to the detector. Carbonate abundance was calculated assuming that the predominant mineral was calcite.

5.5. Results

5.5.1. Results of the Brae Formation sandstones

Table 5.1 displays the carbonate C and O isotopic compositions of 16 samples of the Brae Formation sandstone in well 16/8b-A2. Eleven of them were collected from a concretion between 3992.6 and 3994.7 m. The rest represent pervasive disseminated cements from lightly cemented sandstones. These data are projected in Figure 5.4, together with the data set from the Thermie Reservoir Geochemistry Project (Larter et al., 1995).

In Figure 5.4, $\delta^{18}O$ values range from -13.9 to -4.8 ‰ V-PDB. $\delta^{13}C$ values range from +7.9 to -10.82 ‰ with an average of -2.3 ‰. The data form a trend from heavy to light isotopes. The disseminated cements show small ranges of $\delta^{18}O$ from -10.1 to -7.7 ‰ and of $\delta^{13}C$ from -4.0 to -2.4 ‰, falling in the middle of the trend. It is found that these data are of comparable magnitude to those of the other fields in the region, which also generally show a trend from high to low C and O isotopic values (Greenwood et al., 1994; McLaughlin et al., 1994).

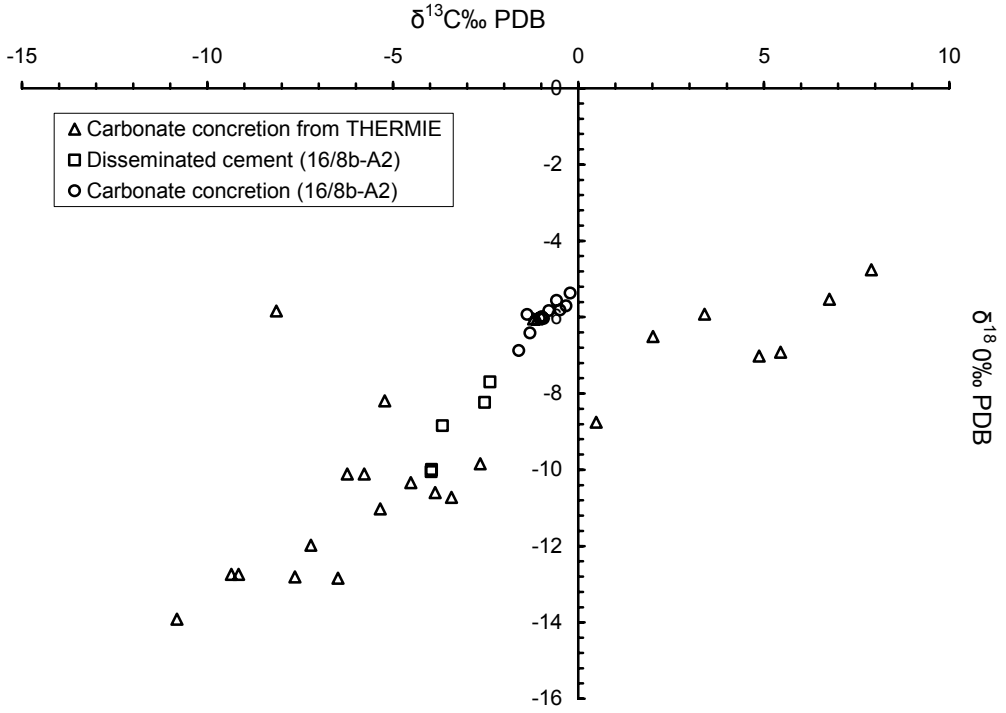

Figure 5.4 Isotopic compositions of carbonate cements in the Brae Formation sandstones, the Miller Field. Sixteen samples from well 16/8b-A2 (squares and circles) are analyzed in this study and the rest of the data (triangles) are from the Thermie project (Larter et al., 1995). Most samples are taken from concretions, except the 5 disseminated cement samples (squares).

5.5.2. Results of the Kimmeridge Clay Formation

Carbonate isotopes of the KCF of the Outer Moray Firth (Scotchman et al., 2002) and the North Brae Field (Greenwood et al., 1994) are presented in Figure 5.5A as a regional background data set. These data exhibit wide ranges of $\delta^{18}O$ and $\delta^{13}C$, with $\delta^{18}O$ ranging from +1.7 to -11.9 ‰ and $\delta^{13}C$ from +9.9 to -7.8 ‰. They constitute a slightly curved trend from high to low values, showing a similar range and pattern to that of the Brae Formation sandstones in the region (e.g. Greenwood et al., 1994; McLaughlin et al., 1994).

Data obtained by this study are reported in Table 5.2 and projected in Figure 5.5. The data of

well 16/8b-A2 of the Miller Field and those of the control well show $\delta^{18}O$ values ranging from -4.98 to -13.70 ‰ and $\delta^{13}C$ from +1.8 to -10.8 ‰. No $\delta^{18}O$ higher than -4 ‰ with positive $\delta^{13}C$ exist. They form a scattered distribution at the lower end of the regional trend (Figure 5.5A).

In the Miller well, the shale lithology exhibits obviously different isotopic compositions from the silt/sand (Figure 5.5B). Shale data of this well have higher carbon isotopic values with an average $\delta^{13}C$ of -4.3 ± 0.41 ‰ (within 95 % confidence interval), while those of silt/sand have an average $\delta^{13}C$ of -7.0 ± 0.51 ‰. Though their $\delta^{18}O$ data do not differ as much as $\delta^{13}C$ do, average $\delta^{18}O$ of the shales (-9.4 ± 0.39 ‰) is also higher than that of silt/sand (-10.2 ± 0.35 ‰). It is worth noting that the shales in different sections also show different isotopes, with reservoir shales showing overall higher $\delta^{13}C$ and lower $\delta^{18}O$ than the shales in the KCF seal (Figure 5.5B).

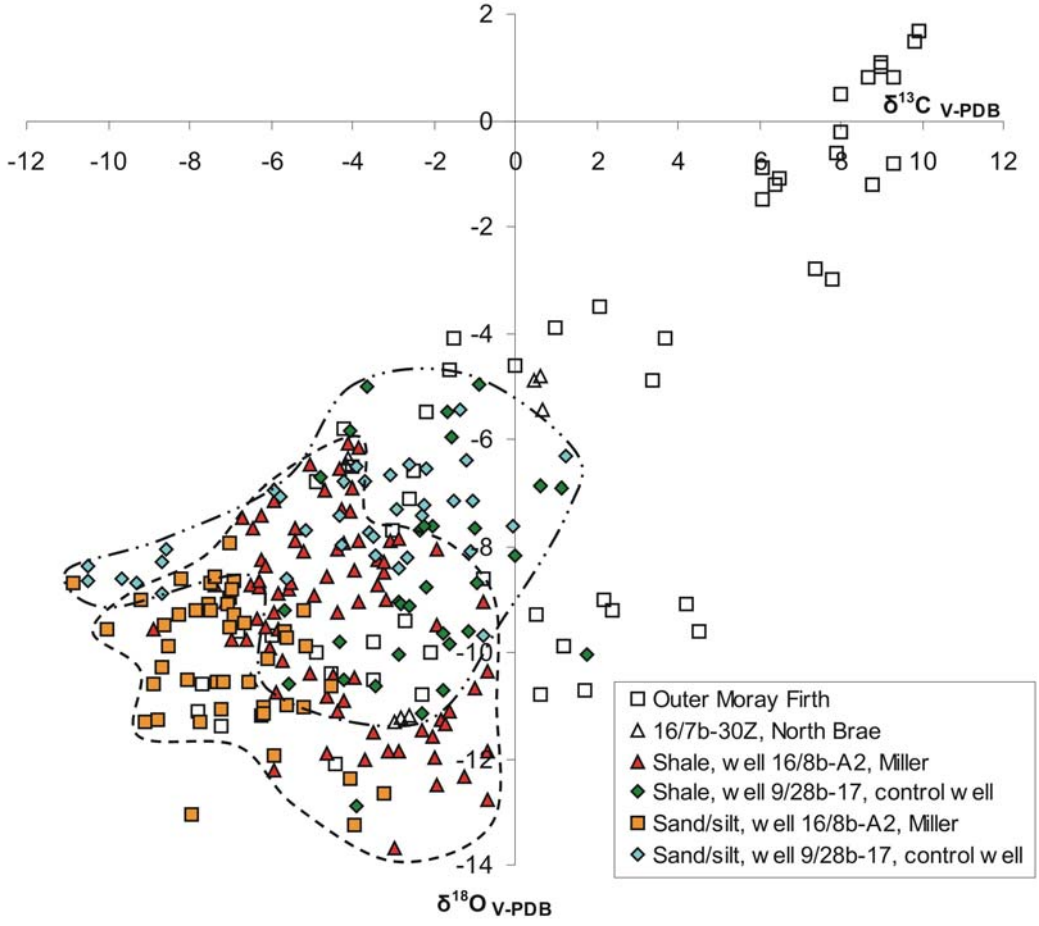

Figure 5.5A Isotopic compositions of the KCF samples of well 16/8b-A2, Miller, and well 9/28b-17, the control well which is located in a low CO_2 area. Data from the Outer Moray Firth (Scotchman et al., 2002) and the North Brae Field (Greenwood et al., 1994) are also projected in the plot as regional background. The two data sets of the Miller well and control well are outlined separately using dash line.

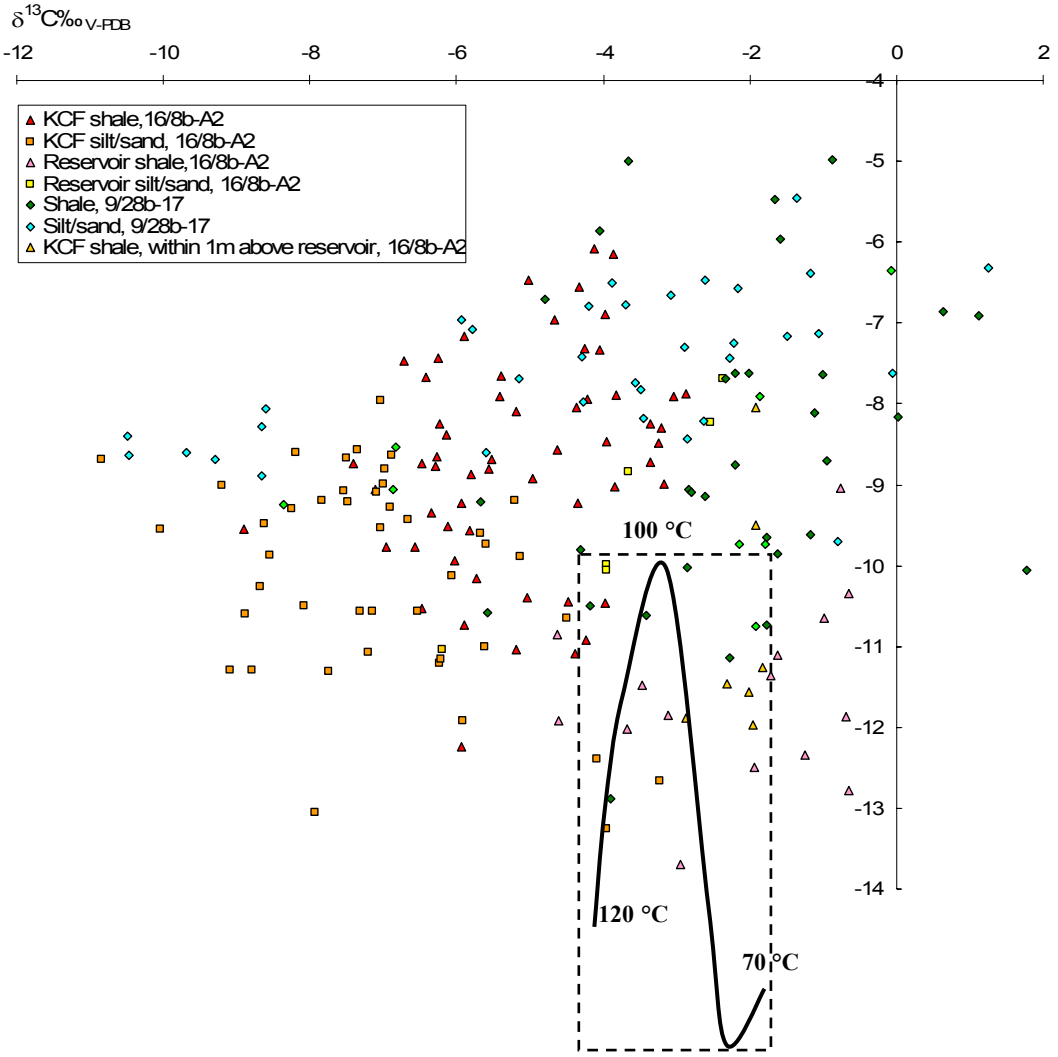

Figure 5.5B Isotopic compositions of the KCF samples of well 16/8b-A2, Miller, and well 9/28b-17, the control well. The regional data is removed. The Miller data are further separated into the KCF and reservoir groups. The curve is a prediction line of C and O isotopes of calcite which would have precipitated from the CO_2 accumulation in the reservoir at temperature from 70 to 120 °C.

The control well samples yield generally higher O and C isotopes than those of the Miller well. Average $\delta^{18}O$ value of the shales of the control well is -8.6 ± 0.68 ‰, higher than the Miller average of -9.4 ± 0.39 ‰. Average $\delta^{13}C$ is -2.6 ± 0.62 ‰, also higher than the Miller average of -4.3 ± 0.41 ‰. Both O and C isotopic compositions of the silt/sand samples of the control well (average $\delta^{18}O$ of -7.8 ± 0.33 ‰; average $\delta^{13}C$ of -4.08 ± 0.91 ‰) are also heavier than those of Miller counterparts ($\delta^{18}O$ of -10.2 ± 0.35 ‰ and $\delta^{13}C$ of -7.0 ± 0.51 ‰).

The plot of $\delta^{13}C$ versus depth of the KCF shales of the Miller well reveals a rather striking

pattern (Figure 5.6). A linear trend can be observed within an interval of ~12 m thick immediately above the reservoir. The data in this interval show very good linear correlation between $\delta^{13}C$ and depth with the square of correlation coefficient of 0.90. This means that 90% of the variance of $\delta^{13}C$ can be "accounted for" by changes in depth and the linear relationship between them. $\delta^{13}C$ evenly decreases upwards from -0.77 to -7.4 ‰ within the interval. Above this interval, $\delta^{13}C$ values are randomly scattered with depth, but generally sit around the low-$\delta^{13}C$ end of the trend, ranging from -3.8 to -6.7 ‰ (except one sample with much lower value of -8.9 ‰), with an average of -5.3‰. $\delta^{13}C$ values in the reservoir section fall on the high-$\delta^{13}C$ end of the trend, ranging from -4.6 to -0.65 ‰ with an average of -2.4 ‰. The C isotopes are obviously different between the reservoir and the KCF. It is worth noting that the lowest values of the trend exceed the range of the data above the trend. This interval is referred as a 'anomalous zone' because this feature is not present in the control well. The silt/sand samples of the Miller well show a similar pattern (Figure 5.7). $\delta^{13}C$ decreases steadily upwards from the reservoir top, though the trend is less well defined. But the anomalous zone is thinner, only ~5 m in thickness.

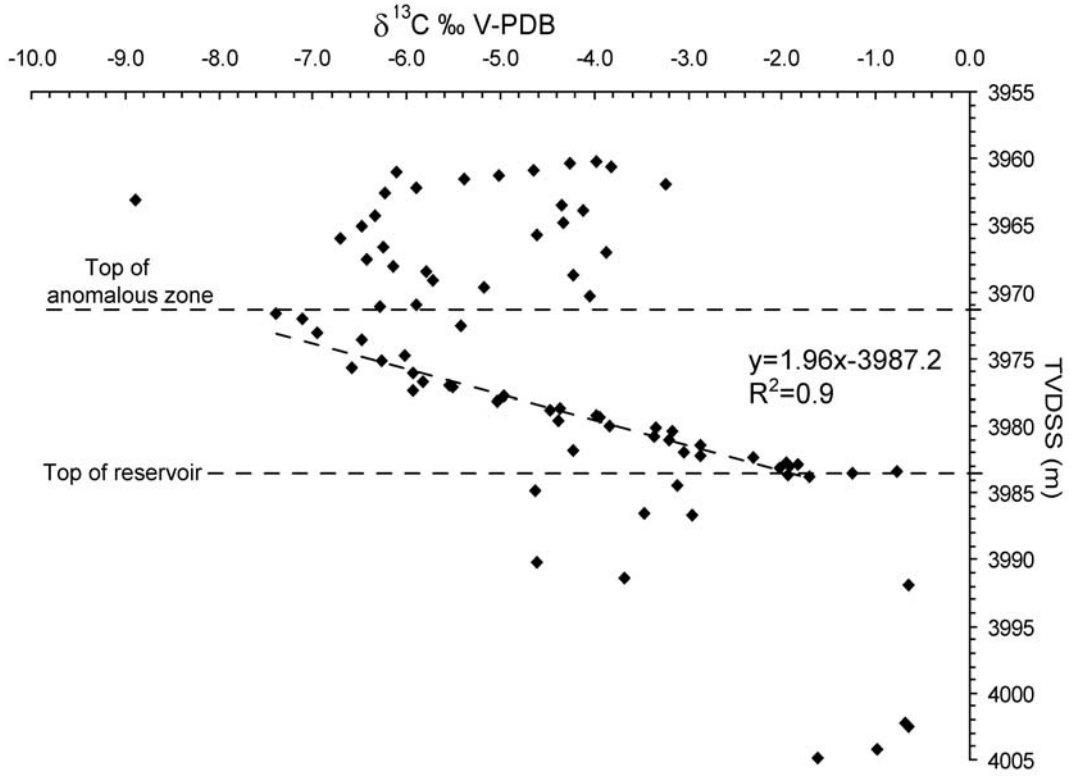

Figure 5.6 $\delta^{13}C$‰ versus depth of whole-rock shale samples in well 16/8b-A2, the Miller Field. A linear decrease of $\delta^{13}C$‰ is present in a 12 m interval above the reservoir sandstone. The square of correlation coefficient is 0.9, indicating good linear correlation between the $\delta^{13}C$ values and depth. It is interpreted as dissolution of original carbonates, followed by re-growth incorporating signatures of reservoired CO_2. The projection of modelled results shows an excellent match to the analyses. Discussed in Section 5.7.5.

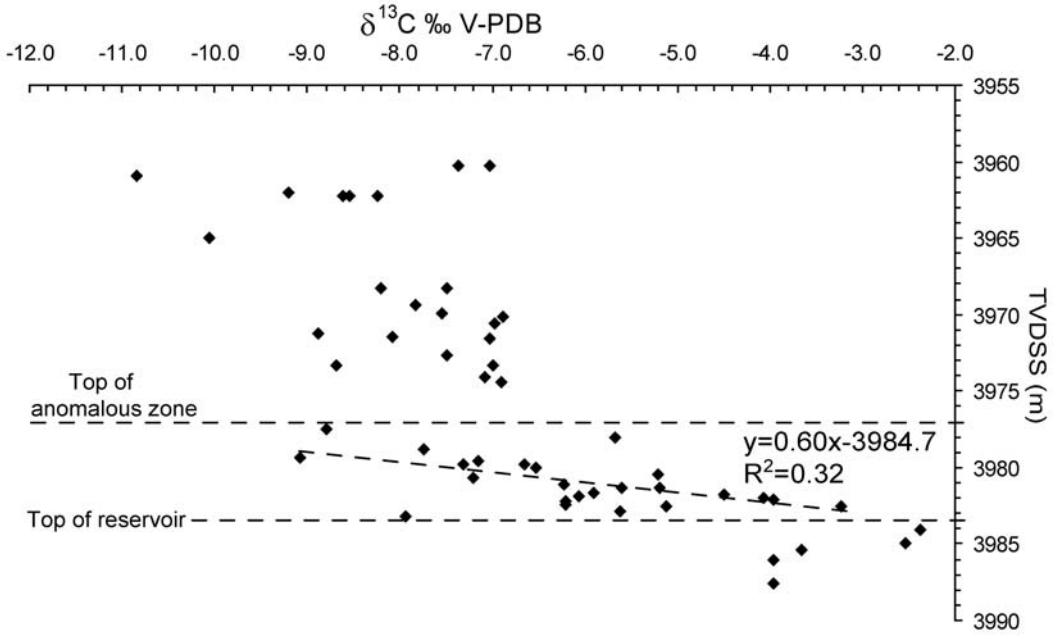

Figure 5.7 $\delta^{13}C$‰ versus depth of silt/sand samples in well 16/8b-A2, the Miller Field, showing a moderate linear correlation between $\delta^{13}C$ and depth with a R^2 of 0.32 in a 5 m interval above reservoir.

Oxygen isotopes of the Miller well vary systematically with depth as well, though the correlation is poorly defined (Figures 5.8 and 5.9). $\delta^{18}O$ values of both shale and silt/sand samples generally increase upwards in their anomalous zones. For shale data, the boundaries of the anomalous zone are not very obvious (Figure 5.8). But the silt/sand data show a rather clear linear trend within the 5 m anomalous zone (Figure 5.9). $\delta^{18}O$ values increase upwards rapidly from ~ -13 to ~ -9 ‰ in the zone while no obvious correlation with depth can be seen above and below it.

KCF $\delta^{18}O$ and $\delta^{13}C$ of the control well are generally higher than those of the Miller well (Figure 5.5B). The average $\delta^{18}O$ and $\delta^{13}C$ are -8.2 ‰ and -3.3 ‰, respectively. Both are more than one unit higher than those of the Miller well (-9.7 ‰ and -5.3 ‰). Despite the differences, control well data still fall on the regional isotopic trend (Figure 5.5A). Both $\delta^{18}O$ and $\delta^{13}C$ isotopes are randomly scattered with depth. No clear linear correlation exists (Figures 5.10 to 5.13), except that the shale $\delta^{13}C$ data seemingly show a linear trend in a 12 m zone above reservoir, but with low correlation coefficient (R2=0.18).

Inorganic carbon content (ICC) data are presented in Table 5.3 (attached at the end of chapter). The ICC data of shale are plotted against depth in Figures 5.14 and 5.15 respectively for the Miller well and the control well. In the Miller well, shale ICC is less than 0.06 % in the reservoir section while it is as high as 0.37 in the KCF (Figure 5.14). A general

upwards increase from 0.02 to 0.37 % can be seen in the 12 m interval above reservoir. The data above the interval show a random distribution.

In the control well, ICC values are generally very low, less than 0.05 % (only five data with higher value) (Figure 5.15). There is no clear linear correlation with depth, though the values further up become higher with wilder scattering. Only two data were obtained from the reservoir section.

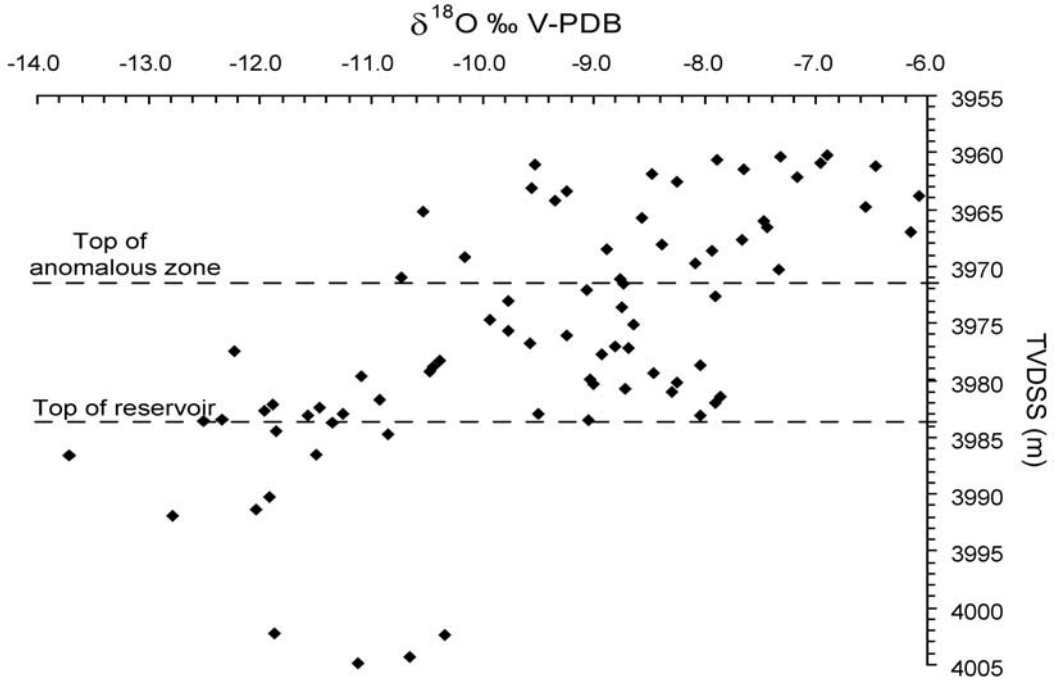

Figure 5.8 $\delta^{18}O$‰ versus depth of shale samples in well 16/8b-A2, the Miller Field.

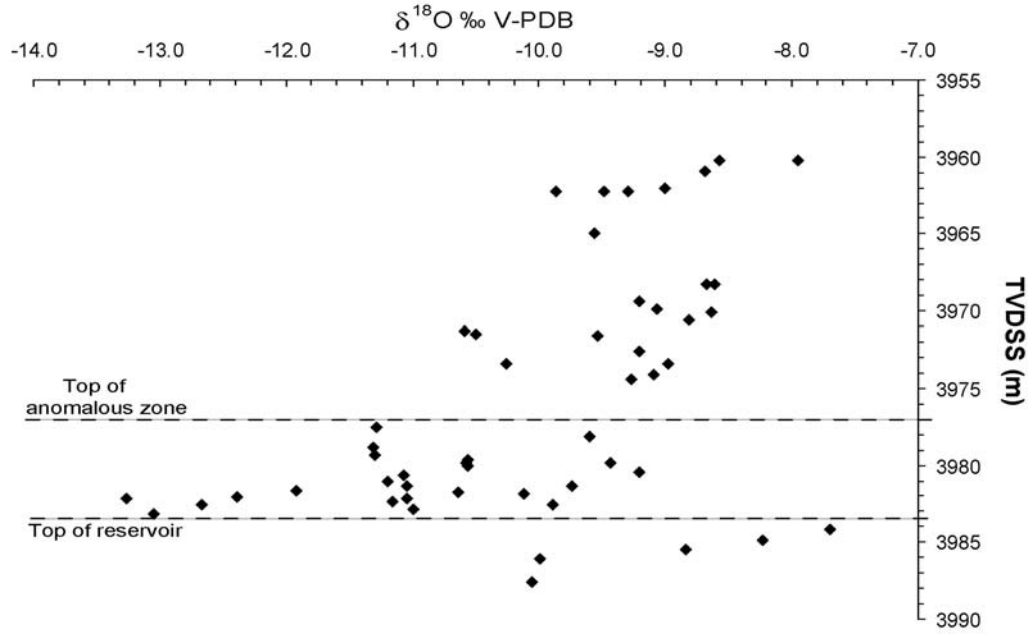

Figure 5.9 $\delta^{18}O$‰ versus depth of silt/sand samples in well16/8b-A2, the Miller Field.

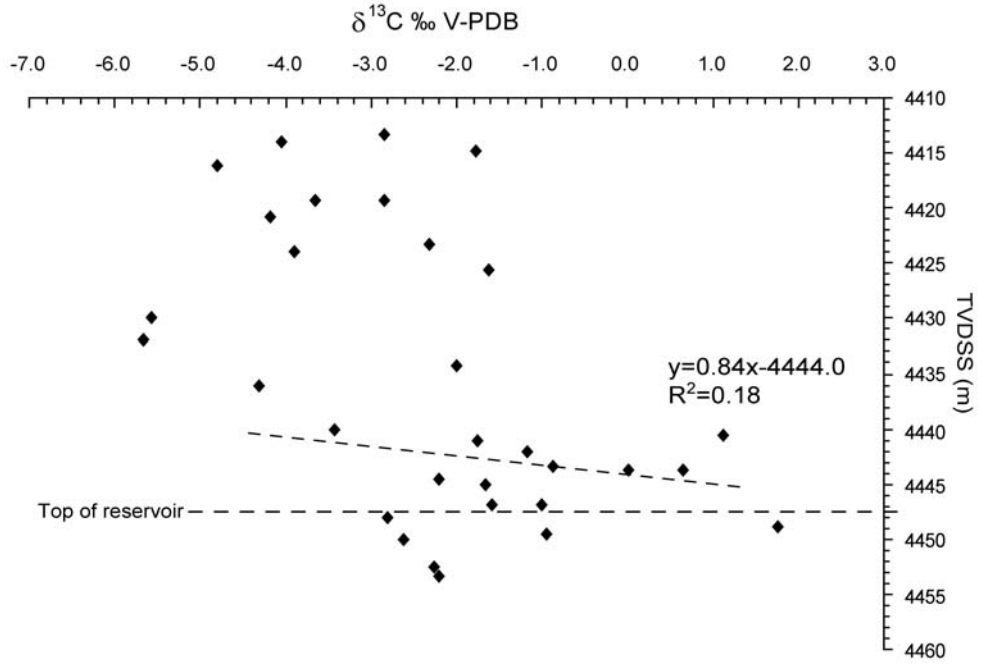

Figure 5.10 $\delta^{13}C$‰ versus depth of shale samples in well 9/28b-17, the Control well. Poor linear correlation between $\delta^{13}C$ and depth exists in a 12 m interval above reservoir, with a low correlation coefficient (R^2=0.18).

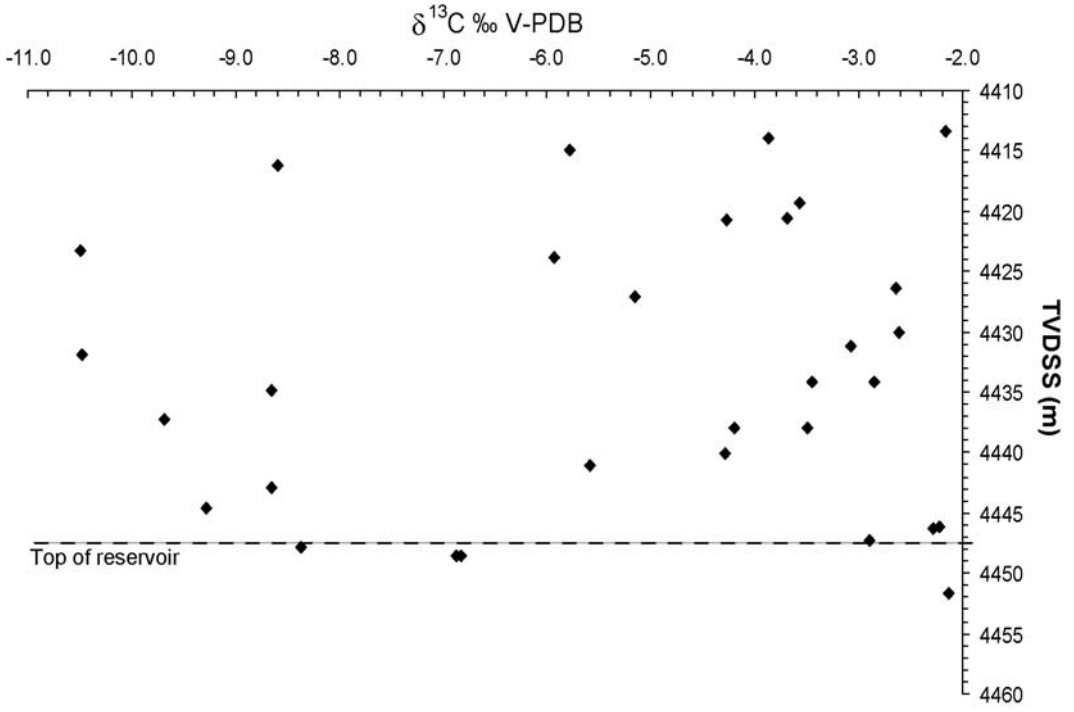

Figure 5.11 $\delta^{13}C$‰ versus depth of silt/sand samples in well 9/28b-17, the control well. No linear correlation can be seen above the reservoir.

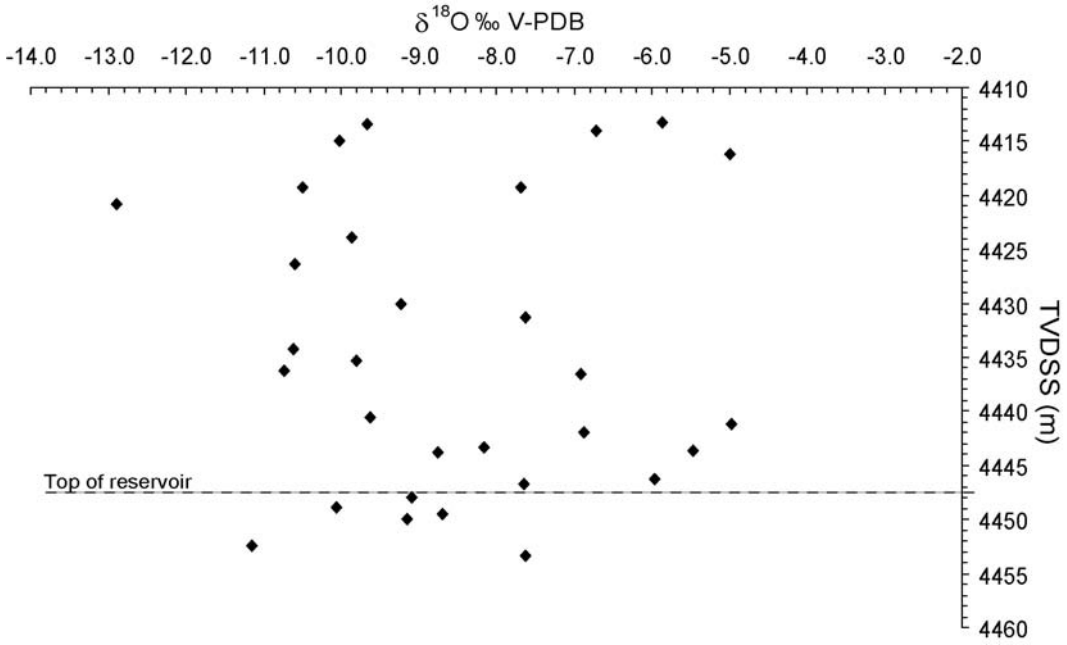

Figure 5.12 $\delta^{18}O$‰ versus depth of shale samples in well 9/28b-17, the Control well.

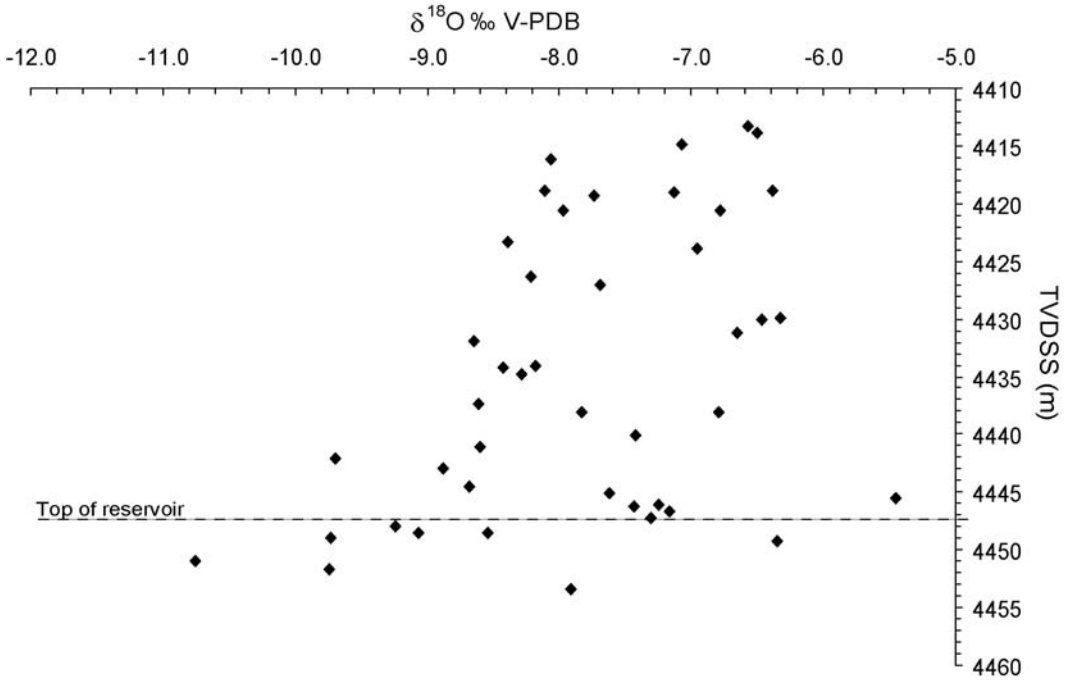

Figure 5.13 $\delta^{18}O$‰ versus depth of silt/sand samples from Well 9/28b-17, the control well.

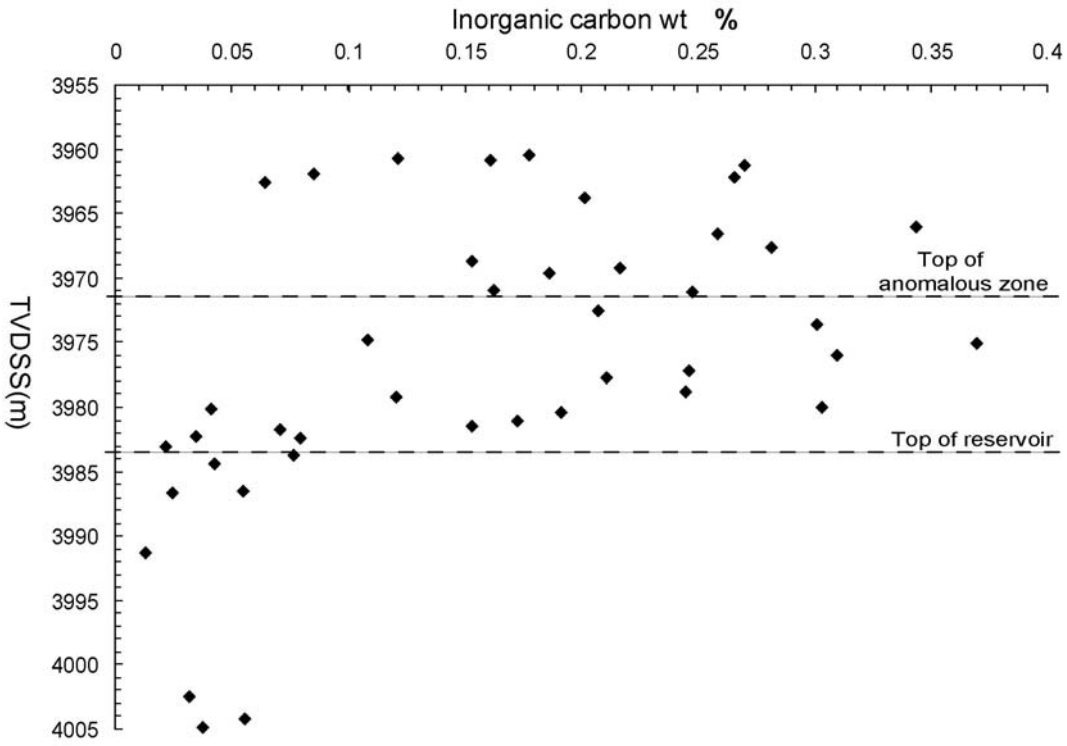

Figure 5.14 Inorganic carbon content in the shale versus depth, well16/8b-A2, the Miller Field.

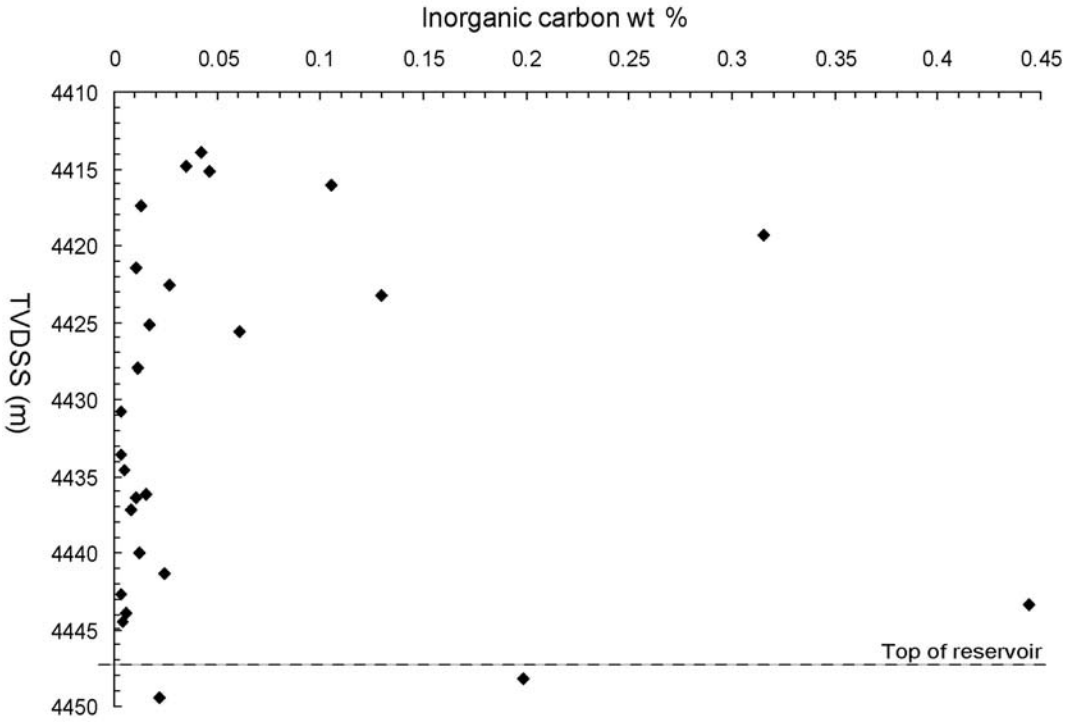

Figure 5.15 Inorganic carbon content in the shale versus depth, well 9/28b-17, the control well.

5.6. Discussion – Isotopes of the Brae Formation sandstone

5.6.1. Oxygen isotopes

Variable oxygen isotopes are indicators of precipitation from different pore fluids and/or at different temperatures. Curtis (1978) noted that if isotopic variation in $\delta^{18}O$ occurs as a result of temperature variation, progressive depletion of heavier isotopes from early to late cements can be expected if precipitation continues during burial to progressively higher temperatures. Concretions in the Miller reservoir sandstones show a similar decreasing trend of $\delta^{18}O$ versus $\delta^{13}C$ to the regional data, indicating a normal porewater and carbon source evolution without obvious evidence of influence from the CO_2 charge. The decrease of $\delta^{18}O$ from -4.8 to -13.9 ‰ represents a temperature-controlled variation (Figure 5.4). The disseminated cements outside of concretions analysed in this study display small $\delta^{18}O$ range between -10.1 and -7.7 ‰, falling on the middle of the trend, suggesting that disseminated carbonate cements precipitated from the same pore fluid as the concretions, but in a narrow temperature window.

The measured $\delta^{18}O$ compositions of calcite can be used to estimate the precipitation temperatures if the porewater from which the carbonate precipitates is known. The equation of fractionation with temperature is shown as follows (Friedman and O'Neil, 1977):

$$1000 ln\alpha_{calcite\text{-}water} = 2.78(10^6 \cdot T^{-2}) - 2.89 \quad (5.1)$$

Note that $1000 ln\alpha_{calcite\text{-}water} \approx (\alpha - 1)\ 1000 \approx \delta^{18}O_{calcite} - \delta^{18}O_{water}$, where $\delta^{18}O_{calcite}$ is the measured oxygen isotopic composition of the calcite, $\delta^{18}O_{water}$ is the oxygen isotopic composition of the porewater from which the calcite precipitated. T is temperature in Kelvin.

In order to assess the effects of the CO_2 charge, it is necessary to study the evolution of the porewater system during burial. The Brae Formation sandstones were deposited in sub-marine settings, therefore the initial porewater from which the early calcite precipitated should be Jurassic marine water. However, several studies on pore fluid evolution in this region argue that meteoric water influx replaced the marine water through re-charge in early burial stage (Bjørlykke, 1989; Haszeldine et al., 1992; Glasmann, 1992; Prosser et al., 1993; Marchand et al., 2002). To test those two initial formation water candidates, various calcite precipitation temperatures were calculated assuming precipitation from Upper Jurassic meteoric water ($\delta^{18}O$ = -7.0 ‰ V-SMOW; -36.8 ‰ V-PDB, Hamilton et al., 1987) and marine water ($\delta^{18}O$ = -1 ‰ V-SMOW; -31.0 ‰ V-PDB, Sheppard, 1986).

According to calculation based on Equation 5.1, if the calcite ($\delta^{18}O$ ranging from -4.8 to -13.9 ‰) precipitated from meteoric water, precipitation temperatures should range from 5 to 51 ˚C. For the marine water case, formation temperatures are higher, ranging from 32 to 95 ˚C. To determine from which of these porewaters the calcite cements precipitated, it is necessary to have other independent constraints on temperature. The minus cement porosity (MCP) pointcount values can be used to estimate the depth range and the temperature interval in which the concretions grew. Concretions from Miller reservoir show MCPs ranging from 21.4 to 40.6 % (Marchand, 2001). The burial depth can be estimated by applying the following equation (Baldwin and Butler, 1985):

$$D = 3.7\ ln\ [0.49/(1–S)] \quad (5.2)$$

Where D is burial depth (km) and S is solidity defined as volume of solid grains as a percent of total volume of sediment. Solidity can be calculated by subtracting MCP from one hundred percent. The above MCP values suggest burial depth between ~700 and ~3100 m. The present-day temperature gradient of the Miller Field is about 30 ˚C/km. The sediment-water interface (SWI) temperature of Late Jurassic in this area is estimated as 14 ˚C in a recent reservoir modelling study on the Snorre Field (Di Primio & Skeie, 2004), which is at 61˚ 33’ N, less than 3˚ further north to the Miller Field. Scotchman (1993) also used a constant geothermal gradient of 30 ˚C/km and seabed temperature of 20˚C for Outer Moray Firth area, ~140 km south of the Miller Field. Therefore, the above estimated burial depth gives a temperature interval of concretion growth between 35 and 107 ˚C, if sediment-water interface temperature of 14 ˚C is assumed.

Comparing the estimated precipitation temperatures from minus cement porosity with those from $\delta^{18}O$ values, it is obvious that a marine-type pore fluid fits well with the MCP data (Table 5.4). Hence, the calcite cements with high $\delta^{18}O$ signatures are more likely to have precipitated from marine water during early burial stage at ~ 700 m (~35 ˚C). Marchand (2001) and Marchand et al (2002) take the SWI temperature of 0 ˚C and argue that early formation water is largely influenced by meteoric water. However, a higher SWI temperature above 10 ˚C is more realistic for subtropic paleo-environment in Late Jurassic. Moreover, the temperature gradient of 30˚C/km is probably underestimated for the active rifting and stretching phases, as several studies suggest a high basement heat flow (80 mW/m^2) in rifting period and an exponential decrease of heat flow to present-day 55 mW/m^2 (McKenzie, 1978). The higher temperature gradient and seabed temperature during the Late Jurassic are even

less favourable for meteoric water. The initial pore fluid in the Brae Formation is more likely to a marine-type water.

Table 5.4 Calculated precipitation temperatures from maximum and minimum oxygen isotopic value and minus cement porosity. Calcite precipitation temperatures, assuming precipitation from meteoric and marine water, are calculated by using the Equation 5.1 (Friedman & O'Neil, 1977). Minus cement porosity values are from Marchand, 2001. Burial depths are calculated by using Equation 5.2 (Baldwin & Butler, 1985). Temperatures corresponding to the burial depths are based a temperature gradient of 30 ˚C/km and sediment-water interface temperature of 14 ˚C.

	$\delta^{18}O$ (‰)		T (˚C) for	T (˚C) for	Minus cement	Depth (m) based	T (˚C) based
	V-SMOW	V-PDB	meteoric water	marine water	porosity (%)	on MCP	on MCP
Early	26.00	–4.76	5	32	40.6	696	35
Late	16.57	–13.91	51	95	21.4	3066	107

Formation water evolution at a later stage has been discussed based on quartz cement oxygen isotopes together with fluid inclusion analyses in the study by Marchand et al (2002). A quartz cement zone with complex cathodoluminescent (CL) pattern which most likely precipitated between 70 ˚C and 90˚C shows $\delta^{18}O$ values between -15.0 ‰ and -12.3 ‰. The porewater from which these quartz cements precipitated, therefore, is suggested to be largely influenced by meteoric water ($\delta^{18}O$ of ~ -36.8 ‰) at ~70 ˚C. This requires a meteoric water flux to alter the initial sea water isotopic compositions. Another type of quartz of homogeneous CL pattern, with ^{18}O compositions from -14.5 to -5.0 ‰, postdates the complex CL-patterned quartz (from ~ 90 ˚C onwards) (Marchand et al., 2002). The high end of measured $\delta^{18}O$ compositions of ~ -5.0 ‰ suggests precipitation from a basinal fluid with heavy oxygen isotopes (~ -27 ‰) at temperatures of ~ 90 ˚C. A shift from a meteoric-type fluid to a basinal fluid (~ -27 ‰) at ~ 90 ˚C is suggested. This can be explained as sediments pass through the meteoric water flux zone and enter the depths where the basinal fluids from deep dominate the porewater. Due to homogenization or mixing with normal formation water, then, porewater $\delta^{18}O$ decrease to present-day value of -29.4 ‰ (Smalley and Warren, 1994) at temperatures about 120 ˚C. This decrease of $\delta^{18}O$ may also be associated with large-scale CO_2 charge. As the CO_2 from deep is likely to have isotopically light oxygen, the equilibrium between CO_2 and porewater is possible to reduce the $\delta^{18}O$ value of the porewater.

Based on the above discussion, a porewater evolution model for Miller reservoir can be established (Figure 5.16). Late Jurassic sea water (~ -31.0 ‰) dominated the initial pore fluid. Meteoric water infiltrated through open surface charge and reduced $\delta^{18}O$ values to ~ -36.8 ‰ at temperatures of ~ 70 ˚C. The porewater was heavily influenced by deep basinal

fluids at ~ 90 ˚C and $\delta^{18}O$ compositions of the porewater increased to as high as -27.1 ‰. Then, $\delta^{18}O$ values gradually decreased to the present-day value of -29.4 ‰ due to homogenizing with normal formation water or equilibrating with the CO_2 charge.

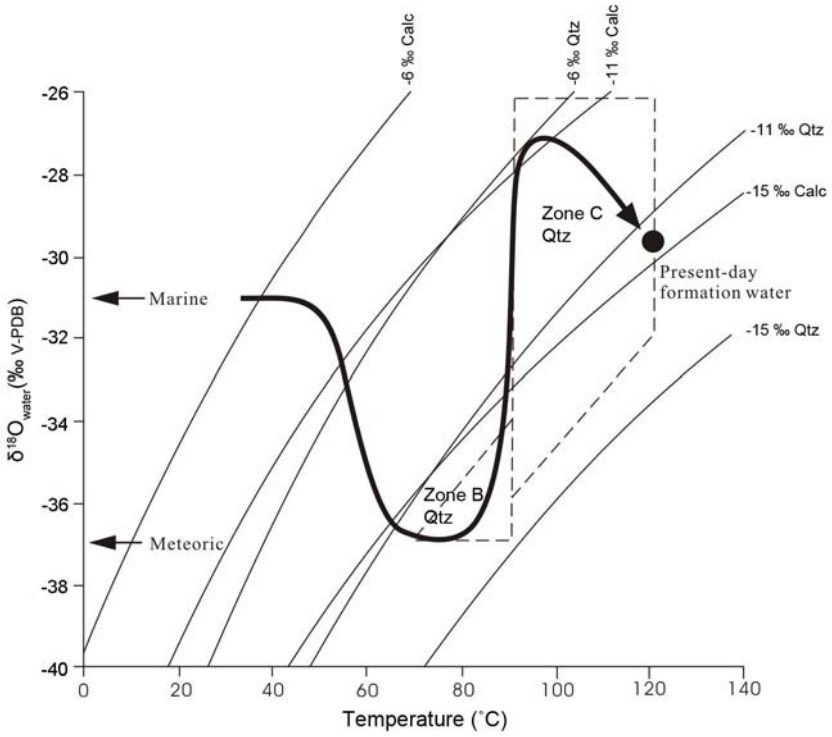

Figure 5.16 Porewater $\delta^{18}O$ evolution model of the Brae Formation, the Miller Field. Also shows oxygen isotope fractionation curves for calcite cement from -6 to -15 ‰ V-PDB and for quartz cement from -6 ‰ to -15 ‰ V-PDB. The black circle represents the present-day formation water $\delta^{18}O$. The early stage of the porewater evolution is constructed by $\delta^{18}O$ of calcite cements. The porewater $\delta^{18}O$ after 70 °C is mainly constrained by the $\delta^{18}O$ composition of the two generations of quartz cements outlined by the shaded areas (Modified after Marchand et al., 2002).

5.6.2. Carbon isotopes

Variations of $\delta^{13}C$ signatures of carbonate cements are more likely to be related to shift of carbon sources than temperature change because temperature effects on carbon isotopic fractionation are smaller than on oxygen isotopic fractionation. $\delta^{13}C$ value of the CO_2 source from which carbonates precipitated can be calculated from measured $\delta^{13}C$ of the carbonates by using isotopic fractionation equations. The following equation is for calculating isotopic fractionation of calcite-$CO_{2(gas)}$ (Deines et al., 1974):

$$1000\ln\alpha_{calcite\text{-}CO2(gas)} = 1.194(10^6 \cdot T^{-2}) - 3.63 \quad (5.3)$$

Note that $1000\ln\alpha_{calcite\text{-}CO2(gas)} \approx (\alpha - 1)\ 1000 \approx \delta^{13}C_{calcite} - \delta^{13}C_{CO2(gas)}$, where $\delta^{13}C_{calcite}$ is the measured carbon isotopic composition of calcite, $\delta^{13}C_{CO2(gas)}$ is the carbon isotopic composition of the CO_2 source. T is the temperature in Kelvin.

Carbonate cements in the Brae Formation exhibit highly variable carbon isotopic compositions, with a wide range from 7.9 to –10.8 ‰. High $\delta^{13}C$ values (7.9 ‰) suggest that methanogenesis (Me) of organic matter ($\delta^{13}C$ = 0-15 ‰) in the surrounding KCF shales had a significant influence during the early burial stage. Dissolution and reprecipitation of marine bioclasts ($\delta^{13}C$ = 0 ‰) may also have had a share in sourcing carbon, though there is little evidence of significant dissolution of shell fragments in the Brae Formation and the KCF. Sulphate reduction which occurs at shallower depth is responsible for abundant pyrite framboids in the overlying KCF. But there is no obvious evidence of sulphate reduction sourcing the earliest carbonates ($\delta^{13}C$ = -25 ‰) in the Brae Formation sandstones, which suggests that the cementation in the sandstones did not take place until the Me phase. Previous studies also note that development of diagenetic carbonates begins in the Me zone in areas of deeper burial such as the North Sea graben system (Scotchman, 1993), while, in the shallower buried section of the onshore UK KCF, diagenetic carbonates formed from SR to Me and D zone (Irwin et al., 1977; Scotchman, 1993).

Both $\delta^{13}C$ and $\delta^{18}O$ become increasingly negative (Figure 5.4), suggesting that precipitation took place in D zone with gradually waning Me zone conditions. It is found that, in some concretions, calcite cements at the concretion margins exhibit the most negative $\delta^{13}C$ and $\delta^{18}O$ values (Figures 5.17A and B) (Larter et al., 1995). Curtis (1978) suggests that decreasing C and O isotopes represents temperature increase and change of organic reactions during thermal maturation. In this case, the centres of concretions, which are sites of initial nucleation, have higher $\delta^{13}C$ values reflecting precipitation from methanogenesis carbon ($\delta^{13}C$ = 0 to 15‰). Progressive depletion of heavy isotopes from concretion centre to margin, therefore, represents heavier De zone influence. This is compatible with the decreasing minus cement porosity (MCP) values towards the concretion margins, which suggest calcite growth through a range of burial depth from ~700 (Me zone) to > 1000 m (D zone).

The rate of variation of $\delta^{13}C$ against $\delta^{18}O$ is constant through the trend. This suggests that carbon supply shifts smoothly from Me to D zone, probably suggesting a constant burial rate during precipitation, and that marine bioclasts was not an important carbon source (Scotchman, 1993).

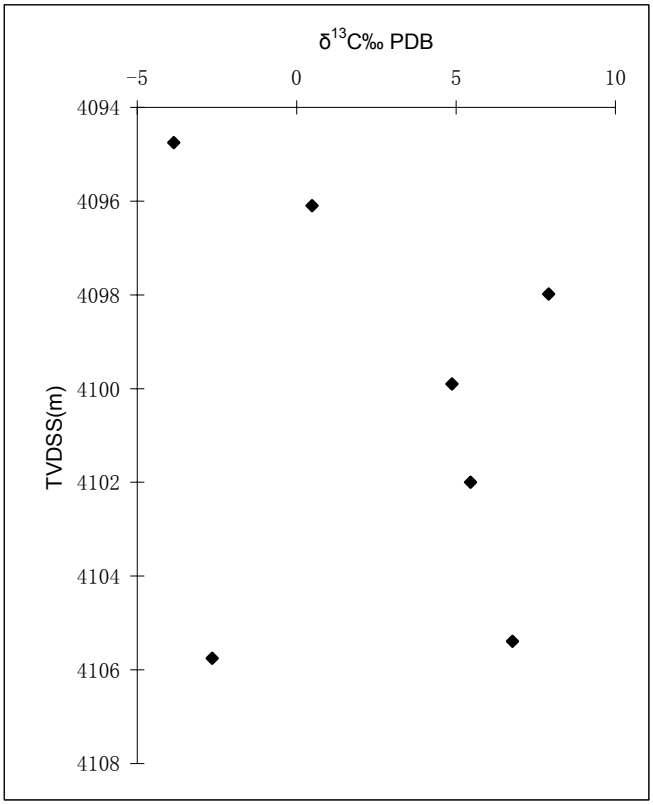

Figure 5.17A $\delta^{13}C$ versus depth across a concretion in well 16/8b-A10 (Larter et al., 1995).

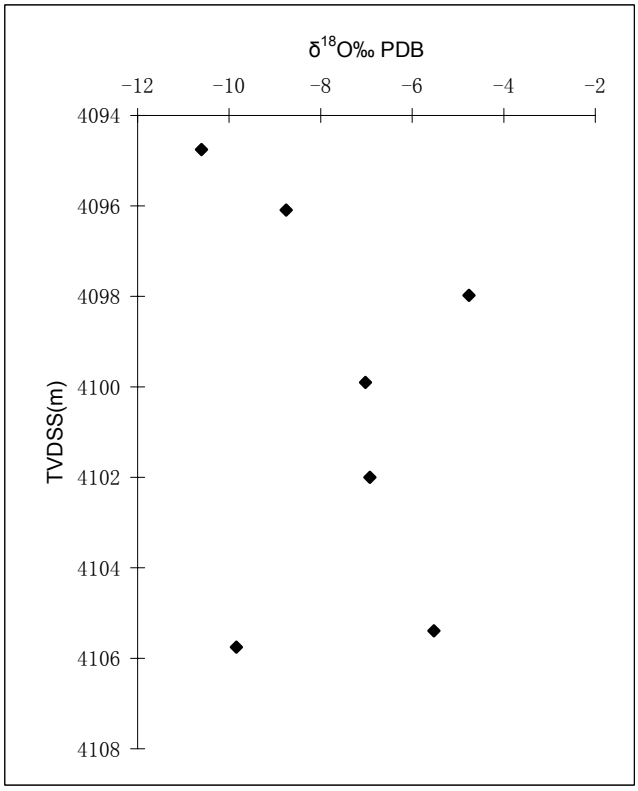

Figure 5.17B $\delta^{18}O$ versus depth across a concretion in well 16/8b-A10 (Larter et al., 1995).

It is worth noting that calcite concretions in the South Brae Field, ~10 km west to the Miller Field, have a similar $\delta^{13}C$ range from 3.6 to –11.7 ‰ (McLaughlin et al., 1994). The variation of $\delta^{13}C$ is also attributed to shift from fermentation to thermal decarboxylation of organic matter with certain degree of bioclasts influence. Calcite concretions display decreasing $\delta^{13}C$ values towards margins. These suggest that the reservoirs share a similar water and carbon source evolution during early burial.

5.7. Discussion – Isotopes of the KCF, well 16/8b-A2, the Miller Field

5.7.1. Comparison with the regional data

In Figure 5.5A, the regional trend from high to low $\delta^{13}C$ and $\delta^{18}O$ can be interpreted as precipitation gradually shifting from shallow Me zone to deeper D zone. The gradual decrease in $\delta^{18}O$ and $\delta^{13}C$ suggests declining Me zone influence combined with a possible input of marine carbonates sourced from dissolution of shell fragments (Scotchman, 1993; Scotchman et al., 2002).

The regional isotopic trend of the KCF shows similar ranges and pattern to those of the Brae Formation trend (Figure 5.4 and 5.5A). This indicates that carbonate cementation in the two formations shared the same carbon sources. It is well known that the diagenetic cement sequences in Upper Jurassic reservoir sandstones and those in the adjacent KCF mudrocks in the Northern and Central North Sea share striking similarities (e.g. Jeans and Fisher,1986; McLaughlin et al., 1994; Macaulay et al., 1997; Hendry et al., 2000b; Scotchman et al., 2002). Many hydrocarbon fields in this region show the similar carbonate isotopic trend for sandstones. These trends usually seen overlap those of the KCF. It is suggested that the organic acid generated in adjacent KCF mudrocks provides a bicarbonate source for cementation not only in KCF itself but also in the sandstones (Worden and Barclay, 2000; Scotchman, 1993; Scotchman et al., 2002). A strong link between mudrock diagenesis and sandstone cementation can be demonstrated with migration of the pore fluids responsible for the carbonate/silicate cements both in mudrock and adjacent sandstones (Worden and Barclay, 2000).

The isotopes of this study exhibit narrow ranges compared with the regional data (Figure 5.5A). The small ranges of $\delta^{18}O$ and $\delta^{13}C$ values may be due to the limited sampling interval (< 40 m). Only a small part of the porewater evolution may be recorded by the samples. The data of the two wells show generally low $\delta^{18}O$ and $\delta^{13}C$, falling on the lower half of the regional trend. The missing high $\delta^{18}O$ with positive $\delta^{13}C$ values suggests that carbonate

precipitation initiated at deeper burial depth.

5.7.2. Difference between shale and silt/sand isotopes in the KCF, the Miller Field

The KCF shale samples show generally higher $\delta^{13}C$ and $\delta^{18}O$ values than the silt/sand samples (Figure 5.5B). The heavier isotopes in shale may indicate earlier growth (lower precipitation temperature). In general, organic acids generated from maturing organic matter, largely in mudrocks, provide carbon source for carbonate precipitation in mudrocks and adjacent sandstones (Worden and Barclay, 2000; Scotchman, 1993; Scotchman et al., 2002). Carbonate precipitation may have occurred earlier in the shales because bicarbonate was first generated there. Due to slow diffusion of bicarbonate, carbonate growth in silt/sand beds may occur later, therefore, under higher temperatures. Furthermore, lack of nucleus for diagenetic carbonate growth may also hinder precipitation in silt/sand beds.

In well 16/8b-A2, the difference of 2.7 ‰ between average $\delta^{13}C$ of shale and silt/sand requires a temperature increase of ~ 50 ˚C if temperature variation is solely responsible. However the difference of average $\delta^{18}O$ between the two data sets is only 0.73 ‰ which represents a temperature increase of ~5 ˚C. Therefore, it is unlikely that temperature increase is the main cause of the $\delta^{13}C$ difference. The shift of carbon source from methanogenesis zone (0 to +15 ‰) to decarboxylation (–20 ‰) can be a more important factor for the $\delta^{13}C$ difference. The lighter carbon compositions of silt/sand samples represent the larger influence of decarboxylation.

High carbon isotopic compositions in the shales may also suggest a larger portion of bicarbonate sourced from marine bioclasts ($\delta^{13}C$ of near zero ‰). KCF shales contain large amounts of organic matter which, during dissolution, might contribute considerable amount of carbon with $\delta^{13}C$ of near zero ‰. Local supply of this type of carbon increases $\delta^{13}C$ of the carbon source and the carbonates precipitated from it.

5.7.3. Porewater evolution in the KCF

The KCF samples of well 16/8b-A2, the Miller Field, show much smaller ranges of $\delta^{18}O$ (from -6.1 to -13.7 ‰) and $\delta^{13}C$ (from -0.65 to -10.8 ‰) than the Outer Moray Firth data do. Positive $\delta^{13}C$ values from 0 to 10 ‰ with relative high $\delta^{18}O$ from -5 to 2 ‰ are not present, suggesting that the carbonates in the sampling interval precipitated in a deeper diagenetic regime (D zone). Me zone pore fluid chemistry was probably not conducive for precipitation.

If these carbonates precipitated from Jurassic marine water with $\delta^{18}O$ value of –1.0 ‰ V-SMOW, the precipitation temperatures would range from 43 to 98 ˚C, which is within the D zone. If the carbonates precipitated from meteoric water, the precipitation temperatures would range from 14 to 53 ˚C, cooler than the D zone. Hence, the majority of the carbonates are likely to have precipitated from marine water and decarboxylation carbon source. Furthermore, unlike in the Brae Formation, meteoric water cannot be easily invoked due to the marine settings with both a lack of subaerial exposure of the KCF at the end of Jurassic or close juxta-position of suitably exposed fault blocks (Scotchman et al., 2002). The marine water may have dominated the pore fluid of the KCF for a longer period.

5.7.4. Influence of the CO_2 accumulation in reservoir

One of the main tasks of this study is to identify any carbonates that might be associated with the CO_2 accumulated in the Miller reservoir. If the CO_2 charge had produced carbonates in the reservoir and the seal, they would bear distinguishable isotopic signatures. Given that the carbon isotopic compositions of the CO_2 and porewater $\delta^{18}O$ in the reservoir are known, the isotopes of associated carbonates can be estimated. Present-day CO_2 in the Miller reservoir has an average $\delta^{13}C$ value of -8.2 ‰ (Baines and Worden, 2004). It is assumed that the CO_2 has maintained the same isotopic composition since its emplacement. The pore water evolution in the Brae Formation has been summarized above. Thus, an estimated C and O isotope curve for precipitation from 70 to 120 °C is made and projected in Figure 5.5B. The data points falling on the curve represents the possible carbonates precipitated from the CO_2 charge. It is found that most of the shale data from the reservoir section and immediately (1m) above the reservoir in the Miller well sit on or near the curve. This implies that these carbonates are in equilibrium with the CO_2 accumulation. Most data further up in the overlying KCF are away from the prediction curve, indicating weak influence of the CO_2.

The reservoir sandstones do not show any isotopic signatures of association with the CO_2 charge (Figure 5.4). As it has been discussed, those concretions and pervasive cements precipitated much earlier and were controlled by depth-related reactions of organic material. The lack of footprint of the reservoir CO_2 may be due to the large quantity of the pre-existing carbonates which overwhelms possible carbonates related to the CO_2.

5.7.5. $\delta^{13}C$ versus depth for shale samples

The distinctive linear trend in Figure 5.6 requires a sound interpretation for its formation. The data reveal several key elements. Firstly, no systematic lithologic heterogeneity was

observed in the drill cores and wireline logs in the 12 m interval above reservoir in the Miller well; and isotopes do not support that such an anomalous zone also exist within the low-CO_2 control well. Therefore, the possibility that the anomalous zone is a primary depositional feature was dismissed. It is suggested to be related to the presence of the CO_2 accumulation in the underlying reservoir.

Secondly, in neither the anomalous zone (except at the very base), nor in the overlying zone, are the carbonates reset to equilibrium with the CO_2 in the reservoir ($\delta^{13}C$ = -8.2‰). The carbonate isotope data above the anomalous zone have an average $\delta^{13}C$ = -5.3‰, simply explained as conventional authigenic carbonates which precipitated from sulphate reduction ($\delta^{13}C$ = -25 ‰) and methanogenesis (0 – 15 ‰) of organic matter during early burial (Irwin et al., 1977). If large quantities of free-phase CO_2 from the reservoir had penetrated above the anomalous zone, then isotopic resetting of these carbonates would have occurred, to result in a vertical profile of constant $\delta^{13}C$ values. Hence, it is concluded that the top of the anomalous zone represents the limit of vertical CO_2 penetration. However, simple mass-balance calculation suggests that dissolved CO_2 is not present in sufficient quantities to produce the isotope trend observed in the anomalous zone. This is because of the low solubility of CO_2 in water under the oilfield conditions (Enick and Klara, 1990; Kohl and Nielsen, 1997). Thus, free-phase CO_2 must be involved within the anomalous zone. It is concluded that limited quantities of free-phase CO_2 have penetrated the anomalous zone.

Thirdly, the quantity of carbonates present within the anomalous zone is slightly smaller (range from 0.17 to 3.1%; average 1.48%) compared to the overlying zone (range from 0.5 to 2.8 %; average 1.66%). This means that the pre-existing conventional authigenic carbonate within the anomalous zone has not been ‘swamped’ by abundant growth of younger carbonate. The linear carbon isotope trend must therefore have been formed by dissolution of conventional carbonate, followed by growth of younger carbonate containing a partial signature from the penetrating CO_2. I attribute dissolution to the initial acidifying effects of the free-phase CO_2, and consider this to be further evidence that such CO_2 has only penetrated into the anomalous zone, and not the overlying unaltered zone.

Next, the timing of CO_2 charge can be estimated using the C isotope ratios of the carbonates sampled from mudrocks of the reservoir section. The highest $\delta^{13}C$ values in the reservoir, ranging from -0.65 to -1.6‰, are in equilibrium with the reservoired CO_2 at ~60-70°C. This suggests that the CO_2 charge was emplaced at about ~70-80Ma, according to the burial curve

of the Miller Field (Figure 2.9) (Marchand et al., 2001). The carbonate at the bottom of the anomalous zone ($\delta^{13}C$ = -0.77 to -1.7‰) is also in equilibrium with that CO_2 at similar temperatures. It is hence deduced that CO_2 started penetrating into the seal immediately after its emplacement. Penetration of the mudrock seal has continued progressively since that time.

Lastly, the large $\delta^{13}C$ range within the anomalous zone (-0.77 to -7.4‰) eliminates temperature as the sole control, because a 60 °C variation could only produce ~3‰ difference in $\delta^{13}C$ value of precipitated carbonates. Carbon models with linearly variable carbon isotopic compositions with depth must be considered.

Two models are present for the formation of carbonates in the anomalous zone mudrocks. The first one involves three carbon sources; the second involves Raleigh fractionation of the infiltrating CO_2.

Table 5.5 Conditions of the three carbon source model (1 m interval). Presented here are abundances of the three sources in the rock, $\delta^{13}C$ of the mixed source, precipitation temperature of present-day carbonate and its $\delta^{13}C$ values. The $\delta^{13}C$ values of the new carbonate are projected against depth in Figure 5.19.

Depth (m)	Source 1 (g/cm3) ($\delta^{13}C$ ~ -7.9 ‰)	Source 2 (g/cm3) ($\delta^{13}C$ ~ -5.3 ‰)	Source 3 (g/cm3) ($\delta^{13}C$ ~ -20 ‰)	$\delta^{13}C$ of Mixed C (‰)	Precipitation T (°C)	$\delta^{13}C$ of New Cc (‰)
3971	0.01125	0.005	0.00875	-11.62	120	-7.52
3972	0.01188	0.005	0.008125	-11.32	118.1	-7.15
3973	0.0125	0.005	0.0075	-11.01	116.2	-6.77
3974	0.01313	0.005	0.006875	-10.71	114.3	-6.39
3975	0.01375	0.005	0.00625	-10.41	112.4	-6.01
3976	0.01438	0.005	0.005625	-10.11	110.5	-5.62
3977	0.01500	0.005	0.005	-9.80	108.6	-5.24
3978	0.01563	0.005	0.004375	-9.50	106.7	-4.86
3979	0.01625	0.005	0.00375	-9.20	104.8	-4.47
3980	0.01688	0.005	0.003125	-8.90	99.0	-3.91
3981	0.0175	0.005	0.0025	-8.59	93.2	-3.33
3982	0.01813	0.005	0.001875	-8.29	87.4	-2.74
3983	0.01875	0.005	0.00125	-7.99	81.6	-2.13
3984	0.01938	0.005	0.000625	-7.69	75.8	-1.51
3985	0.0200	0.005	0.0000	-7.38	70.0	-0.87

Three carbon source model

In the anomalous zone, three carbon sources could have influenced precipitation of the present-day carbonates. The first source is free-phase CO_2 infiltrated into the seal from the reservoir ($\delta^{13}C$ = -8.2‰), which triggers the dissolution of pre-existing carbonates. Its

abundance decreases upwards to zero at the top of the anomalous zone. The dissolved original carbonates form the second carbon source, with an average $\delta^{13}C$ = -5.3‰. Its abundance is assumed constant. The third source is the thermal decarboxylation of organic matter ($\delta^{13}C$ = ~-20‰; Irwin et al., 1977) the abundance of which increases as burial temperature progressively increases. Mixing of these three individual carbon sources at systematically varying ratios results in a source with linearly varying isotopic compositions, which produces the linear isotopic trend.

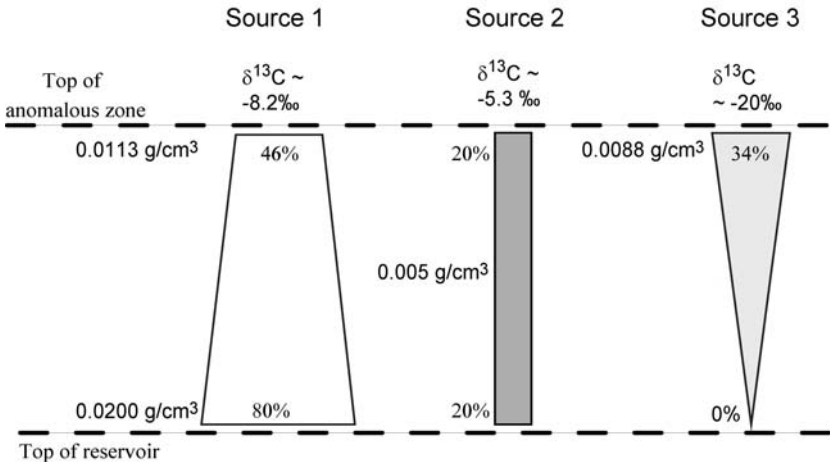

Figure 5.18 Illustration of the three carbon source model. Within the anomalous zone are illustrated three carbon sources, with distinct isotope signatures (-8.2 ‰ is the anomalous charge of free phase CO_2; -5.3 ‰ is conventional shallow burial carbonate cement pre-dating CO_2 influx; -20 ‰ is conventional decarboxylation of organic kerogen, controlled by temperature). Linear mixing of these three sources with increasing temperature from 70 to 120 °C reproduces an excellent match to observed isotopic analyses.

The model is illustrated in Figure 5.18. The model conditions at 1 m interval are presented in Table 5.5. From the bottom to the top of the anomalous zone, the percentage of the first carbon source linearly decreases from 80 to 46% (0.02 to 0.01175g/cm^3); the second provides 20% (0.005 g/cm^3, as average amount of the original carbonates is about 1.6%); the third increases from 0 to 34% (0 to 0.00825g/cm^3). The mixed source would have $\delta^{13}C$ values linearly decreasing from -7.4 to -11.6‰. Precipitation initiated at 70°C at the bottom of the anomalous zone; the precipitation front is steadily moving, to reach the current top at the present-day reservoir temperature of 120°C. Due to the change in depositional rate, burial temperature increased faster during 70 and 40Ma (increasing rate ~ 1.17°C/Ma) than from 40 Ma to present-day (0.38°C/Ma) (Marchand et al., 2001), which explains the slight curve of the observed isotopic trend. This model delivers an excellent match to the measured linear isotope ratios (Figure 5.19). The CO_2 infiltration rate is estimated as an average of 9.8×10^{-7} g.cm^{-2}.y^{-1} over 70 million years.

Raleigh fractionation model

Another model for the linear trend of $\delta^{13}C$ versus depth is Raleigh Fractionation. In this model, the upwards decrease of carbon isotopes in the anomalous zone is explained by gradual depletion of infiltrated CO_2 from the reservoir, the main carbon source, due to continuous precipitation of the new carbonate. It considers the dissolved pre-existing carbonates, but not the source derived from thermal decarboxylation. The free-phase CO_2 infiltrated into the anomalous zone and dissolved the original carbonate. This provided a mixed carbon source for precipitation of the present-day carbonate.

Table 5.6 Conditions of Raleigh fractionation model (1 m interval). The amount of carbon source at each interval is determined by the fixed amount of infiltrated CO_2 (2.5 g/cm^2) plus dissolved original carbonate (0.5 g/cm^2) and minus precipitated new calcite (Cc) in one meter interval. The isotope ratio of the carbon source is determined by adding supply from dissolved original carbonate with $\delta^{13}C$ = -5.3 ‰ and subtracting new carbonate with varying $\delta^{13}C$ value.

Depth (m)	Amount of C Source (g/cm^2)	$\delta^{13}C$ of C source (‰)	Precipitation T (°C)	New Cc (C equiv.) g/cm^2)	$\delta^{13}C$ of New Cc (‰)
3971	1.64	-11.56	120.0	0.88	-7.47
3972	1.99	-11.21	118.1	0.84	-7.04
3973	2.29	-10.89	116.2	0.81	-6.64
3974	2.56	-10.59	114.3	0.77	-6.26
3975	2.79	-10.30	112.4	0.73	-5.90
3976	2.98	-10.04	110.5	0.69	-5.56
3977	3.14	-9.79	108.6	0.65	-5.22
3978	3.25	-9.55	106.7	0.62	-4.90
3979	3.33	-9.32	104.8	0.58	-4.59
3980	3.37	-9.07	99.0	0.54	-4.08
3981	3.37	-8.81	93.2	0.50	-3.54
3982	3.34	-8.52	87.4	0.46	-2.96
3983	3.26	-8.20	81.6	0.43	-2.34
3984	3.15	-7.85	75.8	0.39	-1.68
3985	3.00	-7.47	70.0	0.35	-0.96

Due to isotopic fractionation, the precipitated carbonate bears higher carbon isotope ratios than the carbon source. If the amount of carbon source is relatively limited in quantity compared to the amount of carbonate product, the residual carbon would become more and more depleted in ^{13}C. This is so-called Raleigh fractionation. The precipitation front gradually moved upwards to reach the top of the anomalous zone at the present-day reservoir temperature of 120°C. Hence, the carbonate precipitated from the carbon source gradually depleted in ^{13}C would show the upwards decrease of $\delta^{13}C$.

In this model, the infiltrated free-phase CO_2 amounts to 9.2 g/cm^2 (2.5 g/cm^2 carbon

equivalent). When it moves up, it dissolves original carbonate (0.005 g/cm^3 carbon equivalent) while precipitates new carbonate with linearly upwards increasing quantity (0.0035 to 0.0088 g/cm^3 carbon equivalent). The detailed model conditions at 1 m interval are shown in Table 5.6. The results also match very well with the isotopic trend (Figure 5.19). The infiltration rate is 1.3×10^{-7}g.cm^{-2}.y^{-1}, at the same order as the estimate of the first model. Both models suggest that minimal reservoired CO_2 has passed above the anomalous zone mudrock.

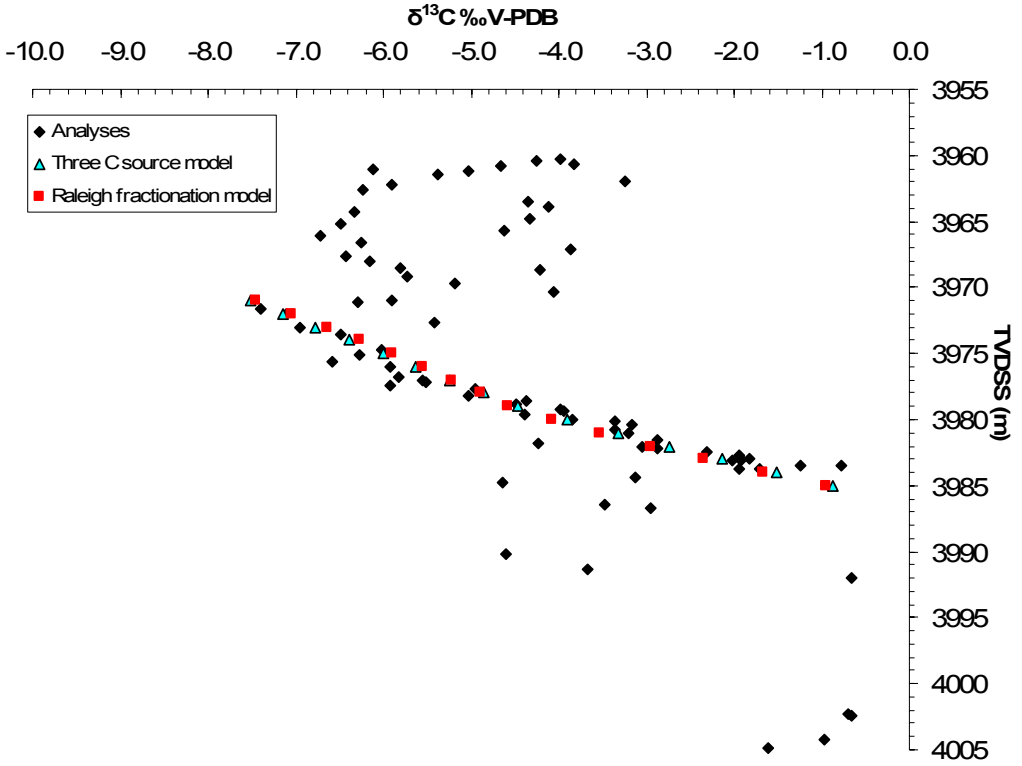

Figure 5.19 Results for three carbon source model (green triangles) and Raleigh fractionation model (red squares).Both showing excellent match to the analyses. The details of model conditions are presented in Table 5.5 and 5.6, respectively.

Though the Raleigh fractionation model can also explain the observed isotopic trend, it is thought to be less favourable than the former model because it cannot match measured inorganic carbon abundances in the anomalous zone while it produces good fit to the isotopes of the new carbonate. Table 5.6 presents the best fit conditions, but the amount of new carbonate in the model is generally higher than the measurements of inorganic carbon abundance in Figure 5.14 and Table 5.3.

In the three carbon source model, the amount of new precipitation is not constrained by the model itself. The downwards decrease of carbonate abundance within the anomalous zone can be interpreted as a downwards decrease of the abundance of cations, i.e. Ca and Mg ions during carbonate reprecipitation. The cation concentrations within the aqueous pore fluids of the Brae Formation sandstones would be very low due to the gaseous CO_2 charge. Cations would tend to diffuse from the overlying seal into the reservoir sandstone, where their concentrations are greatly depressed by the CO_2 accumulation. The decrease of the abundance of new carbonate within the anomalous zone is hence interpreted as the result of cation scavenging by the CO_2-rich reservoir sandstones.

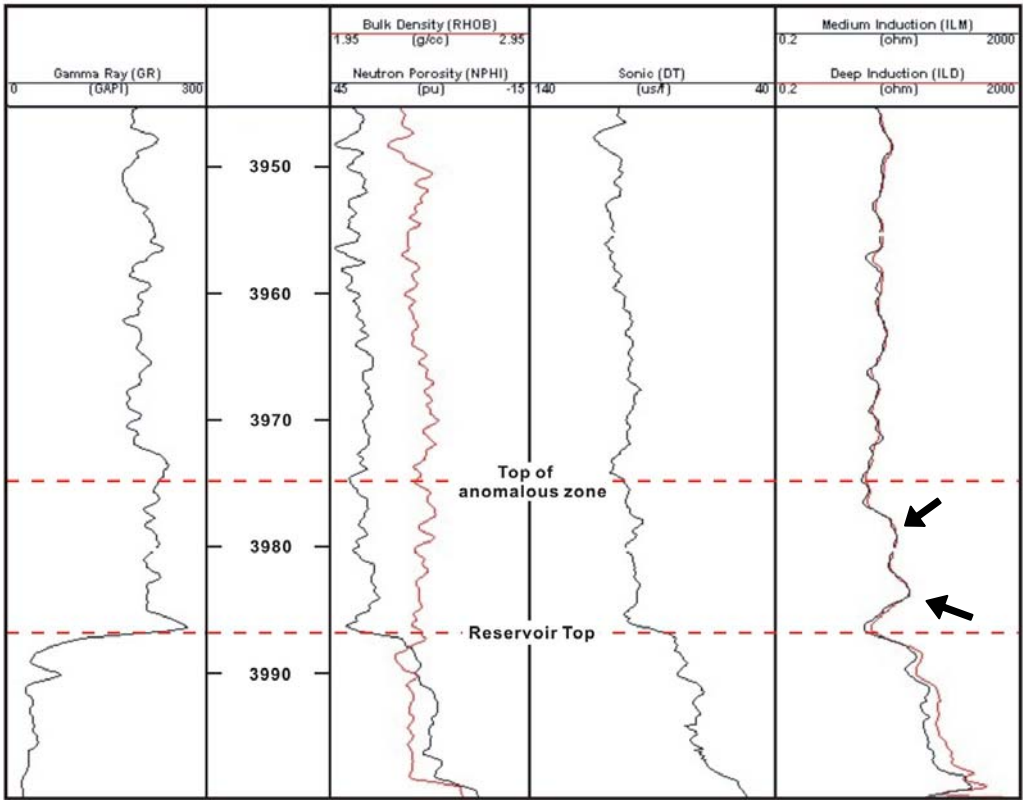

Figure 5.20 Gamma ray, density, neutron, sonic and resistivity logs through the reservoir top, well 16/8b-A2, the Miller Field. The resistivity logs (the most right ones) show high resistivity values in the anomalous zone (marked by the arrows), indicating infiltrated CO_2 replacing porewater.

Evidence of CO_2 infiltration in wireline logs

The wireline logs, including gamma ray, bulk density, neutron, sonic and resistivity logs through the anomalous zone, do not show systematic variations to indicate lithologic variations (Figure 5.20).

The gamma ray log shows a slight drop in radioactivity at ~15 m above the reservoir top, this

may be simply due to variation in the organic content. However, the resistivity logs show relatively high resistivity values in the anomalous zone (the most right logs, Figure 5.20). As free-phase CO_2, similar to hydrocarbons, is infinitely resistive, the high resistivity values may indicate a CO_2-infiltrated zone, where free-phase CO_2 from the reservoir replaced the original formation water and increased formation resistivity. The Medium and Deep resistivity curves show no separation between them in the anomalous zone. This is probably due to the fact that the invasion of mud filtrate into mudrock is negligible and did not result in differentiated resistivity around the bore hole in this case.

5.7.6. $\delta^{13}C$ versus depth for silt/sand samples

The silt/sand samples of the KCF in the Miller well display a similar pattern in the plot of $\delta^{13}C$ versus depth (Figure 5.7). A linear trend of $\delta^{13}C$ values on depth can be observed overlying the reservoir. However, there are some interesting differences from the shale data. The anomalous zone is thinner (~ 5 m) than that of the shale samples (~ 12m). The two trends show similar $\delta^{13}C$ range of about 6.7 ‰ between two ends, therefore, carbon isotope ratios vary greater with depth in silt/sand (-1.3 ‰ /m) than in shale (-0.5 ‰ /m). What is more, the silt/sand data have generally lower $\delta^{13}C$ values (ranging from -3.2 ‰ to -9.1 ‰) than the shale samples (from -0.77 to -7.4 ‰). The average $\delta^{13}C$ of silt/sand is –7.0 ‰ comparing to -4.3 ‰ of shale.

The lower isotopes of silt/sand can be interpreted as a smaller portion of carbon sourced from original marine bioclasts ($\delta^{13}C$ = ~ 0 ‰). As it has been suggested above, the pre-existing carbonates in the anomalous zone had been dissolved by free-phase CO_2 infiltration from the reservoir and provided carbon for precipitation of present-day carbonates. Marine bioclasts should have imposed an influence on the isotopes of the carbon source. Lower $\delta^{13}C$ values samples may represent less bioclast influence in silt/sand lithologies.

The difference in thickness of the anomalous zones may be due to differentiated advancing of the front of carbonate dissolution and reprecipitation in different lithologies. The silt/sands contain larger amount of original carbonate than the shales. According to XRD mineralogical data, the silt/sand samples contain as much as 25 wt % of carbonates above the anomalous zone, while average carbonate abundance is only 1.7 wt % (calcite equivalent) in the shales where the dissolution/precipitation front has advanced to 12 m above reservoir. In silt/sand beds, significant amount of remaining original carbonates may still exist above the 5 m anomalous zone because of higher abundance of the original carbonates, even though the

CO_2 infiltrating front has passed. Thus, the characteristic isotopic trend of new carbonates is only visible in the 5 m zone where original carbonate had been completely dissolved, and is obscured by remaining original carbonates above the 5 m zone. Even within the 5 m zone, the trend is not as clear as that of shale data. This may also be due to remaining of old isotopic signatures.

5.7.7. Geochemical modelling

Both three component model and Raleigh fractionation model require a complete dissolution of the original carbonates in the anomalous zone followed by reprecipitation of present-day carbonates. To demonstrate the possibility of this scenario, geochemical modelling was applied using Geochemist Workbench (GWB).

In the modelling, a virtual cap rock is composed of certain amount of minerals based on XRD mineralogy of the KCF shales. One kilogram of formation water of the Miller reservoir is used as the initial system into which a certain amount of the virtual rock is gradually added as reactant. The same modelling was run with the formation water from the Brent field (a low-CO_2 field) as a comparison. Table 5.7 gives the details of the initial water and mineral input. Precipitation of dawsonite and siderite is suppressed, since neither of them was observed in the rock samples. Eh is set at -0.1 volts because the KCF shales contain a high organic content which produces acids to keep the reaction environment reductive.

Four scenarios were modelled at 70 °C (Table 5.8). Scenario A and B starts with the Miller formation water. Four grams of CO_2 is added as reactant in Scenario A while Scenario B was run without CO_2. The formation water of the Brent Field (low CO_2 field) was used in Scenario C and D with the same conditions.

The carbonate reaction paths of the four runs are present in Figure 5.21. Both Figures 5.21A and 5.21B show initial decrease of calcite and dolomite followed by increase of both. This suggests that the Miller formation water with high bicarbonate concentration is able to dissolve carbonate minerals in the KCF shale at the early stage and reprecipitate them afterwards. During modelling, bicarbonate becomes saturated after initial dissolution of carbonates and reprecipitation follows. CO_2 added into modelling increases bicarbonate concentration, therefore reduces the capacity of dissolving and increases the amount of reprecipitation.

The Brent formation water produces different reaction paths. In Scenario C and D (Figure 5.21C, D), dolomite increases slightly in the early reaction stage and stay constant afterwards, while calcite decreases through the whole process. This water shows much lower capacity of dissolving calcite, which is due to its lower bicarbonate concentration (~1050 mg/l). This further suggests that the high HCO_3^- concentration resulted from high CO_2 content is the main drive for initial carbonate dissolution and reprecipitation. This supports the above models to explain the anomalous zone in the seal. It is found that increasing temperature of reaction increases the amount of carbonate precipitation, but does not change the reaction paths significantly.

Table 5.7 Details of the initial waters chemistry and mineral reactants used in the geochemical modelling. The water analyses of the Miller and Brent Field are taken from Smalley and Warren (1994) and Warren and Smalley (1994) respectively. Proportions of the minerals are based on XRD mineralogical analyses of KCF shale samples in the Miller wells.

Fluid analysis (mg/l)	Na	K	Mg	Ca	Sr	Ba	Fe	Cl	SO_4	HCO_3
Miller (High CO_2)	28 780	1830	115	1060	110	1050	14	47 660	8	2090
Brent (Low CO_2)	9000	200	50	250	25	60		14 300	10	1050

Mineral reactants (g)	Quartz	K-feldspar	Albite	Pyrite	Illite	Kaolinite	Calcite	Dolomite
KCF shale	80	6	1.5	8	60	30	1	0.4

Table 5.8 Modelling input for the four scenarios. Water geochemistry and the mineral reactants see Table 5.7.

Model	Initial water	Mineral reactants	CO_2 reacted (g)
A	Miller	KCF shale	4
B	Miller	KCF shale	0
C	Brent	KCF shale	4
D	Brent	KCF shale	0

5.7.8. $\delta^{18}O$ versus depth

The Miller well also shows linear trends of $\delta^{18}O$ against depth (Figures 5.8 and 5.9). $\delta^{18}O$ values increase upwards, rather than decrease, in the anomalous zones. The thickness of the anomalous zones is also different for shale and silt/sand data. Though the $\delta^{18}O$ anomalous zones help in confirming the existence of the CO_2 breaching zone, they are very difficult to explain.

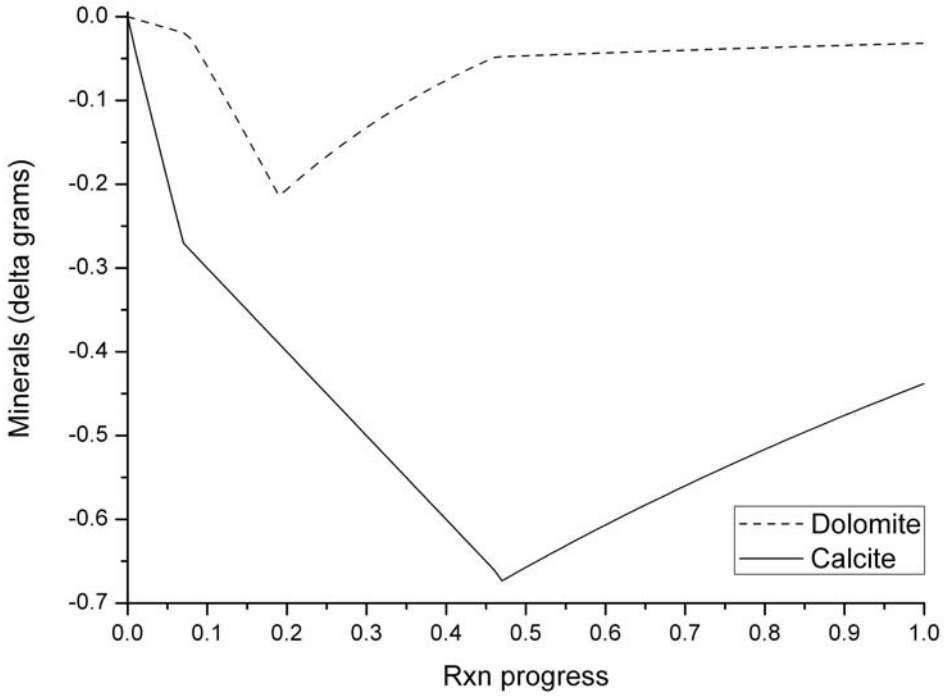

Figure 5.21A Carbonates reaction path for Scenario A. KCF shale reacts with Miller formation water. 4 g CO_2 is added into the reactants.

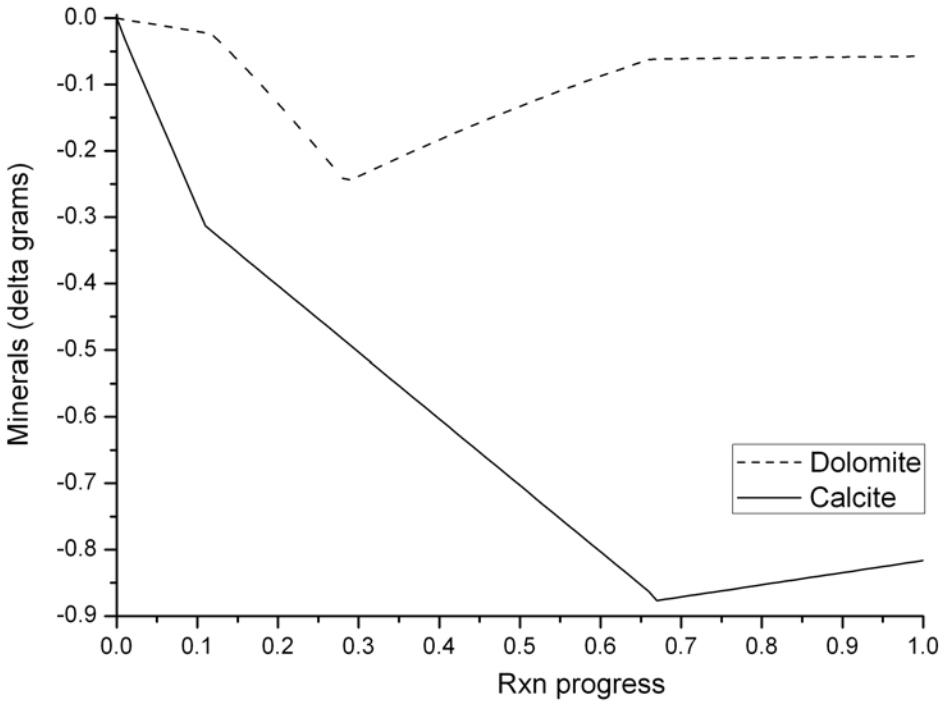

Figure 5.21B Carbonates reaction path for Scenario B. KCF shale reacts with Miller formation water. No CO_2 is added into the reactants.

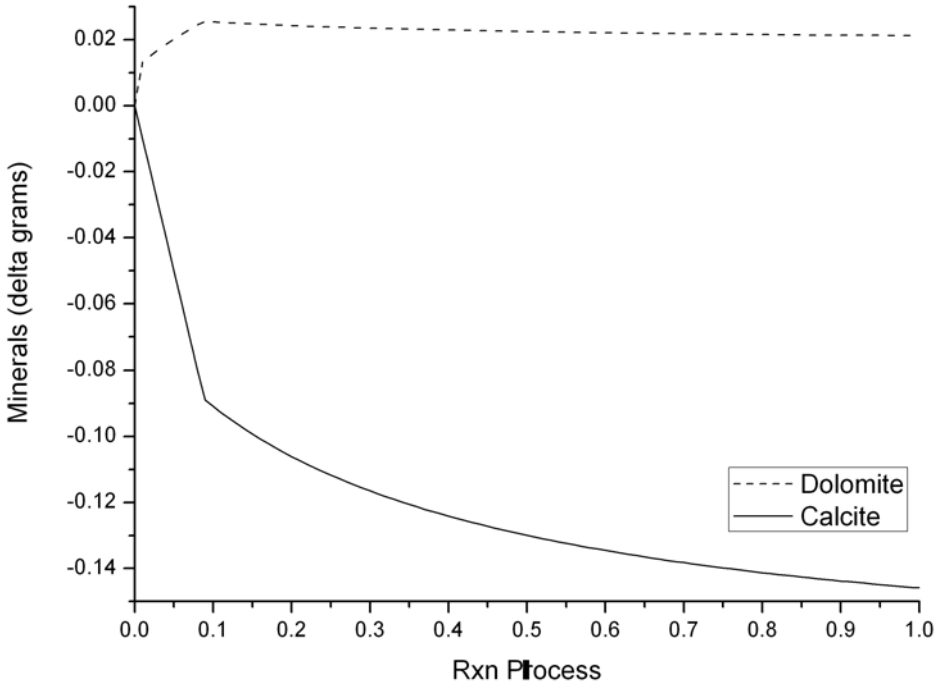

Figure 5.21C Carbonates reaction path for Scenario C. KCF shale reacts with Brent formation water. 4 g CO_2 is added into the reactants.

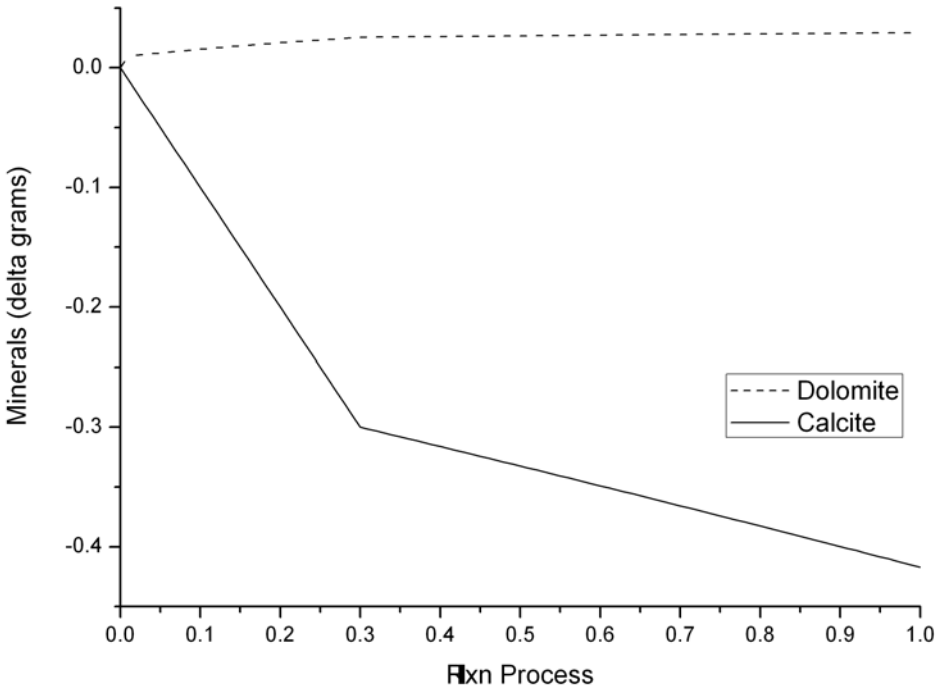

Figure 5.21D Carbonates reaction path for Scenario A. KCF shale reacts with Brent formation water. No CO_2 is added into the reactants.

The upwards enriching rather than depleting in $\delta^{18}O$ excludes the effect of Raleigh fractionation of oxygen isotope. Oxygen isotope fractionation between carbonate and water would lead to a gradual depletion of ^{18}O in residual porewater. A decreasing upwards $\delta^{18}O$ profile in the anomalous zone should be expected if significant Raleigh fractionation had occurred. Moreover, the amount of porewater as oxygen source is much larger than relative to carbonate precipitation, the effect of Raleigh fractionation of oxygen isotope should be insignificant.

The $\delta^{18}O$ trends cannot be explained by increase of precipitation temperature, either. Higher temperatures lead to low $\delta^{18}O$ of precipitation. As has been discussed above, the carbonate precipitation front moved upwards in the anomalous zone. New carbonates at shallower depths should show lower $\delta^{18}O$, which contrasts with the analyses.

Therefore, the $\delta^{18}O$ trends are likely to be mainly controlled by porewater evolution. The formation water of Brae Formation at the Miller Field was heavily influenced by meteoric water ($\delta^{18}O$ = -36.8 ‰) at ~ 70 ˚C. Later basinal water influx elevated the $\delta^{18}O$ value of formation water to -27 ‰. Then it slightly decreases to present-day value of -29.4 ‰. This major increase of $\delta^{18}O$ in the late burial stage may have resulted in the increase of $\delta^{18}O$ in the anomalous zones. However, in shale data (Figure 5.8), the $\delta^{18}O$ values ranging from -12.8 to -7.9 ‰ are not consistent with precipitation from the porewater from 70˚C (~ –36.8 ‰) to 120 ˚C (-29.4 ‰), which should have produced $\delta^{18}O$ ranging from -16.1 to -14.3 ‰. The analyses are too high to be explained by precipitation in such a temperature window.

5.8. Isotopes of well 9/28b-17, the control well

Though carbon and oxygen isotopes of the KCF carbonates in the control well are slightly heavier than those of the Miller well, the data still lie on the regional isotopic trend (Figure 5.5A), indicating that the pore fluid evolution in this area is not significantly different from the regional porewater evolution. The heavier oxygen isotopic compositions may be a result of slightly higher precipitation temperatures.

The plots of carbon isotope against depth (Figures 5.10 and 5.11) do not show the distinct patterns that the Miller well data show. No linear isotopic transitions can be seen above reservoir, except in Figure 5.10 where an upwards decrease of $\delta^{13}C$ seems to above reservoir. But correlating statistics shows very low linear correlation coefficient (R^2=0.18), indicating that the linear trend is poorly confined. Furthermore, the majority of the $\delta^{13}C$ values in

reservoir lie in the middle of the range, with only one data point sitting at the right end of the range. The silt/sand data from the control well do not show any isotopic lineation (Figure 5.11). In simple terms, all the data show no evidence of unusual carbon and oxygen events. Thus, this confirms that the linear isotopic trends in the Miller well are unique features which are related to free-phase CO_2 infiltration.

5.9. Conclusions

- Very interesting patterns are observed in the plots of $\delta^{13}C$ versus depth for both shale and silt/sand samples from well 16/8b-A2, the Miller Field. Both plots (Figures 5.6 and 5.9) exhibit a linear trend immediately above the reservoir section with the rest of the data scattering around the two ends of the trend. Such trends are absent from the control well, where CO_2 is not abundant. It is suggested that the trends are due to the infiltration of free-phase CO_2 from the underlying reservoir, causing the dissolution of pre-existing authigenic carbonate minerals, and then reprecipitation to incorporate small quantities of infiltrating CO_2.

- Isotope $\delta^{13}C$ ratios in the reservoir and the bottom of the KCF, have recorded the earliest CO_2 presence in the reservoir, giving an estimate of first CO_2 charge and infiltration at 70 – 80 Ma. The carbonates above the anomalous zone show no influence of the reservoir CO_2, indicating the limit of the CO_2 infiltration.

- The amount of CO_2 infiltrated into the seal must be limited and this CO_2 has reached only 12m above the reservoir. Infiltration is believed to be ongoing. A three carbon source mixing model and a Raleigh fractionation model are proposed to interpret $\delta^{13}C$ trends. Both display excellent match to the C isotope data. CO_2 infiltration rate is estimated to average 9.8×10^{-7} and 1.3×10^{-7} g.cm^{-2}.y^{-1} during 70 million years, indicating that minimal CO_2 has passed above the anomalous zone. The KCF seal has demonstrated excellent CO_2 retention.

- The C and O isotopes of carbonates in reservoir sandstones at the Miller Field exhibit a pattern of decreasing $\delta^{13}C$ with decreasing $\delta^{18}O$, similar to that of the regional data. It indicates carbonate precipitation over increasing temperature. No influence of the CO_2 charge can be seen in the reservoir sandstones. It is suggested that the high contents of the normal diagenetic carbonate cements obscure the signatures of possible precipitation from the CO_2 charge.

- The porewater evolution of the Brae Formation at Miller is reconstructed based on the $\delta^{18}O$ signatures of calcite and quartz cements together with fluid inclusion analyses from the study by Marchand (2001). The porewater evolution is described as follows. The initial pore fluid was dominated by late Jurassic sea water. Meteoric water flux through open surface charge reduced $\delta^{18}O$ to ~ -36.8 ‰ at temperatures of ~ 70 ˚C. The deep basinal fluid influx occurred at ~ 90 ˚C and increased $\delta^{18}O$ composition of the porewater to as high as -27 ‰. Then, the basinal water was diluted due to mixing and homogenizing with normal formation water and $\delta^{18}O$ values gradually decreased to the present-day oxygen isotope composition (-29.4 ‰).

- The isotopic compositions of the carbonate cements in the KCF in Brae-Miller area and Outer Moray Firth exhibit a similar pattern to that of the Brae Formation sandstones. The overlapping ranges of $\delta^{13}C$ and $\delta^{18}O$ ratios suggest that the KCF mudstones and the adjacent Brae Formation sandstones share the same porewater and carbon source through the burial history. It is suggested that the organic acid generated in adjacent KCF mudrocks provides a bicarbonate source for cementation both in KCF itself and in the sandstones. Migration of the pore fluids from KCF mudstones to adjacent sandstones is likely to be a pervasive process in this region.

- $\delta^{13}C$ values in the Brae Formation and the KCF in this region suggest that development of diagenetic carbonates only begin in the methanogenesis (Me) to decarboxylation (D) zone through a range of burial depth from ~700 (Me zone) to > 1000 m (D zone). The KCF samples in well 16/8b-A2, the Miller Field, however, show smaller ranges of $\delta^{18}O$ (from –6.1 to –13.7 ‰) and $\delta^{13}C$ (from –0.65 to –10.8 ‰) than the regional data set. It is suggested that the diagenetic carbonates in the sampling interval started to precipitate in a deeper diagenetic regime (D zone) from a marine-type pore fluid.

- The shale samples in the KCF in the Miller well 16/8b-A2 show overall higher carbonate isotopic compositions than the silt/sand samples (Figure 5.5). The heavier isotopes in shales may indicate earlier growth due to the fact that carbon source for carbonate precipitation is mainly generated in shale. Correspondingly, carbonate growth in silt/sand beds occurred relatively later, therefore, under higher temperatures, leading to lower $\delta^{18}O$. The lighter carbon compositions of silt/sand

samples represent the larger influence of D zone carbon source ($\delta^{13}C$ = –20 ‰).

- To interpret the characteristic linear isotopic trends with depth, it requires a complete dissolution of the original conventional carbonates in the anomalous zone which is followed by precipitation of present-day carbonates. Geochemical modelling was applied using Geochemist's Workbench (GWB) to demonstrate the feasibility of this scenario. In the modelling, it is found that high bicarbonate concentration in the Miller formation water is capable first to dissolve calcite and dolomite in the KCF cap rock, then to precipitate both. Adding CO_2 in the modelling decreases the quantity of dissolution but increases that of precipitation.

- Linear trends of $\delta^{18}O$ against depth are also observed in the bottom part of KCF (Figures 5.8 and 5.9). The upwards enriching in $\delta^{18}O$ is thought to be induced by the basinal water influx into Miller reservoir which altered the formation water from meteoric type to present-day porewater during late burial. But this explanation is problematic.

- The $\delta^{13}C$ and $\delta^{18}O$ versus depth plots in the control well does not exhibit the distinctive features of those from the Miller well (Figures 5.10 and 5.13). This confirms that the linear isotopic trends are unique features of the Miller Field which are associated with CO_2 breaching.

Table 5.1 Carbon and oxygen isotopes of calcite cements in the Brae Formation sandstones, the Miller Field. The data are displayed in Figure 5.4 together with the data from other wells in the Field analyzed by Thermie Project (Larter et al., 1995).

Well	TVD (m)	Occurrence	$\delta^{13}C$ ‰ V-PDB	$\delta^{18}O$ ‰V-PDB	$\delta^{18}O$ ‰v-SMOW
16/8b-A2	3984.1	Disseminated	–2.38	–7.70	22.98
16/8b-A2	3984.9	Disseminated	–2.53	–8.23	22.42
16/8b-A2	3985.4	Disseminated	–3.66	–8.84	21.79
16/8b-A2	3986.1	Disseminated	–3.96	–9.99	20.61
16/8b-A2	3987.5	Disseminated	–3.96	–10.05	20.55
16/8b-A2	3992.6	Concretion	–1.38	–5.93	24.80
16/8b-A2	3992.8	Concretion	–0.59	–5.57	25.17
16/8b-A2	3993.0	Concretion	–0.94	–6.04	24.68
16/8b-A2	3993.2	Concretion	–1.30	–6.42	24.29
16/8b-A2	3993.5	Concretion	–0.80	–5.83	24.90
16/8b-A2	3993.6	Concretion	–0.33	–5.70	25.03
16/8b-A2	3993.7	Concretion	–1.60	–6.88	23.82
16/8b-A2	3994.0	Concretion	–0.21	–5.37	25.37
16/8b-A2	3994.3	Concretion	–0.50	–5.81	24.92
16/8b-A2	3994.5	Concretion	–0.98	–5.99	24.74
16/8b-A2	3994.7	Concretion	–1.05	–6.03	24.69

Table 5.2 Oxygen and carbon isotopes of bulk carbonate. Most of the samples are from the KCF of well 16/8b-A2, the Miller Field, and well 9/28b-17, the control well. Shale samples from the Brae Formation are also listed here. The base of the Kimmeridge Clay Formation is at 3983.2 m in well 16/8b-A2 and at 4447.3 m in well 9/28b-17. The data are projected in Figure 5.5A, B.

Sample Depth TVD (m)	$\delta^{13}C$ ‰V-PDB	$\delta^{18}O$ ‰V-PDB	$\delta^{18}O$ ‰V-SMOW
Well 16/8b-A2, Sh			
3960.26	-3.98	-6.90	23.80
3960.43	-4.25	-7.31	23.37
3960.66	-3.83	-7.89	22.77
3960.86	-4.66	-6.97	23.73
3961.06	-6.11	-9.52	21.09
3961.22	-5.02	-6.47	24.24
3961.49	-5.39	-7.65	23.02
3961.90	-3.25	-8.48	22.16
3962.16	-5.90	-7.16	23.52
3962.63	-6.23	-8.25	22.40
3963.06	-8.90	-9.55	21.06
3963.45	-4.36	-9.23	21.39
3963.84	-4.12	-6.08	24.65
3964.25	-6.33	-9.35	21.27
3964.78	-4.33	-6.56	24.15

3965.13	-6.48	-10.53	20.06
3965.70	-4.62	-8.56	22.08
3966.06	-6.72	-7.47	23.21
3966.63	-6.25	-7.44	23.24
3967.05	-3.87	-6.15	24.57
3967.61	-6.43	-7.67	23.00
3968.04	-6.15	-8.39	22.26
3968.47	-5.80	-8.88	21.76
3968.69	-4.22	-7.94	22.73
3969.20	-5.73	-10.15	20.44
3969.69	-5.18	-8.09	22.57
3970.32	-4.05	-7.34	23.35
3970.94	-5.89	-10.74	19.84
3971.14	-6.29	-8.76	21.87
3971.58	-7.40	-8.73	21.91
3972.03	-7.12	-9.06	21.57
3972.60	-5.42	-7.90	22.76
3973.00	-6.95	-9.77	20.84
3973.62	-6.48	-8.74	21.90
3974.76	-6.02	-9.93	20.67
3975.14	-6.27	-8.65	22.00
3975.66	-6.58	-9.77	20.84
3976.04	-5.93	-9.24	21.39
3976.73	-5.82	-9.57	21.04
3977.04	-5.55	-8.81	21.83
3977.18	-5.52	-8.68	21.96
3977.42	-5.93	-12.23	18.30
3977.72	-4.96	-8.93	21.71
3978.22	-5.03	-10.39	20.20
3978.63	-4.36	-8.04	22.62
3978.79	-4.48	-10.45	20.14
3979.18	-3.97	-10.47	20.12
3979.37	-3.95	-8.47	22.18
3979.59	-4.39	-11.09	19.47
3979.98	-3.85	-9.03	21.60
3980.17	-3.35	-8.26	22.40
3980.34	-3.17	-9.00	21.63
3980.80	-3.36	-8.72	21.92
3981.06	-3.21	-8.30	22.35
3981.49	-2.87	-7.87	22.80
3981.78	-4.23	-10.92	19.65
3982.01	-3.05	-7.91	22.76
3982.20	-2.88	-11.88	18.67

3982.41	-2.31	-11.46	19.10
3982.75	-1.95	-11.97	18.57
3982.92	-1.83	-11.25	19.31
3983.01	-1.91	-9.50	21.11
3983.05	-1.91	-8.04	22.62
3983.15	-2.02	-11.57	18.98
3983.45	-0.77	-9.05	21.58
3983.49	-1.25	-12.33	18.20
3983.69	-1.94	-12.49	18.03
3983.80	-1.71	-11.36	19.20
3984.41	-3.12	-11.85	18.69
3984.80	-4.63	-10.85	19.73
3986.48	-3.47	-11.49	19.07
3986.65	-2.95	-13.70	16.79
3990.21	-4.61	-11.91	18.63
3991.33	-3.68	-12.03	18.51
3991.95	-0.65	-12.79	17.73
4002.25	-0.69	-11.87	18.67
4002.45	-0.66	-10.34	20.25
4004.25	-0.98	-10.66	19.92
4004.81	-1.62	-11.11	19.45
Well 16/8b-A2, Sst/Slst			
3960.22	-7.04	-7.95	22.71
3960.24	-7.36	-8.57	22.07
3960.91	-10.84	-8.68	21.96
3962.00	-9.20	-9.00	21.63
3962.27	-8.24	-9.29	21.33
3962.29	-8.54	-9.87	20.74
3964.99	-10.05	-9.56	21.06
3962.29	-8.62	-9.49	21.13
3968.24	-8.20	-8.61	22.04
3968.27	-7.50	-8.67	21.97
3969.37	-7.83	-9.20	21.42
3969.92	-7.55	-9.07	21.56
3970.11	-6.89	-8.64	22.00
3970.58	-6.97	-8.81	21.82
3971.29	-8.88	-10.59	19.99
3971.45	-8.07	-10.50	20.09
3971.62	-7.03	-9.54	21.08
3972.64	-7.48	-9.21	21.42
3973.36	-6.99	-8.98	21.65
3973.37	-8.68	-10.26	20.33
3974.13	-7.09	-9.09	21.54

3974.46	-6.91	-9.28	21.35
3977.50	-8.79	-11.29	19.27
3978.09	-5.66	-9.61	21.01
3978.81	-7.74	-11.31	19.25
3979.34	-9.08	-11.29	19.27
3979.60	-7.15	-10.57	20.02
3979.80	-6.65	-9.44	21.18
3979.81	-7.31	-10.57	20.01
3980.04	-6.54	-10.56	20.02
3980.42	-5.20	-9.20	21.42
3980.66	-7.20	-11.07	19.49
3981.09	-6.22	-11.20	19.36
3981.34	-5.19	-11.05	19.52
3981.38	-5.60	-9.74	20.87
3981.61	-5.91	-11.93	18.62
3981.77	-4.50	-10.64	19.94
3981.89	-6.06	-10.12	20.48
3982.15	-3.96	-13.26	17.24
3982.17	-6.20	-11.05	19.52
3982.04	-4.08	-12.39	18.14
3982.40	-6.21	-11.17	19.40
3982.58	-3.23	-12.67	17.85
3982.59	-5.13	-9.89	20.71
3982.88	-5.62	-11.00	19.57
3983.20	-7.93	-13.05	17.46
Well 9/28b-17, Sh			
4413.30	-2.84	-9.07	21.56
4413.97	-4.05	-5.86	24.87
4414.86	-1.78	-9.66	20.95
4416.11	-4.79	-6.72	23.99
4419.31	-2.84	-10.02	20.58
4419.33	-3.66	-4.99	25.76
4420.74	-4.19	-10.50	20.08
4423.27	-2.32	-7.69	22.98
4423.93	-3.91	-12.89	17.62
4425.57	-1.62	-9.86	20.74
4430.01	-5.57	-10.59	20.00
4431.86	-5.66	-9.22	21.41
4434.20	-2.01	-7.61	23.06
4436.08	-4.31	-9.81	20.80
4440.03	-3.42	-10.62	19.96
4440.55	1.12	-6.90	23.79
4441.13	-1.76	-10.73	19.85

4441.99	-1.16	-9.62	20.99
4443.32	-0.88	-4.98	25.78
4443.79	0.65	-6.87	23.83
4443.69	0.01	-8.16	22.50
4444.62	-2.21	-8.76	21.88
4445.10	-1.67	-5.47	25.27
4446.92	-1.58	-5.96	24.76
4446.96	-1.00	-7.64	23.03
4447.97	-2.80	-9.09	21.54
4448.85	1.77	-10.05	20.55
4449.52	-0.96	-8.70	21.94
4450.03	-2.61	-9.15	21.48
4452.49	-2.27	-11.14	19.42
4453.38	-2.21	-7.63	23.05
Well 9/28b-17, Sst/Slst			
4413.34	-2.17	-6.57	24.13
4413.92	-3.87	-6.50	24.21
4414.89	-5.79	-7.07	23.62
4416.18	-8.59	-8.07	22.59
4418.91	-1.11	-8.11	22.55
4418.93	-1.17	-6.38	24.33
4418.98	-1.06	-7.13	23.56
4419.37	-3.56	-7.74	22.93
4420.62	-3.69	-6.78	23.92
4420.67	-4.27	-7.97	22.69
4423.31	-10.50	-8.39	22.26
4423.90	-5.94	-6.96	23.74
4426.33	-2.64	-8.21	22.44
4427.12	-5.15	-7.69	22.99
4429.94	1.25	-6.33	24.39
4430.05	-2.61	-6.47	24.24
4431.14	-3.08	-6.66	24.05
4431.87	-10.47	-8.64	22.00
4434.12	-3.45	-8.17	22.48
4434.15	-2.85	-8.43	22.22
4434.83	-8.66	-8.28	22.37
4437.32	-9.69	-8.61	22.04
4438.03	-3.49	-7.83	22.84
4438.01	-4.20	-6.79	23.91
4440.10	-4.29	-7.42	23.26
4441.14	-5.59	-8.60	22.04
4442.89	-8.66	-8.88	21.75
4444.57	-9.29	-8.68	21.96

4446.28	-2.28	-7.43	23.25
4447.29	-2.89	-7.31	23.38
4442.03	-0.80	-9.69	20.92
4445.13	-0.06	-7.62	23.06
4445.53	-1.36	-5.45	25.29
4446.13	-2.22	-7.24	23.44
4446.61	-1.48	-7.17	23.52

Table 5.3 Inorganic carbon content of shale samples of both the KCF and the Brae Formation.

Sample Depth TVD (m)	Inorganic C content wt%
Well 16/8b-A2, Sh	
3960.43	0.18
3960.66	0.12
3960.86	0.16
3961.22	0.27
3961.90	0.09
3962.16	0.27
3962.63	0.06
3963.84	0.20
3966.06	0.34
3966.63	0.26
3967.61	0.28
3968.69	0.15
3969.20	0.22
3969.69	0.19
3970.94	0.16
3971.14	0.25
3972.60	0.21
3973.62	0.30
3974.76	0.11
3975.14	0.37
3976.04	0.31
3977.18	0.25
3977.72	0.21
3978.79	0.25
3979.18	0.12
3979.98	0.30
3980.17	0.04
3980.34	0.19
3981.06	0.17
3981.49	0.15
3981.78	0.07

3982.20	0.03
3982.41	0.08
3983.49	0.08
3984.41	0.04
3986.48	0.06
3986.65	0.02
3991.33	0.01
4002.45	0.03
4004.25	0.06
4004.81	0.04
Well 9/28b-17, Sh	
4413.97	0.04
4414.86	0.04
4415.18	0.05
4416.11	0.11
4417.45	0.01
4419.33	0.32
4421.43	0.01
4422.53	0.03
4423.27	0.13
4425.14	0.02
4425.57	0.06
4428.03	0.01
4430.74	0.00
4433.57	0.00
4434.59	0.00
4436.16	0.02
4436.40	0.01
4437.23	0.01
4439.96	0.01
4441.39	0.02
4442.74	0.00
4443.32	0.44
4443.96	0.01
4444.47	0.00
4448.21	0.20
4449.47	0.02

CHAPTER VI

FLUID INCLUSION RAMAN MICROSPECTROSCOPY AND MICROTHERMOMETRY

6.1. Introduction

Based on carbonate isotopic compositions in the shales, it is estimated that CO_2 emplacement in the Miller reservoir initiated at c. 70-80 Ma (see Section 5.7.5). But there is uncertainty in this estimation because of the lack of constraints on the isotopes of the early CO_2 accumulation. The assumption that the carbon isotope ratio of the reservoired CO_2 has remained unchanged since its emplacement may be faulty. This would lead to incorrect estimation of precipitation temperature, and therefore, timing. Independent evidence on timing of CO_2 charge is needed.

Fluid inclusions provide important information on the composition and pressure-temperature conditions of the trapped ancient porewater. By measuring the homogenization temperatures, the fluid inclusions which trapped a high content of CO_2 would shed light on the timing of CO_2 emplacement. Multiple species including CO_2 in a fluid inclusion can be identified by laser Raman microprobe (LRM) spectroscopy (Wopenka and Pasteris, 1987), which provides a convenient tool for an extensive search for CO_2 trapped in fluid inclusions. It is possible to determine the timing of emplacement by applying microthermometric measurements to the

CO_2-rich fluid inclusions, providing that the oldest of them are found. Additionally, Raman quantitative analysis based on Placzek's polarizability theory can be applied to derive a compositional analysis for Raman active species (e.g. CO_2, N_2, H_2S, CH_4, O_2, H_2, SO_2) in a fluid inclusion (Placzek, 1934). This allows possible relative quantitative estimation on the reservoir gas compositions during the burial history.

In this study, laser Raman spectroscopic and microthermometric analyses were conducted on fluid inclusions in quartz cements of the Brae Formation sandstones in the Miller Field. This chapter reports the results of qualitative and semi-quantitative analyses of laser Raman spectrum. The homogenization temperatures of these fluid inclusions of a number of CO_2 and CH_4 bearing fluid inclusions are presented and discussed.

6.2. Methodology

When crystals grow or recrystallize in a fluid medium, growth irregularities result in the trapping of small portions of the fluid in the solid crystal. Such irregularities may be sealed off during the growth of the surrounding part of the host crystal, yielding primary fluid inclusions. Healing of fractures occurred during crystal growth also can form fluid inclusions. Fluid inclusions provide a record of fluids existing at some time in the geological history of a rock. They are important clues in understanding the past geologic processes in the subsurface.

6.2.1. Microthermometry

The determination of temperatures of phase changes within fluid inclusions during heating or cooling of samples is termed microthermometry. Measurement of the homogenization temperature (T_h) and temperature of last ice melting (T_m) in fluid inclusions provides information on the minimum temperature of the fluid inclusions formation and the salinity of fluids from which the quartz cements precipitated (Roedder, 1984).

6.2.1.1. T_h

A conspicuous feature of many aqueous fluid inclusions is a vapour or gas bubble. The two phases (liquid and vapour) is a result of differential shrinkage of the host mineral and the inclusion fluid on cooling from the temperature of trapping to that of observation. Upon cooling to room temperature, the fluid shrinks far more than the host, thus, the pressure in the inclusions drops below the saturation vapour pressure of the contained fluid and the fluid splits into two phases: liquid and vapour. By heating the inclusion to the temperature of disappearance of the vapour bubble, a minimum temperature at which the inclusion was formed is obtained. The temperature at which the two phases in the inclusion homogenize is called the homogenization temperature (T_h) (Roedder, 1984). The homogenization temperatures only represent the minimum temperatures of entrapment, since the homogenization of a two-phase inclusion occurs along the liquid–vapour curve and then follows the isochore slope which depends on the physical-chemical character of the inclusion, there can be a large difference between the measured T_h and the true trapping temperature (T_t).

In order to obtain the true trapping temperatures (T_t) of the inclusions in the mineral, a pressure correlation needs to be applied. According to Hanor (1980), however, homogenization temperatures of methane-bearing fluid inclusions are very similar to trapping temperatures and no pressure correlation is required. Within an oilfield, it is a reasonable assumption that the porewaters are methane-bearing.

6.2.1.2. T_m

By freezing aqueous inclusions and subsequently warming them up to room temperature, information on the composition and salinity of the fluid which the fluid inclusions trapped can be obtained. The temperature at which the final melting of ice occurs is termed as melting temperature (T_m). T_m is controlled by the salinity of the fluid. Salt in solution in the fluid contained in the inclusion will cause a depression of the final ice melting temperature.

The relationship between freezing point depression and salinity varies slightly for the various species dominant in the fluid. Most researchers report their interpretations of freezing point depression in weight % NaCl equivalent, simply stating the salinity of fluid inclusions assuming all dissolved species to be NaCl. This yields a salinity that is fairly close to reality for many diagenetic systems (Roedder, 1984).

The presence of CO_2 in the fluid inclusions might affect the melting temperatures obtained from phase relations in the CO_2-free system. But in the fluid inclusions which has both liquid and vapour phases, most of CO_2 is contained in the vapour phase at the temperature of NaCl melting. Therefore, only very small CO_2 concentrations exist in the liquid phase, and thus the affect of CO_2 on the temperature of NaCl melting is considered insignificant (Frantz et al., 1992). At room temperature and 85 bars pressure, the solubility of CO_2 in pure water is about 3 mol% (Kohl and Nielsen, 1997) and that of CH_4 about 0.2 mol% (Bonham 1978). In fact, in the microthermometric study by Frantz et al. (1992), the effect on the melting temperature of the presence of up to 43.2 mol% CO_2 in the fluid inclusions is considered as insignificant and neglected.

6.2.1.3. Pressure correction

In evaluating thermometry, pressure is of concern mainly in that it controls the density of the fluids and hence the magnitude of the pressure corrections that must be added to T_h to get the true formation temperature, T_t. If a fluid inclusion is trapped from a homogeneous fluid along the boiling curve (i.e. under P-T conditions such that it was in equilibrium with either a vapour or gas phase), $T_h = T_t$, and no pressure correction is needed. It would make no difference whether the gas bubble that formed had the same composition as the liquid (e.g. a steam bubble in pure water) or had a completely different composition (e.g. a CO_2 bubble in an aqueous inclusion) (Roedder, 1984).

However, most inclusions have trapped fluids at a P-T combination above the liquid/vapour

curve. In these, a bubble disappears on heating up from room temperature when the pressure and temperature have increased to the liquid/vapour curve. This homogenization temperature (T_h) is lower than true trapping temperature (T_t). The difference between T_h and T_t is called the "pressure correction"; it must be added to T_h to obtain T_t. As the density stays essentially constant under these conditions, the change in P and T inside the inclusion must be represented by a vertical line in temperature-density plot and by a sloping isochore in a P-T plot. Only if P_t can be calculated from geological field data on the depth of cover, or from some other independent geobarometer, T_t can be obtained at P_t on the isochore which passes through P_h and T_h (Roedder, 1984).

6.2.2. Laser Raman spectroscopy

6.2.2.1. Basic theory

Microthermometric analysis can detect the presence of "additional volatiles" in an aqueous fluid inclusion by their effect on the temperatures of phase changes. Unfortunately, several gases have similar effects on certain phase changes, which can also be affected by differences in the molar volume, and so if more than one component other than CO_2 is present, they cannot be identified or quantified by microthermometry alone (Murphy and Roberts, 1995). Also, low concentrations of CO_2 are not easily detected during routine heating and cooling studies (Sasada, 1985; Ulrich and Bodnar, 1988).

However, in contrast to microthermometry, laser Raman spectroscopy analysis can uniquely identify multiple species in an inclusion rather than simply allowing one to infer their presence based on known or assumed phase relations. If the inclusions show different melting and homogenization temperatures, the questions concerning these variations are whether they are due to different proportions of already identified species in the inclusions, different amounts of unidentified contaminants, different densities, or a combination of the above conditions. The Raman spectroscopy plays a unique role in distinguishing among these possibilities (Pasteris et al., 1988). Compared to microthermometry, it provides

improved detection limits for gases such as CO_2 (Wopenka and Pasteris, 1987). Therefore, in this study, laser Raman microprobe spectroscopy was used to search for the fluid inclusions trapped with high CO_2 contents in the Miller reservoir.

In laser Raman microprobe (LRM) spectroscopy, a monochromatic laser beam is focused through a microscope objective into a fluid inclusion or into an individual solid, liquid or vapour phase within the inclusion. The Raman scattered light is collected through the same objective by a photon-counting device (Seitz et al., 1987). Analysing the spectra collected enables identification of the species that the fluid inclusions contain by identifying the unique band assemblage of each species.

6.2.2.2. The spectrum of CO_2

The CO_2 molecule is linear and thus has four modes of vibration, a symmetric stretching mode (v_1), an antisymmetric stretching mode (v_3) , and two bending modes (v_{2a} and v_{2b}) which have the same frequency of vibration and form a degenerate pair. These vibrations are shown schematically in Figure 6.1. The symmetric stretching mode is the only predicted Raman-active vibration because the derivative of the change in total molecular polarizability during this motion is nonzero (Rosso and Bodnar, 1995).

Due to Fermi resonance, the admixed excited v_1 and $2v_2$ states are split apart and two strong CO_2 bands are present in Raman spectrum. These two bands are referred to as the v_1-$2v_2$ Fermi diad and have the frequencies 1388.2 cm^{-1} (upper band) and 1285.4 cm^{-1} (lower band) (Gordon and McCubbin, 1966; Rosso and Bodnar, 1995) (Figure 6.2).

Another band type is represented by low intensity peaks flanking the Fermi diad, which are referred to as hot bands. Their resultant frequencies are 1264.8 cm^{-1} and 1409.0 cm^{-1} (Figure 6.2). They arise from transitions that originate in excited vibrational states higher in energy than the ground vibrational state due to the thermal energy of the molecules. The hot bands

are also perturbed by Fermi resonance (Dickinson et al., 1929).

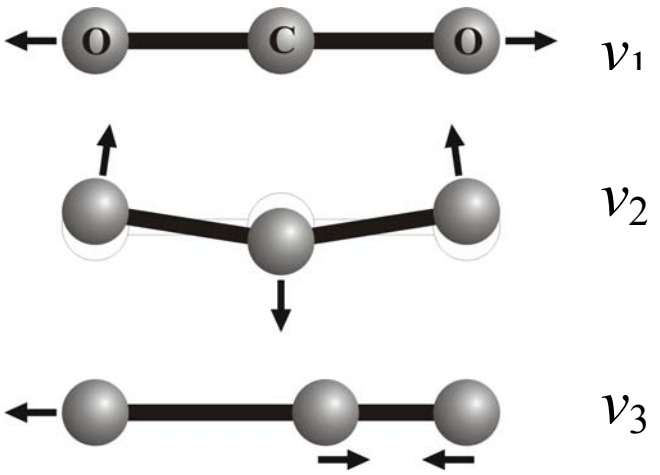

Figure 6.1 Schematic representation of the three fundamental vibrations of CO_2 (Rosso and Bodnar, 1995).

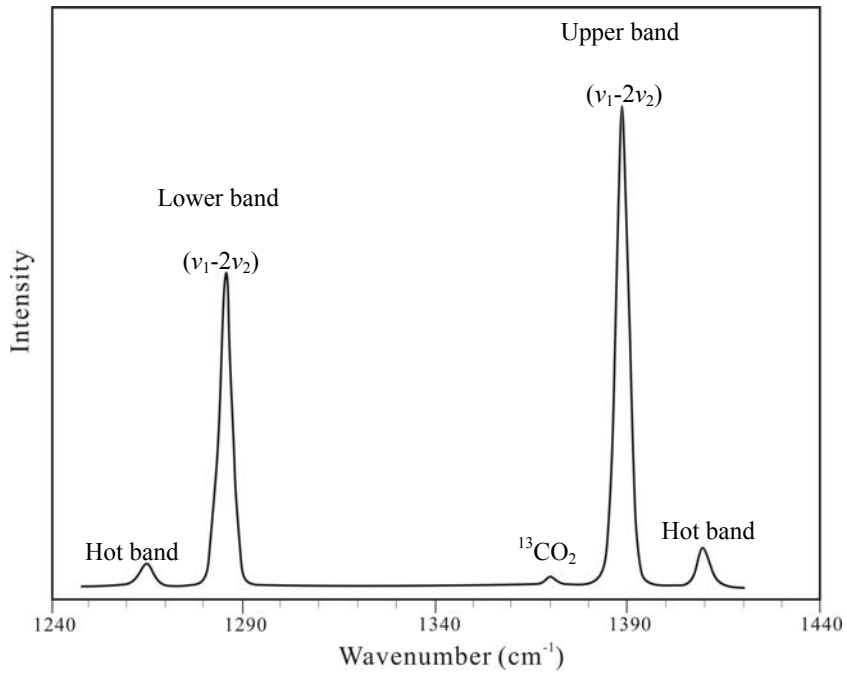

Figure 6.2 Typical Raman spectrum of CO_2 with background subtracted. Peaks marked (v_1-2v_2) comprise the v_1-2v_2 Fermi diad. The hot bands are also coupled through Fermi resonance (modified after Rosso and Bodnar, 1995).

6.2.2.3. Raman quantitative analysis

According to Placzek's (1934) polarizability theory, the area of a Raman peak (over a finite range of wavenumbers) is a function of (1) the number of molecules of a certain species in

the scattering volume (absolute concentration of the species), (2) the Raman scattering cross section of the species, (3) the irradiance of the specimen, and (4) the solid angle of light collection. If two or more Raman-active species in the same phase of a fluid inclusion are analyzed either at the same time or one immediately after the other, the irradiance, the scattering volume, and the angle of collection of light are assumed to be the same for all the species. Since the approach to quantitative fluid inclusion analysis is to determine the ratio of two or more species, the latter unknown parameters cancel each other. In practice, for a two-component system, the experimental result in units of mole percentages (C_a, C_b) is the function of three ratios: one for the determined Raman peak area (A_a, A_b), one for the relative scattering cross sections (σ_a, σ_b) of the two species, and one for the instrumental efficiencies (η_a, η_b) for Raman scattered light at specific wavelengths and polarization orientation. The σ's and η's can be combined into "Raman quantification factors" (F_a, F_b) (Wopenka and Pasteris, 1987). The quantitative relationship between the relative concentration of two components, *a* and *b*, and their Raman peak areas reduces to a simple formula:

$$A_a/A_b = (C_a/C_b) \times (\sigma_a/\sigma_b) \times (\eta_a/\eta_b) = (C_a/C_b) \times (F_a/F_b) \quad (6.1)$$

$A_{a,b}$ = peak area for Raman signal of species *a* or *b*,

$C_{a,b}$ = mol% of species of *a* or *b*,

$\sigma_{a,b}$ = relative Raman scattering cross-section for species *a* or *b*,

$\eta_{a,b}$ = instrumental efficiency for spectral region and polarization distribution of species *a* or *b*,

$F_{a,b}$ = "Raman quantification factor" for species *a* or *b*, which incorporates Raman scattering cross-section (at appropriate pressure) and differential instrumental efficiency.

This equation requires knowledge of the Raman scattering efficiencies (σ's) for the different components and the instrumental efficiencies (η's) for Raman scattering radiation arising

from those components. Given that the Raman peak areas (*A*'s) can be determined for the components, Equation 6.1 yields their relative concentrations, e.g., in mol % (*C*'s).

It has long been realized that the cross-section of a volatile changes with the total pressure in a given fluid inclusion. For CH_4 and CO_2 in calibration gas mixtures up to about 15 bars total pressure, Wopenka and Pasteris (1987) determined *F*-factors (relative to N_2) of about 6.7 and 1.5, respectively, for their laser Raman microprobe. The ratio of these *F*-factors is 4.4. Such ratios for low density gas mixtures are the ones most appropriate for the species in gas bubbles in this study, therefore, are adopted to quantify the contents of the gas species. For a CH_4-CO_2 supercritical fluid with a density of about 80 cm^3/mole (about 80 bars at room temperature), the empirically determined F-factor ratio is 2.9, a relative decrease of about 34% compared to the ratio obtained at low pressure (Seitz et al., 1987).

However, the fact that there are several instrument-specific parameters makes it problematic to apply the above empirical *F*-factors to different instruments. Among the most important instrumental factors are the different sensitivities of the gratings and the detector system for Raman scattered light of different polarization orientations and/or wavelengths. The use of the microscope of a laser Raman spectrometer will cause additional optical effects due to different components (e.g., objective, beam splitter, lenses) (Wopenka and Pasteris, 1987). Since each optical component has its own spectral characteristics that are a function of both wavelength and polarization orientation of the interacting light, the published *F*-factors are only approximate solutions for the Raman instruments used in this study.

6.3. Sample material

Polished wafers for fluid inclusion analyses were made from the Brae Formation sandstones in four wells in the Miller (16/7b-20, 16/8b-3, 16/8b-5 and 16/8b-A2) and one in the South Brae Field (16/7b-26). The depth of the samples ranges from 4012.0 to 4103.6 m TVD. The samples were examined are from 4103.6 m, well 16/8b-5; 4012.1 m, 4020.0 m, 4034.6 m,

well 16/8b-3; 4047.0 m, 4086.4 m, well 16/7b-20; 4008.9 m, well 16/8b-A2 and 4101.4 m, 4186.4 m, well 16/7b-26. In these samples, quartz is the most abundant mineral comprising 87.9±4.4 % of the detrital framework mineralogy. Most quartz is monocrystalline, but composite or polycrystalline quartz is also present.

6.4. Analytical methods

The wafers were examined first using an optical microscope to search for the ideal fluid inclusions. For each target fluid inclusion, a set of photomicrographs were taken under various magnifications. The target fluid inclusions were marked in the photographs so that they can be easily found again for Raman spectroscopic and microthermometric analyses.

The laser Raman spectrometer used in this study is a LabRam 300 provided by Jobin Yvon-Horiba. The spectral resolution is 3.2 cm^{-1}. The laser power is 11 mW at the surface of the sample for 100× objective, excited by 632.81 nm continuous wave laser. Integration time used for the stretching band of water is 100 s with a few accumulations.

Raman spectra were collected at room temperature in the spectral window of 700 – 3500 cm^{-1} which covers the v_1-$2v_2$ bands of CO_2 at 1285.4 cm^{-1} and 1388.2 cm^{-1} and its two hot bands at 1264.8 cm^{-1} and 1409.0 cm^{-1} (Figure 6.2); the N_2 band at 2328.4 cm^{-1}; the SO_2 band at 1151 cm^{-1}; the large stretching band of H_2O (2900 – 3700 cm^{-1}) and the υ_1 band of CH_4 at 2916.8 cm^{-1} (Pasteris et al., 1988). Overlap of Raman bands from volatiles in inclusions with bands from quartz hosts usually does not occur. This makes it possible to resolve all those major volatiles from the background of quartz bands.

For each fluid inclusion, the laser beam was targeted at three areas: the gas bubble, the aqueous phase and the host quartz. Three Raman spectra were obtained respectively. By comparing them, CO_2 and other volatile species can be easily identified in the gas and aqueous phase if there is any.

Microthermometric measurements on the CO_2-bearing fluid inclusions were conducted at Fluid Inclusion Technologies (FIT), Inc.. A USGS-type Gas-Flow heating/freezing stage was used. This stage allows highly accurate measurement of the various phase transitions observable within fluid inclusions that are used to constrain pressure-temperature-timing relationships of inclusion formation. It was calibrated using the temperature of the CO_2 triple point (56.6 °C) and H_2O triple point (0 °C) and the critical homogenization of an H_2O fluid inclusion (374.1 °C). The accuracy of measurement is ±0.1 °C in the range of -100 °C to +25 °C, ±0.5 °C between 25 °C and 250 °C and increases linearly to ±1 °C at 374.1 °C.

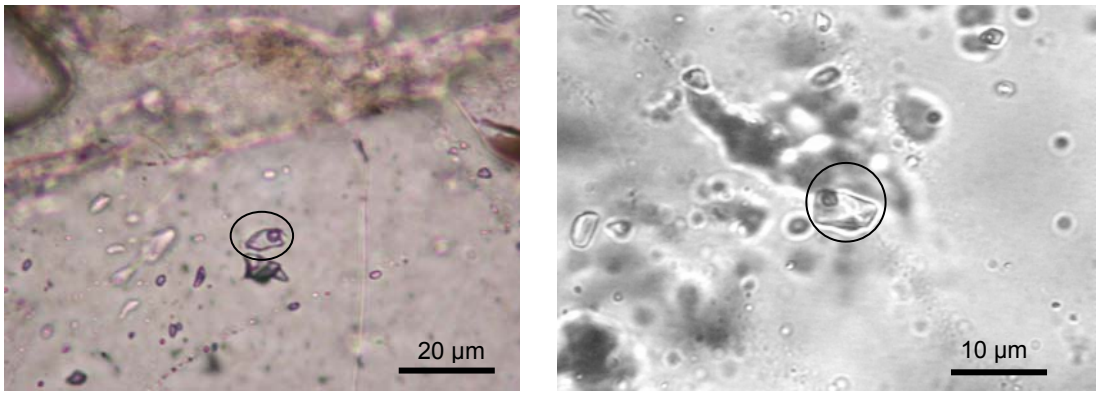

A B

Figure 6.3 Photomicrographs of a fluid inclusion. (A) Fluid inclusion occurs in quartz overgrowth. Type I inclusion, only containing CO_2 in the gas bubble. 4103.6 m TVD, well 16/8b-5. Inclusion 1, in Table 6.1; (B) Fluid inclusion found in a microfracture. Type II fluid inclusion containing both CO_2 and CH_4. T_h of 136 °C suggesting recent formation. 4047.0 m TVD, well 16/7b-20. Inclusion 11 in Table 6.1.

6.5. Results

6.5.1. Laser Raman spectroscopy

Fluid inclusions occur both in detrital quartz grains and in quartz overgrowths. Most of the fluid inclusions examined in this study are found in healed microfractures which commonly cross-cut quartz grains. The others are found on the boundary between detrital grains and overgrowths (“dust rim”) and, less commonly, within the overgrowths themselves (Figure 6.3). Most fluid inclusions show a subhedral to euhedral negative crystal shape.

Necking-down or stretching textures were observed and avoided.

The optical properties of fluid inclusions that are 'ideal' for Raman analysis are basically the same as those that are desirable for microthermometric analysis, i.e., high optical clarity, sufficient size (> 5 μm desirable), and shallow depth below the sample surface. The chosen inclusions are generally between 5 to 15 μm in size. They occur in clusters or have an isolated occurrence. All the fluid inclusions which are examined by LRM spectroscopy and microthermometry contain two phases, liquid and vapour at room temperature. The vapour phase volume ranges from ~ 10 to ~ 30 %. Inclusions sufficiently large to allow reliable LRM analysis on their gas bubbles proved difficult to find. Vibration of gas bubbles makes it difficult to target the laser beam at them. During collecting spectra, movement of gas bubbles would lead to distorted spectra, with enhanced bands of the volatiles when the bubbles are on target and subdued bands when the bubbles moved off the laser beam.

Over 200 fluid inclusions were examined by LRM in this study. CO_2, CH_4, C_2H_6 and N_2 were detected as volatiles. It was found that the content CO_2 and CH_4 varies strongly in these inclusions: some show high intensities for the CO_2 or CH_4 bands or both, while others show only weak or no signal. Most of the gas bubbles contain only H_2O and no other components are detected.

CO_2 was identified in 13 fluid inclusions. CH_4 was found in nine. They coexist in four. Four inclusions were observed to contain only CH_4 as volatile. The compositions of volatile species of these fluid inclusions are displayed in Table 6.1.

As Figure 6.4 shows, the CO_2 bands can be easily resolved against the bands of the quartz host in the spectrum of a gas phase. Superposition of the two huge v_1-$2v_2$ bands and the two smaller hot bands of CO_2 on the broad but low quartz bands is the most obvious characteristics for a CO_2-rich gas bubble in a fluid inclusion in quartz. No other volatiles

were found in this fluid inclusion, indicating that this inclusion primarily contains water vapour and CO_2. In the spectrum for the aqueous phase (A), the band at 1381.8 cm^{-1} is dedicated to the dissolved CO_2 phase. It is the v_1-$2v_2$ upper band of CO_2 broadened and shifted to lower wavenumber.

Nine inclusions were found to contain CH_4 as sole volatile or as coexisting species. In Figure 6.5, the gas phase spectrum (B), for example, show that the CH_4 band at 2917 cm^{-1} is present together with the two v_1-$2v_2$ bands of CO_2, suggesting that the gas bubble mainly consists of CO_2 and CH_4.

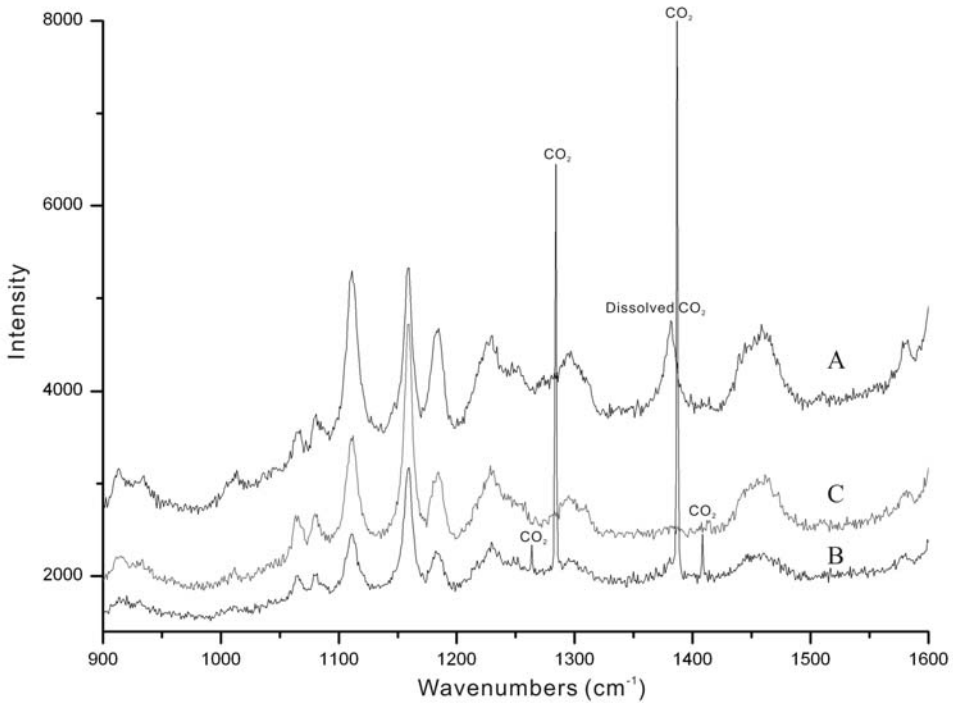

Figure 6.4 LRM spectra of a CO_2-bearing aqueous inclusion (Inclusion 1 in Table 6.1), 4103.6 m, well 16/8b-5. Analytical conditions: 632.81 nm Ar+ laser extraction, 11mW at sample surface for 100× objective. The three spectra were obtained at aqueous phase (A), vapour phase (B) of the inclusion and the host quartz (C) just beside the inclusion. Spectrum B shows two high *v*1-2*v*2 bands and two smaller hot bands for CO_2 among the quartz bands in background. Spectrum C reveals a lowered and broadened v_1-$2v_2$ band for dissolved CO_2 in the liquid phase. No other volatile species were detected.

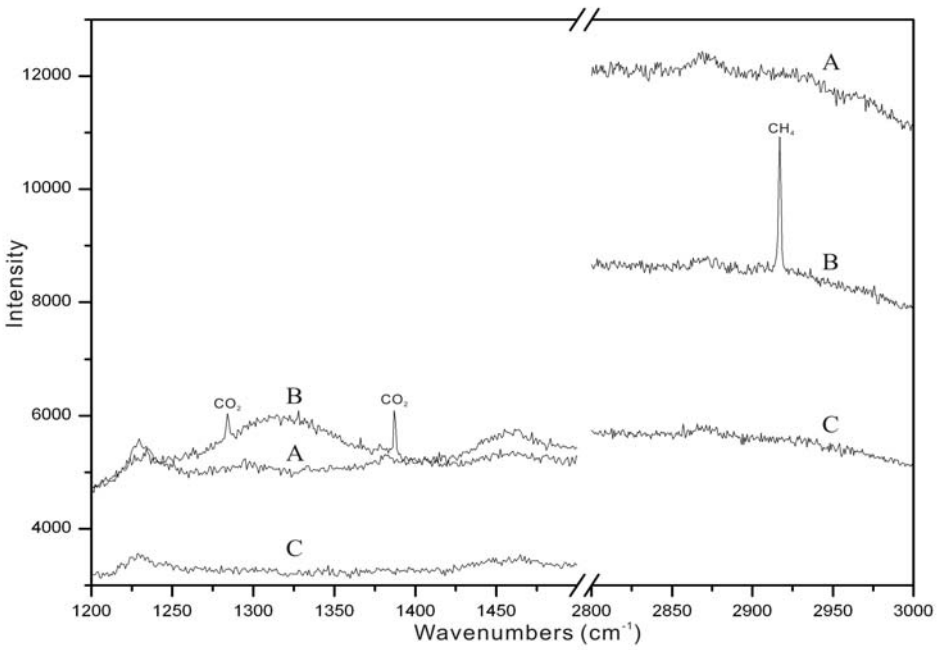

Figure 6.5 LRM spectra of a CO_2 and CH_4-bearing aqueous inclusion (Inclusion 12 in Table 6.1), 4047.0 m, well 16/7b-20. Analytical conditions: 632.81 nm Ar^+ laser extraction, 11mW at sample surface for 100× objective. The three spectra were obtained at the aqueous phase (A), the vapour phase (B) and the host quartz (C) of the inclusion. Spectrum B shows two v_1-$2v_2$ bands of CO_2 and a CH_4 band at 2917 cm^{-1}. No other volatile species were detected.

6.5.2. Microthermometry

T_h and T_m of those fluid inclusions containing CO_2 and/or CH_4 (Inclusion 1-13) are displayed in Table 6.1. All the inclusions homogenized into the liquid phase during heating. Inclusion 2 decrepitated during heating and no T_h was obtained. Only four fluid inclusions which contain CH_4 yielded T_m. Those containing only CO_2 in gas phase did not freeze when cooled down to -193 °C, therefore no melting temperatures were obtained from them.

The homogenization temperatures fall into two groups (Figure 6.6). The fluid inclusions containing CO_2 as the only volatile species show T_h ranging from 226 to 265 °C (Type I), much higher than the present day reservoir temperature at ~ 120 °C. Four fluid inclusions which contain methane or both methane and CO_2 yielded T_h similar to the present-day

reservoir temperature (Type II). T_m of the Type II fluid inclusions ranges from -5.1 to -0.1°C.

Table 6.1 List of sample depths (TVD) of the fluid inclusion wafers of the Brae Formation sandstone in the Miller Field. Compositions of gas phase in the fluid inclusions are indicated in mole % for the gas bubbles containing two or more species. Also showing T_h and T_m measured by FIT Inc., USA. The fluid inclusions are divided into Type I (pre-existing) and Type II (newly formed during burial).

(*) Fluid inclusions do not freeze down to -193 °C.

(**) Fluid inclusions decrepitated during heating.

Inclusion	Well	Depth (m TVD)	Gas phase composition	T_h (°C)	T_m (°C)
Type I					
1	16/8b-5	4103.6	CO_2	264	*
2	16/8b-5	4103.6	CO_2	**	*
3	16/8b-5	4103.6	CO_2	265	*
4	16/8b-5	4103.6	CO_2	253	*
5	16/8b-5	4103.6	CO_2	238	*
6	16/8b-5	4103.6	CO_2	245	*
7	16/8b-5	4103.6	CO_2	226	*
8	16/8b-5	4103.6	CO_2	233	*
9	16/7b-20	4086.4	CO_2	228	*
Type II					
10	16/7b-26	4186.4	CO_2 (58 %), CH_4 (42 %)	123	-3.4
11	16/7b-20	4047.0	CO_2 (39 %), CH_4 (61 %)	136	-2.8
12	16/7b-20	4086.4	CH_4 (100 %)	113	-5.1
13	16/8b-A2	4008.9	CH_4 (100 %)	112	-0.1
14	16/7b-20	4047.0	CO_2 (30%), CH_4 (69%), C_2H_6 (1%)	N/A	N/A
15	16/8b-3	4020.0	CO_2 (2%), CH_4 (11%), N_2 (87%)	N/A	N/A
16	16/8b-3	4020.0	CH_4 (100 %)	N/A	N/A
17	16/8b-A2	4008.9	CH_4 (100 %)	N/A	N/A
18	16/8b-A2	4008.9	CH_4 (3.5%), N_2 (96.5%)	N/A	N/A

6.6. Discussion

Aqueous solutions contain CO_2 as the major volatile components in many geological environments. At ambient temperature, the typical phase assemblage in these fluid inclusions

consists of a CO_2-rich vapour phase and an aqueous phase containing dissolved salt and some dissolved salt and some dissolved CO_2 (Bodnar et al., 1985). In the present-day Miller reservoir, the gas phase contains an average of 28 mol% CO_2. Hydrocarbon emplacement in the reservoir initiated at ~40 Ma (Marchand, 2001) while CO_2 charge is though to be around 70-80 Ma as has been discussed in the previous chapters. Hence, the relatively young fluid inclusions which were formed after CO_2 and hydrocarbon charge are expected to contain high contents of CO_2 and CH_4 or other hydrocarbon volatiles. However, LRM was only able to detect these species in very few inclusions (18 out of over 200). The small number of detection suggests that most of the fluid inclusions only trapped the fluid containing very low volume of dissolved gas species. The solubility of CO_2 in the formation water with TDS (~8 wt %) is less than 5 wt% under the reservoir conditions (pressure = 1-500 bar; temperature = 15-120 °C), according to data on CO_2 solubility in pure water (Kohl and Nielsen, 1997) and salinity affect (Enick and Klara, 1990). Solubility of CH_4 is even lower. Therefore, these concentrations of the dissolved species are probably below the resolution of the LRM (the resolution of the Raman spectrometer applied in this study is not defined because of lack of standard samples).

Previous studies on petrographic and fluid inclusion suggest retarding effects of oil charge on quartz cementation in the reservoirs of the Miller and Kingfisher Fields (Marchand, 2001). It is found that the mean T_h of fluid inclusion in quartz cements in oil zone is consistently lower than mean T_h of inclusions in water zone (Figure 6.7). The maximum T_h measured in the crestal areas of the reservoirs are around 95-105 °C which coincides with the hydrocarbon emplacement time (~40 Ma). The low T_h together with low quartz cement abundances is believed as evidence of hydrocarbon emplacement inhibiting quartz cementation. Most of the wafer samples examined in this study are from the oil zone. The lack of CO_2 and CH_4-rich fluid inclusions, therefore, may be due to the fact that quartz overgrowth has been largely hindered since hydrocarbon emplacement and little CO_2 and CH_4 were trapped in fluid inclusions.

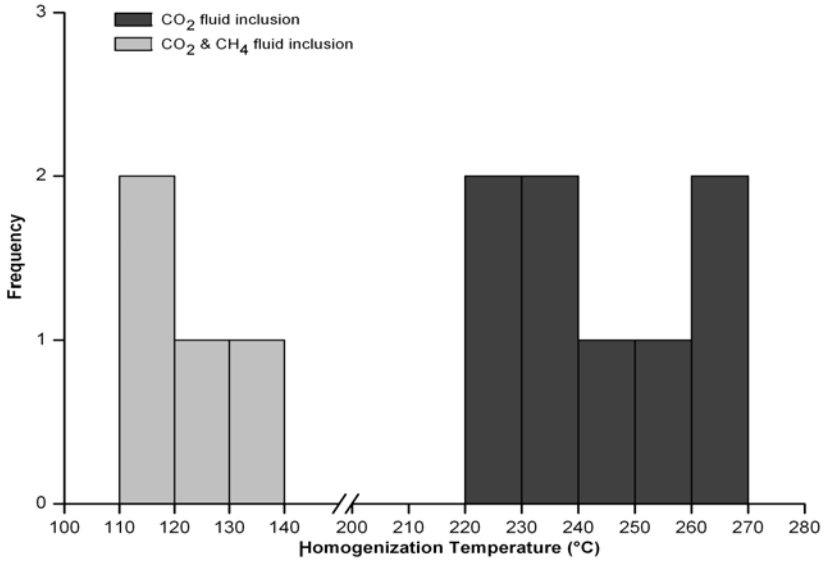

Figure 6.6 Histograms of homogenization temperatures (T_h) measured in aqueous fluid inclusions in quartz cement. Detailed data showed in Table 6.1. Two different types of fluid inclusions show distinctly different T_h. The fluid inclusions which contain CO_2 as the only gas component show high T_h ranging from 226°C to 265 °C, while those containing methane or both CH_4 and CO_2 have T_h similar to the present-day reservoir temperature of ~120 °C.

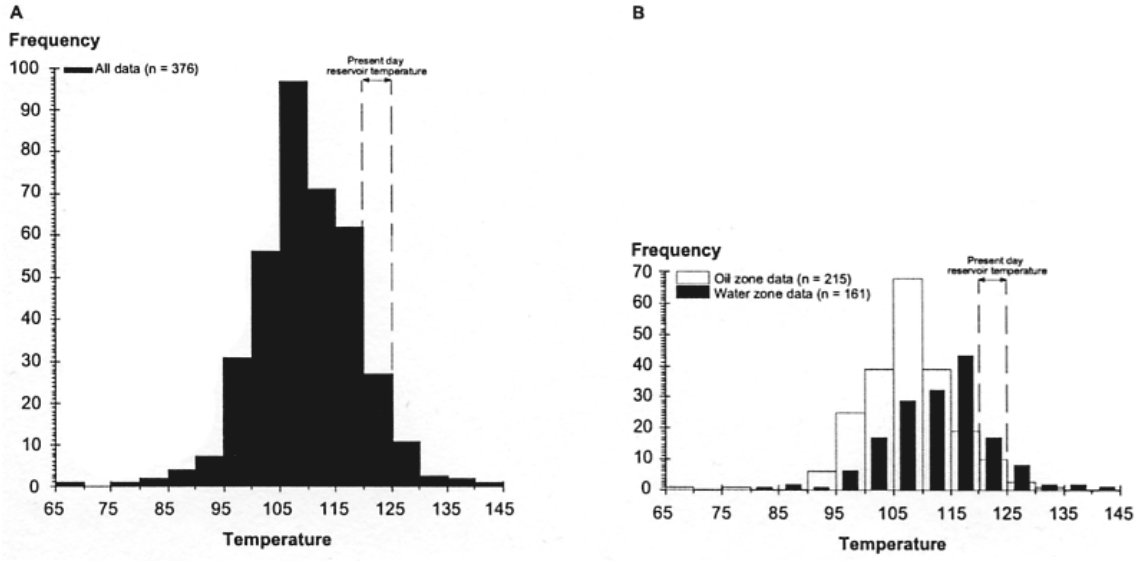

Figure 6.7 Histograms of homogenization temperatures (T_h) measured in aqueous fluid inclusions in quartz cements from Brae Unit 2 reservoir in the Miller Field. (A) all measurements; (B) Th data split into oil zone (blank bars) and water zone (black bars) groups. The peak temperatures in the oil zone group (105-110 °C) are lower than those of the water zone group (115-120 °C), suggesting that oil hindered quartz cementation (Marchand, 2001).

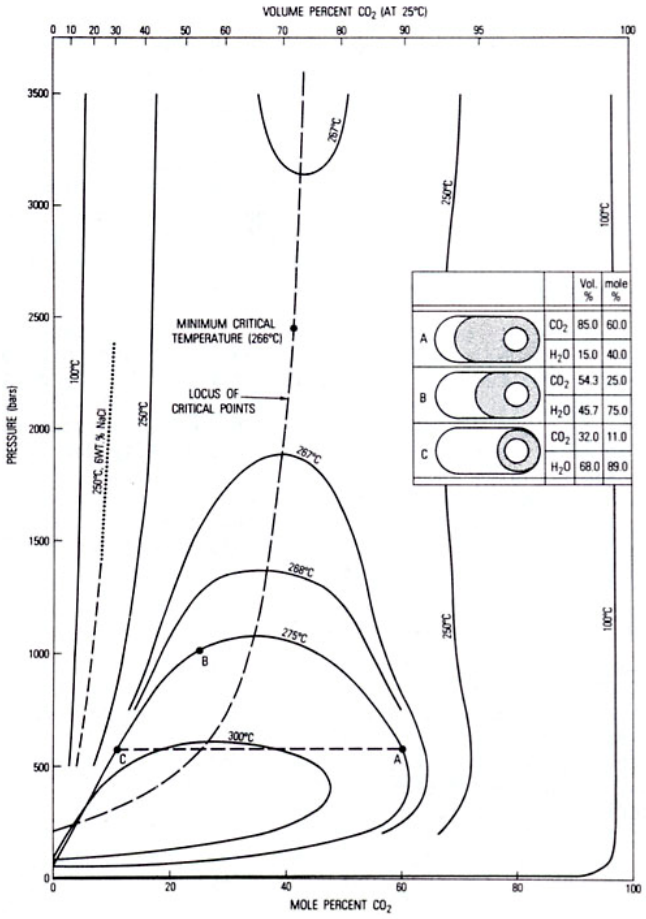

Figure 6.8 P-X plot of isotherms showing compositions of coexisting phases in system H_2O-CO_2. The upper abscissa shows volume percent CO_2 at 25 °C along the CO_2 liquid-vapour curve (64 bar), assuming densities of CO_2 liquid, CO_2 vapour and H_2O liquid of 0.71, 0.24 and 1.0 g/cm^3, respectively. The inset shows the two-dimensional appearance at the stated conditions for the three cylindrical inclusions having compositions as given (liquid CO_2 shaded), which are also shown on the diagram. The 250 °C isotherm for a 6 wt% NaCl solution from Takenouchi and Kennedy (1965) is shown for comparison (Roedder, 1984).

6.6.1. Type I inclusions

These inclusions contain two phases – gaseous CO_2 with small amount of H_2O vapour, and liquid H_2O with dissolved CO_2 (and, probably, dissolved salt). The H_2O vapour in the gaseous phase is difficult to detect by LRM. Dissolved CO_2 in aqueous phase was identified (Figure 6.4).

Salinity has a huge influence on pressure estimation of CO_2 and H_2O fluid inclusions. For example, if a 10 mol% CO_2 inclusion that had a T_h of 250 °C were trapped as a homogeneous fluid, Figure 6.8 shows that it would have had a minimum P_t of 750 bars, if we assume that the inclusion consists of CO_2 and pure H_2O. However, most CO_2-bearing fluid inclusions contain an aqueous salt solution rather than pure H_2O, adding further complexity to pressure and composition determination. When NaCl is added to the CO_2-H_2O system, the critical solubility of CO_2 at a given temperature and pressure decreases. The 250 °C isotherm for CO_2 solubility in a 6 wt % NaCl solution is shown in Figure 6.8 for comparison with pure H_2O. The minimum trapping pressure would have been ~2500 bars, much higher than that of non-salt inclusion.

The total CO_2 mol% in the inclusions can be estimated by referring T_h to the CO_2 solubility diagram when assuming the solution was CO_2 saturated during trapping. It is also can be estimated roughly from the volume percentage of the gas bubbles. In this study, the gas bubbles are smaller than 30 volume % of the fluid inclusions, suggesting CO_2 content of < 10 mole %. The P-X plot of isotherms show almost vertical isotherms for T_h lower than 250 °C (Figure 6.8) (Roedder, 1984). The T_h of Type I inclusions range from 226 to 265 °C, which allows very poor constraints on pressure, but suggests CO_2 content of below 10 mol%.

The need of pressure correction of the T_h measurements can be evaded by assuming that the aqueous and CO_2-rich fluids were in equilibrium at the time of their trapping. This assumption of simultaneous entrapment is supported by the similarity in shape, distribution, and mode of occurrence of the CO_2-rich inclusions. Consequently, the aqueous inclusions should have been CO_2 saturated at the time of trapping. Since any saturated fluid will exsolve its solute when cooling, a CO_2-rich gas phase should have exsolved at the beginning of cooling from the trapping temperature. Thus, the T_h measured represent the real trapping temperature, without a need for pressure correction, and the T_h intercepts on the isochores of

the CO_2-rich inclusions approximate the P-T conditions of trapping (Kisch and Van den Jerkhof, 1991).

The trapping temperatures which the T_h of Type I inclusions suggest are much higher than present-day reservoir temperatures of ~120 °C. This indicates that they formed during ancient igneous activities, rather than during quartz cementation during the burial. The CO_2 component these fluid inclusions trapped is that derived from ancient magma degassing, not that accumulated in the Miller reservoir. Hence, unfortunately, those fluid inclusions provide little information on the CO_2 charge during the burial of the Miller reservoir

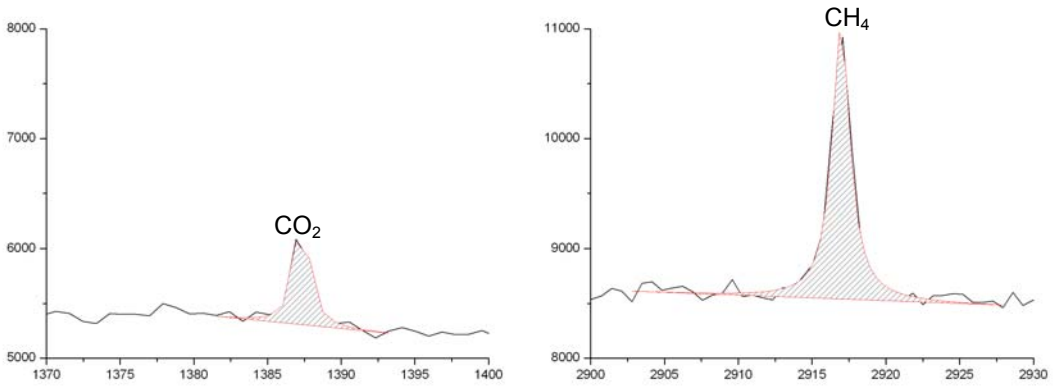

Figure 6.9 The curve fitting method to estimate the peak areas for CO_2 and CH_4 in Inclusion 10, 4186.4 m, well 16/7b-26. Area of the v_1-$2v_2$ upper band of CO_2 is calculated as 1854 units and that of the u_1 band of CH_4 is 5740 units, which give 42 mol% of CH_4 and 58 mol% of CO_2.

6.6.2. Type II inclusions

The presence of methane is believed to make the H_2O isotherms in P-T plot to near vertical; therefore, it makes pressure correction unnecessary because temperature changes little along the isotherms and T_h is very similar to T_t (Roedder, 1984). Type II fluid inclusions yield T_h similar to the present-day reservoir temperature, which suggests they formed at very late burial stage.

The concentrations of CO_2 in the gas phase in Inclusions 10, 11 and 14 are higher than those in normal sedimentary basins where CO_2 contents are depth-related and usually lower than 5 % (James, 1990). Therefore, those fluid inclusions had likely trapped the CO_2 accumulated in the Miller reservoir. T_h of Inclusion 10 and 11 are 123 and 136 °C, respectively, similar to present-day reservoir temperature, which suggest that they formed recently.

The compositional analysis was conducted on the gas bubbles of the inclusions. As the Raman activity of H_2O vapour is extremely weak, it is not possible to estimate its quantity. However, relative quantification of CO_2 and CH_4 in gas phase can be estimated from Raman spectrum based on polarizability theory. It was found that the contents of CO_2 and CH_4 vary strongly in different inclusions: some bubbles show high intensities for the CO_2 or CH_4 bands or both, while others show only a weak or no signal. The proportions of these two species in the gas bubbles were estimated using Equation 6.1 (Placzek, 1934). *F*-factors (relative to N_2) for CH_4 and CO_2 were taken from the study of Wopenka and Pasteris (1987) as 6.7 and 1.5 respectively. These *F*-factors are for low-density CH_4 and CO_2 gas mixtures up to about 15 bars total pressure. Such ratios for low density gas mixtures are the ones most appropriate for the inclusions in this study.

The peak areas were calculated using curve fitting method in OriginPro 7.5 provided by OriginLab Corporation. The upper v_1-$2v_2$ CO_2 band at 1388.2 cm^{-1} and the CH_4 band at 2916.8 cm^{-1} are used as the comparative bands in quantitative calculation. In inclusion 10, for example, CO_2 concentration in the gas phase is estimated at 58 mol% (Figure 6.9).

Salinity of the trapped solution can be estimated by converting T_m into wt% of NaCl equivalent using the conversion table from Bodnar (1992). The four T_m measurements (-0.1, -2.8, -3.4 and -5.1 °C) from Type II inclusions give salinity values of 0.2, 4.7, 5.6 and 8.0 wt % NaCl equivalent. Some of these values are comparable with the salinity of the present-day

formation water ranging from 7.3 to 8.3 wt % (Smalley and Warren, 1994). Both T_h and salinity of Type II fluid inclusions are similar to present-day reservoir conditions, confirming that they formed during late stage of burial. Unfortunately, they are not very informative in determining the timing of initial CO_2 emplacement.

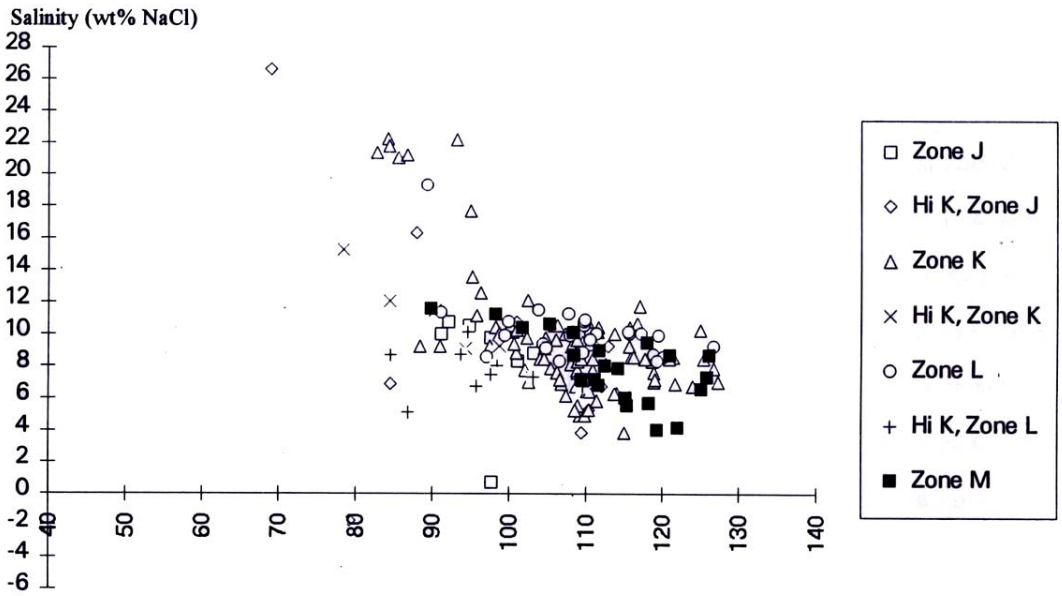

Figure 6.10 T_h (aqueous) versus salinity for Miller Wells 16/8b-3 and 16/8b-6 (Larter et al., 1995).

Previous fluid inclusion studies show that high salinities, up to 26 wt%, are recorded in the fluid inclusions with homogenizing temperature of ~ 70 °C in the Miller reservoir (Figure 6.10). Salinity decreases towards the present-day level as homogenization temperature increases. This indicates that a basinal water with high salinity was once imported into Miller at temperature of ~ 70 °C or lower. This timing coincides with estimated CO_2 charge at ~60-70 °C (~70-80 Ma) based on the carbonate isotopes. The underlying Zechstein evaporites is suggested as one possible source for the highly saline fluids (Larter et al., 1995; Wycherley et al., 1999). The associated graben boundary fault may have been the conduits for migration of the saline fluids and the CO_2 (Wycherley et al., 1999). Therefore, it is suggested that CO_2 migrated from deep along the boundary fault of the graben together with the basinal water which originated from the underlying Zechstein evaporates.

6.7. Conclusions

- Laser Raman spectroscopy is demonstrated as a powerful tool for qualitative analysis of fluid inclusions. It is demonstrated to be able to identify CO_2, CH_4 and N_2 in low-density gas phase in fluid inclusions at room temperature. The relatively young fluid inclusions which were formed after CO_2 and hydrocarbon charge are expected to contain high contents of CO_2 and CH_4. However, only 13 out of 200 fluid inclusions examined were detected to contain CO_2 or CH_4 or both. Nine of these 13 yielded homogenization temperatures much higher than reservoir temperatures, indicating that they formed during ancient igneous activities. The limited number of detection implies that quartz cementation was inhibited by hydrocarbon emplacement so that little free CO_2 and CH_4 were trapped by quartz cements.

- The fluid inclusions which contain only CO_2 as volatile species (Type I) yielded T_h ranging from 226 to 265 °C, much higher than the reservoir temperatures, suggesting that they were not formed during basin burial, but during ancient magmatic activities in the source area. Therefore, they are not able to provide information on timing of the CO_2 emplacement in the reservoir.

- The limited number of type II fluid inclusions show T_h close to present-day reservoir temperature of ~ 120 °C, suggesting very recent formation. They are not helpful to constrain the timing of CO_2 and methane emplacement, either.

- Relative quantitative analysis of gas phase in the fluid inclusions was conducted using Placzek's polarizability method. Three Type II inclusions were found to contain CO_2 contents higher than the levels in normal sedimentary basins, confirming that those fluid inclusions trapped the high CO_2 contents in the Miller reservoir. This demonstrates the feasibility of using this technique to trace

reservoired CO_2.

- T_m of Type II fluid inclusions range from -0.1 to -5.1 °C. They suggest low salinity values from 0.2 to 8.0 wt % NaCl equivalent, similar to the reported values of present-day formation water, also suggesting their young age.

CHPATER VII

GEOCHEMICAL MODELLING

7.1. Introduction

In a geological storage site, CO_2 could exist as a gas, a supercritical fluid, carbonic acid, a carbonate mineral, or some combination of some or all of these forms. However, the long-term fate of CO_2 in a geological formation is not well studied. The effect and the extent of the effect of CO_2 accumulation on reservoir rocks and cap rocks are not well understood.

Use of geochemical modelling to understand the long-term behaviour of injected CO_2 inengineered storage suffers from the lack of precise knowledge on the rates of the geochemical and physiochemical processes of various components under geological conditions. Previous studies aimed at understanding the impact of CO_2 on the geological system have commonly been designed using short-term experimental studies to replicate the expected conditions during CO_2 injection and retention (e.g. Gunter et al., 1997; Johnson et al., 2004). These use either measurements of present day physical and chemical conditions, or a range of values as primary inputs for forward modelling the final state of the CO_2. The short-term laboratory experiments, performed at elevated temperatures to produce results on a much shorter timescale, are limited and deal with only several variables instead of the huge complexity of nature. These approaches rely on generally incomplete datasets over short timescales, at least three or more orders of magnitude less than those required for geological storage. Furthermore, geochemical models have commonly been created in isolation of a detailed petrological assessment and without any calibration to natural analogues. Predicted mineralogy from poorly constrained geochemical models frequently does not match the mineralogy of natural sites. To accurately predict the long-term behaviour of CO_2 in a

geological storage site, geochemical models must be applied with calibration to observations from nature.

A large volume of CO_2 has been present in the Miller reservoir for ~70-80 millions years. The chemical reactions between CO_2, the rocks and the porewater are thought to have reached equilibrium over such a long time span. Thus the mineralogy of the rocks and the chemistry of the current formation water offer the opportunity for investigating long-term CO_2 reactions in the reservoir. Understanding the geochemical evolution of this natural CO_2-rich system will help in accessing the impact of high concentrations of CO_2 in geological formations.

The approach adopted in this chapter includes data selection of present-day mineral assemblage and formation water chemistry of the Miller reservoir, and extrapolation of the pre-CO_2 mineral assemblage and fluid chemistry. A geochemical evolution model of the reservoir is set up based on the data given by the previous chapters and the published studies (e.g. Larter et al., 1995; Marchand, 2001; Marchand et al., 2002; Baines and Worden, 2004). The model outputs are calibrated to the site-specific observations. The modelling applied in this study goes through a series of calibration steps to produce model outputs that closely match the field data. By varying input parameters, the diagenetic consequences of addition of CO_2 to the reservoir are thus inferred.

7.2. Methodology

Before commencing geochemical modelling, the conditions of the system must be fully defined. They include: mineral assemblage and proportion, aqueous species concentration, temperature, pH, Eh, and gas fugacity. In general, the models were designed for a fluid-mineral system from 10 to 120 ° C, with 1 kilogram water as solution. The modelling starts from an initial system of one litre of pore fluid and a virtual rock with approximately 30 % porosity (~2300 cm^3) into which various amount of CO_2 is progressively added to simulate the geological charge of CO_2. The mineralogical data of the Brae Formation sandstones are taken from the previous study by Marchand (2001). Formation water chemical data are obtained from the water analyses of the Miller Field (Smalley and Warren, 1994).

Geochemical modeling was then carried out using one of the many currently available codes – Geochemist's Workbench (GWB) with a standard thermodynamic database of minerals (Bethke, 2006). The modelling packages were then used to develop equilibrium based

reaction path models to predict the rock and fluid reactions. The model is refined, if necessary, to follow reaction pathways similar to those inferred from the Miller field.

Since a large volume of CO_2 has been present in the Miller reservoir since 70-80 Ma ago, it is assumed that equilibrium of the reactions between CO_2 and the reservoir rock has been achieved. In the modelling, mineral reactions are controlled by thermodynamic equilibrium and reaction kinetics is not considered. Equilibrium between the minerals and fluid compositions is achieved by dissolving under-saturated minerals, or precipitating super-saturated phases. The initial equilibrium state is constrained by applying parameters such as the amount of chosen minerals, the amount of dissolved components in the fluid, the fugacities of gases, pH and the oxidation state (Bethke, 1996). Where possible, the resulting predictions for CO_2-induced reactions are compared with observed diagenesis in the reservoir sandstones.

Once the initial equilibrium state of the system is reached, the model can trace a reaction path. Mass of any mineral or gas as reactant can be added or removed at each step over the course of the path. The React™ program of GWB then adds or removes a small amount of each of the phases specified and repeats the process. Under-saturation of the reactants results in dissolution, and over-saturation of the product phases results in precipitation until saturation is achieved. At saturation with respect to the added phase, there is an incremental increase of that specific phase from that point onwards (Kirste et al., 2004). Mineral content, solution composition and gas content diagrams can then be plotted.

7.3. Modelling configuration

The modelling is conducted in a temperature window between 10 and 120 °C. Each run is separated into two stages, the earlier one from 10 to 70 °C and the later one from 70 °C to 120 °C. The modelling starts from an initial water, which is represented by Jurassic sea water, reacting with a mineral assemblage. When equilibrium achieves at 70 °C, the entire system is picked up and packed as the initial system for the late stage modelling. A saline basinal water and certain amount of CO_2 are added as reactants into the new system. The modelling then runs until equilibrium is reached at 120 °C. The amount of basinal water and CO_2 input can be changed in different runs in order to find the best fitting case. The resulting quantities of the minerals, aqueous species and elements together with other status information are given relative to 1 kg of water at each stage.

Table 7.1 Mineral input and output per kg water for the modelling. The initial mineral input and the modelling results of the mineral assemblage at 70 °C and the final stage (120°C) are present. Two scenarios were run and their final outputs reported, one with 15 gram of CO_2 input at 70 °C and the other without.

Modelling stage	**Qrz**	**K-f**	**Py**	**Alb**	**Cal**	**Dol**	**Mus**	**Ill**	**Kao**	**Mesolite**	**Total**
Initial Input (g)	4200	900	60	120	300	0	60	180	180	0	6000
Result at 70 °C	4343	718.6	60	0	258.2	31.41	432.3		0	151.6	5995
Final (15 g CO_2)	**4412**	**607**	**60**	**0**	**293**	**35.45**	**576.6**		**0**	**17.33**	**6005**
Final (No CO_2)	4357	686	60	0	261	35.02	445.7		0	154.8	6003

Table 7.2 Formation Water analyses of the Miller Field (Smalley and Warren, 1994).

Sample No.	Well	Reservoir	Depth (m)	T (°C)	P (bar)	Density (g/cm)	R_w (Ω)	TDS (mg/kg)	pH
1	16/8b-2	Brae	4159	120	504	1.058	0.116	78157	6.7
2	16/8b-2	Brae	4159	120	504	1.058	0.114	78166	6.95
3	16/8b-3	Brae	4103	120	503	1.055	0.134	72211	7.66
4	16/8b-5	Brae	3980	120	500	1.052	0.125	69093	7.66
5	16/7b-24	Brae	4099	120	497		0.113	72363	7.5
6	16/7b-25	Brae	4099	120	492		0.112	74669	7.5

Sample No.	Cations (mg/kg)							Anions (mg/kg)		
	Na	K	Mg	Ca	Sr	Ba	Fe	Cl	SO4	HCO3
1	27221	1720	109	1002	104	974	9	45066	7	1957
2	27202	1730	109	1002	104	974	13	45047	8	1975
3	25595	1267	99	695	170	733	165	41267	5	2382
4	25274	818	109	477	77	799	2	40775	3	983
5	25898	1399	82	307	39	643	1	41767	4	2221
6	26560	1541	107	581	61	728	3	43526	4	1564

Table 7.3 The contents of the aqueous components at different modelling stage. Sea water composition, taken from Drever (1988), serves as the initial fluid of the modelling. The final fluid compositions of the two scenarios are presented together with the fluid composition at 70 °C (the end of the earlier modelling stage).

Modelling stage	Temperature (°C)	Density (g/cm^3)	Eh (volt)	pH	TDS (mg/kg)
Initial (sea water)	10			8.2	34,400
Before CO_2	70	0.996	-0.21	6.8	40692
Final (15 g CO_2)	**120**	**0.982**	**-0.17**	**5.7**	**77268**
Final (No CO_2)	120	0.983	-0.16	5.5	76568

Cations (mg/kg)								Anions (mg/kg)		
Na	Al	K	Mg	Ca	Sr	Ba	Fe	Cl	SO_4	HCO_3
10768	0.002	399	1292	412.3	8.14	0.02	0.002	19353	2712	140
14600	0.001	317	0.551	16.3	0.593	0.006	0.007	18600	2610	4630
27400	**0.003**	**2380**	**16**	**618**	**80**	**0.425**	**0.055**	**44700**	**1040**	**1260**
23400	0.002	3870	60.4	3110	199	2.28	0.079	45100	289	610

7.3.1. Mineral input

The mineralogy of the Brae Formation reservoir sandstone is conceptualized based on point-count results from the study by Marchand (2001). The reservoir sandstones consist predominantly of quartz (~ 89 %) and clays such as illite and kaolinite (~ 3 %) as well as

feldspars (mostly K-feldspar, occasionally plagioclase) (~ 3 %) and muscovite (~ 1 %). Rock fragments comprise a further ~4 % of the sandstone.

The main diagenetic events for the Brae Formation sandstones include calcite cementation, pyrite precipitation, K-feldspar dissolution, quartz overgrowth, clay mineral alteration and precipitation (Marchand, 2001). Calcite cement abundances range from 20 to 40 % in the concretion centres. These concretions are believed to start to form at very early burial stage. K-feldspar dissolution is extensive, and accounts for up to 15 % secondary porosity (Baines and Worden, 2004). Quartz overgrowth ranges from 3 to 15 %. Detrital clay minerals amount to ~ 2 % and authigenic clay is about the same amount. The virtual original composition of the reservoir sandstone is, therefore, inferred to consist of quartz (70 %), K-feldspar (15 %), Albite (2 %), Muscovite (1 %), calcite (5 %), kaolinite (3 %), illite (3 %) and pyrite (1 %) (Table 7.1). Calcite is introduced to present the shell fragments existing in the submarine deposits. Pyrite precipitation is among the earliest diagenetic events so that it is added into the initial system. In the modelling, muscovite is used as a proxy for illite and maximum microcline for K-feldspar. Six kilogram of minerals is added as reactants (the density of the virtual rock is taken as 2.6 g/cm^3). Table 7.1 shows the amount of the input minerals.

7.3.2. Fluid input

The formation water in the Miller reservoir has moderate salinity, with TDS ranging from 69093 to 78166 mg/kg (Smalley and Warren, 1994). Six analyses of produced water from five wells across the Miller Field are presented (Table 7.2). The waters are relatively high in K, low in Sr, very high in Ba and bicarbonate. Note that waters in other Brae Formation reservoirs in Brae-Miller area show very similar compositions, containing high concentration of Ba and bicarbonate.

As has been discussed above, the initial pore water of the Brae Formation is believed to be Jurassic marine water in origin whose chemical composition is shown in Table 7.3. However, geochemical modelling of sea water reacting with the minerals cannot produce the high salinity of the present-day formation water. A simple modelling of a closed system of the Brae Formation sandstone and sea water results in a final fluid with less than half of total dissolved solids (TDS) of the measurements. This suggests that there must be an additional input of the main components such as Na, K, Sr, Ba, Fe and Cl through a saline fluid charge. A saline basinal fluid flux is also suggested by the carbonate isotopic analysis. As it is

mentioned in Chapter 6, the fluid inclusion study found high salinities, up to 26 wt%, in the paleofluids at temperature of ~ 70 °C (Fig. 1). This indicates that a saline water was imported into the reservoir at temperature of ~ 70 °C or lower (~70 Ma or earlier).

The apparent source for such a water is the underlying Zechstein evaporites. In the Southern North Sea, most formation waters of the Permian Rotliegendes petroleum fields show salinities higher than 200 000 mg/kg (Warren and Smalley, 1994). High salinity formation waters are also reported in the oil reservoirs in Central Graben, such as the Gyda Field (TDS 232628 -252854 mg/kg) (Oxtoby, 1994), the Buchan Field (TDS 173748 and 173023 mg/kg) (Smalley and Warren, 1994), the Clyde Field (TDS 160865 -175907 mg/kg) (Wallis and Milton, 1994) and the Puffin Field (TDS 277360 mg/kg) (Warren and Smalley, 1994). These reservoirs either underlie or overlie Zechstein Group evaporates. Egeberg and Aagaard (1989) suggest that the highly saline formation waters are largely controlled by the brines originated from the underlying Zechstein evaporates.

Table 7.4 Formation Water analyses from the Gyda Field, the Central Graben, North Sea (Warren and Smalley, 1994).

Water No.	Well	Reservoir	Depth (m)	T (°C)	TDS (mg/kg)	pH
1	N2/1-6	Gyda	4225	154	252854	5.40
2	N1/3-3A	Gyda			239089	5.63
3	N2/1-6A	Gyda	4000		232628	5.40

Cations (mg/kg)							Anions (mg/kg)			
Na	K	Mg	Ca	Sr	Ba	Fe	Cl	Br	SO_4	HCO_3
59553	5414	2210	28771	987	488		154610	821	1697	79
51343	3319	2764	31898	828	259	405	148180			63
54749	4991	2036	26490	910	451	88	142808			74

Thus, in the case of the Miller Field, a basinal saline fluid derived from the underlying Zechstein evaporates may also be responsible for the high salt contents recorded by the fluid inclusions and the medium salinity of the formation water. Assuming the highly saline formation waters in the hydrocarbon fields mentioned above preserved the original element proportions of the basinal fluid derived from evaporates, they can be used as a proxy of the basinal fluid. The Gyda Field is located in the Central Graben, geographically closer to the Miller field. The reservoir formation of the field is also late Jurassic in age and is underlain by Zechstein salt at depth. Its formation water is amongst the most saline of all central North Sea waters (Oxtoby, 1994), suggesting a direct association with the evaporites. Therefore, a Gyda Field formation water (Water 1 in Table 7.4) is chosen to represent the basinal fluid which is added into the modelling system at 70 °C.

CO_2 is introduced as a gas reactant in modelling. Its quantity is variable in order to match the modelling results to the reality. During repetitive run, it is found that an input of 15g CO_2 produces fluid compositions fit best for the present-day formation water. The best fitting scenario is presented here. CO_2 is added in the model at temperature of 70 °C. Different temperatures were tested, but the results do not vary significantly.

7.4. Modelling Results

Numerous scenarios were run with various amount of input of basinal water and CO_2. The results match the reality best when 0.25 kg of the basinal water (Gyda Formation Water 1, Table 7.4) and 15 g CO_2 are added at 70 °C. The mineral and fluid data at final stage of the modelling are presented in Table 7.1 and 7.3. The results of the scenario without additional CO_2 being added are also presented in Table 7.3. This serves as a comparison to highlight the effect of CO_2 on the system. The mineral reaction paths for the late modelling stage between 70 and 120 °C are shown in Figure 7.1 and 7.2, respectively for the CO_2-charge and non-CO_2 scenarios.

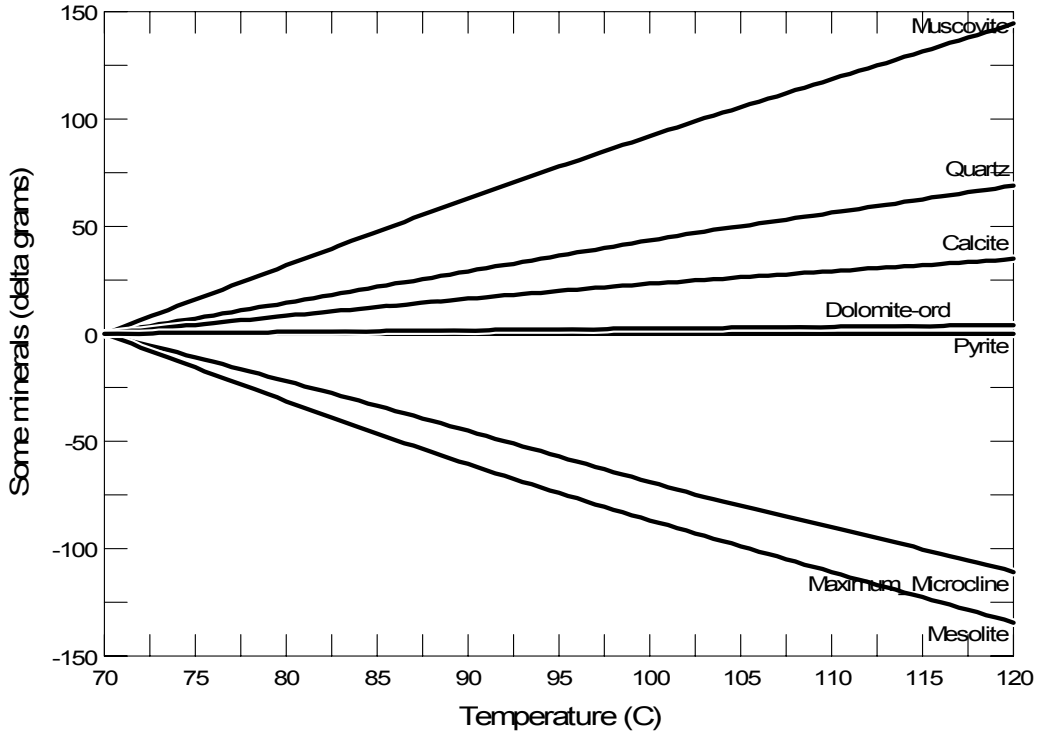

Figure 7.1 Mineral reaction paths from 70 to 120 °C for the CO_2-charge scenario. 0.25 kilogram of Gyda water 1 (Table 7.4) and 15 CO_2 are added into modelling system at 70 °C. Then temperature continuously increases to 120 °C. It shows that quartz, illite (muscovite) and calcite precipitate during the process while zeolite (mesolite) and K-feldspar (Maximum microcline) undergo constant dissolution. The amounts of mineral change are relative to 1 kg of water.

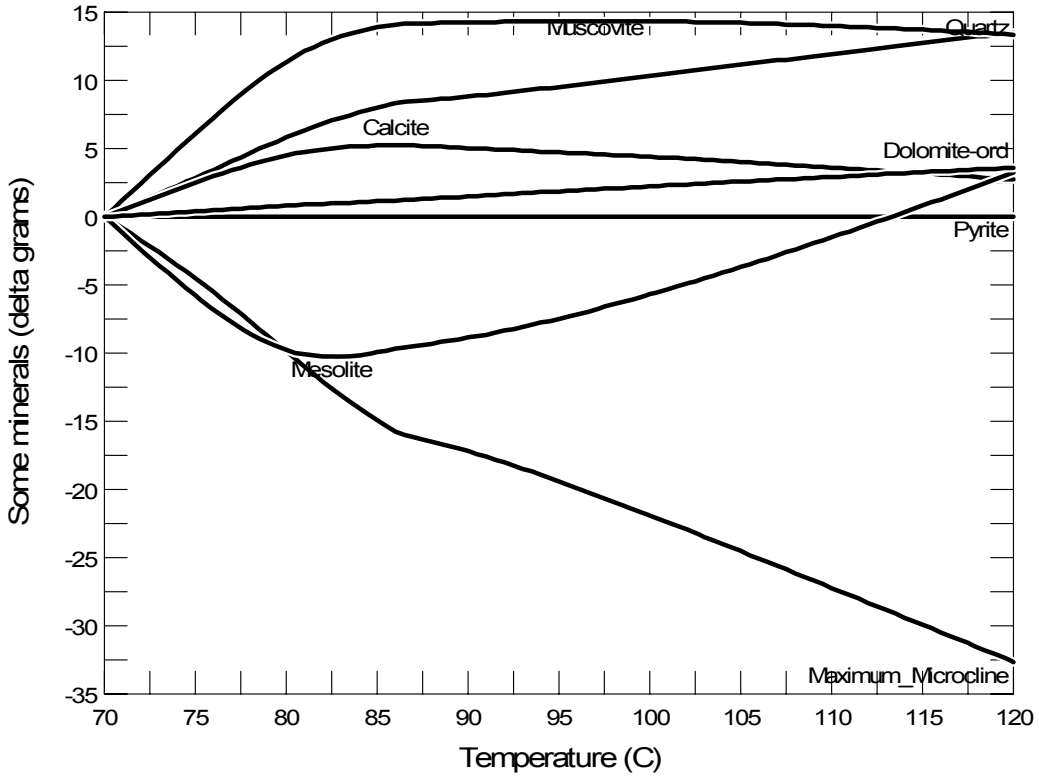

Figure 7.2 Mineral reaction paths from 70 to 120 °C for the non-CO_2 scenario. Same initial conditions are applied, but no CO_2 is added. Quartz, illite (muscovite) and calcite precipitation is much less than in the case with CO_2 added. The amount of K-feldspar (Maximum microcline) dissolution is also reduced. Note the difference in scale between Figure 7.1 and this.

It is found that the amount of feldspar decreases through the whole modelling process of both scenarios (Table 7.1, Figure 7.1 and 7.2). In the earlier stage of the modelling, over 180 gram of K-feldspar and all albite (120 g) are dissolved by sea water. Another 120 g of K-feldspar dissolves after CO_2 and the basinal water are added at 70 °C. In the non-CO_2 scenario, the basinal water only dissolves about 30 g K-feldspar in the later stage.

Over 570 g of muscovite is present in the final mineral assemblage of the CO_2-charge scenario, amounting to 9.6 % of the whole rock, while there is 445 gram of muscovite in the non-CO_2 scenario. 180 gram of kaolinite dissolves completely by the sea water and it does not precipitate in the later modelling stage.

Quartz increases in the both cases, though the amount of precipitation in CO_2-charge scenario is much greater than non-CO_2 case. The model shows that 143 gram of additional quartz precipitates before 70 °C and another 70 g from 70 to 120 °C. However, the amount of quartz only increases 14 gram in the later stage of non-CO_2 scenario.

Calcite decreases in the earlier stage. But about 35 gram of it precipitates after CO_2 is added, while only 3 g does without CO_2. Sea water is found to be able to dissolve calcite while producing dolomite. The basinal water and CO_2 do not insignificantly increase dolomite precipitation.

Large volumes of mesolite, a sodium calcium zeolite, forms during the earlier stage. Between 70 and 120 °C, it largely dissolves in the presence of CO_2, while its volume increases slightly when no CO_2 is added.

Comparing the final fluids of both scenarios to the present-day formation water, it is clear that the scenario with additional CO_2 produces the better match (Table 7.2 and 7.3). In this scenario, most of the main aqueous components of the final fluid show similar concentrations to the reality. Aqueous calcium concentration decreases from 412.3 to 16.3 mg/kg before CO_2 charge and increases to 618 mg/kg after CO_2 is added (Table 7.3). Bicarbonate concentration increases rapidly from 140 to 4630 mg/kg between 10 and 70 °C. Surprisingly, additional CO_2 reduces bicarbonate concentration to 1260 mg/kg in the following stage. Adding the basinal fluid and CO_2 increases the other main components, such as Na, K, Cl, Mg, to the present levels.

The resultant barium and sulphate ion concentrations, however, differ greatly from the formation water. Aqueous barium concentration of the CO_2 scenario is 0.425 mg/kg, much lower than the real content in the formation water which ranges from 643 to 974 mg/kg. Sulphate ion concentration in the modelling (1040 mg/kg) is much higher than the reality (< 10 mg/kg). It is not possible to produce a fluid with right contents of both the components in this model.

Overall, CO_2-charge scenario produces higher total dissolved solids (TDS). 15 gram of additional CO_2 leads to an increase of TDS of 700 mg/kg. Besides increasing HCO_3 and reducing Ca concentration, CO_2 greatly increases Na concentration by 4000 mg/kg and reduces K by 1400 mg/kg.

7.5. Discussion

7.5.1. Mineral reactions

CO_2 solubility is controlled by the temperature, pressure and composition of the formation water. In an unbuffered system, dissolution of CO_2 acidifies the formation water. However,

in a system containing reactive mineral phases, the decrease in pH is buffered by reactions involving mineral phases (i.e. aluminosilicates, carbonates etc.) or hydrogen ions (H^+). These reactions can be divided into two types; one that buffers the pH only, and the other that incorporates the carbonate molecule (i.e. the formation of carbonates) (Gunter et al., 1993).

Equations 7.1 and 7.2 show the reaction series where iron-rich chlorite reacts to form kaolinite, and the free iron and magnesium is subsequently available to form siderite. This series of reactions have been proposed in the study based on the natural accumulations of CO_2 in the Pretty Hill Formation of the Otway Basin, south eastern Australia (Watson et al., 2003).

$$Fe_4MgA_{l2}Si_3O_{10}(OH)_8 + 10H^+ \rightarrow 4Fe^{2+} + Mg^{2+} + Al_2Si_2O_5(OH)_4 + SiO_{2(aq)} + 7H_2O \quad (7.1)$$

$$4Fe^{2+} + Mg^{2+} + 5HCO_3^- \rightarrow 5Fe_{0.8}Mg_{0.2}(CO_3)_5 + 5H^+ \quad (7.2)$$

Ca/Mg/Fe-bearing silicate minerals (such as feldspar and micas) are believed to be able to form significant pH-buffer. High CO_2 contents tend to dissolve silicate minerals and precipitate clay minerals, carbonates and quartz when the acidity has been reduced by silicates dissolution. The two types of reactions can be incorporated into a single reaction system (Gunter et al., 1997; Hitchon et al., 1999):

$$\text{Feldspar} + \text{Clays} + CO_{2(aq)} + H_2O \rightarrow \text{Kaolinite} + \text{Ca/Mg/Fe carbonate} + \text{Quartz} \quad (7.3)$$

Dissolution of plagioclase feldspar as a pH-buffer is also proposed by Kirste et al. (2004):

$$2NaAlSi_3O_8 + 2H^+ + H_2O \rightarrow 2Na^+ + Al_2Si_2O_5(OH)_4 + 4SiO_{2(aq)} \quad (7.4)$$

These reactions all predict dissolution of feldspar minerals, while dissolution or precipitation of carbonates depends on actual water acidity and chemistry. In each case the dissolution and precipitation reactions are a function of the thermodynamic factors and the rates of these reactions are a function of the chemical kinetic parameters.

This modelling study suggests that the additional CO_2 does increase feldspar dissolution, carbonate and illite precipitation. Especially for K-feldspar, adding CO_2 increases corrosion by three times. CO_2 seems to drive the following reaction.

$$3KAlSi_3O_8 + H_2O + CO_2 + Ca^{2+} \rightarrow 2K^+ + KAl_2(Si_3Al)O_{10}(OH)_2 + 6SiO_2 + CaCO_3 \quad (7.5)$$

Precipitation of muscovite, the proxy of illite, is the most significant reaction revealed in the modelling. CO_2 is found to be responsible for the additional 130 g muscovite precipitation in the CO_2-charge scenario. Large quantity of illite precipitation absorbs K and Al released from dissolution of K-feldspar and in the solution. This explains that the final K concentration in this scenario, where larger volume of K-feldspar dissolves, is lower than that of the non-CO_2 scenario.

The modelling of CO_2-charge scenario, total dissolution of K-feldspar and albite amounts to 7 wt % of the whole rock. In reality, dissolution of feldspar is estimated to have created up to 15 % amounts of secondary porosity (Baines and Worden, 2004). Pointcount data from Marchand (2001) suggest that feldspar dissolution only produced 1.7 ± 1.2 % secondary porosity. Note that in pointcount study feldspar dissolution is only recognized when remains of K-feldspar grains exist, or when large secondary pores are outlined by relict clay. This inevitably leads to underestimation of the dissolution. Therefore, 7 % of feldspar dissolution in the modelling could be a reasonable match to reality.

The modelling shows that the typical product of feldspar dissolution, kaolinite, does not form. In fact, the initial input of 180 gram of kaolinite is dissolved. It is a well known problem that kaolinite is not commonly observed in the Brae Formation reservoir sandstones in the Brae-Miller area, although feldspar dissolution is extensive (McLaughlin et al., 1994). The modelling indicate that illite, instead of kaolinite, is the product of feldspar dissolution. But the mass balance is still a problem. 7 wt% of feldspar dissolution would produce 5.5 wt% of authigenic illite according to the modelling, while pointcount study reveals that authigenic clay in the Brae Formation sandstones is less than 3.5 % (Marchand, 2001). This indicates that part of the aluminium released from feldspar dissolution was exported from the sandstones, as has been proposed by McLaughlin et al. (1994).

Quartz overgrowth is the main cementation in the Miller reservoir, ranging from 2.7-15.4 % (Marchand, 2001; Marchand et al., 2001). Quartz overgrowths are observed in early calcite

concretions, suggesting quartz precipitation at burial depth < 1.5 km (burial temperatures < 60 °C). Homogenization temperatures of the fluid inclusions in quartz overgrowths range from 70 °C to 120 °C, indicating that quartz cementation occurred over long periods and is still ongoing at the present time (Marchand, 2001). Our modelling does predict a continuous quartz precipitation. Quartz precipitation amounts to 140 g in the early stage and 70 g after the basinal fluid and CO_2 are introduced. Silicon is mainly sourced by dissolution of K-feldspar and albite.

In the modelling, the majority of the quartz precipitation occurs between 10 and 70 °C while only an small portion of the total authigenic quartz forms from 70 – 120 °C, suggesting that the sea water and the mineral assemblage have large capacity of producing quartz. However, precipitation of quartz is believed to mainly occur during deep burial (> 2.5 km) at elevated temperatures, typically 70 -130 °C (Giles et al., 1992; Gluyas et al., 1993), though small amounts of quartz cement may develop slowly at lower temperature (Bjørkum et al., 1998). This is because, at low temperatures in the early burial stage, it is likely that the kinetics of the geochemical processes rather than temperature controls the reaction rates (Worden and Morad, 2000). The modelling does not incorporate reaction rate laws from the field of geochemical kinetics. This probably leads to an overestimate of quartz precipitation at low temperatures.

However, the modelling shows that sea water dissolves pre-existing calcite rather than precipitates it. Over 40 gram of calcite dissolves during the earlier modelling stage. Clearly, sea water encourages calcite dissolution rather then precipitation. But, large volume of calcite concretions in the Brae Formation sandstones is believed to have started forming in very early burial (Marchand 2001). This mismatch is possibly due to the fact that early calcite cements is largely sourced by dissolution of bioclasts in reality. The transformation from bio-carbonate to carbonate cements is not considered as chemical reaction in the modelling.

Modelling suggests that additional CO_2 greatly increases calcite precipitation from the basinal water charge. From 70-120 °C in the CO_2-charge scenario, 35 g calcite and 4 g dolomite precipitate which equal to 17 g CO_2 sequestration. 15 g CO_2 input is completely consumed. Bicarbonate, whose concentration decreases from 4630 mg/kg at 70 °C to 1260 mg/kg at 120 °C, also supply a fraction of carbon for the carbonate precipitation. But overall

abundance of the precipitated carbonates is less than 1 %, which explains why no isotopic evidence of CO_2 charge-associated carbonates is found in the Brae Formation sandstones.

The volume of zeolites (mesolite) increases in the later stage of the non-CO_2 scenario, while it is almost completely consumed in the CO_2-charge scenario. It indicates that addition of CO_2 greatly dissolves zeolite. Baines and Worden (2004) also suggest that the zeolite minerals containing bivalent cations would act as pH-buffer to the aqueous dissolution of CO_2. These minerals are capable of supplying bivalent cations to carbonate precipitation. This modelling shows that zeolite dissolution provides Ca cations for calcite precipitation. Zeolite is not found in the Miller reservoir sandstones. It is difficult to determine whether it was dissolved by CO_2 charge, or there was not any through the whole burial history.

7.5.2. Aqueous components

Most aqueous components in the final fluid of the CO_2-charge scenario, except barium and sulphate ion, show concentrations within or close to the ranges of those of the water sample (Table 7.2 and 7.3). The agreement between the modelled fluid and actual formation water supports the hypothesis of basinal fluid and CO_2 charge.

In the early stage of modelling (10-70 °C), aqueous calcium released from calcite dissolution is largely absorbed by precipitation of zeolite and dolomite. Precipitation of them results in the decrease of Ca from 412.3 to 16.3 mg/kg despite the fact that over 40 gram of calcite dissolves. Increase of Ca concentration after the CO_2 charge is resulted from zeolite dissolution even when relatively large amount of calcium is consumed by carbonate precipitation. Therefore, in the modelling, zeolite serves as a calcium reservoir which stores it when carbonates dissolves and supplies it when carbonate precipitation is favoured.

Bicarbonate ion (HCO_3) concentration is controlled by carbonate reactions. It is raised by 30 times when large amount of calcite dissolves in the early stage, and then decreases when both calcite and dolomite precipitates after the basinal fluid and CO_2 are added. The modelling indicates that the capacity of CO_2 sequestration as dissolved bicarbonate phase is relatively small in this case. The final fluid of the CO_2-charge scenario contains 1260 mg/kg HCO_3 which accounts for less than 1 g CO_2 equivalent.

Very high contents of barium occur in the Brae Formation in the Brae-Miller area. Barium concentration is as high as 2322 mg/kg in the Central Brae Field, the highest in the North

Sea (Hardy and Hart, 1994). High barium content in the Miller formation water (up to 974 mg/kg) caused severe scaling problems during production. Such high barium content cannot be explained by this modelling. Ba in sea water (0.02 mg/kg) obviously can contribute only a very small fraction of the high Ba content. The saline formation waters in the Central and South North Sea, also containing lower barium contents, fail to reproduce the high Ba content at Miller. Apparently, there must be additional source for barium besides initial captured sea water in pore space and the later basinal water flux. This additional source and migration path is constrained to the Brae-Miller area. The modelled fluid contains much higher sulphate ion content than the measurements. This mismatch is the other side of barium problem. In the Brae Formation water, the very high barium content tends to precipitate barite which greatly reduces the concentration of sulphate ion.

7.5.3. Reservoir evolution model

The modelling suggests that the reactions between sea water and the original mineral assemblage of the Miller reservoir are not capable of producing the salinity and composition of the formation water. The equilibrium between sea water and the original reservoir sandstone produces lower salinity (40692 mg/kg), little over half of measurements (69093-78166 mg/kg) (Table 7.2 and 7.3). The proportions between the main aqueous components, such as Na, K, Ca, Cl and HCO_3, are different from the present-day formation water. This suggests the Miller reservoir has undergone a more complex fluid evolution history.

It is demonstrated in the modelling that the basinal water derived from the underlying Zechstein evaporites may have played an important role in the geochemical evolution of the formation water. The modelling found that an addition of the saline fluid which is represented by the Gyda formation water (Table 7.4) is necessary to match modelling results to the present-day water analyses. A saline fluid influx at the ratio of 1 to 4 original marine type pore water can produce a fluid with similar chemical composition to that of the Miller formation water. This supports the hypothesis of basinal water influx at about 70 °C inferred by the fluid inclusion microthermometric data (Larter, 1995; Marchand, 2001).

The modelling reveals that CO_2 can be an important influence on the mineral reactions, and consequently, the mineralogy and the pore fluid chemistry. By comparing the CO_2-charge scenario with the non-CO_2 scenario, it is clear that the additional CO_2 drives certain chemical reactions, such as dissolution of feldspar and zeolite, precipitation of quartz, carbonates and

illite. These reactions control the concentrations of the main aqueous components, such as K, Ca, Mg, HCO_3 etc.

7.6. Conclusions

- Geochemical modelling is demonstrated to be able to improve understanding the complex reactions in the geological system. It helps to explain the formation water evolution in the Brae Formation reservoir of the Miller Field. The overall good agreement between the modelling results and the observations supports the evolution model, in which the initial pore water mainly consisted of sea water and a later basinal fluid influx together with a CO_2 charge largely shaped the chemistry of the present-day formation water.

- It is demonstrated that the basinal water derived from the underlying Zechstein evaporites may have influenced the geochemical evolution of the Miller formation water. The modelling found that mixing between the saline fluid represented by Gyda formation water and the original marine type pore water at ratio of 1 to 4 could produce a fluid with the chemical composition of the Miller formation water. This supports the hypothesis of a basinal water influx at about 70 °C inferred from microthermometric data (Larter, 1995; Marchand, 2001).

- Modelling suggests that CO_2 should have played an important role in diagenesis. The modelling results of different scenarios indicate that the additional CO_2 would enhance dissolution of feldspars which is coupled by precipitation of clay mineral, quartz and carbonates. But observations on the reservoir sandstones in the previous chapters fail to identify any significant CO_2-induced reactions. This may be because that the CO_2-affects are relatively small and swamped by earlier diagenetic and original deposition processes.

- Illite, instead of kaolinite, is found in the modelling to be the product of feldspar dissolution. This coincides with the well known problem of ‘missing’ kaolinite in the Brae Formation sandstones in the region (McLaughlin et al., 1994). It suggests that kaolinite does not always accompany feldspar dissolution. But, in reality, the extensive feldspar dissolution with low authigenic illite abundance indicates an export of aluminium from the sandstones.

- The very high barium contents in the Brae-Miller area can not be explained by this model. Sea water and the basinal fluid from the evaporites account for only a fraction of Ba content measured in the formation water. Apparently, there must be additional barium sources. High barium content consequently depresses sulphate ion concentration in the real formation water.

CHAPTER VIII

SYNTHESIS AND SUMMARY OF THESIS

The Miller Oil Field contains naturally high contents of CO_2 (~28 mol%) (Baines and Worden, 2004). With accessible drilling cores, logs and published data, the field constitutes an ideal analogue site for engineered geological CO_2 storage. An extensive investigation on the reservoir and cap rocks was conducted in order to understand the long-term fate of retained CO_2 in the geological formation and predict effects of injected CO_2 on the storage sites.

The Miller Field is situated in the western margin of the South Viking Graben in block 16/7b and 16/8b of the UK North Sea (Figure 2.1 and 2.2). The reservoir is located in the Upper Jurassic Brae Formation sandstones at depth of 3970 – 4090 m TVD. It is a combined structural and stratigraphic trap (Garland, 1993). The reservoir sandstones comprise the mid-fan part of an extensive syn-rift submarine fan complex which was sourced from the west. The Kimmeridge Clay Formation (KCF) laterally interfingers with the reservoir sandstones. Thus it directly overlies and underlies the reservoir sandstones and provides the source and seal for the reservoirs in the region (MacKenzie et al., 1987; Rooksby, 1991).

The Brae Formation underwent continuous burial since the time of deposition until the present-day depth of ~4 km and burial temperature of ~120 °C. It is composed of three main lithofacies: dominant clean well-sorted quartzose sandstone; thinly bedded alternations of sandstone and mudstone; and isolated mudstones locally interbedded within the main part of the reservoir. The KCF was deposited in a deep water anoxic environment during regional rifting and subsidence in the latest Jurassic, leading to deposition of organic-rich ‘black’

shales interbedded with thin sand/silt beds in most of the graben areas of the North Sea (Ziegler, 1982). The anoxic water with stratified water oxygenation and high sedimentation rates preserved the organic matter.

In the Brae-Miller region, CO_2 contents in the hydrocarbon reservoirs show a decrease away from the Central and South Brae Fields which are bounded by the western boundary fault of the South Viking Graben (Figure 2.4). The CO_2 distribution indicates that it migrated up the boundary fault and first filled the Central Brae and South Brae Field before migrated laterally to reach the surrounding fields.

At Miller, maturity calculations indicate that the KCF source rocks started generating oil at around 40 Ma, when they were buried to 3100-3400 m (Figure 2.9) (Marchand, 2001). Oil was generated on the flanks of the structure in the immediately surrounding source rocks and, thus, the migration path is very short (e.g. Turner and Allen, 1991; Marchand et al., 2002). Oil entered the reservoir via the flanks of the anticline structure and migrated the along shale barriers (Figure 2.11). The first oil accumulated in small closures in shales while some ponded at the crestal part of the reservoir. With progressive filling, oil migrated upwards and accumulated in the crest (Smalley et al., 1993).

Most of the samples examined in this study are from the shales and the coarser-grained silty and sandy beds in the overlying KCF. The KCF samples extend from the reservoir top to 60 m above reservoir crest. The mudstones and sandstones within the Brae Formation were also sampled and analyzed using the same techniques. The interval immediately above and below the reservoir top was sampled with the highest sampling frequency (~20 cm).

SEM analyses reveal that the coarser-grained silty and sandy lithologies within the KCF have undergone a diagenetic history similar to that of the Brae Formation sandstones, while the shales in the KCF show a distinctly different diagenesis.

Overall, the KCF shales suffered extensive dissolution of quartz and feldspar with little evidence of precipitation except very early growth of framboidal pyrite. Dissolution initiated at the earliest burial stage and prevailed through the whole burial stage. Quartz and feldspar grains are ubiquitously corroded. The severe corrosion is thought to be encouraged by high organic content which generates organic acids in the ambient porewater (Carothers and Kharaka, 1978; Drever and Stillings, 1997). Solubility of quartz and other silicates can be enhanced through complexing with organic compounds which are released during

transformation of organic materials (Taguchi et al.; 1988). Little quartz overgrowth occurred in the KCF, implying that the dissolved silica had been exported. This may have been a source for quartz cementation in the adjacent sandstones. Astin and Evans (1990) estimated that shales may typically lose 10-20 % of their solid volume during digenesis, primarily through quartz dissolution and silica export. The KCF shales contain a large quantity of framboidal pyrite precipitated prior to significant compaction. Pyrite precipitation was associated with the reactions of organic matter through microbial sulphate-reducing.

The silty and sandy lithologies in the KCF have gone through more complex diagenetic sequences. Shortly after deposition of the sediments, framboidal pyrite was first to precipitate, though its abundance is much lower than in the shales. Dissolution of quartz and feldspar began at early burial stage. Quartz overgrowth initiated prior to main compaction phase and lasted until recent time. Calcite, dolomite and ankerite cementation commonly postdate quartz and feldspar dissolution and early quartz cementation. Pore-filling carbonate cementation continued until very recent times. Kaolinite precipitation occurred in the same period as carbonate cementation. Euhedral albite, pyrite and the heavy minerals such as apatite, anatase, rutile and zircon are among the latest precipitation products. The overall diagenetic sequences of the KCF are summarized in Figure 4.21A.

In the Brae Formation sandstones, the early diagenetic events include the precipitation of framboidal pyrite and calcite concretions. This was followed by quartz overgrowth. Feldspar dissolution occurred either concomitantly with, or shortly after the onset of quartz precipitation, producing significant secondary porosity (up to 15 %). K-feldspar dissolution is sometimes accompanied by diagenetic kaolinite. The diagenesis of the Brae Formation sandstones is shown in Figure 4.21B.

The influx of CO_2 into the Miller reservoir has been proposed to be the driving factor for feldspar dissolution in the Brae Formation sandstones (e.g. Hitchon et al., 1999; Baines and Worden, 2004; Kirste et al., 2004). K-Feldspar is the most important pH-buffer mineral in the Brae Formation sandstones. Its dissolution is coupled with calcite precipitation. This reaction is sensitive to pH which can be controlled by CO_2 (Worden and Morad, 2000). Geochemical modelling within this current study also suggests that CO_2 charge enhances feldspar dissolution and produced carbonates. However, these CO_2-related reactions are not identified in the following mineralogical data and carbonate isotopes in the reservoir section. This may be because that the quantities of the resulting carbonate and other mineral products

are very small so that their isotope signatures and associated mineralogical variations are swamped by the early depositional signals.

Three Miller wells show rather abrupt vertical variations in mudrock mineralogy across the reservoir top, including upwards increase of quartz, decrease of feldspar and increase of kaolinite (Figure 3.6, 3.10 and 3.11). No such variations are present in the low-CO_2 control well (Figure 3.3). This suggests that these mineralogical variations are probably associated with the CO_2 accumulation in the reservoir. The reaction of dissolving K-feldspar to produce quartz, clay minerals and carbonates (Equation 3.2) is thought to have occurred in the bottom part of the KCF seal, while it was largely inhibited in the reservoir shales by hydrocarbon charge. The uneven reactions caused mineralogical variations between the seal and reservoir shale.

However, the above interpretation has several difficulties. Firstly, SEM study revealed extensive quartz dissolution with little evidence of quartz overgrowth in the KCF shales (e.g. Figure 4.1). This means that the high quartz content in the KCF has a primary sedimentary origin. Secondly, the variation of quartz abundance in shale across the boundary between the KCF and the Brae Formation is too large to be explained solely by the CO_2 reactions. In well 16/8b-3, 16/8b-A1 and 16/8b-A2, for example, average quartz abundance in the KCF shales is up to 35 % higher than that of the shales in oil leg. Such large mineralogical variations can only be derived from original sedimentary heterogeneity. Thirdly, no obvious and consistent mineralogical variations across the oil-water contact can be seen. This also argues against the hypothesis that CO_2 reactions took place in the seal but were hindered by oil in the oil leg. But, there is possibility that the OWC has been in the present position for only a short period. If so, the CO_2 reactions may have yet to produce detectable mineralogical differences across the OWC. Similar mineralogy between the oil leg and the water leg cannot be used to argue against the CO_2 reactions.

Therefore, it can be concluded that the observed mineralogical variations across the formation boundary, especially those of quartz, are likely to be associated with the original sedimentary heterogeneity rather than CO_2-induced reactions. The lack of definite mineralogical evidence does not necessarily rule out CO_2 reactions. But it means that the CO_2 did not necessarily cause significant alterations which whole rock XRD analysis can detect. The alterations are largely obscured by the original heterogeneities of the rocks. The strong varying content of original quartz makes it difficult to identify any relatively small

mineral variations related to CO_2 reactions. Further mineralogical analyses on CO_2-low fields are needed in order to quantify the original sedimentary variations and the CO_2-induced mineralogical alterations.

In well 16/8b-A2 of the Miller Field, the stable carbon isotopes of carbonates in shale reveal a striking linear trend with depth in an 'anomalous zone' of ~12m thick overlying the reservoir. Above this zone, $\delta^{13}C$ values are scattered randomly. The $\delta^{13}C$ in the reservoir sit around the high-$\delta^{13}C$ end of the trend (Figure 5.6). The control well does not show such a linear isotopic trend (Figure 5.10). No systematic lithologic heterogeneity in this part of the KCF was observed in the drill cores or wireline logs. Hence, the isotopic trend is not a sedimentary feature, but is related to the CO_2 accumulation in the underlying reservoir.

The randomly scattered data above the trend represent the conventional diagenetic carbonates which precipitated from sulphate reduction and methanogenesis of organic matter during early burial stage. The average $\delta^{13}C$ -5.3‰ of these carbonates reflect the influence of both processes. The carbonates in the thin shale beds within the reservoir section are in equilibrium with the CO_2 accumulated in the reservoir ($\delta^{13}C$ = -8.2 ‰) at ~60-70 °C, suggesting that the CO_2 charge initiated at about ~70-80 Ma. The carbonate at the bottom of the trend ($\delta^{13}C$ = -0.77 to -1.7‰) is also in equilibrium with that CO_2 at similar temperatures. It can be deduced that CO_2 started penetrating into the seal immediately after its emplacement and triggered and influenced the resetting of carbon isotopic composition of the carbonates in the anomalous zone.

In the 'anomalous zone', the large $\delta^{13}C$ range within the anomalous zone (-0.77 to -7.4‰) eliminates temperature as the sole control, because a 60 °C variation could only produce ~3‰ difference in $\delta^{13}C$ value of precipitated carbonates. A carbon model with linearly variable carbon isotopic compositions with depth must be considered.

A model of mixing of three carbon source is preferred to explain the observed isotopic versus depth trend very well. In the model, the anomalous zone constitutes an interval where three individual carbon sources mix. The first is the infiltrated CO_2 from the reservoir accumulation with $\delta^{13}C$ signature of -8.2 ‰. Its percentage in the mixing source linearly decreases upwards from 80 to 46 %. The second carbon source with $\delta^{13}C$ of -20 ‰ is produced by decarboxylation of organic matter in the KCF. Its percentage increases upwards from 0 to 34%. The third carbon source is derived from the dissolution of the original

carbonates (average $\delta^{13}C$ value of -5.3 ‰). Mixing of these three individual carbon sources at such proportions leads to a mixing source with linearly varying isotopic compositions. Carbonates precipitated from the mixing source in the time span from 70 Ma to present-day fit the observed trend very well.

The important conclusion of the model is that, to produce such a trend, the amount of reservoir CO_2 which infiltrates into the cap rock must be limited. If a large flux of CO_2 had occurred, the carbonate isotopic values would have simply been set to a more or less constant value in the anomalous zone. This argues against wholesale transport of CO_2 through the seal. The estimated CO_2 infiltration rate is about $9.8\times10^{-7}g\cdot cm^{-2}\cdot y^{-1}$ over last 70 million years. This small leakage rate gives great safety margin for engineered storage of CO_2 under such a mudrock seal.

Coarser grained-silty and sandy lithologies in the KCF show similar $\delta^{13}C$ versus depth pattern in the Miller well 16/8b-A2. However, the anomalous zone is thinner (~ 5 m) than that of the shale (~ 12m). The difference in thickness of the anomalous zones may be due to differential advancing of the front of carbonate dissolution and reprecipitation in different lithologies. The coarser lithologies contain much higher original carbonates than the shales. Though the CO_2 infiltrating front has reached further up, the front of complete dissolution of original carbonate may have only reached 5 m up in the silt/sands of the seal. Significant amounts of remaining original carbonates may remain in the silts/sands above the 5 m anomalous zone, obscuring the isotopes of the new carbonates precipitated from the infiltrating CO_2.

Except the unusual carbonate isotopic trends, there is no other evidence of abnormality within the ‘anomalous zone’. XRD mineralogical data of well 16/8b-A2 do not show any obvious systematic variations across the anomalous zone to suggest CO_2-induced reactions (Figure 3.11). In fact, feldspar abundance within the zone is slightly higher (5.6 %) than that above it (4.0 %). Inorganic carbon contents in the anomalous zone of well 16/8b-A2 increases upwards and the average content within the zone is lower than that of the overlying unaltered zone (Figure 5.14). No evidence suggests that breaching CO_2 resulted in feldspar dissolution and carbonate precipitation in the anomalous zone. CO_2 infiltration did not cause any noticeable mineral reactions, except that it induced isotope resetting of the carbonates in the breaching zone. This further demonstrates the integrity of the mudrock seal in face of the high contents of CO_2.

A previous fluid inclusion study (Larter et al., 1995) found high salinities, up to 26 wt%, in the paleo-fluids trapped at temperature of ~ 70°C (70Ma) in the Miller reservoir (Figure 6.9). Salinity decreases towards the present day level. This indicates that a basinal water with high salinity was imported into the reservoir at that time. This coincides with the estimated timing of the CO_2 charge at 70-80 Ma from the isotopic data. Hence, it is suggested that CO_2 migrated from depth together with the very saline basinal water at ~70 Ma.

Geochemical modelling confirms that the basinal fluid influx together with CO_2 charge largely controlled the chemistry of the reservoir formation water. It is found that the reactions between sea water and minerals are not capable of producing the high salinity of the present-day formation water. The basinal water is likely to be derived from the underlying Zechstein evaporites. The formation water of the Gyda Field, which is very saline and is heavily influenced by the evaporites, was used as a proxy for the basinal water flux in modelling and delivered a good match to reality. This confirms the hypothesis of a basinal water influx together with the CO_2 charge at about 70 Ma (~70 °C, ~1800 m).

Present-day CO_2 in the Miller reservoir has an average $\delta^{13}C$ value of -8.2 ‰ V-PDB, within the range of those from other CO_2-rich fields in the region (James, 1990). The stable carbon isotope signatures of the CO_2 accumulations in this area are variable (-3.0 to -10.4 ‰), suggesting mixing in varying proportions between different types of sources (James, 1990; Baines and Worden, 2004). The relative heavy values indicate an inorganic origin most likely related to thermal degradation of deeper marine carbonates (Baines and Worden, 2004). The lighter carbon isotopic compositions, as James (1990) suggests, are typical of that derived from thermal maturation of organic matter. As a consequence, the variability of $\delta^{13}C$ of CO_2 observed in the South Viking Graben appears to be a mixture of inorganic CO_2, generated from thermal destruction of deep carbonates, migrating up through the graben boundary fault to the shallower reservoirs, with organically-derived CO_2 component.

The timing of CO_2 charge coincides with the general phase of uplift in the British area and the sudden increase of subsidence rate in the North Sea from the late Cretaceous. At the beginning of the Tertiary, ancient faults lines in the North Sea were reactivated. This is interpreted as a renewed phase of rifting during which the axial zone of the North Sea began a major phase of subsidence, and simultaneously the Scotland-Shetland Platform was uplifted along the western margin (Selley, 1976). Subsidence and deposition rates in the

South Viking Graben show a sudden increase at the beginning of the Tertiary due to the renewed activity of the boundary fault (Figure 2.9). The migration and infilling of CO_2 and the basinal water are likely to be associated with the fault activities at the graben margin, which may have opened up conduits for fluid migration from depth. Thermal alteration of the underlying carbonates may also be induced by the rapid burial.

An attempt to investigate the trapped gas species in quartz fluid inclusion was made. Laser Raman Microprobe (LRM) was demonstrated as a powerful tool to detect CO_2, CH_4 and N_2 in low-density gas phase in fluid inclusions. However, CO_2 and CH_4 were detected only in a very limited number of fluid inclusions, implying that quartz cementation was largely hindered by hydrocarbon emplacement and little free CO_2 and CH_4 phases were trapped.

Relative quantitative analysis of gas phase in the fluid inclusions was conducted using Placzek's polarizability method. CO_2 concentrations higher than those in normal sedimentary basins were detected in three inclusions which formed during basinal burial. This demonstrates the feasibility of using this technique to trace reservoired CO_2. Other CO_2-rich fluid inclusions yielded T_h ranging from 226 to 265 °C, much higher than the reservoir temperatures, suggesting that they were formed during ancient magmatic activities in the source area. The trapped CO_2 in those inclusions is a product of magma degassing.

Results presented in this thesis offer a valuable insight into long-term interactions between CO_2, brine and rock-forming minerals and the effects CO_2 could have on the rocks. This study demonstrated that the high content of CO_2 in the Miller reservoir did not result in any significant petrographic and mineralogical alterations both in the reservoir rock and the cap rock. Considering that CO_2 was emplaced at ~70 Ma, the rates of the alterations of the rocks are very slow. For engineered storage of man-made CO_2, injected CO_2 would not severely damage reservoir rocks and mudrock seals during designed storage time. Leakage through an integral mudrock seal is also unlikely, as the KCF mudrocks appear to have retained the CO_2 charge successfully for ~70-80 million years. This will assure the science communities and the public that long-term safe storage of man-made CO_2 at suitable sites is a safe solution to increasing atmospheric CO_2 levels.

Conclusions

- The Miller Field has a naturally high content of CO_2 (~28 mol %), charged when the reservoir was at ~1.8 km burial, from carbonates in the deep Viking Graben. The

CO_2 has been reservoired for the past 70 Ma, and predates the charge of oil.

- The high contents of CO_2 have not caused significant effects on reservoir sandstones. Carbonate cements in the reservoir sandstones, the potential products of CO_2 reactions, precipitated primarily at early burial stage, without isotopic signatures of the reservoired CO_2. The CO_2 accumulation has been retained as dissolved phases and free phase, rather than solids.

- Detailed mineralogical data on the mudstone in the reservoir and the seal failed to identify definite CO_2-related reactions, suggest that the accumulated CO_2 has not induced mineralogical alterations beyond depositional heterogeneities.

- The additional CO_2 has produced a characteristic ^{13}C isotope signature in carbonate cements within the bottom of the seal. This suggests that vertical seepage has been minor, so that mudrocks are dominated by pore-scale isotopic effects, not swamped by leakage from the reservoir. CO_2 infiltration can be detected up to 5m above the reservoir in siltstones, and up to 12m above the reservoir in mudrocks.

- This mudrock seal, now at 4km, 120 ºC, has successfully retained CO_2 for geologically long periods with no adverse effects. Mudrock seals, of similar mineralogy and grainsize, for engineered CO_2 storage in similar temperature and depth settings should be secure.

Future work

- The future study on CO_2-mudrock reaction should focus on building a larger baseline dataset of sealing mudrocks mineralogy both of CO_2-rich and CO_2-low fields. This study shows that the effects of high concentration of CO_2 on mudrock is not significant and are obscured by original mineralogical variations. A large database of mineralogy of mudrocks which have not been in contact with high concentration of CO_2 would be helpful in eliminating background depositional variations and making the CO_2 reactions obvious.

- The origin of the abnormally high concentrations of CO_2 in this region is still not well understood. It is noticed that CO_2 $\delta^{13}C$ roughly decreases from -3 to -12 ‰ from west to east in the Sleipner area (James, 1990). The Sleipner CO_2 is

consequently interpreted as mixing of inorganic CO_2 source with CO_2 derived from maturation of organic matter. The isotopic variations are suggested to be related to migration, mixing and differences in migration pathways. But the correlation between $\delta^{13}C$ and location is uncertain due to the small number of data. And there is only one $\delta^{13}C$ value is available in the Miller Field and no data in the Brae fields to allow analysing the regional variations. Therefore, a detailed survey of carbon isotopic composition of CO_2 accumulation in the region is needed to address this problem. The variability of CO_2 $\delta^{13}C$ from well to well, field to field, will help in determining the CO_2 sources and the varying proportion between them across the region.

- The carbonate carbon isotopic data provides evidence on the distance of CO_2 infiltrating into the bottom of the seal. This proves that the infiltration rate is very low. Mass balance calculation suggests that the infiltration was in the form of free phase CO_2 fluid (see section 5.7.5). But the mechanism of CO_2 breaking through is poorly understood. It is not sure whether it was through pores, through dense microfractures, or through scarce fractures. Future study on this will improve understanding on CO_2 migration through sealing mudrocks.

- The timing of the CO_2 charge is not very well constrained. Fluid inclusions which trapped ancient pore fluids can provide direct evidence for the presence of early CO_2 in the past. Laser Raman Microprobe (LRM) was demonstrated in this study as a powerful tool to detect CO_2 in low-density gas phase in fluid inclusions, though it failed to find a large enough number of CO_2-rich fluid inclusions. Future work should aim at increasing the detecting limit for CO_2 and analysing more fluid inclusions. If a large dataset of homogeneous temperature of CO_2-rich fluid inclusion is obtained, the uncertainty on the time of CO_2 emplacement will be greatly reduced.

- Geochemical modelling based on equilibrium was demonstrated to be able to assess the fluid evolution in the reservoir. But modelling incorporated with kinetics is worth pursuing in order to estimate the rates of diagenetic reactions and the effects of additional CO_2 on the reaction rates.

REFERENCES

Arts R., Brevik I., Eiken O., Sollie R., Causse E. and Van Der Meer L., 2001. Geophysical methods for monitoring marine aquifer CO_2 storage: Sleipner experiences. In: Williams D., Durie B., McMullan M., Paulson C. and Smith A. (eds.) Proceedings of the 5th International Conference on Greenhouse Gas Control Technologies. Cairns, Australia, p. 366-371. CSIRO Publishing, Collingwood, Australia.

Astin T.R. and Evans I.J., 1990. Volume-loss through silicate dissolution during shale diagenesis; implications for modelling the compaction and maturation histories of clastic sequences. 13th International sedimentological congress; Abstracts of papers. p. 29.

Baines S.J. and Worden R.H., 2004. The long-term fate of CO_2 in the subsurface: natural analogues for CO_2 storage. In: Baines S.J. and Worden R.H. (eds.) Geological storage of carbon dioxide. Geological Society of London, Special Publications 233, p. 59-85.

Baldwin B. and Butler C.O., 1985. Compaction curves. AAPG Bulletin, v. 69, p. 622-626.

Barnard P.C. and Bastow M.A., 1991. Petroleum generation, migration, alteration, entrapment and mixing in the Central and Northern North Sea. In: England W. and Fleet A. (eds.) Petroleum migration. Geological Society of London, Special Publication, 59, p. 167-190.

Berner R.A., 1984. Sedimentary pyrite formation: an update. Geochimica et Cosmochimica Acta, v. 48, p. 605-615.

Bethke C.M., 1996. Geochemical reaction modelling. Oxford University Press, Oxford.

Bethke, C.M., 2006, The Geochemist's Workbench, version 6.0, A User's Guide to Rxn, Act2, Tact, SpecE8, and Aqplot, Hydrogeology Program: Oxford, Oxford University Press, 397 p.

Bish D.L., 1994. Quantitative X-ray diffraction analysis of soil. In: Amonette J E and Zelazny L W (eds.) Quantitative method in soil mineralogy. Soil Science Society of America, Madison, USA. p. 267-295.

Bish D.L. and Post J.E., 1989. Modern powder diffraction. Mineralogical Society of America, Reviews in Mineralogy 20, p. 369.

Bjørkum P.A., Oelkers E.H., Nadeau P.H., Walderhaug O. and Murphy W.M., 1998. Porosity prediction in quartzose sandstones as a function of time, temperature, depth, stylolite frequency, and hydrocarbon saturation. AAPG Bulletin, v.82 (4), p. 637-648.

Bjørlykke K., 1989. Formation of secondary porosity: how important is it? In: McDonald D. A. and Surdham R.C. (eds.) Clastic diagenesis. AAPG Memoirs 37, p. 227-286.

Bodnar R.J., 1992. Current research on fluid inclusions – a brief introduction. Geochimica et Cosmochimica Acta, v. 56 (1), p. 3.

Bodnar R.J., Reynolds T.J. and Kuehn C.A., 1985. Fluid inclusion systematics in epithermal systems. In: Berger B.R. and Bethke P.M. (eds.) Geology and Geochemistry of Epithermal Systems. Review of Economic Geology, v. 2, p. 73-97.

Bonham L.C., 1978. Solubility of methane in water at elevated temperatures and pressures. AAPG Bulletin, v. 62, no. 12, p. 2478-2481.

BP and Conoco (UK), Santa Fe Minerals (UK) and Saxon Oil, 1988. Miller Oil Field development and production programme, Annex B,

Brosse E., Yan le Galle and Magnier C.C., 2002. Long-term mineral trapping of CO_2 in aquifers and reservoirs: integration of thermodynamics and kinetics in reservoir engineering and geological simulation. Environmental Geosciences. Abstract, v. 9, no. 3, p. 159.

Buhrig C., 1989. Geopressured Jurassic reservoirs in the Viking Graben: modelling and geological significance. Marine and Petroleum Geology, v. 6, p. 31-48.

Burley S.D., Mullis J. and Matter A., 1989. Timing diagenesis in the Tartan Reservoir (UK North Sea); constraints from combined cathodoluminescence microscopy and fluid inclusion studies. Marine and Petroleum Geology, v. 6, p. 98-120.

Calvert C.S., Palkowsky D.A. and Pevear D.R., 1989. A combined X-ray powder diffraction and chemical method for the quantitative mineral analysis of geological sample. In: Pevear D.R. and Mumpton F.A. (eds.) Clay Mineral Workshop Lectures Volume 1. Quantitative mineral analysis of clays. Clay Mineral Society, Evergreen, Colorado, USA. p. 154-166.

Carothers W.W. and Kharaka Y.K., 1978. Aliphatic and anions in oil-field waters - Implication for origin of natural gas. AAPG Bulletin, v. 62, p. 2441-2453.

Chadwick R.A., Holloway S. and Riley N., 2000. Deep CO_2 sequestration offshore, a provable greenhouse mitigation strategy. Offshore Magazine, p. 124-135.

Chadwick R.A., Holloway S., Brook M.S. and Kibby G.A., 2004. The case for underground CO_2 sequestration in northern Europe. In: Baines S.J. and Worden R.H. (eds.) Geological storage of carbon dioxide. Geological Society of London, Special publications 233, p. 17-28.

Chadwick R.A., Zweigel P., Gregersen U., Kirby G.A., Holloway S. and Johannessen P.N., 2003. Geological characterization of CO_2 storage sites: lessons from Sleipner, Northern North Sea. In: Gale J. and Kaya Y. (eds.) Greenhouse gas control technologies. Elsevier Science. v.1, p. 321-326.

Clayton J.L., Spencer C.W., Koncz I. and Szalay A., 1990. Origin and migration of hydrocarbon gases and carbon dioxide, Békés Basin, southeastern Hungary. Organic Geochemistry, v. 15(3), p. 233-247.

Cole H.K., Steger G.R. and Spencer D., 1993. The capacity of the deep oceans to absorb carbon dioxide. Energy Conversion and Management. V.34, No. 9-11, p. 991-998.

Cornford C., 1998. Source rocks and hydrocarbons of the North Sea. In: Glennie K.W. (ed.) Petroleum geology of the North Sea: basic concepts and recent advances, 4th edition. Oxford : Blackwell Science, p.376-462.

Curtis C.D., 1978. Possible links between sandstone diagenesis and depth related geochemical reactions occurring in enclosing mudstones. Journal of Geological Society, London, v. 135, p. 107-117.

Curtis C.D., 1987. Inorganic geochemistry and petroleum exploration. In: Brooks J. and Welte D. (eds.) Advances in petroleum geochemistry, Academic Press, London, v. 2, p. 91-140.

Czernichowski-Lauriol I., Banjum B., Rochelle C., Bateman K., Pearce J. and Blackwell P., 1996. Analysis of the geochemical aspects of the underground disposal of CO_2. In: Apps J.A. and Tsang C. (eds.) Deep injection disposal of hazardous and industrial waste. Academic Press, p. 565-683.

Davison J., Freund P. and Smith A., 2001. Putting carbon back in the ground, IEA Greenhouse R&D Programme, Cheltenham, UK, February.
http://www.ieagreen.org.uk/ccs.html.

Deines P., Langmuir D. and Harmon R.S., 1974. Stable carbon isotope rations ad the existence of a gas phase in the evolution of carbonate ground water. Geochimica et Cosmochimica Acta, v. 38, p. 1147-1164.

Di Primio R. and Skeie J.E. (2004): Development of a compositional kinetic model for hydrocarbon generation and phase equilibria modelling: A case study from Snorre Field,

Norwegian North Sea. In: Cubitt J.M., England W.A. and Larter S.R. (eds.) Understanding petroleum reservoirs: towards an integrated reservoir engineering and geochemical approach, Geological Society, London, p. 157-174.

Dickinson R.G., Dillon R.T. and Rasetti F., 1929. Raman spectra of polyatomic gases. Physical Review, v. 24, p. 582–589.

Drever J.I., 1988. The geochemistry of natural waters, 2nd edition. Prentice-Hall, Englewood Cliffs, New Jersey, USA.

Drever J.I., and Stillings L.L., 1997. The role of organic acids in mineral weathering. Colloids and Surfaces A: Physicochemical and Engineering Aspects, v. 120, p. 167-181.

Egeberg P.K. and Aagaard P., 1989. Origin and evolution of formation waters from oil fields on the Norwegian shelf. Applied Geochemistry, v. 4, p. 131-142.

Enick P.M. and Klara S.M., 1990. CO_2 solubility in water and brine under reservoir conditions. Chemical Engineering Communications, v. 90, p. 23-33.

Etheridge D.M., Steele L.P., Langenfelds R.L., Francey R.J., Barnola J.M. and Morgan V.I., 1998. Historical CO2 record derived from a spline fit (75 year cutoff) of the Law Dome DSS, DE08, and DE08-2 ice cores. http://cdiac.ornl.gov/ftp/trends/co2/lawdome.smoothed.yr20.

Field J.D., 1985. Organic geochemistry in exploration of the northern North Sea. In: Thomas B.M., Dore A.G., Eggen S.S., Home P.C. and Lasen R.M. (eds.) Petroleum Geochemistry and exploration of the Norwegian Shelf. Graham & Trotman, London, p. 39-57.

Fletcher K.J., 2003a. The Central Brae field, Blocks 16/07a, 16/07b, UK North Sea. In: Gluyas J.G. and Hichens H.M. (eds.) United Kingdom Oil and Gas fields, Commemorative Millenium Volume. Geological Society of London, Memoir 20, p. 183 –190.

Fletcher K.J., 2003b. The South Brae field, Blocks 16/07a, 16/07b, UK North Sea. In: Gluyas J.G. and Hichens H.M. (eds.) United Kingdom Oil and Gas fields, Commemorative Millenium Volume. Geological Society of London, Memoir 20, p. 211 – 221.

Frantz J.D., Popp R.K. and Hoering T.C., 1992. The compositional limits of fluid immiscibility in the system H_2O-NaCl-CO_2 as determined with the use of synthetic fluid inclusions in conjunction with mass spectrometry. Chemical Geology, v.98, p. 237-255.

Friedman I., and O'Neil J.R., 1977. Compilation of stable isotope fractionation factors of geochemical interest. In: Fleischer M. (ed.) Data of geochemistry, United States Geochemical Survey professional paper 440KK, sixth edition: Reston, Virginia, p. 1-12.

Gambardo M. and Donagemma V., 2003. The T-Block fields, Block 16/17, UK North Sea. In: Gluyas J.G. and Hichens H.M. (eds.) United Kingdom Oil and Gas fields, Commemorative Millenium Volume. Geological Society, London. p. 369 – 382.

Garland C.R., 1993. Miller Field: reservoir stratigraphy and its impact on development. In: Parker J.R. (ed.) Petroleum Geology of Northwest Europe: Proceedings of 4th Conference. Geological Society, London. p. 401-414.

Garland C.R., Haughton P., King R.F. and Moulds T.P., 1999. Capturing reservoir heterogeneity in a sand-rich submarine fan, Miller Field. In: Fleet A.J. and Boldy S.A.R. (eds.) Petroleum geology of Northwest Europe: Proceedings of the 5th Conference. Geological Society, London. v. 2, p. 1199-1208.

Glasmann J.R., 1992. The fate of feldspars in Brent Group reservoirs, North Sea: a regional synthesis of diagenesis in shallow, intermediate and deep burial environments. In: Morton A.C., Haszeldine R.S., Giles M.R. and Brown S. (eds.) Geology of Brent Group. Geological Society of London, Special Publication 61, p. 329–350.

Glasmann J.R., Clark R.A., Larter S., Briedis N.A. and Lundegard P.D., 1989. Diagenesis and hydrocarbon accumulation, Brent Sandstone Jurassic, Bergen High area, North Sea. AAPG Bulletin, v. 73, no. 11, p. 1341-1360.

Gluyas J.G., Robinson A.G., Emery D., Grant S.M. and Oxtoby N.H., 1993. The link between petroleum emplacement and sandstone cementation. In: Parker J.R. (ed.) Petroleum geology of NW-Europe. Geological Society of London, p. 1395-1402.

Greenwood P.J., Shaw H.F. and Fallick A.E., 1994. Petrographic and isotopic evidence for diagenetic processes in middle Jurassic sandstone and mudrocks from the Brae area, North Sea. Clay Minerals, v. 29, p. 637-650.

Gunter W.D., Perkins E.H. and McCann T.J., 1993. Aquifer disposal of CO_2-rich greenhouse gases: reaction design for added capacity. Energy Conversion and Management, v. 34 (9-11), p. 941-948.

Gunter W.D., Wiwchar B. and Perkins E.H., 1996. Autoclave experiments and geochemical modelling. In: Hitchon B. (ed.) Aquifer Disposal of Carbon Dioxide, Hydrodynamic and Mineral Trapping-Proof of Concept. Geoscience Publishing Ltd., p. 115-161.

Gunter W.D., Wiwchar B., Perkins E.H., 1997. Aquifer disposal of CO_2-rich greenhouse gases: extension of the time scale of experiment for CO_2-sequestering reactions by geochemical modelling. Mineralogy and Petrology, v. 59, p. 121-140.

Hanor J.S., 1980. Dissolved methane in sedimentary brines: potential effect on the PVT properties of fluid inclusions. Economic Geology, v. 75, p. 603-609.

Hardy J.A. and Hart R.G., 1994. The Central Brae Field. In: Warren E.A. and Smalley P.C. (eds.) North Sea Formation Waters Atlas. Geological Society of London, Memoir 15, p. 16.

Hardy R.G. and Tucker M.E., 1988. X-ray powder diffraction of sediments. In: Tucker M.E. (ed.) Techniques in Sedimentology. Blackwell, Oxford, p. 191-228.

Harris J.P. and Fowler R.M., 1987. Enhanced prospectivity of the Mid-Late Jurassic sediments of the South Viking Graben, northern North Sea. In: Brooks J. and Glennie K., (eds.) Petroleum geology of North West Europe. Graham & Trotman. p. 879-898.

Haszeldine R.S., Brint J.F., Fallick A.E., Hamilton P.J., and Brown S., 1992. Open and restricted hydrologies in Brent Group diagenesis: North Sea. In: Morton A.C., Haszeldine R.S., Giles M.R., and Brown S. (eds.) Geology of the Brent Group. Geological Society of London, Special Publication 61, p. 401-419.

Haszeldine R.S., Quinn O., England G., Wilkinson M., Shipton Z.K., Evans J.P., Heath J., Crossey L., Ballentine C.J. and Graham C.M., 2005. Natural Geochemical Analogues for Carbon Dioxide Storage in Deep Geological Porous Reservoirs, a United Kingdom Perspective. Oil & Gas Science and Technology - Review. IFP 60 (1), p. 33-49.

Haugen P.M. and Drange H., 1992. Sequestration of CO_2 in the deep ocean by shallow injection. Nature, v. 357, p. 318-320.

Hendry J.P., Wilkinson M., Fallick A.E. and Haszeldine R.S., 2000a. Ankerite cementation in deeply buried Jurassic sandstone reservoir of the Central North Sea. Journal of Sedimentary Research, v. 70 (1), p. 227-239.

Hendry J.P., Wilkinson M., Fallick A.E. and Trewins N.H., 2000b. Disseminated "jigsaw piece" dolomite in Upper Jurassic shelf sandstones, central North Sea; an example of cement growth during bioturbation? Sedimentology, v. 47, p. 631-644.

Hepple R.P. and Benson S.M., 2003. Implications of surface seepage on the effectiveness of geologic storage of carbon dioxide as a climate change mitigation strategy. In: Gale J. and Kaya Y. (eds.) Greenhouse gas control technologies. Elsevier Science. v.1, p. 261-266.

Hillier S., 2000. Accurate quantitative analysis of clay and other minerals in sandstones by XRD: comparison of a Rietveld and a reference intensity ratio (RIR) method and the importance of sample preparation. Clay minerals, v. 35, p. 291-302.

Hillier S., 2003. Quantitative analysis of clay and other minerals in sandstones by X-ray powder diffraction (XRPD). In: Worden R.H. and Morad S. (eds.) Clay Mineral Cements in

Sandstones. Special Publication of the International Association of Sedimentologists, No. 34, Blackwell Science, Oxford. p. 213-252.

Hitchon B., Gunter W.D., Gentzis T. and Bailey R.T., 1999. Sedimentary basins and greenhouse gases: a serendipitous association. Energy Conversion and Management, v. 40, p. 825 – 843.

Holloway S. and Savage D., 1993. The potential for aquifer disposal of carbon dioxide in the UK. Energy Conversion and Management, v. 34, p. 925-932.

Hower J., Eslinger E.V., Hower M.E. and Perry E.A., 1976. Mechanism of burial metamorphism of argillaceous sediments: I. Mineralogical and chemical evidence. Geological Society of America Bulletin, v. 87, p. 725–737.

Hughes H. and Hurley P.W., 1987. Precision and accuracy of test methods and the concept of K-factors in chemical analysis. Analyst, v. 112, p. 1445-1449.

Huggett J. M. and Shaw H.F., 1993. Diagenesis in Jurassic mudrocks of the North Sea. In: Manning D.A.C., Hall P.L. and Hughes C.R. (eds.) Geochemistry of clay-pore fluid interactions. Chapman & Hall, London. p. 107-126.

Hutcheon I. and Abercrombie H. J., 1990. Carbon dioxide in clastic rocks and silicate hydrolysis. Geology, v. 18 (6), p. 541-544.

IEA Greenhouse Gas R&D Programme, 1999a. Depleted Oil & Gas Fields for CO_2 Storage. http://www.ieagreen.org.uk/ccs.html.

IEA Greenhouse Gas R&D Programme, 1999b. Ocean storage of CO_2. ISBN 1 898 373 25 6. http://www.ieagreen.org.uk/ccs.html.

IPCC Fourth Assessment Report, 2007. Climate Change 2007, http://www.ipcc.ch/index.htm.

Irwin, H., Curtis C. and Coleman M., 1977. Isotopic evidence for source of diagenetic carbonates formed during burial of organic-rich sediments: Nature, v. 269, p. 209-213.

James A.T., 1990. Correlation of reservoired gases using the carbon isotopic compositions of wet gas components. AAPG Bulletin, v. 74 (9), p. 1441-1458.

Jeans C.V. and Fisher M.J., 1986. Diagenesis in Upper Jurassic marine sandstones from the North Sea well 14/26-1 and its significance. Clay Minerals, v. 21, p. 513-535.

Johnson J.W. and Nitao J.J., 2002. Enhanced cap rock integrity and self-sealing of the

immiscible plume through mineral trapping during prograde and retrograde CO_2 sequestration in saline aquifers. Environmental Geosciences. Abstract, v. 9, no. 3, p. 161.

Johnson J.W., Nitao J.J., Steefel C.I. and Knauss K.G., 2001. Reactive transport modeling of geologic CO_2 sequestration in saline aquifers: the influence of intra-aquifer shales and the relative effectiveness of structural, solubility, and mineral trapping during prograde and retrograde sequestration. First National Conference on Carbon Sequestration. Washington, DC. http://www.doe.gov/bridge.

Johnson J.W., Nitao J.J., Steefel C.I. and Knauss K.G., 2004. Reactive transport modeling of CO_2 storage in saline aquifers to elucidate fundamental processes, trapping mechanisms and sequestration partitioning. In: Baines S.J. and Worden R.H. (eds.) Geological Storage of Carbon Dioxide, Geological Society of London, Special Publications 233, p. 107-123.

Jürgen E.S. and Hillis R.R., 2003. Building Geomechanical models for the safe underground storage of carbon dioxide in porous rock. In: Gale J. and Kaya Y. (eds.) Greenhouse gas control technologies. Elsevier Science. v.1, p. 495-500.

Kheshgi H.S., Jain A.K. and Wuebbles D.J., 1996. Accounting for the missing carbon sink with the CO_2 fertilization effect. Climatic Change, v. 33, p.31-62.

Kirste D.M., Watson M.N. and Tingate P.R., September, 2004. Geochemical modelling of CO_2-water-rock interaction in the Pretty Hill Formation, Otway Basin. PESA Eastern Australasian Basins Symposium II. Adelaide.
http://www.co2crc.com.au/PUBFILES/STOR0405/EABS2_Kirste.pdf

Kohl A.L. and Nielsen R.B., 1997, Gas purification. Gulf Publishing Company, Houston, TX, USA.

Larter S.R., Aplin A.C., Bjoroy M., Carpentier B., Chen M., Curtis C., England W.A., Espitalie J., Fleet A.J., Goodwin N.S., Hall P.B., Huc A.Y., Hughes C., Jackson D.E., Jensen H.K.B., Lafargue E., MacAulay G., Macleod G., Oxtoby N.H., Petch G.S., Primmer T., Smalley C.P. and Trabelsi K., 1995. THERMIE Reservoir Geochemistry Project: Miller Field Demonstration. CEC THERMIE Reservoir Geochemistry Project, 44 p.

Lindeberg E., 2002. The quality of a CO_2 repository: what is the sufficient retention time of CO_2 stored underground. In: Gale J. and Kaya Y. (eds.) Proceedings of 6th greenhouse gas control technologies conference, Elsevier, p. 255-260.

Macaulay C.I., Boyce A.J., Fallick, A.E. and Haszeldine R.S., 1997. Quartz veins record vertical flow at a graben edge; Fulmar oil field, central North Sea. AAPG Bulletin, v. 81, p. 2024-2035.

Macaulay C.I., Fallick A.E., McLaughlin O.M., Haszeldine R.S. and Pearson M.J., 1998. The significance of $\delta^{13}C$ of carbonate cements in reservoir sandstones; a region perspective from the Jurassic of the northern North Sea. In: Morad S. (ed.) Carbonate cementation in sandstones: distribution patterns and geochemical evolution. Special Publication of the International Association of Sedimentologists, Blackwell, Oxford, v. 26, p. 395-408.

Macaulay C.I. and Haszedline R.S, 1993. Distribution, chemistry, isotopic composition and origin of diagenetic carbonates: Magnus sandstone, North Sea. Journal of Sedimentary Petrology, v. 63 (1), p. 33-43.

MacKenzie A.S., Price I., Leythaeuser D., Muller P., Radke M. and Schaefer R.G., 1987. The expulsion of petroleum from Kimmeridge Clay source-rocks in the area of the Brae Oilfield, UK continental shelf. In: Brooks J. and Glennie K. (eds.) Petroleum Geology of North West Europe. Graham & Trotman, p. 865-877.

Marchand A.M.E., 2001. Diagenesis and Porosity preservation in deepwater oilfield sandstones, PhD thesis, The University of Edinburgh, Edinburgh, Scotland, 231 p.

Marchand A.M.E., Haszeldine R.S., Smalley P.C., Macaulay C.I. and Fallick A.E., 2001. Evidence for reduced quartz cementation rates in oil-filled sandstones. Geology, v. 29, p. 915-918.

Marchand A.M.E., Macaulay C.I., Haszeldine R.S., and Fallick A.E., 2002. Pore water evolution in oilfield sandstones: constraints from oxygen isotope microanalysis of quartz cement. Chemical Geology, v.191, p. 285-304.

Marchetti C., 1977. On geoengineering and the CO_2 problem. Climate Change, v. 1, no. 1, p. 59-68.

McClue N.M. and Brown A.A., 1990. Miller Field: a subtle Upper Jurassic submarine fan trap in the South Viking Graben, UK Sector North Sea. In: Halburty M.T., (ed.) Giant oil and gas fields of the Decade 1978-1988. AAPG Memoir 54, p. 307-322.

McKenzie D., 1978. Some remarks on the development of sedimentary basins. Earth and Planetary Science Letters, v. 40, p. 25-32.

McLaughlin O.M., Haszeldine R.S. and Fallick A.E., 1996. Quartz diagenesis in layered fluids in the South Brae Oilfield, North Sea. In: Crossey L.J., Loucks R. and Totten M.W., (eds.) Siliciclastic diagenesis and fluid flow: concepts and applications. Society of Economic Paleontologists and Mineralogists Special Publication 55, p. 103-113.

McLaughlin O.M., Haszeldine R.S., Fallick A.E. and Rogers G., 1994. The case of the missing clay, aluminium loss and secondary porosity, South Brae oilfield, North Sea. Clay Minerals, v. 29, p. 651-663.

Metz B., Davidson O., de Coninck H., Loos M. and Meyer L., 2005. IPCC Special Report on Carbon Dioxide Capture and Storage. Cambridge University Press, UK, p. 431.

Moore D.M. and Reynolds R.C., 1997. X-ray diffraction and the identification and analysis of clay minerals, 2nd edition. Oxford University Press, Oxford, p. 378.

Moore J., Adams M., Allis R., Lutz S. and Rauzi S., 2005. Mineralogical and geochemical consequences of the long-term presence of CO_2 in natural reservoirs: An example from the Springerville–St. Johns Field, Arizona, and New Mexico, U.S.A.. Chemical Geology, v. 217, p. 365 - 385.

Murphy P.J. and Roberts S., 1995. Laser Raman spectroscopy of differential partitioning in mixed-gas clathrates in H_2O-CO_2-N_2-CH_4 fluid inclusions: Implication for microthermometry. Geochimica et Cosmochimica Acta, v. 59, p. 4809-4824.

Ohga K., Sasaki K., Deguchi G. and Fujioka M., 2003. Fundamental tests on carbon dioxide sequestration into coal seams. In: Gale J. and Kaya, Y. (eds.) Greenhouse gas control technologies. Elsevier Science, v.1, p. 531-537.

Okamoto I., Li X. and Ohsumi T., 2003. Effects of supercritical CO_2 on the integrity of cap rock. In: Gale J. and Kaya Y. (eds.) Greenhouse Gas Control Technologies. Elsevier Science, v. 1, p. 483-488.

Oxtoby N.H., 1994. The Gyda Field. In: Warren E.A. and Smalley P.C. (eds.) North Sea Formation Waters Atlas. Geological Society of London, Memoir 15, p. 40.

Pasteris J.D., Wopenka B.W. and Seitz J.C., 1988. Practical aspects of quantitative laser Raman microprobe spectroscopy of the study of fluid inclusions. Geochimica et Cosmochimica Acta, v. 53, p. 979-988.

Pearce J.M., Holloway S., Wacker H., Nelis M.K., Rochelle C. and Bateman K., 1996. Natural occurrences as analogues for the geological disposal of carbon dioxide. Energy Conversion and Management, v. 37 (6-8), p. 1123-1128.

Pearson M.J., Watkins D., Pittion J.L., Caston D. and Small J.S., 1983. Aspects of burial diagenesis, organic maturation and palaeothermal history of an area in the South Viking Graben, North Sea. In: Brooks J. (ed.) Petroleum Geochemistry and Exploration of Europe, Geological Society of London, Special Publication 12, Blackwell Scientific Publications Oxford, p. 161-173.

Petch G.S., Aplin A.C., Chen, M., Jachson D.E., Larter S.R., and Macleod G., 1994. Miller THERMIE project final NRG report. University of Newcastle.

Placzek G., 1934. Die Rayleigh und Raman streuung. In: Marx E. (ed.) Handbuch der Radiologie, Akademische Verlagasgesellschaft, Leipzig, v. 6, p. 209-219.

Prosser D.J., Daws J.A., Fallick A.E. and Williams B.P.J., 1993. Geochemistry and diagenesis of stratabound calcite cement layers within the Rannoch Formation of the Brent Group, Murchison Field, North Viking Graben (northern North Sea). Sedimentary Geology, v. 87, p. 139-164.

Ranaweera H.K.A., 1987. Sleipner Vest. In: Spencer A.M. et al. (eds.) Geology of the Norwegian Oil and Gas Fields, Graham & Trotman, London, p. 253-264.

Reeves, S., 2003. Enhanced CBM recovery: Coal-bed CO_2 sequestration assessed. Oil and Gas Journal, v. 101, no. 27, p. 49-53.

Reeves S., Pekot L. and Clarkson C., 2001. Geologic sequestration of CO_2 in deep, unmineable coal-beds: An integrated research and commercial scale field demonstration project, SPE 71749. Proceedings of the SOE Annual Technical Conferences and Exhibition, New Orleans.

Rietveld H.M., 1969. A profile refinement method for nuclear and magnetic structures. Journal of Applied Crystallography, v. 2, p. 65-71.

Roedder E., 1984. Fluid inclusions. Mineralogical Society of America Reviews in Mineralogy. v. 12, 644 p.

Rojey A. and Torp T.A., 2005. Capture and geological storage of CO_2: an overview. Oil & Gas Science and Technology – Review, IFP, v. 60 (3), p. 441-448.

Rooksby S.K., 1991. The Miller Field, blocks 16/7b, 16/8b UK North Sea. In: Abbotts I.L. (ed.) United Kingdom Oil and Gas Fields, 25 years Commemorative volume, Geological Society of London, Memoir 14, p. 159-164.

Rosso K. M. and Bodnar R. J., 1995. Microthermometric and Raman spectroscopic detection limits of CO_2 in fluid inclusions and the Raman spectroscopic characterization of CO_2. Geochimica et Cosmochimica Acta, v. 59, No. 19, p. 3961-3975.

Royal Society of London policy document 12/05, June, 2005. Ocean acidification due to increasing atmospheric carbon dioxide. http://www.royalsoc.ac.uk/document.asp?id=3249.

Ruan C. and Ward C.R., 2002. Quantitative X-ray powder diffraction analysis of clay minerals in Australian coals using Rietveld methods. Applied Clay Science, v. 21, p. 227-240.

Sasada M., 1985. CO_2-bearing fluid inclusions from geothermal fields. 1985 International symposium on geothermal energy, Transactions – Geothermal Resources Council. v. 9, p. 351-356.

Seitz J.C., Pasteris J.D. and Wopenka B., 1987. Characterization of CO_2-CH_4-H_2O fluid inclusions by microthermometry and laser Raman microprobe spectroscopy: Inferences for clathrate and fluid equilibria. Geochimica et Cosmochimica Acta, v. 51, p. 1651-1664.

Scotchman I.C., 1989. Diagenesis of the Kimmeridge Clay Formation, onshore UK. Journal of Geological Society, London, v. 146, p. 285-303.

Scotchman I.C., 1991. The geochemistry of concretions from the Kimmeridge Clay Formation of southern and eastern England. Sedimentology, v. 38, p. 79-106.

Scotchman I.C., 1993. Diagenetic pore fluid evolution in the Kimmeridge Clay Formation: from concretions to sandstone cements, in D. A. C Manning, P. L. Hall, and C.R. Hughes, eds., Geochemist of clay-pore fluid interactions: Chapman & Hall, London, p. 128-159.

Scotchman I.C., Carr A.D., Astin T.R., and Kelly J., 2002. Pore fluid evolution in the Kimmeridge Clay Formation of the UK Outer Moray Firth: implication for sandstone diagenesis: Marine and Petroleum Geology, v. 19, p. 247-273.

Selley R.C., 1976. The habit of North Sea oil. Proceedings of the Geologists Association, v. 87, p. 359-387.

Shaw H.F. and Primmer T.J., 1991. Diagenesis of mudrocks from the Kimmeridge Clay Formation of the Brae Area, UK North Sea. Marine and Petroleum Geology, v. 8, p. 270-277.

Shipton Z.K., Evans J.P., Kirschner D., Kolesar P.T., Williams A.P. and Heath J., 2004. Analysis of CO_2 leakage through 'low-permeability' faults from natural reservoirs in the Colorado Plateau, east-central Utah. In: Baines S.J. and Worden R.H. (eds.) Geological storage of carbon dioxide. Geological Society of London, Special Publications 233, p. 43-58.

Smalley P.C., Primmer T., Garland C., Oxtoby N. and Hopkins M., 1993. Miller Field: reservoir fluid communication and reservoir quality. BP internal report SST/16/93.

Smalley P.C., and Warren E.A., 1994. The Miller Field. In: Warren E.A. and Smalley P.C. (eds.) North Sea formation waters atlas. Geological Society of London, Memoir 15, p. 52.

Smalley P.C., and Warren E.A., 1994. The Buchan Field. In: Warren E.A. and Smalley P.C. (eds.) North Sea formation waters atlas. Geological Society of London, Memoir 15, p. 15.

Sminchak J., Gupta N., Byrer C. and Bergman P., 2002. Journal of Energy and Environmental Reservation. v.2, p. 32.

Smith J.T. and Ehrenberg S.N., 1989. Correlation of carbon dioxide abundance with temperature in clastic hydrocarbon reservoirs: relationship to inorganic chemical equilibrium. Marine and Petroleum Geology, v. 6, p. 129-135.

Snyder R.L. and Bish D.L., 1989. Quantitative analysis. In: Bish D.L. and Post J.E. (eds.) Modern powder diffraction. Reviews of Mineralogy, v. 20, Mineralogy Society of America, USA.

Spence S. and Kreutz H., 2003. The Kingfisher field, Block 16/8a, UK North Sea. In: Gluyas J.G. and Hichens H.M. (eds.) United Kingdom Oil and Gas fields, Commemorative Millenium Volume. Geological Society, London, p. 305 -314.

Stern N., 2006. The economics of climate change, Stern Review. Cambridge University Press.

Stevens S.H., Kuuskraa V.K. and Gale J., 2000. Storage of CO_2 in depleted oil and gas fields: global capacity and barriers to overcome. 5th International Conference on Greenhouse Gas Control Technologies, Cairns, Australia, August p. 13–16.

Stow D.A.V., Bishop C.D. and Mill S.J., 1982. Sedimentology of the Brae Oilfields, North Sea: fan models and controls. Journal Petroleum Geology, v. 5, no. 2, p. 129-148.

Środoń J., 1984 X-ray powder diffraction identification of illitic materials. Clay and Clay minerals, v. 32 (5), p. 337-349.

Taguchi K., Hasegawa K. and Suzuki T., 1988. The relationship between silica minerals and organic matter diagenesis: its implications for the origin of oil. Organic Geochemistry, v. 13, p. 97-107.

Takenouchi S. and Kennedy G.C., 1965. The solubility of carbon dioxide in NaCl solutions at high temperatures and pressures. American Journal of Science, v. 263, p. 445-454.

Tans P., 2007. Globally averaged CO_2 concentration at the surface, full Mauna Loa record. NOAA/ESRL. www.cmdl.noaa.gov/gmd/ccgg/trends.

Thrasher J., and Fleet A.J., 1995. Predicting the risk of carbon dioxide 'pollution' in petroleum reservoirs. In: Grimalt J.O. and Dorronsoro C. (eds.) Organic Geochemistry: Developments and Applications to Energy, Climate, Environment and Human History, Proceedings 17th International Meeting on Organic Geochemistry, San Sebastian, Spain. p. 1086-1088.

Turner C.C. and Allen P.J., 1991. The Central Brae Field, Block 16/7a, UK North Sea. In: Abbotts I.L. (ed.) United Kingdom Oil and Gas Fields, 25 years Commemorative volume. Geological Society of London, Memoir 14, p. 49-54.

Turner C.C., Cohen J.M., Connell E.R. and Cooper D.M., 1987. A depositional model for the South Brae oilfield. in: Brooks J. and Glennie K. (eds.) Petroleum Geology of Northwest Europe. Graham and Trotman, London. p. 853-864

Ulrich M.R. and Bodnar R.J., 1988. Systematics of stretching of fluid inclusions II: barite at 1 atm confining pressure. Economic Geology, v. 83, p. 1037-1046.

Underhill J.R., 1998. Jurassic. In: Glennie K.W. (ed.) Petroleum geology of the North Sea: Basic concepts and recent advances. Blackwell Science. Oxford, p. 245-293.

Wallis R.J. and Milton C., 1994. The Clyde Field. In: Warren E.A. and Smalley P.C. (eds.) North Sea Formation Waters Atlas. Geological Society of London, Memoir 15, p. 19.

Warren E.A. and Smalley P.C., 1994. The Brent Field (including Brent South). In: Warren E.A., and Smalley P.C. (eds.) North Sea formation waters atlas: Geological Society of London, Memoir 15, p. 13.

Watson M.N., Zwingmann N., Lemon N.M. and Tingate P.R., 2003. Onshore Otway Basin carbon dioxide accumulations: CO_2-induced diagenesis in natural analogues for underground storage of greenhouse gas. The Australian Petroleum Production & Exploration Association (APPEA) Journal; v. 43(1), p. 637-653.

Winthaegen P., Arts R. and Schroot B., 2005. Monitoring Subsurface CO2 Storage. Oil & Gas Science and Technology – Rev. IFP, v. 60(3), p. 573-582.

Wopenka B. and Pasteris J.D., 1987. Raman intensities and detection limits of geochemically relevant gas mixtures for a laser Raman microprobe. Analytical Chemistry, v. 59 (17), p. 2165-2170.

Worden R.H. and Barclay S.A., 2000. Internally-sourced quartz cement due to externally-derived CO_2 in sub-arkosic sandstones, North Sea. Journal of Geochemical Exploration, v. 69, p. 645-649.

Worden R.H. and Morad S., 2000. Quartz cementation in oil field sandstones: a review of the key controversies. In: Worden R.H. and Morad S. (eds.) Quartz cementation in

sandstones. Special Publication of International Association of Sedimentologists, no. 29, p. 1-20.

Wycherley H., Fleeta A. and Shaw H., 1999. Some observations on the origins of large volumes of carbon dioxide accumulations in sedimentary basins. Marine and Petroleum Geology, v. 16, p. 489-494.

Young M.J., Gawthorpe R.L. and Hardy S., 2001. Growth and linkage of a segmented normal fault zone: the Late Jurassic Murchison-Statfhord North Fault, northern North Sea. Journal of Structural Geology. v. 23, p. 1033-1952.

Ziegler P.A., 1982. Faulting and graben formation in Western and Central Europe. Philosophical Transactions of the Royal Society of London. A305, p. 113-143.

Zweigel P., Arts R., Bidstrup T., Chadwick A., Eiken O., Gregersen U., Hamborg M., Johanessen P., Kirby G., Kristensen L. and Lindeberg E., 2001. Results and experiences from the first industrial-scale underground CO_2 sequestration case, Sleipner. AAPG Annual Meeting, Denver, Extended Abstract, p. 6.